Noise in adaptive excitable systems and small neural networks

Dissertation
zur Erlangung des akademischen Grades

doctor rerum naturalium
(Dr. rer. nat.)

im Fach Physik

Spezialisierung: Theoretische Physik

eingereicht an der

Mathematisch-Naturwissenschaftlichen Fakultät
der Humboldt-Universität zu Berlin

von

Dipl.-Phys. Justus Alfred Kromer

Präsident der Humboldt-Universität zu Berlin:
Prof. Dr. Jan-Hendrik Olbertz

Dekan der Mathematisch-Naturwissenschaftlichen Fakultät:
Prof. Dr. Elmar Kulke

Gutachter/innen:
1. Prof. Dr. Lutz Schimansky-Geier
2. Prof. Dr. Reynaldo Daniel Pinto
3. Prof. Dr. Alessandro Torcini

Tag der mündlichen Prüfung: 4. März 2016

Abstract

Neurons are excitable systems, i.e. only excitations above a certain threshold can cause a response, a so-called spike. In many cases, even single-neuron dynamics is very complex and the spike generation is shaped by several feedback mechanisms that can act on slow time scales. Those can lead to phenomena like spike-frequency adaptation, reverse spike-frequency adaptation, or bursting. Furthermore, neurons interact with each other, when they are connected in a neural network.

In the present thesis, we examine how spike generation in noise-driven excitable systems is influenced by slow feedback processes and coupling to other excitable systems. To this end, we consider the spike generation in three setups: first in a single excitable system, which is complemented by a slow feedback mechanism, second in a set of coupled excitable systems in the absence and in the presence of feedback, and third in a set of strongly-coupled bursting neurons in the pyloric central pattern generator, a neural network that controls muscles that dilate and constrict the pylorus of crustaceans. In these setups, we investigate the statistics of spiking by the use of analytical methods and computer simulations. Furthermore, in the third case, results are compared to experimental data. Our main objective is to identify mechanisms that allow for an enhancement of certain aspects of the spike generation, for instance, for an increase of the firing rate or for a reduction of spike train variability.

The main result in the first setup is that the interplay of strong positive (excitatory) feedback and noise leads to noise-controlled bistability, a phenomenon that enables excitable systems to switch between different modes of spike generation in response to noisy inputs. In case of the coupled excitable systems, we find that the spike generation of the individual systems is strongly affected by the choice of the coupling strengths and the number of connections. By means of analytical approximations, we are able to predict how coupling and connections should be chosen in order to enforce a given firing rate or spike train variability. In the third scenario, we find that negative feedback causes very irregular behavior in the isolated bursters, while strong coupling to the network regularizes the bursting. Furthermore, we find that certain coupling strengths lead to bursting that enhances the robustness of the network rhythm.

Zusammenfassung

Neuronen sind erregbare Systeme. Das heißt, dass nur Anregungen oberhalb eines bestimmten Schwellwertes eine Reaktion hervorrufen können, einen sogenannten Puls. In vielen Fällen ist bereits die Dynamik einzelner Neuronen sehr komplex und die Erzeugung von Pulsen wird von verschiedenen Rückkopplungsmechanismen beeinflusst, die auf langsamen Zeitskalen agieren. Das kann zu Phänomenen wie Feuerraten-Adaptation, umgekehrter Feuerraten-Adaptation oder zum Feuern von Pulsen in Salven führen. Weiterhin wechselwirken Neuronen miteinander, wenn sie in neuronalen Netzen verbunden werden.

In der vorliegenden Arbeit untersuchen wir wie die Pulserzeugung in erregbaren Systemen, die durch Rauschen getrieben werden, von langsamen Rückkopplungsmechanismen und der Wechselwirkung mit anderen erregbaren Systemen beeinflusst wird. Zu diesem Zweck betrachten wir die Pulserzeugung in drei Szenarien: erstens, in einem einzelnen erregbaren System, das um einen langsamen Rückkopplungsmechanismus erweitert wurde, zweitens, in gekoppelten erregbaren Systemen mit und ohne Rückkopplung und drittens, in stark gekoppelten salvenfeuernden Neuronen im „pyloric central pattern generator“, einem neuronalen Netz, das Muskeln kontrolliert, die den Pylorus von Krustentieren erweitern und zusammenziehen. In jedem dieser Szenarien untersuchen wir die Pulsstatistik mit analytischen Methoden und Computersimulationen. Die Resultate im dritten Fall werden außerdem mit experimentellen Daten verglichen. Unser wichtigstes Ziel ist es Mechanismen zu finden, die eine Verbesserung bestimmter Eigenschaften der Pulserzeugung ermöglichen, also beispielsweise eine Erhöhung der Feuerrate oder eine Reduzierung der Pulszugvariabilität erlauben.

Das wichtigste Resultat im ersten Szenario ist, dass das Zusammenspiel von einer stark anregenden Rückkopplung und Rauschen zu rauschkontrollierter Bistabilität führt, einem Phänomen, das es dem System erlaubt durch verrauschte Anregungen zwischen verschiedenen Modi der Pulserzeugung zu wechseln. Im Falle der gekoppelten erregbaren Systeme beobachten wir, dass die Pulserzeugung stark von der Wahl der Kopplungsstärken und der Anzahl der Verbindungen abhängt. Hier ermöglichen es uns analytische Näherungen vorherzusagen, wie die Verbindungen zwischen den Neuronen und die dazugehörigen Kopplungsstärken gewählt werden müssen um vorgegebene Pulsraten und Pulszugvariabilitäten zu realisieren. Im dritten Szenario stellen wir fest, dass eine hemmende Rückkopplung zu sehr unregelmäßigem Verhalten der isolierten Neuronen führt, wohingegen eine starke Kopplung mit dem Netzwerk ein regelmäßigeres Feuern von Salven hervorruft. Weiterhin erlauben bestimmte endliche Kopplungstärken Salven, die zu einem robusteren Netzwerkrhythmus führen.

Contents

List of symbols

$\delta(x)$	Dirac delta function
δ_{ij}	Kronecker delta
$H(x)$	Heaviside step function
$\xi(t)$	white Gaussian noise of unit intensity
$\langle x \rangle$	ensemble average or average over a set of discrete values
$\overline{x(t)}$	time average of a continuous function
(x_1, x_2)	open interval
$[x_1, x_2]$	closed interval
$[x_1, x_2)$ and $(x_1, x_2]$	half-open intervals
$\mathrm{sgn}(x)$	sign of x
$I_n(z)$	modified Bessel function of the first kind
$\binom{n}{m}$	n choose m

1 Introduction

The unique ability to transmit electrical signals over long distances, makes neurons one of the most fascinating cell types. Generating short electrical pulses – so-called spikes or action potentials – they can communicate with other neurons via synaptic connections and, thereby, transmit and process information about sensory stimuli, control muscle contraction, or give rise to what we call thinking. Since synaptic interaction is usually triggered by the action potentials, the information is mainly encoded in the sequence of spikes – the spike train.

Remarkably, even spike trains of the same neuron display a high trial-to-trial variability in response to identical stimuli. This variability arises from various noise sources and makes a statistical analysis of spike trains indispensable. But how can neurons transmit information about a stimulus if their response is highly irregular and how is the information about the stimulus actually encoded in their spike trains? These questions have been intensively discussed in the past decades. In recent years, two coding schemes seem most promising [26, 53]. First, a rate code [214] in which information about the stimulus is mainly stored in the shape of the firing rate, i.e. in the number of spikes per unit time that is produced by a neuron or a neuronal population and second, a temporal code in which information is stored in the precise timing of individual spikes [42]. However, in both cases the system has to extract the important stimulus-related information from the noisy part. For this purpose, nature has developed various remarkable ways to achieve a most reliable information transfer in noisy environments [170, 263, 71]. For instance, in order to extract rate codes, huge neural populations produce averaged responses to stimuli and, thereby, extract the stimulus-related time-dependent shape of the firing rate and suppress noisy fluctuations [73].

In studies of large neural networks, the dynamics of the individual neurons – being the nodes in the network – is often described by minimal models. These models solely capture the very basic properties, for instance, whether the neuron acts like an excitable system, i.e. the neuron is not capable of producing spikes in the absence of input from other neurons or noisy excitations, or like an oscillator, i.e. it spikes even in the absence of external input.

One of the most popular models, which captures oscillatory dynamics, is the Kuramoto model [148, 147]. In the model, the repetitive spiking of the neuron is mapped on a circle and described by a single phase variable, which determines the position on the circle and, in the absence of input from other cells, evolves according to an intrinsic frequency. Thus, the occurrence of an action potential is associated with a certain value of the phase. In such phase oscillator models, the coupling between neurons is reduced to a coupling between the corresponding phases. This allows for an analytical treatment of collective phenomena in huge populations of oscillators [2]. These phase oscillator models

have become very popular over the past decades in various fields and are frequently used to describe the interaction of oscillatory systems. Furthermore, due to the rather abstract modeling the application of phase oscillator models is not restricted to the field of neuroscience. Some other examples are synchronization in chemical oscillators [131], in the power grid [77, 62], or collective dynamics in financial markets [197]. Consequently, the results obtained for such rather abstract models can often be applied to systems in various fields and allow for an understanding of very basic mechanisms.

Unfortunately, the classical Kuramoto model is only capable of describing oscillatory behavior, whereas one of the most prominent features of neurons is their excitability, i.e. their ability to produces spikes only in response to stimuli or noisy perturbations. In order to extend the classical Kuramoto model to include even excitable dynamics, so-called active rotator models have been introduced [237]. These models can describe both, oscillatory and excitable behavior, as well as transitions between both. Therefore, they are more suited to capture neuronal dynamics. Networks of active rotator models have been intensively studied over the past decades, see for instance refs. [237, 277, 165, 250, 242, 243].

However, even active rotator models are solely capable of capturing most basic properties of the individual neurons' dynamics, namely excitable or oscillatory behavior. This may suffice to describe collective phenomena of huge neural populations, but, in many biological systems single neurons or rather small groups of neurons are critical for the functionality of the system. In such small networks, the neurons' intrinsic dynamics strongly influences network functionality and the interplay of the individual neurons' dynamics, network connectivity, and noise has to be studied in more detail. Furthermore, the reduction of variability may be an even harder task in such systems, since the influence of noise cannot be averaged out in an adequate time window.

Two mechanisms that allow for a reduction of variability at the level of single neurons are stochastic resonance [20, 21, 86] and coherence resonance [202]. These mechanisms were found in various single neuron models [192, 160, 208, 150, 195, 272, 163, 260], neural networks [115, 252], and have been observed in experimental studies even beyond the field of neuroscience [205, 63, 90, 132, 233]. Remarkably, even the simple active rotator model is capable of describing these effects [165], which indicates the universality of these mechanisms in excitable systems. Further mechanisms arise, if neuron models are coupled. In fact, variability in the output of coupled neurons can be much lower than in isolated neurons [115]. In particular it can be reduced by choosing an optimal number of neurons in the network [200, 252] or an optimal network topology [94].

While most studies of these phenomena use rather simple models for the individual nodes, further interesting mechanisms, which allow for a reduction of variability, may arise if individual nodes possess more complex intrinsic dynamics that interacts with that of other neurons in a noisy environment. One prominent example of a network in which individual neurons possess complex intrinsic dynamics is the pyloric central pattern generator (CPG) of *crustaceans*. Here, individual neurons show bursting behavior, i.e. time intervals of fast spiking are separated by intervals in which the neuron is in a resting state and no spikes are produced. CPGs are neurons or neuronal networks that,

when activated, produce a robust rhythm that typically controls muscle contraction [230, 174, 173]. They control, for instance, locomotion of animals and humans [106, 64], breathing [265, 27], and heart beating [44]. Thus, in many cases the robustness of the rhythm with respect to changes of environmental conditions or noisy perturbations is crucial for the organism's survival. Therefore, CPGs have been intensively studied and, especially, the generation of robust rhythms has received huge attention in recent years. The latter has given rise to detailed experimental studies of the interplay of single neuron dynamics and synaptic input, and the influence of changes in environmental condition on both [175, 172, 215]. Remarkably, the pyloric CPG is build out of neurons that display very irregular, often even chaotic dynamics when isolated from the circuit, while their synaptic connection leads to robust network rhythms [211, 232, 213]. In the pyloric CPG the network rhythm is mainly controlled by a pacemaker group, which consists of two groups of neurons that are coupled by a strong electrical synapse. Thus, in the pyloric CPG, the interplay between complex node dynamics and network structure causes a most regular network rhythm.

In order to study systems like the CPG, one has to construct models that capture the complex dynamics of individual neurons. To derive such models, one usually starts from the intrinsic ionic currents that are present in the neuron. By investigating the dynamics of these currents, Alan L. Hodgkin and Andrew F. Huxley were able to derive a mathematical model in the 1950s, which is capable of describing spike generation in the *squid giant axon* [112]. In the last decades, several ionic currents have been identified, which act on the neuron's dynamics on different time scales ranging from a few milliseconds to seconds or even minutes, see for instance [125] for an overview of ionic currents. While fast currents are typically involved in the generation of single spikes, slow currents can lead to patterns in the sequence of interspike intervals. Furthermore, slow currents are influenced by the spiking dynamics itself and thereby act like a slow spike-triggered feedback mechanisms. In particular, such feedback can be positive, i.e. it increases the spike frequency – the inverse interspike interval, or negative, i.e. it decreases the spike frequency. Prominent phenomena caused by slow-feedback mechanisms are spike-frequency adaptation [167, 18] (negative feedback), reverse spike-frequency adaptation [267] (positive feedback), or bursting (usually a combination of both), as it occurs in neurons of the pyloric CPG. The former two describe the response of a neuron to a step-like current, which can be applied by an experimenter. In this setup, spike-frequency adaptation causes a reduction of the spike-frequency among the first interspike intervals, while reverse spike-frequency adaptation leads to an increase of the spike frequency. In particular spike-frequency adaptation is a recent topic in neurophysics and has been studied intensively in neuron models, see for instance [70, 167, 18, 228, 75, 259, 226, 236].

Besides the generation of action potential due to an interplay of electrical currents, Hodgkin and Huxley uncovered a powerful connection between nonlinear dynamics and neuroscience, which was intensified in the following years in rigorous works of FitzHugh [79, 80] and Nagumo [189]. The relation between nonlinear dynamics and neuroscience led to a much deeper geometrical understanding of neural excitability and the generation of spikes in response to external stimuli [216, 125]. Understanding neurons as dynamical

systems, the rhythmic generation of spikes can be associated with oscillations on a stable limit cycle and resting with a stable fixed point in the corresponding dynamical system. Applying methods from nonlinear dynamics allowed for a reduction of Hodgkin-Huxley-like models to several low-dimensional neuron models. Popular examples are integrate-and-fire (IF) models, which are able to reproduce the dynamics of biological neurons remarkably well [76, 123, 124, 38]. However, they have one big disadvantage compared to other models, if indeed, the trace of the membrane potential during a spike is only achieved by an instantaneous reset condition. This results into problems when the exact shape of the spike is needed, as it is, for instance, in case of electrical coupling between neurons [50]. Furthermore, it was shown that not only the presence of excitable or oscillatory behavior, i.e. the presence of limit cycles or fixed points, but also the type of transition between both regimes, i.e. the bifurcations of the dynamical structures, define many characteristics of the spiking behavior [125].

Although reduced models reproduce the dynamics of many neurons very well, they do not account for the influence of slow feedback to the spiking dynamics and are thereby not able to describe complex neuronal behavior, like adaptation or bursting. First steps towards more complex node dynamics have been made by adding a slow feedback mechanism to low-dimensional neuron models, in particular IF models have been extended by an adaptation current [167, 18], which provides negative feedback to the spiking dynamics and is activated during a spike (spike-triggered adaptation) or controlled by the dynamics between spikes (subthreshold adaptation). Both mechanisms have been intensively studied in single IF [167, 190, 255, 228, 259, 238, 226, 236] and networks of IF models [151, 9, 54]. However, much less is known about the influence of positive feedback mechanisms on the spike generation, the behavior of adapting neurons in small networks, or whether the interplay of noise, slow feedback, and coupling to other neurons provides novel mechanisms for variability reduction in the neuron's output.

In order to address these questions, we consider three setups. First a noise-driven active rotator model, which is subject to spike-triggered positive or negative feedback, second a set of coupled active rotators, and third, strongly-coupled bursting neurons in the pyloric central pattern generator. In these setups, we investigate how the spike generation is influenced by the interplay of noise, feedback, and coupling.

This thesis is organized as follows. In the remaining part of the introduction chapter, we introduce the neuron models and statistical analysis techniques that are used later on. In particular, since we use neuron models with different degrees of abstractness throughout this thesis, i.e. active rotator models, integrate-and-fire models, and conductance-based neuron models, we work out the relations between the different models in more detail. In chapter 2, numerical simulation and analyze techniques are presented. In chapter 3, we start with the highest degree of abstractness and study noise and feedback in a single active rotator model. Here, general results on noise in adaptive excitable systems are obtained. In chapter 4, we investigate the spike generation in coupled noisy active rotators in the absence and in the presence of feedback. In particular, we focus on a star network structure. In chapter 5, we extend our investigations to a small neural network, the pyloric CPG, and study electrically-coupled bursting neurons by using a

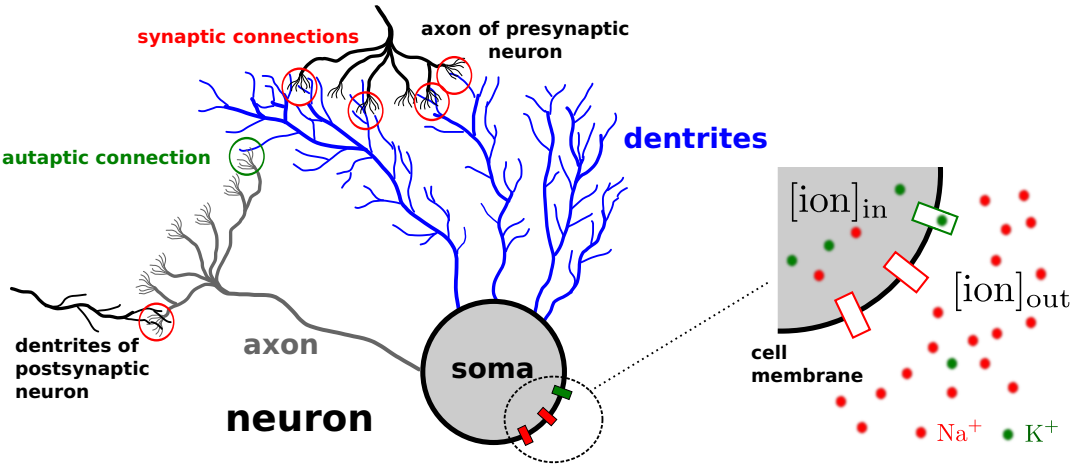

Figure 1.1: Schematic sketch of a neuron and ionic concentration inside and outside the cell.

conductance-based and a noisy integrate-and-fire model, which is subject to negative feedback. The main focus lies on the shaping of the bursting by the interplay of noise, feedback, and coupling. Finally, in chapter 6, we present our conclusions.

1.1 Neuronal dynamics

A neuron typically consists of several dendrites the soma and its axon, see fig. 1.1. Through its dendrites it receives input from other neurons via synaptic connections. On the other hand its axon is connected with the dendrites of other neurons. The soma is the main cell body and its cell membrane has several ion channels that allow ions to pass through the membrane, which generates an electrical current. The flow of each ion species is determined by two forces: the diffusion, which acts contrary to the ion concentration gradient, and the coulomb interaction, which acts in direction of the gradient of the resulting electric potential. In general both forces balance at a nonzero potential difference called equilibrium or reversal potential V_{ion}, which follows from the Nernst equation [193]:

$$V_{\text{ion}} = \frac{RT}{zF} \log \frac{[\text{ion}]_{\text{out}}}{[\text{ion}]_{\text{in}}}. \tag{1.1}$$

'ion' represents the ion type, for instance sodium Na^+, calcium Ca^{2+}, or potassium K^+; R the universal gas constant $8,315$ mJ/K° Mol; T the temperature in K°; F Faraday's constant $96,480$ coulombs/Mol; and z the ion's valence, compare [125] p. 26. Furthermore, $[\text{ion}]_{\text{out/in}}$ represents the ion concentration outside and inside the cell, respectively.

1.1.1 Conductance-based neuron models

In general several ionic currents are present and lead to a potential difference between intra and extracellular space, the membrane potential V. While individual ionic currents vanish when the membrane potential equals the corresponding equilibrium potential, it is proportional to the voltage difference otherwise, i.e.

$$I_{\text{ion}} = g_{\text{ion}}(V - V_{\text{ion}}). \tag{1.2}$$

The proportionality factor is called the conductance g_{ion} corresponding to the particular ion type and is measured in mS/cm^2. Finally, the change of the membrane potential can be obtained by considering the membrane as a capacitor with capacity C_{M}, which is parallel connected with the ionic currents and measured in $\mu\text{F/cm}^2$. Following Kirchhoff's law yields a dynamic equation for the voltage V at the capacitor, i.e. for the membrane potential,

$$C_{\text{M}}\dot{V} = I - \sum_{\text{ions}} I_{\text{ion}}. \tag{1.3}$$

In particular, V is the potential difference between intracellular and extracellular space, thus, inward currents increase V and outward currents reduce V. Furthermore, I is the total current flowing through the membrane, which is measured in $\mu\text{A/cm}^2$. Nonzero I can, for instance, account for external currents that are applied by an experimenter or currents that result from presynaptic input.

Equation (1.3) will typically lead to equilibration at a constant membrane potential. The latter can be obtained by setting the left-hand side to zero. However, individual ion channels are often sensitive to changes of the membrane potential, to changes of ion concentrations in the cell or in the extracellular space, or to changes of the concentration of neuromodulators. All these effects can change the actual values of the ionic conductances. In order to account for voltage-dependent conductances, Hodgkin and Huxley introduced so-called gating variables [112], which describe the probabilistic dynamics of the ion channels. In their famous model of the squid giant axon, they considered the ionic currents for sodium I_{Na} and potassium I_{K}, and a leak current I_{L}. The corresponding ionic currents that have to be considered in eq. (1.3) are:

$$\begin{aligned} I_{\text{Na}} &= g^*_{\text{Na}} m^3_{\text{Na}} n_{\text{Na}} (V - V_{\text{Na}}), \\ I_{\text{K}} &= g^*_{\text{K}} m^4_{\text{K}} (V - V_{\text{K}}), \\ I_{\text{L}} &= g_{\text{L}} (V - V_{\text{L}}). \end{aligned} \tag{1.4}$$

g^*_{ion} represents the maximal conductance and the gating variables m_{ion} and n_{ion} vary between zero and one and can be interpreted as the fraction of open ion channel subunits of the respective ion type. In general there are activating ones, denoted as m_{ion} in eq. (1.4), that open the ion channels and inactivating ones, denoted as n_{ion}, that close the channels. The dynamics of the gating variables is typically given by a first order

differential equation of the form

$$\tau_{\text{ion}}(V)\dot{m}_{\text{ion}} = m_{\text{ion}}^{\infty}(V) - m_{\text{ion}}, \tag{1.5}$$

which is shown for an activation variable here. The time scale $\tau_{\text{ion}}(V)$ depends on the membrane potential and has a unimodal shape and the voltage-dependent equilibrium activation function $m_{\text{ion}}^{\infty}(V)$ has sigmoidal shape. The equilibrium activation function $m_{\text{ion}}^{\infty}(V)$ approaches one for high values of V and zero for low values, i.e. m_{ion} activates the current as V increases. In contrast the equilibrium inactivation function $n_{\text{ion}}^{\infty}(V)$ approaches zero for high and one for low values of V. Consequently, n_{ion} deactivates the ionic current as V increases. Note that Hodgkin and Huxley used a slightly different notation for the dynamics of the gating variables in their original paper [112].

From the general form eq. (1.3) the full class of conductance-based neuron models can be obtained, by considering different sets of ionic currents. One prominent conductance-based model is the Morris-Lecar model of the barnacle giant muscle fiber [186], which we will use in chapter 5. In contrast to the giant axon investigated by Hodgkin and Huxley, experiments indicated that the muscle fiber can be described by considering ionic currents for calcium Ca^{2+} and potassium K^{+} and a leak current I_{L}. The resulting dynamics reads

$$C_{\text{M}}\dot{V} = I - g_L(V - V_{\text{L}}) - g_{\text{Ca}}^{*} m_{\text{Ca}}(V - V_{\text{Ca}}) - g_{\text{K}}^{*} m_{\text{K}}(V - V_{\text{K}}). \tag{1.6}$$

m_{Na} and m_{K} obey first order differential equations like eq. (1.5). In particular, the corresponding equilibrium activation functions are of the form

$$m_{\text{ion}}^{\infty}(V) = \frac{1}{2}\left(1 + \tanh\left[\frac{V - V_{\text{ion},1}}{V_{\text{ion},2}}\right]\right) \tag{1.7}$$

and the time scales are given by

$$\tau_{\text{ion}}(V) = \tau_{\text{ion}}^{*} \cosh^{-1}\left[\frac{V - V_{\text{ion},1}}{2V_{\text{ion},2}}\right]. \tag{1.8}$$

The parameters $V_{\text{Ca},1}$, $V_{\text{Ca},2}$, $V_{\text{K},1}$, $V_{\text{K},2}$, and $\tau_{\text{Ca/K}}^{*}$ are free parameters, that specify the shape of the functions and have to be adjusted to measurements.

1.1.2 Synaptic coupling

Neurons interact via synapses, see fig. 1.1. In general one can distinguish between *chemical synapses* and *electrical synapses*. In chemical synapses, an action potential arriving at the synapse results in the release of neurotransmitters that diffuse through the synaptic cleft to the other side and activate receptors that cause a excitatory or inhibitory postsynaptic current. A common way to model interaction via chemical synapses is to add a current $I_{\text{ch,syn}}(t)$ to the total current I in the conductance-based model eq. (1.3),

see for instance [89]

$$I_{\mathrm{ch,syn}}(t) = -g_{\mathrm{ch,syn}}(t)(V - V_{\mathrm{ch,syn}}). \tag{1.9}$$

$g_{\mathrm{ch,syn}}$ is a time-dependent conductance and $V_{\mathrm{ch,syn}}$ the synaptic reversal potential. The function $g_{\mathrm{ch,syn}}(t)$ shapes the increase and subsequent decay of the synaptic conductance if a presynaptic spike arrives. Furthermore, $V_{\mathrm{ch,syn}} \approx -75\mathrm{mV}$ for inhibitory and $V_{\mathrm{ch,syn}} \approx 0\mathrm{mV}$ for excitatory synapses [89]. The shape of $g_{\mathrm{ch,syn}}(t)$ is usually given by a very fast exponential increase, which is followed by an exponential decay of several milliseconds [53].

In contrast, electrical synapses are connections between different neurons that allow for an exchange of various substances, for instance, ions and neurotransmitters. Usually, electrical synapses are modeled by an additional current $I_{\mathrm{coup}}(t)$ in eq. (1.3), with

$$I_{\mathrm{coup}}(t) = g_{\mathrm{coup}}(V_2 - V). \tag{1.10}$$

g_{coup} is the coupling conductance and V_2 the membrane potential of the second neuron. Such synapses have been studied in various neuronal systems, see refs. [55, 240, 108] for related review articles.

1.2 Noise in neural systems

In addition to highly complex nonlinear dynamics, neurons, like most biological systems, are subject to different sources of noise [73], which can lead to spontaneous activity and trial-to-trial variability in the responses to identical external stimuli [88, 214, 31, 263, 12]. This demands a statistical description of neural spiking and the application of corresponding analyze methods. The latter will be introduced in section 1.7.

Known sources of noise in neural systems are, for instance, *stochastic input from other neurons*, *random opening of ion channels*, and *unreliability of synaptic connections* [165]. We will discuss these sources in more detail in the following.

- *Stochastic input from other neurons*: The human brain consists of some 100 billion neurons with about 10^4 synaptic connections per neuron. Thus, individual neurons are subject to massive synaptic input, which can be regarded as noise in the individual neurons' dynamics [58, 59]. Massive synaptic input is typically considered as the strongest source of noise in neurons that are embedded in large neural networks. A common way to account for such noise in neuron models is to sum up the synaptic currents to a fluctuating current I_{noise} in the voltage dynamics eq. (1.3). Considering independent spiking of the presynaptic neurons, a high input firing rate, and infinitesimal small increments of the neurons' membrane potential per arriving spike, a diffusion approximation can be performed and I_{noise} can be approximated by a white Gaussian noise [45, 152], i.e.

$$I_{\mathrm{noise}} = \sqrt{2D}\xi(t). \tag{1.11}$$

$2D$ is the variance of the noise and $\xi(t)$ has zero mean and is delta correlated, i.e.

$$\langle \xi(t) \rangle = 0, \quad \langle \xi(t)\xi(t') \rangle = \delta(t - t'). \tag{1.12}$$

$\langle x \rangle$ denotes averaging over different realizations of the noise $\xi(t)$. If the finite decay time of the synaptic conductance is considered, the noise becomes correlated in time. Such correlations lead to low-pass filtering of the presynaptic input, see for instance ref. [37]. Although the diffusion approximation is frequently used, it actually neglects any higher order statistics of the incoming spike trains. This is motivated by the assumption that correlations, which are present in the individual spike trains, vanish if many spike trains are summed up. However, recent studies have shown that parts of the higher order statistics of the individual spike trains are still present when the spike trains are summed up [159].

- *Random opening of ion channels*: Channel noise is usually considered to be the strongest internal noise source and arises from the finite number of ion channels and respective channel subunits [224, 266]. While solely the fraction of open subunits enters the Hodgkin-Huxley equation, eqs. (1.3) and (1.4), real neurons possess only a discrete number of channels and corresponding subunits, each switching between open and closed states randomly. This produces deviations from the continuous gating variables in the Hodgkin-Huxley model, which are called channel noise and are most pronounced for small numbers of channels. Depending on the set of gating variables, for instance three activating gates m_{Na} and one inactivating gate n_{Na} for the sodium current in eq. (1.4), which can be either in open or in closed state, each channel can randomly jump between different states. Only if all gates are in open state ions can pass through the channels. Consequently, the individual channel dynamics can be described by a continuous-time Markov process, see, for instance, ref. [98]. Detailed conductance-based neuron models using this approach have been successfully used to describe variability in neural responses, see for instance [57]. A disadvantage of this approach is that the kinetics of each ion channel has to be simulated, which provides high computational costs. In contrast, the description by a stochastic differential equation would cause lower computational costs and provide a connection to the powerful theory of nonlinear dynamics of stochastic systems, see refs. [187, 8, 5, 84] and others. This connection was found by Fox and Lu [83, 82], who derived a *Langevin equation* for the ratio of open channel subunits. Here, fluctuating terms are added to the equations for the activation and inactivation variables, eq. (1.5). However, in general their approach leads to *multiplicative noise*, i.e. the variance of the noisy current in eq. (1.11) depends on the state. This leads to numerical problems that are still subject of recent research, see for instance ref. [156]. Resent research on the modeling of channel noise is reviewed in ref. [93].

- *Unreliability of synaptic connections*: As described in section 1.1.2 an incoming action potential from the presynaptic neuron results into the release of neurotransmitters into the synaptic cleft. This release is highly probabilistic, which

C_M [μF/cm^2]	g_K^* [mS/cm^2]	g_{Ca}^* [mS/cm^2]	V_L [mV]	V_K [mV]	V_{Ca} [mV]	τ_K^* [s]	$V_{Ca,1}$ [mV]	$V_{Ca,2}$ [mV]	$V_{K,2}$ [mV]
20 (chapter 1) 40 (chapter 5)	8	4	−60	−80	120	15	−1.2	18	6

Table 1.1: Parameter values for the Morris-Lecar model according to ref. [257].

leads to fluctuations in the postsynaptic current or even a failure of the synaptic transmission, see for instance refs. [138, 30].

1.3 Reduction techniques

Since the analysis of high-dimensional conductance-based neuron models is often very difficult and the derivation of analytical results in most cases impossible, several reduction techniques have been developed in the past decades. The main idea of these techniques is to reduce the dimension of the system by keeping its main properties unaffected.

1.3.1 Separation of time scales

In many cases, the individual activation and inactivation variables evolve on different time scales. For instance in the Morris Lecar model for the giant muscle fiber eq. (1.6) the times scale of the Ca^{2+} activation is much faster than that of the potassium activation [186]. In such a case the dimension of the model can be reduced by setting

$$m_{Ca} = m_{Ca}^{\infty}(V) \tag{1.13}$$

in eq. (1.6). Hence, $m_{Ca}(V)$ is assumed to approach its equilibrium value instantaneously. The resulting reduced Morris Lecar model reads

$$\begin{aligned} C_M\dot{V} &= I - g_L(V - V_L) - g_{Ca}^* m_{Ca}^{\infty}(V)(V - V_{Ca}) - g_K^* m_K(V - V_K) \\ \tau_K(V)\dot{m_K} &= m_K^{\infty}(V) - m_K \end{aligned} \tag{1.14}$$

and has only two dynamic variables. This allows for a better illustration and analysis of its dynamics.

Further simplifications can be done, if the geometry of spiking is considered. For the reduced Morris Lecar model eq. (1.14), the spiking can be illustrated geometrically in the (V, m_K)-plane, see fig. 1.2. The nullclines – the sets of state variables (V, m_K) for which the right-hand side of the respective line in eq. (1.14) vanishes – are plotted. Setting the right-hand sides of eq. (1.14) to zero, we find for the V-nullcline

$$m_K = \frac{I - g_L(V - V_L) - g_{Ca} m_K^{\infty}(V)(V - V_{Ca})}{g_K(V - V_K)} \tag{1.15}$$

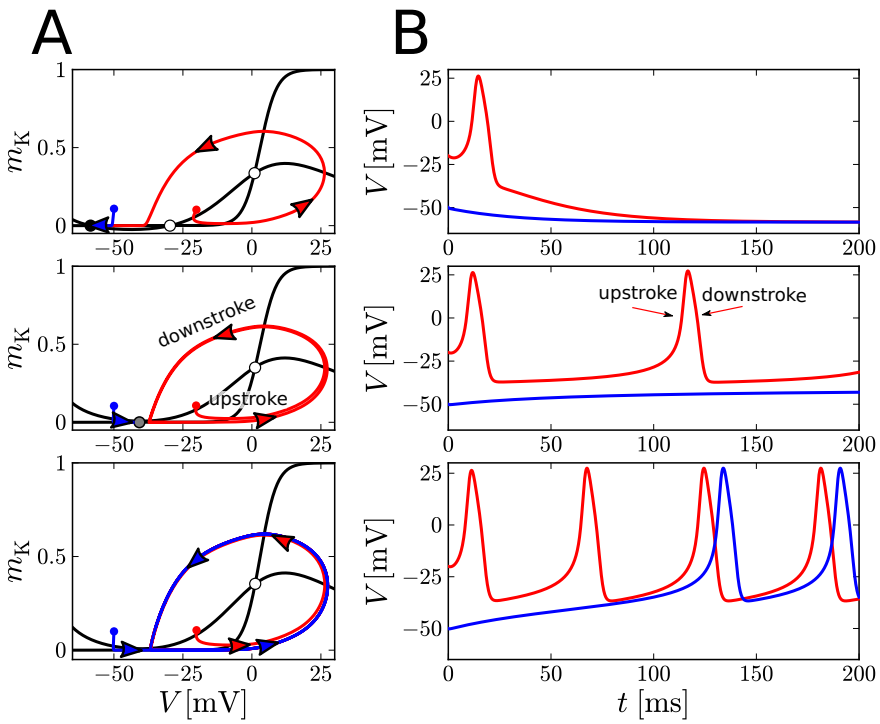

Figure 1.2: Illustration of the dynamics of the reduced Morris-Lecar model, eq. (1.14), in the resting state (top), close to the saddle-node bifurcation (center), and in the spiking state (bottom). Two representative trajectories with different initial conditions (blue and red) are shown in the phase plane (A) and corresponding time traces of the membrane potential in (B). Stable fixed points (black dots), unstable equilibria (white dots), and saddle-nodes (gray dots), as well as the nullclines (black lines) are illustrated. Colored dots mark initial conditions and colored arrows the direction of motion. Parameters: $C_M = 20\ \mu\text{F/cm}^2$, $g_L = 0.8\ \text{mS/cm}^2$, $V_{K,1} = 3\ \text{mV}$ and $I = 0\ \mu\text{A/cm}^2$ (top); $I = 7.56\ \mu\text{A/cm}^2 \approx I_{sn}$ (center); $I = 10\ \mu\text{A/cm}^2$ (bottom). All other parameters are set to the values in table 1.1, which are taken from ref. [257].

and for the m_K-nullcline

$$m_K = m_K^\infty(V). \tag{1.16}$$

Both are illustrated in fig. 1.2A as black lines. Furthermore, fixed points are illustrated as black dots (stable) and white dots (unstable).

In the resting state, trajectories with different initial conditions are attracted by a equilibrium (or fixed point). Thus, the membrane potential relaxes to a constant equilibrium value. While initial conditions beyond a certain voltage threshold cause the occurrence of a spike before the system decays to the resting state (red curve in fig. 1.2A-B, top), small perturbations from the resting state solely decay (blue curve in fig. 1.2A-B, top). If I increases, the low-voltage stable and unstable equilibria approach and, finally, annihilate at $I = I_{sn}$ in a saddle-node bifurcation (fig. 1.2, center). For I close

to, but smaller than I_{sn} the system is bistable, i.e. depending on the initial conditions the system either relaxes to the resting state (blue curve in fig. 1.2A-B, center) or to a limit cycle, which corresponds to the spiking state (red curve in fig. 1.2A-B, center). For higher values of I no stable fixed point exists in the range of physically-plausible voltage values and trajectories are attracted by the stable limit cycle, see fig. 1.2 (bottom). Oscillations on that cycle cause periodic spiking behavior.

Besides a saddle-node bifurcation between resting and spiking state, several other bifurcations are possible, see sec. 1.4. Each bifurcation causes distinct geometrical properties, which allow for applying respective geometrical reduction techniques. In this thesis, we focus on the saddle-node bifurcation and present the corresponding techniques that are used in chapter 5.

1.3.2 Geometric reduction

In fig. 1.2 a saddle-node bifurcation occurs at $I \approx I_{\mathrm{sn}}$ in the Morris-Lecar model and leads to the annihilation of the resting state equilibrium with one of the unstable equilibria. In the vicinity of the bifurcation, the system spends most of the time in the low-voltage region, where both nullclines are close to each other and the shape of the voltage nullcline is approximately parabolic. Following dynamical systems theory [247, 125] the dynamics of the Morris-Lecar model in this region is *topologically equivalent* to the system

$$\dot{v} = \Delta I + v^2. \tag{1.17}$$

The latter is called the *topological normal form* of the saddle-node bifurcation. v is a rescaled membrane potential and ΔI a bifurcation parameter. In the following, we consider the injected current I as the bifurcation parameter, which yields

$$\Delta I \propto I - I_{\mathrm{sn}}. \tag{1.18}$$

The easiest way to bring the Morris-Lecar model into the normal form is to approximate the sum of the currents in the eqs. (1.14)– or in the full Morris-Lecar model eq. (1.6) – close to the saddle node by a parabola of the form [125]

$$C_{\mathrm{M}}\dot{V} = I - I_{\mathrm{L}} - I_{\mathrm{Ca}} - I_{\mathrm{K}} \approx I - I_{\mathrm{sn}} + k(V - V_{\mathrm{sn}})^2. \tag{1.19}$$

I_{L}, I_{Ca}, and I_{K} represent the leak, the calcium, and the potassium currents, respectively. For the set of parameters shown in fig. 1.2, we find $I_{\mathrm{sn}} \approx 7.56\ \mu\mathrm{A/cm^2}$, $V_{\mathrm{sn}} \approx -40.894$ mV, and $k \approx 1.3 * 10^{-4}\ \mu\mathrm{A/cm^2mV^2}$. Finally, a rescaling of the membrane potential and the system time yields the normal form eq. (1.17). Note that the reduction becomes more complicate, when the bifurcation parameter is not the injected current.

The location of the fixed points in eq. (1.17) can be easily obtained by setting $\dot{v} = 0$. Depending on the sign of ΔI, this yields a regime with two fixed points ($v_{\mathrm{fp}} = \pm\sqrt{\Delta I}$) for negative ΔI and no fixed points for positive ΔI. At $\Delta I = 0$ the saddle-node bifurcation

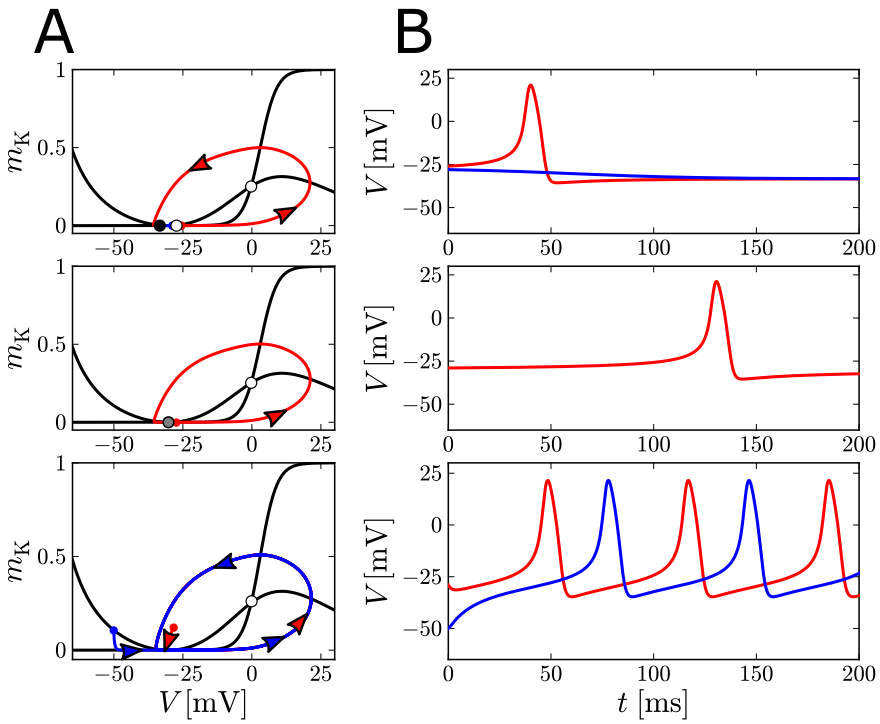

Figure 1.3: Illustration of the dynamics of the reduced Morris-Lecar model, eq. (1.14), in the resting state (top), close to the saddle-node on invariant circle bifurcation (center), and in the spiking state (bottom). Symbols are chosen like in fig. 1.2. Parameters: $g_L = 2.3$ mS/cm^2 and (top) $I = 44.52$ μA/cm^2; (center) $I = 45.52$ μA/cm^2 $\approx I_{sn}$; (bottom) $I = 50$ μA/cm^2. All other parameters are set to the values used in fig. 1.2

occurs. In order to obtain a spiking neuron model from the *topological normal form*, it is convenient to introduce a cutoff voltage v_{cut} and a reset voltage v_{res}. Due to the quadratic term in eq. (1.17) the rescaled voltage v runs to infinity in a finite time for $\Delta I > 0$ or $\Delta I < 0$ and $v > \sqrt{\Delta I}$, which accounts for the spike upstroke. Next, the system is said to spike if $v = v_{cut}$ and the spike's downstroke is realized by an instantaneous voltage reset to $v = v_{res}$, i.e.

$$\text{if } v = v_{cut}, \text{ do } v \to v_{res}. \tag{1.20}$$

Equation (1.17) combined with the reset condition eq. (1.20) is called the quadratic-integrate-and-fire (QIF) neuron. Versions of the QIF neuron have been used in various numerical and analytical studies, see for instance [36, 164, 238].

Interestingly, two kinds of saddle-node bifurcations can be obtained in the QIF model. First, the same kind of bifurcation, as presented in fig. 1.2. Here, the trajectories in the resting state relax towards the stable fixed point, by coming from higher voltage values and, for $I = I_{sn}$, the periodic orbit does not reach the saddle-node point. This leads to $v_{res} > 0$ in the normal form. This kind of saddle-node bifurcation will be referred to

as *Fold* in the following. In contrast, $v_{\mathrm{res}} < 0$ accounts for another kind of saddle-node bifurcation, a *saddle-node on invariant circle bifurcation*, which will be referred to as *Circle*. A *Circle* bifurcation occurs in the Morris-Lecar model for a slightly different choice of parameters, see fig. 1.3. In the resting state, trajectories that start from initial conditions between the stable and unstable fixed points approach the stable fixed point directly, but trajectories that start from high voltage values make a large excursion around the second unstable fixed point and, in contrast to the Fold bifurcation, approach the stable fixed point by coming from low voltages values. Furthermore, there is an invariant circle to the saddle-node at the *Circle* bifurcation (red in fig. 1.3, center). This has several consequences for the spike generation, which will be discussed in section 1.4.

The combination of a first order equation like eqs. (1.17) for the membrane potential and the reset condition, eq. (1.20), can be generalized to the class of one-dimensional integrate-and-fire models, which follow from approximating the shape of the V-nullcline by other functions $f(V)$. Thus, the dynamics of the rescaled membrane potential becomes

$$\dot{v} = I + f(v). \tag{1.21}$$

Besides the QIF model, other choices of $f(v)$ lead to the popular leaky-integrate-and-fire model ($f_{\mathrm{leaky}}(v) \propto -v$), which only accounts for the voltage dynamics at low voltage values, see for instance [38, 39], and the exponential integrate-and-fire model in which an exponential term is added to $f_{\mathrm{leaky}}(v)$ [81, 32]. Furthermore, the low-voltage region in the spiking state can be described by $f(v) = 0$, which yields the perfect integrate-and-fire model. In order to account for noisy perturbations different noise sources can be added to the dynamics. Noisy versions of the different integrate-and-fire models have been intensively studied in the last ten to fifteen years and it has been shown that theses rather simple models are capable of describing a variety of neuronal behavior, see for instance ref. [203, 163, 36, 157, 48, 165, 227].

Other popular models can by obtained, if an approximation of the shape of the v-nullcline and a linear approximation of the m_{K}-nullcline close to the fixed point are considered. The resulting system has two dynamic variables and the form [254]

$$\begin{aligned} \dot{v} &= f(v) - w + I \\ \dot{w} &= a(bv - w). \end{aligned} \tag{1.22}$$

w is an inhibitor variable and has a similar role as m_{K} in the reduced Morris-Lecar model. While a and b describe the shape of the second nullcline close to the fixed point, $f(v)$ approximates the voltage nullcline. One popular model, which considers a quadratic function for $f(v)$, is the so-called 'Izhikevich model' [123, 124]. A second, much older model, which has the form of eq. (1.22), but does not need a reset condition due to a cubic shape of $f(v)$, is the Fitz-Hugh-Nagumo model [80, 189]. In the last decades noisy versions of the Fitz-Hugh-Nagumo model have been studied as well [160, 34].

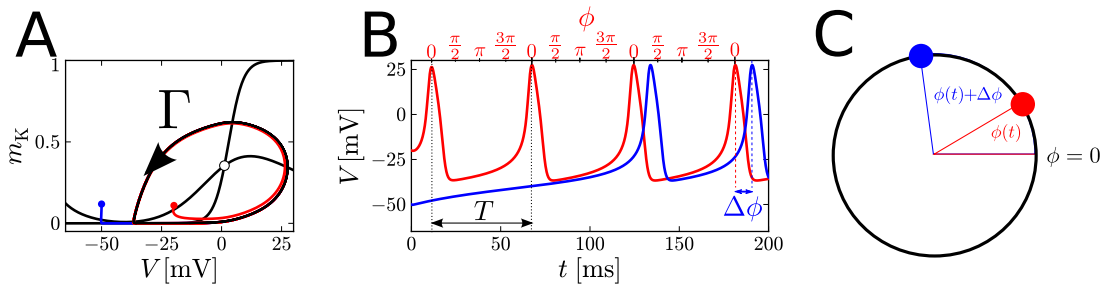

Figure 1.4: Illustration of the phase reduction for the reduced Morris-Lecar model, eq. (1.14), in the spiking state, see fig. 1.2 (bottom). A: phase portrait of the periodic orbit $\mathbf{\Gamma}$ and trajectories from two initial conditions (red and blue) that converge to it; B: Time trace of the membrane potential for both trajectories; C: illustration of the corresponding asymptotic phases on the unit circle. Parameters: same as in fig. 1.2 (bottom).

1.3.3 Phase reduction

Another reduction technique can be applied if the system evolves on a limit cycle, like the Morris-Lecar model in fig. 1.2 (bottom). In that case the interspike intervals equal the period of the limit cycle oscillations T. A general approach, which goes beyond the field of neuroscience and can be applied to most oscillatory systems, is the concept of *phase reduction*. Consider a dynamical system of the form

$$\dot{\mathbf{X}} = \mathbf{f}(\mathbf{X}(t)), \tag{1.23}$$

which has a periodic orbit given by $\mathbf{\Gamma}$. $\mathbf{X}$ is the vector of state variables. The points on the periodic orbit can be parametrized by a single phase variable ϕ, which describes a point on the unit circle, such that

$$\mathbf{X}(t) = \mathbf{\Gamma}(\phi(t)) \tag{1.24}$$

describes all points on the T periodic orbit. Consequently, $\mathbf{\Gamma}(\phi(t)) = \mathbf{\Gamma}(\phi(t+T))$, see illustration in fig. 1.4A and 1.4B. Using eq. (1.24), we can transform the dynamical system, eq. (1.23), into an equation for the phase dynamics

$$\dot{\phi} = g(\phi(t)). \tag{1.25}$$

In particular, if a proper parametrization of $\mathbf{\Gamma}$ is chosen, for instance if ϕ is chosen proportional to the time, the function $g(\phi(t))$ becomes a constant $g(\phi(t)) \to \Omega_0$ and

$$\dot{\phi} = \Omega_0. \tag{1.26}$$

Thus, if $\phi \in [0, 2\pi)$, $\Omega_0 = 2\pi/T$ is the frequency of limit cycle oscillations. Now, the spiking of a neuron can be mapped on the unit circle, see fig. 1.4.

The phase ϕ is well-defined when the system evolves on the periodic orbit, however,

small perturbations may cause deviations from that orbit. In order to include such deviations in the phase description, the definition of the phase has to be extended to an environment of $\mathbf{\Gamma}$. In this context, a well-accepted approach is that of the asymptotic phase [51]. The asymptotic phase is obtained by comparing trajectories with different initial conditions in the periodic orbit's basin of attraction. As t runs to infinity the trajectories are attracted by the cycle and approach it in the limit of $t \to \infty$. However, in general the trajectories will possess finite phase shifts $\Delta\phi$ in the limit $t \to \infty$, which depend on the respective initial conditions, see blue and red trajectories in fig. 1.4. These phase shifts are used to extend the definition of the phase to the starting points of the trajectories. Applying this concept to all points in an environment, which lies in the periodic orbit's basin of attraction, yields phase shifts for any two points in the environment. In particular, sets of points with zero phase shifts are called isochrons and mapped on the same phase. Finally, defining a isochron that is mapped on $\phi = 0$ yields a well-defined phase for all points in the environment. Throughout this thesis, we will map the isochron, which passes the high-voltage end of $\mathbf{\Gamma}$ on $\phi = 0$. Thus, $\phi = 0$ marks spikes of the neuron and, thus, the beginnings of the interspike intervals, see illustration in fig. 1.4B. Obviously, the approach of the asymptotic phase causes problems in the presence of noise in which the phase shift is additionally altered by the realization of noise perturbations. For such systems, the definition of the phase is still subject of recent research, see for instance [225, 251, 198].

In order to account for small perturbations from the cycle, for instance due to phase-dependent forces or inputs from other oscillators, a phase-dependent sensitivity function $\mathbf{Z}(\phi(t))$ was introduced by Winfree [268, 269]. It describes the phase-dependent change of the *instantaneous frequency* $\dot{\phi}$ due to delta-like perturbations in the system coordinates $\mathbf{\Pi}(\phi)$. This can be used to describe coupling between oscillators. Weak coupling between oscillators hardly affects the shape of the limit cycle and the coupling can be described as a coupling of the oscillators phases. Considering the phase-dependent sensitivity function $\mathbf{Z}(\phi)$, the influence of the jth oscillator on the ith oscillator's phase can be described by

$$\dot{\phi}_i \quad = \quad \Omega_i + \epsilon \mathbf{Z}_i(\phi_i) \cdot \sum_{j=1}^{N} \mathbf{C}_{ij}(\mathbf{\Gamma}_i(\phi_i(t)), \mathbf{\Gamma}_j(\phi_j(t))). \tag{1.27}$$

ϵ is a small parameter, $\cdot$ marks the scalar product, and $\mathbf{C}_{ij}(\mathbf{X}_i, \mathbf{X}_j)$ describes the coupling between the ith and j oscillator. If the phases are rescaled according to $\theta_i = \phi_i/\Omega_i$, this can be rewritten into

$$\dot{\theta}_i \quad = \quad 1 + \epsilon \sum_{j=1}^{N} m_{ij}(\theta_i, \theta_j). \tag{1.28}$$

We introduced $m_{ij}(\theta_i, \theta_j) = \mathbf{Z}_i(\Omega_i\theta_i) \cdot \mathbf{C}_{ij}(\mathbf{\Gamma}_i(\Omega_i\theta_i(t)), \mathbf{\Gamma}_j(\Omega_j\theta_j(t)))/\Omega_i$. Next, by introducing the phase differences ψ_i from a common oscillation $\theta_i = t + \psi_i$, we can transform

eq. (1.28) into

$$\dot{\psi}_i \;=\; \epsilon \sum_{j=1}^{N} m_{ij}(t+\psi_i, t+\psi_j). \tag{1.29}$$

Since the coupling is weak ($\epsilon \ll 1$), the phase differences ψ_i evolve slowly compared to the individual periods T_i and, the function $m_{ij}(t+\psi_i, t+\psi_j)$ can be approximated by its time average [221]

$$M_{ij}(x) := \lim_{T\to\infty} \frac{1}{T} \int_0^T dt \;\; m_{ij}(t, t+x). \tag{1.30}$$

This, yields

$$\dot{\psi}_i \;\approx\; \epsilon \sum_{j=1}^{N} M_{ij}(\psi_j - \psi_i) \to \dot{\theta}_i \approx 1 + \epsilon \sum_{j=1}^{N} M_{ij}(\theta_j - \theta_i) \tag{1.31}$$

and, thus, the components $M_{ij}(x)$ of the coupling function depend only on the phase difference between the oscillators. Furthermore, the x-dependence of $M_{ij}(x)$ vanishes in the limit of $T \to \infty$ unless the periods T_i and T_j are integer multiples of each other, i.e. $nT_i = mT_j$ with integers n and m. A popular choice of $M_{ij}(\theta_j - \theta_i)$ for attractive coupling between oscillators is

$$M_{ij}(\theta_j - \theta_i) = \sin(\theta_j - \theta_i). \tag{1.32}$$

This choice has been introduced by Y. Kuramoto [148, 147] and yields a solvable model that describes the synchronization of infinitely many, all-to-all coupled oscillators. Therefore, we use this coupling function in chapter 4. The fact that weak coupling between different oscillators can be reduced to a coupling of the oscillators phases, is the main advantage of the phase reduction and allows for an analytical treatment of systems of coupled oscillators [148, 147].

The phase description, eq. (1.25), can be extended to excitable systems by introducing zeros in the function $g(x)$. Then, the system does not describe limit cycle oscillations anymore and the zeros of $g(x)$ correspond to the fixed points of the dynamical system. Throughout this thesis, we consider *active rotator models* in which the phase dynamics is given by

$$\dot{\phi} = \omega_0 + G(\phi). \tag{1.33}$$

In particular the choice $G(\phi) = -e\sin(\phi)$ resembles an excitable system in the vicinity of a Circle bifurcation. The corresponding phase dynamics reads

$$\dot{\phi} = \omega_0 - e\sin(\phi). \tag{1.34}$$

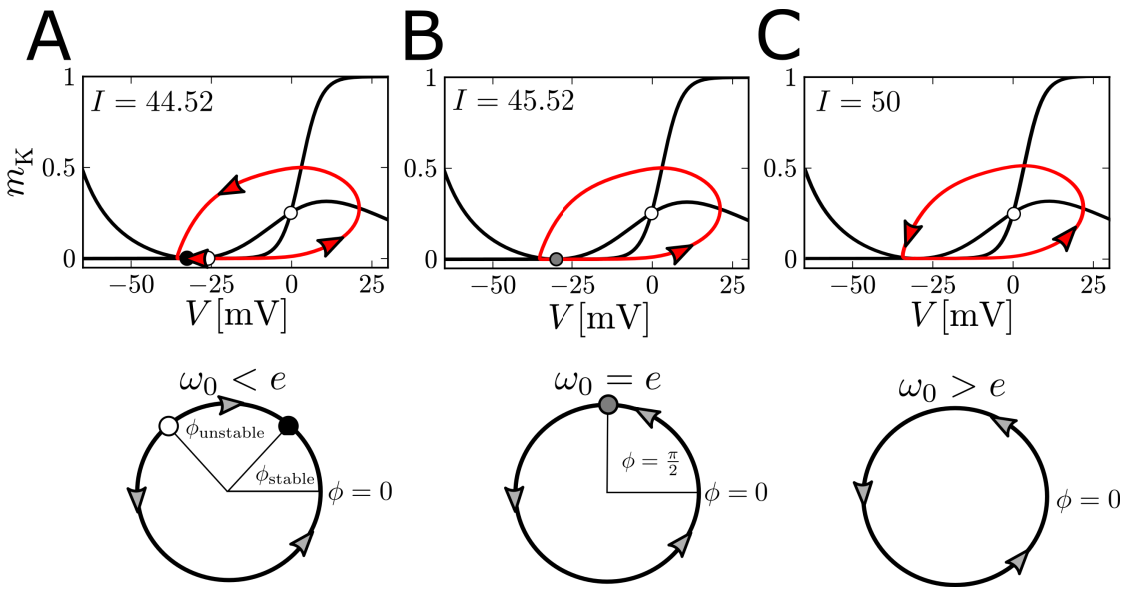

Figure 1.5: Comparison of the phase portraits of the reduced Morris-Lecar model (top), eq. (1.14), in the resting state (A), at the Circle bifurcation (B), and in the spiking state (C), with corresponding regimes in the active rotator model eq. (1.34) (bottom). Parameters for the Morris-Lecar model are the same as in fig. 1.3 (bottom).

and is known as *Adler's equation* [3]. ω_0 is a driving parameter and e scales the strength of the phase-dependent forcing. Furthermore, the Circle bifurcation occurs at $\omega_0 = e$ and separates a regime with a stable fixed point at $\phi_{\mathrm{stable}} = \arcsin(\omega_0/e)$ and an unstable fixed point at $\phi_{\mathrm{unstable}} = \pi - \arcsin(\omega_0/e)$ for $\omega_0 < e$ from a regime, in which the phase increases monotonically for $\omega_0 > e$. At $\omega_0 = e$ both fixed point annihilate in a Circle bifurcation. Thus, eq. (1.34) causes similar dynamics as presented for the Morris-Lecar model in fig. (1.3). This is illustrated in fig. 1.5. In particular, the driving parameter ω_0 switches the system between resting and spiking state and, therefore, has a similar role as the external current I in the Morris-Lecar model, eq. (1.14). Adler's equation is also often used beyond the field of neuroscience, for instance, to describe excitability in laser systems with optical feedback [87, 95], or the onset of resistance in superconducting Josephson junctions [244, 247]. Furthermore, active rotator models are frequently used to study synchronization of excitable units [237, 277, 250, 139, 242, 243].

Of particular interest in this thesis is the noisy *Adler's equation*:

$$\dot{\phi} = \omega_0 - e\sin(\phi) + \sqrt{2D}\xi(t). \tag{1.35}$$

The noise intensity is scaled by the parameter D and $\xi(t)$ is zero mean and delta-correlated white Gaussian noise, eq. (1.12). Note that we consider just the simplest case of a constant noise intensity D, which accounts for stochastic fluctuations in the direction of the limit cycle. However, if the active rotator model is derived from a conductance-based neuron model close to a Circle bifurcation, which includes noisy terms, it contains

a multiplicative noise and is called Θ-neuron [68, 100, 165].

Equation (1.35) can be transformed in dimensionless units by dividing both sides by e and introducing the dimensionless parameters

$$\begin{aligned} \tilde{\omega_0} &:= \frac{\omega_0}{e} \\ \tilde{D} &:= \frac{D}{e} \end{aligned} \tag{1.36}$$

and applying the transformations

$$\begin{aligned} \tilde{t} &:= et \\ \tilde{\xi}(\tilde{t}) &:= \frac{\xi(t)}{\sqrt{e}}. \end{aligned} \tag{1.37}$$

This yields the noisy Adler's equation in dimensionless units

$$\dot{\phi} = \tilde{\omega_0} - \sin(\phi) + \sqrt{2\tilde{D}}\tilde{\xi}(\tilde{t}). \tag{1.38}$$

In chapter 3 and 4 we study single active rotators and networks of active rotators with node dynamics given by eq. (1.38), which are subject to a feedback. The latter will be motivated in section 1.5.

1.4 Excitability

As we saw in fig. 1.2 for the Morris Lecar model, the injection of a current can excite a neuron in resting state and lead to spike generation. In 1948 Alan L. Hodgkin [111] studied the onset of spiking in response to step currents of different amplitudes and observed two major types of behavior[1]. He classified these types as *Class 1 excitability* – the neuron can spike at arbitrary low spike frequencies – and *Class 2 excitability* – spikes occur at a finite frequency, which is relatively insensitive to the amplitude of the step current. Here and in the following, we refer by spike frequency to the inverse interspike intervals. Later on, by applying dynamical systems theory, it was found that the classes of excitability are connected to the type of bifurcation that leads to the vanishing of the stable fixed point, corresponding to the resting state [121, 125], when an external current is injected. If we restrict on bifurcations of codimension one, which are most observable in nature since they require just one bifurcation parameter, there are only four possible types of bifurcations [99] that cause the vanishing of a stable fixed point (or its loss of stability). These and the related spiking properties are listed below. Note that we use the notation of Izhikevich [125].

- *Saddle-node bifurcation* (Fold): The stable equilibrium annihilates with an unstable one, see illustration in fig. 1.2. After the bifurcation, the spike frequency and the

[1] He also introduced *Class 3 excitability* for which a step current is followed by a single spike in a broad range of step current amplitudes.

spike amplitudes are relatively insensitive to changes of the injected current. This bifurcation leads to Class 2 excitability.

- *Saddle-node on invariant circle bifurcation* (Circle): The stable equilibrium annihilates with an unstable one. At the saddle-node bifurcation there is an invariant circle to the saddle-node, see fig. 1.3. The spikes' amplitudes are relatively insensitive to changes of the injected current, but the spike frequency increases according to

$$f(I) \propto \sqrt{I - I_{\mathrm{sn}}}, \quad I > I_{\mathrm{sn}}, \tag{1.39}$$

  if I passes its value at the bifurcation I_{sn}. This bifurcation leads to Class 1 excitability.

- *Supercritical Andronov-Hopf bifurcation* (Hopf): The stable equilibrium becomes unstable and a stable periodic orbit with zero amplitude is born. The spike amplitude increases according to

$$A(I) \propto \sqrt{I - I_h}, \quad I > I_{\mathrm{h}}, \tag{1.40}$$

  if I passes its value at the bifurcation I_{h}. For $I < I_h$ but close to I_h small deviations from the stable equilibrium result in subthreshold oscillations. This bifurcation leads to Class 2 excitability.

- *Subcritical Andronov-Hopf bifurcation* (subHopf): An unstable periodic orbit joins the stable equilibrium, which loses stability. For subHopf bifurcations, both, the spike amplitude and the spike frequency are relatively insensitive to the injected current. Furthermore, small perturbations result in subthreshold oscillations. This bifurcation leads to Class 2 excitability.

The two former bifurcations occur in so-called *integrator* neurons in which the behavior is dominated by a Fold or Circle bifurcation. In such neurons, each excitation with sufficiently high amplitude evokes a response. Thus, the occurrence of a spike solely depends on the amplitude and not on the frequency of excitations. In contrast, the two later bifurcations result in subthreshold oscillations and corresponding neurons are called *resonator* neurons. These neurons can resonate with excitations of particular frequencies, i.e. excitations of certain frequencies can cause a spiking response, while excitations at other frequencies do not. A popular reduced model for such neurons is the resonate-and-fire model [122], which has also been studied in the presence of noise, see for instance refs. [264, 66].

1.5 Slow spike-triggered feedback mechanisms

The geometric reduction or the phase reduction techniques, which have been presented in the sections 1.3.2 and 1.3.3, respectively, lead to simple models for the different types of

excitability. However, many neurons are subject to several slow feedback processes that influence their spike generation on a slow timescale, i.e. slow compared to the individual interspike intervals (ISI)s. Prominent phenomena that are caused by such processes are spike-frequency adaptation, reverse spike-frequency adaptation, and bursting. While bursting refers to slow switching between a spiking and a resting state, both, spike-frequency adaptation and reverse spike-frequency adaptation are observed in neurons that are excited by a step current. In particular they describes the shape of the spike frequency of the first spikes after the application of the current. In case of spike-frequency adaptation, the spike frequency decreases among the first spikes, whereas it increases in case of reverse spike frequency adaption.

Throughout this thesis, we focus on a special kind of feedback, which is called spike-triggered feedback. Such feedback is solely controlled by the timing of the spikes. We distinguish between a negative feedback, i.e. a spike temporally inhibits the neurons, and positive feedback, i.e. a spike temporally excites the neuron. If the dynamics is dominated by a negative feedback mechanisms, which acts on a time scale that is slow compared to the interspike intervals of the neuron, spike-frequency adaptation can be observed. In contrast if positive feedback dominates, reverse spike-frequency adaptation can be observed. Furthermore, bursting typically occurs due to an interplay between a positive feedback, which causes the onset of spiking, and negative feedback, which ends the spiking.

1.5.1 Spike-frequency adaptation

Spike-frequency adaptation has been extensively studied in the last decades in neurophysics, see for instance [167, 18, 228, 11, 259, 151, 236]. Furthermore, several sources of negative feedback in neurons have been identified. Examples are: voltage-gated potassium currents (M-type currents), the interplay of calcium currents and the intracellular calcium dynamics with calcium gated potassium channels (AHP-type currents), and the slow recovery from inactivation of fast sodium currents. The influence of these mechanisms has been studied in various neuron models and it has been shown that their influence on the spike generation can be covered by adding a single adaptation current to the voltage-dynamics in conductance-based neuron models, eq. (1.3) [18]. In reduced models, a common approach is to implement a spike-triggered negative feedback mechanism, i.e. one feedback variable is added, which receives an instantaneous offset when a spike occurs, decays on a slow time scale during the interspike intervals, and inhibits the generation of spikes. In the last decades, such feedback has been implemented in different biologically plausible ways. Prominent example have been presented, for instance, by Liu and Wang [167]. In their work, two implementation of such feedback were studied. At first they considered a leaky integrate-and-fire model, see eq. (1.21) with $f(c) \propto -v$, similar to that studied by Treves before [256], which is complemented by an AHP-type current $I \to I + I_{\mathrm{AHP}}$

$$I_{\mathrm{AHP}} = -g_{\mathrm{AHP}}[\mathrm{Ca}^{2+}]_{\mathrm{in}}(V - V_{\mathrm{K}}). \tag{1.41}$$

g_{AHP} is the maximum conductance and V_{K} the reversal potential for potassium, see tab. 1.1. In this model, the feedback variable is the intracellular calcium concentration $[\mathrm{Ca}^{2+}]_{\mathrm{in}}$. Each spike causes a calcium influx, which is modeled by an instantaneous offset to $[\mathrm{Ca}^{2+}]_{\mathrm{in}}$ after each spike. Between spikes $[\mathrm{Ca}^{2+}]_{\mathrm{in}}$ decays exponentially on a slow[2] time scale τ. Since V_{K} is below physically plausible values of V, I_{AHP} provides a spike-triggered negative feedback to the voltage dynamics. Note that the implementation in a leaky integrate-and-fire model neglects the influence of such currents on the shape of the spike. Nevertheless, the approach of Liu and Wang is able to capture the effect of spike-frequency adaptation on neural spiking very well. In the second model, the negative feedback was realized by a dynamic spiking threshold for the integrate-and-fire model. In the model, the distance between cutoff v_{cut} and reset voltage v_{res} has been increased after each spike and decays exponentially on the slow[3] time scale τ. Models with dynamic threshold have also been studied by other authors, see, for instance, refs. [48, 19, 11] and references therein.

An even simpler way to account for spike-frequency adaptation was proposed in refs. [18, 123]. In particular, in ref. [123] the feedback arises from a spike-triggered adaptation current u, which is added to the QIF model. This current receives an offset d after each spike and decays exponentially during ISIs on a slow time scale τ. Such an integrate-and-fire model is described by the dynamics [123]

$$\begin{aligned} \dot{v} &= I + v^2 - u \\ \tau \dot{u} &= -u \end{aligned} \tag{1.42}$$

and the reset condition:

$$\begin{aligned} \text{if } v = v_{\mathrm{cut}}, \text{ then} \qquad & v \to v_{\mathrm{res}}, \\ & u \to u + d. \end{aligned} \tag{1.43}$$

This rather dynamical approach was then also used in other integrate-and-fire models, see for instance [32, 228, 151] and is used in chapter 5 of the present thesis.

In order to study adaptive excitable systems, we will apply this approach to active rotator models, eq. (1.38) and use that both, the driving parameter ω_0 in the active rotator model and the current I in conductance-based neuron models act as bifurcation parameters and drive the systems through the saddle-node bifurcation. Thus, dynamically, they have the same role. Therefore, we will account for adaptation currents in the active rotator model by applying a time-dependent offset to the driving parameter, which receives an instantaneous offset after each spike and decays exponential during interspike intervals. More details on this will be given in chapter 3.

[2] In ref. [167] 50ms $< \tau <$ 600ms is used, which is slow compared the ISIs of $\approx$ 6ms
[3] Liu and Wang used $\tau = 80$ms in ref. [167]

1.5.2 Reverse spike-frequency adaptation

Reverse spike-frequency adaptation has been observed in subthalamic neurons at high firing rates, see refs. [101, 267, 56]. In ref. [267] this phenomenon is investigated in more detail using a leaky integrate-and-fire-like model and a conductance-based neuron model. Furthermore, a spike-triggered inward current that provides a positive feedback to the neuron after a spike has been identified as a possible biophysical mechanism for reverse spike-frequency adaptation. In the reference, the feedback current acts on a timescale of the order of 50 ms, which is slow compared to the steady state interspike intervals (< 10 ms) of the neurons in the corresponding regime of high firing rates. Applying the approach used in refs. [18, 123] to describe adaptation currents, yields a model like eqs. (1.42) and (1.43), except that u has to be replaced by a current, which enters with a positive sign in the equation for the membrane potential. Thus, in order to account for reverse spike-frequency adaptation in the active rotator model, we will add a time-dependent positive offset to the driving, which behaves similar to that used for spike-frequency adaptation, see chapter 3 for more details.

1.5.3 Autaptic coupling

Another source of spike-triggered feedback are so-called *autapses* [118] – synaptic connections onto the neuron itself, see fig. 1.1. Autapses have been observed in several brain regions in vivo [261, 196, 127, 168, 207], in isolated neurons [17], and in neurons in the *Aplysia* buccal ganglia [220, 16]. Interestingly, some neurons in the cat visual cortex have been found to develop many autaptic connections ($\approx 10-30$) and are, therefore, subject to extensive feedback from its own activity [249]. Feedback due to autaptic coupling can be positive (excitatory autapses), see for instance refs. [17, 234, 220], or negative (inhibitory autapses) [17, 249]. Autapses are usually modeled as chemical synapses, eq. (1.9), with a conductance g_{aut}, that receives an offset at the neuron's spike and decays exponentially afterwards. Thus, an autaptic current I_{aut}, can be modeled as

$$\begin{aligned} I_{\mathrm{aut}} &= -g_{\mathrm{aut}}(V - V_{\mathrm{ch,syn}}) \\ \tau \dot{g}_{\mathrm{aut}} &= -g_{\mathrm{aut}}. \end{aligned} \tag{1.44}$$

τ is the synaptic time scale. Furthermore, g_{aut} receives an instantaneous offset when the neuron spikes. $V_{\mathrm{ch,syn}}$ is the synaptic reversal potential presented in section 1.1.2. In particular, for excitatory autapses $V_{\mathrm{ch,syn}}$ is much higher than the neurons membrane potential in the subthreshold regime, and the influence of an excitatory autapse on the neurons dynamics can be captured using the approach presented for reverse spike-frequency adaptation, i.e. by a positive spike-triggered current. In particular, the time scale of g_{aut} can be slow compared to the neuron's interspike intervals. The influence of such slow autapses has been studied, for instance, in ref. [234][4]. Other studies have modeled autapses as a delayed feedback to the neurons membrane potential [155].

[4] The authors chose $\tau = 100$ ms

1.5.4 Fluctuations in extracellular ion concentrations

A further source of spike-triggered feedback are fluctuations in the external ion concentrations. The ratio of extracellular and intracellular ion concentrations determines the reversal potential of the corresponding ion currents. The latter is given by the Nernst equation (1.1). Furthermore, the different ion channels cause a release of ions in the extracellular space. In most cases the resulting changes of the extracellular concentrations can be neglected. However, for instance, the extracellular potassium concentration $[K^+]_{out}$ in neocortical circuits is small compared to the intracellular one[5] and the release of potassium in the extracellular space during individual spikes leads to noticeable increases in the extracellular concentration and, thereby, affects the reversal potential. This acts as a positive feedback to the voltage dynamics. This, can be easily understood, if $[K^+]_{out}$ is considered as a baseline concentration $[K^+]_{out}^{base}$ and a time dependent part $\Delta[K^+]_{out}$, which receives an offset at each spike and decays during interspike intervals due the slow potassium diffusion in the extracellular space[6] and the binding of potassium in buffers. Considering the reversal potential V_K from the Nernst equation (1.1) yields

$$V_K = \frac{RT}{zF} \log \frac{[K^+]_{out}^{base} + \Delta[K^+]_{out}}{[K^+]_{in}} \approx V_K^{base} + \Delta V_K, \tag{1.45}$$

in case of small $\Delta[K^+]_{out}$. We set $V_K^{base} = (RT/zF)\log([K^+]_{out}^{base}/[K^+]_{in})$ and $\Delta V_K = (RT/zF)\Delta[K^+]_{out}/[K^+]_{out}^{base} > 0$. Thus, the potassium currents in the conductance-base neuron models eq. (1.3), can be represented by

$$I_K \approx g_K(V - V_K) \approx g_K(V - V_K^{base}) - g_K \Delta V_K. \tag{1.46}$$

Since I_K enters the voltage dynamics with a negative sign, the resulting positive spike-triggered feedback current reads $I_K^+ \approx g_K \Delta V_K$. By accounting for changes of the extracellular potassium concentration, studies of complex neuron models have shown that the potassium dynamics can cause a slow switching between tonic spiking and bursting states [15, 85]. Furthermore, the influence of positive feedback from the extracellular potassium concentration has been studied in arrays of excitable cells modeled by an extended Fitz-Hugh-Nagumo model [206].

1.6 Bursting

Another phenomenon, which is often observed in neural systems, is bursting, i.e. the neuron fires groups of spikes, which are separated by time intervals of quiescence. The voltage-time trace of a bursting neuron in the *spiny lobster* is depicted in fig. 1.6. A popular concept of understanding neural bursting is that of a *Fast-Slow Burster*. Here

[5] Concentrations used in ref. [15] are $[K^+]_{in} \approx 130$ mM and ≈ 3 mM for the equilibrium value of $[K^+]_{out}$.

[6] The diffusion constant has been measured and is of order 10^{-6} cm^2/s. Intracellular distances are of the order of 100 μm, see refs. [78, 15].

Figure 1.6: Time trace of the membrane potential of an isolated pyloric dilator neuron in the pyloric central pattern generator of the *spiny lobster* stomatogastric ganglion. Data have been published in ref. [176].

the dynamics can be divided into fast variables $\mathbf{u}$, for instance the membrane potential, and slow variables $\mathbf{w}$. The corresponding dynamical system reads

$$\begin{aligned} \dot{\mathbf{u}} &= \mathrm{f}(\mathbf{u}, \mathbf{w}) \\ \tau\dot{\mathbf{w}} &= \mathrm{g}(\mathbf{u}, \mathbf{w}). \end{aligned} \tag{1.47}$$

$\tau \gg 1$ scales the time scale separation between fast and slow variables. The first line of eq. (1.47) describes the fast subsystem

$$\dot{\mathbf{u}} = \mathrm{f}(\mathbf{u}, \mathbf{w}), \tag{1.48}$$

which, for fixed $\mathbf{w}$, possesses a periodic orbit in the spiking state and a stable equilibrium in the resting state. The slow subsystem

$$\tau\dot{\mathbf{w}} = \mathrm{g}(\mathbf{u}, \mathbf{w}) \tag{1.49}$$

leads to oscillations of $\mathbf{w}$ on the time scale τ. This causes slow transitions of the fast subsystem from spiking to resting state and vice versa.

1.6.1 Classification of bursting behavior

In order to classify bursting behavior, we follow Izhikevich [121, 125] and consider the slow variables $\mathbf{w}$ as bifurcation parameters in the fast subsystem eq. (1.48). When switching from resting to spiking state, the actual value of $\mathbf{w} = \mathbf{w}_{\mathrm{r}\to\mathrm{s}}$ causes the stable, resting-state equilibrium to become unstable (or vanish) and the fast variables $\mathbf{u}$ are attracted by a stable periodic orbit corresponding to the spiking state. As described in section 1.4, this switching can only be caused by four codimension-one bifurcations. Accordingly, when switching from spiking to resting state, the stable periodic orbit in eq. (1.48) becomes unstable (or vanishes) at $\mathbf{w} = \mathbf{w}_{\mathrm{s}\to\mathrm{r}}$ and $\mathbf{u}$ relaxes to the stable resting state equilibrium. Again restricting on codimension-one bifurcations, there are only four possible bifurcations. Those and the corresponding properties for the spiking behavior in the burst's tail are listed in the following.

- *Saddle-node on invariant circle bifurcation* (Circle): Same as presented before except that the bifurcation parameter is varied in the opposite direction. At the

bifurcation the periodic orbit becomes an invariant circle to the saddle-node with infinite period. This bifurcation leads to a decrease of the spiking frequency in the burst's tail.

- *Supercritical Andronov-Hopf bifurcation* (Hopf): Same as presented before. This bifurcation leads to a decrease of spike amplitudes in the burst's tail.
- *Fold limit cycle bifurcation* (FoldLC): The stable periodic orbit annihilates with an unstable one. This bifurcation leads to an almost constant spike amplitude and spike frequency in the burst's tail.
- *Saddle homoclinic orbit bifurcation* (Homoclinic): The stable periodic orbit becomes a homoclinic orbit to a saddle and vanishes. This bifurcation leads to an almost constant spike amplitude and a scaling of the spike frequency according to

$$f(I) \propto \frac{1}{\log(b - b_\mathrm{h})}, \quad b > b_\mathrm{h}. \tag{1.50}$$

  b is a scalar bifurcation parameter with $b = b_\mathrm{h}$ at the bifurcation, corresponding to $\mathbf{w} = \mathbf{w}_{\mathrm{s}\to\mathrm{r}}$.

In order to cause bursting behavior, all combinations of the four types of bifurcations of the resting-state equilibrium and the four types of bifurcations of the spiking-state periodic orbit can be combined. This leads to 16 types of bursters, which can be classified according to these bifurcations as: *Fold-Homoclinic* burster, *Circle-Circle* burster, *subHopf-Homoclinic* burster, and so on [121, 125]. The first part names the bifurcation in the fast subsystem that occurs between resting and spiking state, listed in section 1.4, and the second one the bifurcation between spiking to resting state.

1.7 Statistics of neural spiking

In the following, we introduce basic statistical measures and relations between them. These will be used in the next chapters.

1.7.1 Basic statistical measures

We are mainly interested in statistical properties of the spike train $x(t)$, the interspike intervals Δt_i, and the spike count $N(t, T)$ – the number of spikes in a time interval of length T starting at t. These quantities are illustrated in fig. 1.7.

Spike train statistics

At first, we consider the statistics of the spike train

$$x(t) = \sum_{i=1}^{M} \delta(t - t_i). \tag{1.51}$$

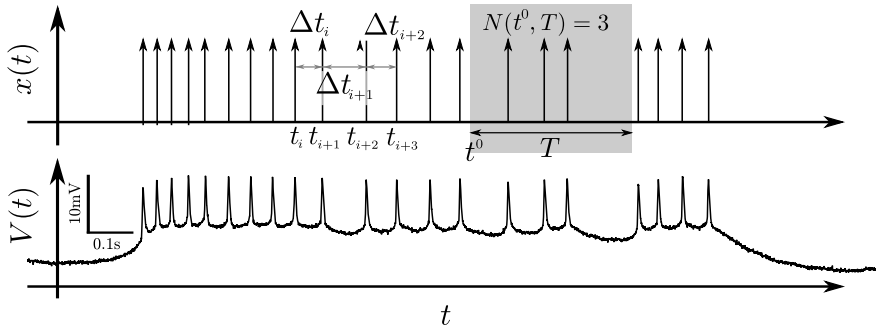

Figure 1.7: Illustration of the statistical measures (top) for recordings of the membrane potential during one burst of the pyloric dilator neuron (bottom). Data are the same as in fig. 1.6

t_i is the time of the ith spike, M the total number of spikes in the spike train, and $\delta(t)$ the Dirac delta function. In fig. 1.7 spike times are associated with the peak voltage values of the spikes. Since neuronal responses are noisy, $x(t)$ is a stochastic quantity and the spikes are generated by a *stochastic process*. We define the ensemble average over different realizations of the spike train $\langle x(t) \rangle$ at time t as the instantaneous firing rate

$$r(t) := \langle x(t) \rangle. \tag{1.52}$$

However, for stationary spike trains the ensemble average $\langle x(t) \rangle$ and the time average $\overline{x(t)}$ calculated for a long time interval T coincide and we will talk about the asymptotic firing rate r

$$r = \langle x(t) \rangle \approx \overline{x(t)} = \frac{1}{T} \int_{t_0}^{t_0+T} dt\ x(t), \quad T \gg \frac{1}{r} \text{ and stationary.} \tag{1.53}$$

Next, we introduce the *spike train autocorrelation function* $c(\tau)$. It is defined as

$$c(\tau) := \langle (x(t) - \langle x(t) \rangle)\,(x(t+\tau) - \langle x(t+\tau) \rangle) \rangle \tag{1.54}$$

and dependents only on the time lag τ, if $x(t)$ is stationary. In the latter case, it can be rewritten as

$$c(\tau) := r\,(m(\tau) - r) + r\delta(\tau). \tag{1.55}$$

$m(\tau)dt$ is the probability to observe a spike in the interval $[\tau, \tau + dt)$ given a spike at $t = 0$. Besides the autocorrelation function, its Fourier transformation $S(f)$, known as the *spike train power spectrum*, is often used to quantify higher order statistics of $x(t)$.

It is given by

$$S(f) := \int_{-T}^{T} d\tau \; c(\tau) e^{2\pi I f \tau} = 2 \; \mathrm{Re} \int_{0}^{T} d\tau \; c(\tau) e^{2\pi I f \tau}. \tag{1.56}$$

I is the imaginary unit and we used that the autocorrelation function is symmetric, i.e. $c(\tau) = c(-\tau)$. Furthermore, $\mathrm{Re}(z)$ is the real part of a complex number z and f a frequency in the frequency domain. The finite integration time T accounts for the limited observation time.

Count statistics

Another important statistics is the so-called *count statistics* in which the quantity of interest is the spike count $N(t^0, T)$, which measures the number of spikes in a time interval of length T, following some starting time t^0, see illustration in fig. 1.7. The spike count is related to the spike train by

$$N(t^0, T) = \int_{t^0}^{t^0+T} dt \; x(t), \tag{1.57}$$

which yields an estimate of the asymptotic firing rate for stationary spike trains and long T

$$r = \lim_{T \to \infty} \frac{N(t^0, T)}{T}. \tag{1.58}$$

Furthermore, for sufficiently long intervals T, $N(t^0, T)/T$ can be used as an approximate for the firing rate in the time interval $[t^0, t^0 + T]$.

By averaging over a large ensemble of independent starting points t^k, one can define the average spike count

$$\langle N(T) \rangle = \frac{1}{M} \sum_{k=1}^{M} N(t^k, T). \tag{1.59}$$

Furthermore, in order to quantify the variability of the spiking on a time scale T, a common measure is the Fano factor:

$$F(T) = \frac{\mathrm{Var}(N(T))}{\langle N(T) \rangle} = \frac{\langle (N(T) - \langle N(T) \rangle)^2 \rangle}{\langle N(T) \rangle}. \tag{1.60}$$

$\mathrm{Var}(N(T))$ denotes the variance of the ensemble of spike counts and is given by

$$\mathrm{Var}(N(T)) = \frac{1}{M} \sum_{k=1}^{M} (N(t^k, T) - \langle N(T) \rangle)^2. \tag{1.61}$$

Interspike interval statistics

The third statistics is that of the *interspike intervals* (ISI) $\Delta t_i = t_{i+1} - t_i$, see illustration in fig. 1.7. In more detail, for an ordered sequence of spiking times $t_1 < t_2 < ... < t_M$, we define the corresponding sequence of ISIs as $(\Delta t_1, \Delta t_2, ...\Delta t_{M-1}) = (t_2 - t_1, t_3 - t_2, ..., t_M - t_{M-1})$. For the latter, we can calculate the mean ISI by

$$\langle \Delta t \rangle = \frac{1}{M-1} \sum_{k=1}^{M-1} \Delta t_k \tag{1.62}$$

and the variance by

$$\mathrm{Var}(\Delta t) = \langle (\Delta t_k - \langle \Delta t \rangle)^2 \rangle = \frac{1}{M-1} \sum_{k=1}^{M-1} (\Delta t_k - \langle \Delta t \rangle)^2. \tag{1.63}$$

Finally, the variability of the interspike intervals can be quantified by the coefficient of variation (CV), which is given by

$$C_V = \frac{\sqrt{\mathrm{Var}(\Delta t)}}{\langle \Delta t \rangle}. \tag{1.64}$$

Thus, for a sequence of constant ISIs, i.e. perfectly periodic spiking, one finds $C_V = 0$, for a Poisson spike train one finds $C_V = 1$, and for bursting neurons $C_V > 1$. Alternatively, we can introduce the *interspike interval distribution* $\rho(t)$. Then, $\rho(\Delta t)dt$ is the probability to find an ISI of length $\Delta t \in [t, t + dt)$ in the sequence. This allows for the calculation of the mean ISI and the ISI variance from the moments of $\rho(t)$. In particular, the nth moment $\langle \Delta t^n \rangle$ of $\rho(t)$ is given by

$$\langle \Delta t^n \rangle = \int_0^\infty dt \; t^n \; \rho(t). \tag{1.65}$$

Accordingly, we introduce the nth order interspike interval distribution $\rho^n(t)$. In more detail, $\rho^n(t)dt$ yields the probability to pick an $i \in \{1, 2, ..., M - n - 1\}$ such that $\Delta t_i + \Delta t_{i+1} + ... + \Delta t_{i+n} \in [t, t + dt)$. In case of a renewal process, i.e. in the absence of ISI correlations, the nth order distribution equals the nth convolution of the ISI distribution, i.e.

$$\rho^n(t) = \underbrace{\rho(t) * \rho(t) * ... * \rho(t)}_{n \text{ times}}, \quad \text{renewal.} \tag{1.66}$$

In this case, $m(t)$ in eq. (1.55) can be written as

$$m(t) = \sum_{n=1}^{\infty} \rho^n(t). \tag{1.67}$$

In order to distinguish between a renewal and a nonrenewal ISI statistics, we introduce the serial correlation coefficient (SCC) for ISIs of lag n in the series as

$$\rho_n = \frac{\langle(\Delta t_i - \langle\Delta t\rangle)(\Delta t_{i+n} - \langle\Delta t\rangle)\rangle}{\langle(\Delta t_i - \langle\Delta t\rangle)^2\rangle}. \tag{1.68}$$

Since, this measure quantifies the correlations between ISIs of lag n, it is zero for all lags $n > 0$ in case of a renewal ISI statistics, whereas a nonrenewal statistics leads to $\rho_n \neq 0$ for at least one lag $n > 0$.

All these measures include averages over the whole ISI sequence. However, in case of bursting neurons the ISI statistics in the beginning of the burst can differ from that of ISIs in the bursts tail. Thus, averaging over the entire sequence may wash out important characteristics. In order to obtain more detailed information about the sequence of ISI, experimenters consider, for instance, the ISI signature of a neuron, also called first return map. It describes the set of pairs

$$(\Delta t_i, \Delta t_{i+1})^T, \quad i = 1, 2, ..., M-2. \tag{1.69}$$

This can also be described in terms of the joint probability density $\rho_r(\Delta t_{i+1}, \Delta t_i)$. Then, $\rho_r(\Delta t_{i+1}, \Delta t_i)dt^2$ yields the probability to find an ISI in the interval $[\Delta t_i, \Delta t_i + dt)$ and the subsequent ISI in the interval $[\Delta t_{i+1}, \Delta t_{i+1} + dt)$.

1.7.2 Relations between measures

The different types of statistics, quantify different aspects of the spiking behavior, nevertheless several quantities can be related[7]. In the following, we present some of those relations, which will be used in this thesis, for a deeper understanding of spike train statistics and statistical relations between measures, we recommend the book of Cox and Lewis [52] in which theses relations and their derivations are presented in more detail.

nth order statistics and first order statistics

Denoting the ith nth order ISI by $\Delta_n t_i$, i.e. $\Delta_n t_i = \Delta t_i + \Delta t_{i+1} + ... + \Delta t_{i+n-1}$, the mean nth order ISIs $\langle\Delta_n t\rangle$ follows from

$$\langle\Delta_n t\rangle = n\langle\Delta t_i\rangle. \tag{1.70}$$

[7] Professor Benjamin Lindner (Institut für Physik, Humboldt-Universität zu Berlin, Berlin, Germany), personal communication, April 17, 2012

Furthermore, the variance of nth order intervals $\mathrm{Var}(\Delta_n t)$ is given by

$$\begin{aligned}\mathrm{Var}(\Delta_n t) &= \langle(\Delta_n t - \langle\Delta_n t\rangle)(\Delta_n t - \langle\Delta_n t\rangle)\rangle \\ &= \langle(\underbrace{\Delta t_1 - \langle\Delta t_1\rangle + \Delta t_2 - \langle\Delta t_2\rangle + ...}_{n \text{ times}})(\underbrace{\Delta t_1 - \langle\Delta t_1\rangle + \Delta t_2 - \langle\Delta t_2\rangle + ...}_{n \text{ times}})\rangle \\ &= n\mathrm{Var}(\Delta t) + 2\sum_{k=1}^{n-1}\sum_{l=1}^{n-k}\underbrace{\langle(\Delta t_k - \langle\Delta t_k\rangle)(\Delta t_{k+l} - \langle\Delta t_{k+l}\rangle)\rangle}_{\mathrm{Var}(\Delta t)\rho_l}.\end{aligned}$$

Interchanging the order of the sums, one obtains

$$\begin{aligned}\mathrm{Var}(\Delta_n t) &= \mathrm{Var}(\Delta t)\left(n + 2\sum_{l=1}^{n-1}\sum_{k=1}^{n-l}\rho_l\right) \\ &= n\mathrm{Var}(\Delta t)\left(1 + 2\sum_{l=1}^{n-1}(1 - \frac{l}{n})\rho_l\right). \qquad (1.71)\end{aligned}$$

Asymptotic firing rate and mean interspike interval

In the stationary case, the asymptotic firing rate r can be related to the mean ISI. For a long time interval T, one finds

$$r = \overline{x(t)} \approx \frac{1}{T}\int_{t_0}^{t_0+T} dt\ x(t) = \frac{N(T)}{T} \approx \frac{N(T)}{N(T)\langle\Delta t\rangle} = \frac{1}{\langle\Delta t\rangle}. \qquad (1.72)$$

Asymptotic Fano factor and ISI statistics

The asymptotic Fano factor

$$F_\infty := \lim_{T\to\infty} F(T) = \lim_{T\to\infty}\frac{\mathrm{Var}(N(T))}{\langle N(T)\rangle}, \qquad (1.73)$$

can be related to the CV and the serial correlations by

$$F_\infty = C_V^2\left(1 + 2\sum_{l=0}^{\infty}\rho_l\right). \qquad (1.74)$$

More details on this are given in appendix A.1.1.

1.8 Stochastic differential equations

In many neurons spiking can be regarded as a threshold phenomenon, i.e. a spike is evoked when the system crosses a particular boundary. Then, an ISI corresponds to the time between two subsequent passings of this spiking-threshold. Furthermore, in

integrate-and-fire models, each spike is followed by a reset of the membrane potential, see eq. (1.20). Thus, each ISI starts with the same initial condition for the membrane potential. Therefore, the ISIs correspond to the time the membrane potential needs to reach the threshold for the first time when initially starting at the reset value. In statistical physics, this time is called *first-passage time*. In the presence of noise, first-passage times obtained from individual trials differ and the resulting distribution of first-passage times is called the density of the waiting time distribution [5], which corresponds to the ISI distribution $\rho(t)$. In the last decades, a whole theoretical framework has been developed to obtain information on the distribution of first-passage times for a given stochastic differential equation, see for instance [217, 5].

As we saw in sec. 1.2 several sources of noise in neural systems can be described by adding white Gaussian noise to the equations for membrane potential or to those for the gating variables in conductance-based neuron models. This results in a *Langevin equation*, which has the form

$$\dot{\mathbf{x}} = \mathbf{f}(\mathbf{x}, t) + \mathbf{G}(\mathbf{x}, t)\boldsymbol{\xi}(t). \tag{1.75}$$

$\mathbf{x}$ is the vector of state variables, $\mathbf{f}(\mathbf{x})$ is the deterministic drift, $\mathbf{G}(\mathbf{x})$ is the, in general state-dependent $d \times d$ matrix of noise intensities, and $\boldsymbol{\xi}(t)$ is the white Gaussian noise vector, with components $\xi_i(t)$ fulfilling eq. (1.12).

In the following, we will restrict on one-dimensional problems for which exact equations for all moments of the density of the waiting time distribution can be derived [204, 239]. We first present the general derivation of the corresponding formulas and illustrate how they can be applied to active rotator models later on. First, we follow ref. [5] and consider the one-dimensional Langevin equation

$$\dot{x} = f(x, t) + \sqrt{2D}g(x, t)\xi(t). \tag{1.76}$$

The corresponding forward *Fokker-Planck equation* for the transition probability density $p(x, t|x_0, t_0)$ to find the system at x at time t given x_0 at time t_0 reads [5]

$$\partial_t p = -\frac{\partial K_1(x, t)p}{\partial x} + \frac{\partial^2 K_2(x, t)p}{\partial x^2}. \tag{1.77}$$

With the kinetic coefficients:

$$\begin{aligned} K_1(x, t) &= f(x, t) + 2Dq\frac{\partial g(x, t)}{\partial x}g(x, t), \\ K_2(x, t) &= Dg^2(x, t). \end{aligned} \tag{1.78}$$

Here and in the following, we suppress the arguments of $p(x, t|x_0, t_0)$. The parameter q is a constant and has to be chosen according to the interpretation of the stochastic differential equation, i.e. $q = 0$ (Itô), $q = 1/2$ (Stratonovich), or $q = 1$ (Klimontovich),

see [271, 7, 262, 135, 241]. Additionally, the backward Fokker-Planck equation reads

$$-\partial_{t_0} p = K_1(x_0, t_0)\partial_{x_0} p + K_2(x_0, t_0)\partial_{x_0}^2 p. \tag{1.79}$$

The latter yields the transition probability density at some state x_0 at a prior time $t_0 < t$. Furthermore, by defining the probability current $j(x,t)$ as

$$j(x,t) := K_1(x,t)p - \frac{\partial K_2(x,t)p}{\partial x}, \tag{1.80}$$

the Fokker-Planck equation, eq. (1.77), can be reformulated as a continuity equation

$$\partial_t p = -\partial_x j(x,t). \tag{1.81}$$

In the following, we consider $x = b$ as the spiking threshold.

1.8.1 First-passage time problems

Since we are only interested in trajectories that hit the spiking threshold b for the first time, each trajectory that has already reached b can be excluded. This can be realized by an absorbing boundary at b. One yields the boundary condition

$$p(b, t|x_0, 0) = 0. \tag{1.82}$$

In the following, we associate the initial time $t_0 = 0$ with the beginning of an ISI. Furthermore, we introduce a reflecting boundary at some other point $a < b$, by claiming that

$$j(a,t) = 0, \tag{1.83}$$

and, thereby, confine x to the interval (a,b).

Following ref. [5], we first introduce the probability $P_{a,b}(t,x_0)$ to find x at time t in the interval (a,b), if it has started at $a < x_0 < b$ at time $t_0 = 0$. In addition, we apply the initial condition $p(x,0|x_0,0) = \delta(x - x_0)$. Thus, $P_{a,b}(t,x_0)$ results from $p(x,t|x_0,t_0)$ by

$$P_{a,b}(t,x_0) = \int_a^b dx\ p(x,t|x_0,0), \tag{1.84}$$

and the probability $W_{a,b}(t,x_0)$ that x has left the region before time t is given by

$$W_{a,b}(t,x_0) = 1 - P_{a,b}(t,x_0).$$

Then, the amount of probability that leaves the region in the time interval $[t, t+dt)$ is

given by

$$w_{a,b}(t,x_0)dt = \partial_t W_{a,b}(t,x_0)dt = -\partial_t P_{a,b}(t,x_0)dt. \tag{1.85}$$

In particular, if x is associated with the membrane potential in an integrate-and-fire model, b with the spiking threshold, x_0 with the reset value of the membrane potential, and a is far away from the voltage values of physical relevance, $w_{a,b}(t,x_0)$ equals the ISI density of the neuron model. However, in general $w_{a,b}(t,x_0)$ is called waiting time density.

By integrating the continuity equation, eq. (1.81), over the region $a < x < b$ and applying the reflecting boundary condition eq. (1.83), the waiting time density can be related to the probability current at the absorbing boundary $j(b,t)$. The latter can be further simplified by applying the absorbing boundary condition eq. (1.82), which yields

$$w_{a,b}(t,x_0) = j(b,t) = -\left.\frac{\partial K_2(x,t)p}{\partial x}\right|_{x=b}. \tag{1.86}$$

Furthermore, a dynamic equation for the waiting time density can be derived by integrating the backward Fokker-Planck equation eq. (1.79) over the region $a < x < b$, which yields

$$-\partial_{t_0}\int_a^b dx\ p = K_1(x_0)\partial_{x_0}\int_a^b dx\ p + K_2(x_0)\partial_{x_0}^2\int_a^b dx\ p. \tag{1.87}$$

Note that we dropped the argument $t_0 = 0$ of the kinetic coefficients. Assuming stationarity of the process $x(t)$, i.e. that $P_{a,b}(t,x_0)$ depends just on the time distance $t - t_0$ to the initial distribution, we get $\partial_{t_0} p(x,t|x_0,t_0) = -\partial_t p(x,t|x_0,t_0)$ [5]. Furthermore, using eq. (1.84) and considering the time derivative of eq. (1.87), we can apply eq. (1.85) and obtain the evolution equation for the waiting time density

$$\partial_t w_{a,b}(t,x_0) = K_1(x_0)\partial_{x_0} w_{a,b}(t,x_0) + K_2(x_0)\partial_{x_0}^2 w_{a,b}(t,x_0), \tag{1.88}$$

with initial and boundary conditions

$$w_{a,b}(0,x_0) = 0 \text{ for } a < x_0 < b; \quad w_{a,b}(t,b) = \delta(t); \quad \left.\partial_{x_0} w_{a,b}(t,x_0)\right|_{x_0=a}. \tag{1.89}$$

Moments of the waiting time density

In general, the nth moment of the waiting time density reads

$$T_{a,b}^{(n)}(x_0) := \int_0^\infty dt\ t^n w_{a,b}(t,x_0). \tag{1.90}$$

Furthermore, an iterative scheme for $T_{a,b}^{(n)}(x_0)$ has been derived in refs. [204, 239, 158, 5]. For its derivation, we multiply eq. (1.88) by t^n and integrate over time, using integration by parts (P.I.). This yields

$$\int_0^\infty dt\ t^n \partial_t w_{a,b}(t,x_0) \overset{P.I.}{=}$$

$$t^n\ w_{a,b}(t,x_0)|_0^\infty - nT_{a,b}^{(n-1)}(x_0) = K_1(x_0)\partial_{x_0}T_{a,b}^{(n)}(x_0) + K_2(x_0)\partial_{x_0}^2 T_{a,b}^{(n)}(x_0) \tag{1.91}$$

for $n > 0$ and

$$\int_0^\infty dt\ \partial_t w_{a,b}(t,x_0) = w_{a,b}(t,x_0)|_0^\infty \tag{1.92}$$

for $n = 0$. If $a < x < b$, $w_{a,b}(t,x_0)|_0^\infty = 0$, and $t^n\ w_{a,b}(t,x_0)|_0^\infty = 0$, which is a necessary condition for the existence of the nth moment of $w_{a,b}(t,x_0)$, this yields the iterative scheme for the nth moment $n > 0$:

$$-nT_{a,b}^{(n-1)}(x_0) = K_1(x_0)\partial_{x_0}T_{a,b}^{(n)}(x_0) + K_2(x_0)\partial_{x_0}^2 T_{a,b}^{(n)}(x_0). \tag{1.93}$$

Additionally, $T_{a,b}^{(0)}(x_0) = 1$ is given by the normalization of the waiting time density. Furthermore, the boundary conditions are

$$T_{a,b}^{(n)}(b) = 0 \text{ and } \left.\partial_{x_0}T_{a,b}^{(n)}(x_0)\right|_{x_0=a}. \tag{1.94}$$

In order to solve eq. (1.93) for $T_{a,b}^{(n)}(x_0)$, we follow ref. [5] and define

$$u_{a,b}^{(0)}(x) := \partial_x T_{a,b}^{(n)}(x). \tag{1.95}$$

Then, eq. (1.93) reduces to

$$-nT_{a,b}^{(n-1)}(x_0) = K_1(x_0)u_{a,b}^{(0)}(x_0) + K_2(x_0)\partial_{x_0}u_{a,b}^{(0)}(x_0), \tag{1.96}$$

which can be solved using the variation of constants method. This leads to

$$u_{a,b}^{(n)}(x) = \exp(-A(x))\left(C_n - n\int_a^x dx'\ \frac{T_{a,b}^{(n-1)}(x')}{K_2(x')}\exp(A(x'))\right), \tag{1.97}$$

with $A(x)$ given by

$$A(x) = \int dx''\ \frac{K_1(x'')}{K_2(x'')}. \tag{1.98}$$

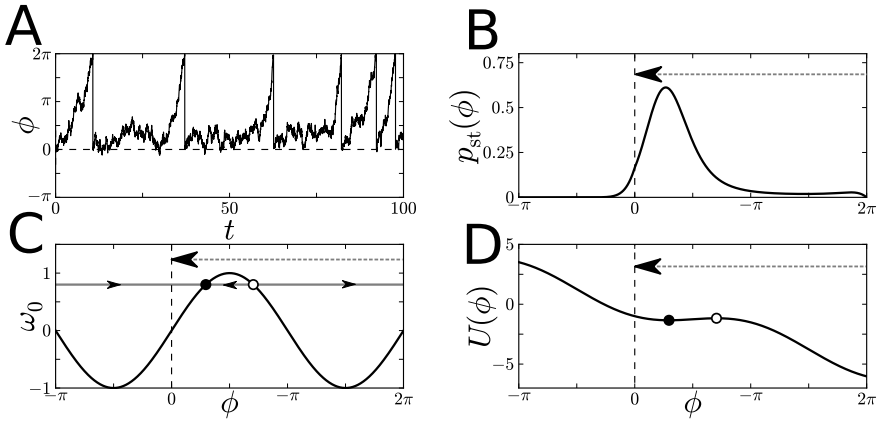

Figure 1.8: Illustration of the noisy active rotator model. Time trace of the phase (A), stationary probability distribution eq. (1.114) (B), illustration of the phase portrait (C), and the potential $U(x)$ eq. (1.104) (D). Dashed lines and arrows mark the phase reset, black and white dots stable and unstable fixed points, respectively, and corresponding extrema of $U(x)$. C: Black small arrows mark the phase velocity, the gray horizontal line the actual value of ω_0, and the black curve the negative phase dependent force $\sin(x)$. Parameters: $\omega_0 = 0.8$, $D = 0.2$.

Furthermore, the boundary conditions eq. (1.94) imply that $u^{(n)}_{a,b}(a) = 0$ and $T^{(n)}_{a,b}(b) = 0$. Finally, the integration of eq. (1.97) yields

$$T^{(n)}_{a,b}(x_0) = n \int_{x_0}^{b} dx \ \exp(-A(x)) \left(\int_{a}^{x} dx' \ \frac{T^{(n-1)}_{a,b}(x')}{K_2(x')} \exp(A(x')) \right). \tag{1.99}$$

Thus, the first moment ($n = 1$), which corresponds to the *mean first-passage time*, is given by

$$T^{(1)}_{a,b}(x_0) = \int_{x_0}^{b} dx \ \exp(-A(x)) \left(\int_{a}^{x} dx' \ \frac{\exp(A(x'))}{K_2(x')} \right) \tag{1.100}$$

and the second moment follows from

$$T^{(2)}_{a,b}(x_0) = 2 \int_{x_0}^{b} dx \ \exp(-A(x)) \int_{a}^{x} dx' \ \frac{\exp(A(x'))}{K_2(x')} \int_{x'}^{b} dx'' \ \exp(-A(x'')) \int_{a}^{x''} dx''' \ \frac{\exp(A(x'''))}{K_2(x''')}. \tag{1.101}$$

Application to active rotator models

In the following, we relate the general results obtained so far to the moments of the ISI density of the models considered in the next chapters. In the chapters 3 and 4, we consider noisy active rotator models, eq. (1.38) that are complemented by a spiking

threshold $\phi = 2\pi$ and an instantaneous reset after each spike to $\phi = 0$. Considering eq. (1.38) and eq. (1.78) and dropping the tildes, we obtain for the kinetic coefficients

$$\begin{aligned} K_1(x,t) &= K_1(x) = \omega_0 - \sin(x) \\ K_2(x,t) &= D. \end{aligned} \tag{1.102}$$

A trajectory of the noisy active rotator model with reset is shown in fig. 1.8A. Furthermore, the dynamics is illustrated in fig. 1.8C.

The mean ISI is given by the mean first passage time, eq. (1.100), to reach the spiking threshold $b \to 2\pi$, when starting at the reset value $x_0 \to 0$. Furthermore, we put the reflecting boundary to $a \to -\infty$. This yields

$$\langle \Delta t \rangle = T^{(1)}_{-\infty,2\pi}(x_0) = \frac{1}{D} \int_0^{2\pi} dx\ e^{\frac{U(x)}{D}} \int_{-\infty}^{x} dx'\ e^{-\frac{U(x')}{D}}. \tag{1.103}$$

Here, we have introduced the potential function associated with the drift $K_1(x) = -\partial_x U(x)$, which yields

$$U(x) = -\omega_0 x - \cos(x). \tag{1.104}$$

The shape of $U(x)$ is illustrated in fig. 1.8D. Furthermore, in the excitable regime $U(x)$ has local extrema, which annihilate at the critical tiling $\omega_0 = 1$, which corresponds to the saddle-node bifurcation in the active rotator model. In particular, $U(x)$ is a tilted periodic potential and it holds that $U(x - 2\pi) = U(x) + 2\pi\omega_0$. Furthermore, we can apply general results on first passage time problems in such potentials presented in refs. [212, 162]. In particular the second integral in eq. (1.103) can be simplified according to

$$\int_{-\infty}^{x} dx'\ e^{-\frac{U(x')}{D}} = \sum_{k=0}^{\infty} e^{-\frac{2\pi\omega_0}{D}k} \int_{x-2\pi}^{x} dy\ e^{-\frac{U(y)}{D}} = \frac{\int_{x-2\pi}^{x} dy\ e^{-\frac{U(y)}{D}}}{1 - e^{-\frac{2\pi\omega_0}{D}}}. \tag{1.105}$$

The last relation follows from the *geometric series* for $\omega_0 > 0$. Applying this in eq. (1.103) yields for the mean ISI

$$\langle \Delta t \rangle = \frac{\int_0^{2\pi} dx\ e^{\frac{U(x)}{D}} \int_{x-2\pi}^{x} dx'\ e^{-\frac{U(x')}{D}}}{D\left(1 - e^{-\frac{2\pi\omega_0}{D}}\right)}. \tag{1.106}$$

Additionally, applying this to the second moment, eq (1.101), we obtain

$$\langle \Delta t^2 \rangle = \frac{2}{D\left(1 - e^{-\frac{2\pi\omega_0}{D}}\right)} \int_0^{2\pi} dx\; e^{\frac{U(x)}{D}} \int_{-\infty}^{x} dx'\; e^{-\frac{U(x')}{D}} \int_{x'}^{2\pi} dx''\; e^{\frac{U(x'')}{D}} \int_{x''-2\pi}^{x''} dx'''\; e^{-\frac{U(x''')}{D}}. \tag{1.107}$$

In particular the calculation of the CV, eq. (1.64), requires the calculation of the variance of the ISI density $\mathrm{Var}(\Delta t) = \langle \Delta t^2 \rangle - \langle \Delta t \rangle^2$ for which a simplified formula has been derived in ref. [212]. Following their calculations we obtain

$$\mathrm{Var}(\Delta t) \approx \frac{2 \int_0^{2\pi} dx\; e^{\frac{U(x)}{D}} \left(\int_{x-2\pi}^{x} dy\; e^{-\frac{U(y)}{D}} \right)^2 \int_x^{x+2\pi} dz\; e^{\frac{U(z)}{D}}}{D^2 (1 - e^{-\frac{2\pi\omega_0}{D}})^3}. \tag{1.108}$$

More details on the derivation can be found in appendix A of ref. [212]. Furthermore, we present the main steps in appendix A.1.2 of this thesis.

1.8.2 Stationary probability distribution

Besides the first-passage time, we are interested in the stationary distribution p_{st} of the active rotator's phase. In order to calculate the latter from the Fokker-Planck equation (1.77), we have to account for the amount of probability that is reset after reaching the absorbing boundary. This is done by an additional source term, which is proportional to probability current at the threshold $j(2\pi, t)$[8], i.e. $j(2\pi, t)dt$ yields the probability to reach the threshold in the time interval $[t, t+dt)$. Thus, the Fokker-Planck equation with the kinetic coefficients for the active rotator model, eq. (1.102), the potential (1.104), and the reset at $\phi = 0$, becomes

$$\partial_t p = \frac{\partial \left(\frac{\partial U(\phi)}{\partial \phi} p \right)}{\partial \phi} + D \frac{\partial^2 p}{\partial \phi^2} + j(2\pi, t)\delta(\phi), \tag{1.109}$$

with an absorbing boundary, eq. (1.82), at $\phi = 2\pi$ and a reflecting one, eq. (1.83), at $\phi = -\infty$. Restricting on the stationary probability distribution p_{st}, the left-hand side vanishes and we obtain

$$\frac{\partial \left(\frac{\partial U(\phi)}{\partial \phi} p_{\mathrm{st}} \right)}{\partial \phi} + D \frac{\partial^2 p_{\mathrm{st}}}{\partial \phi^2} = -r\delta(\phi). \tag{1.110}$$

[8] Professor Benjamin Lindner (Institut für Physik, Humboldt-Universität zu Berlin, Berlin, Germany), personal communication, May 29, 2012

r is the constant asymptotic firing rate, which equals the stationary probability current at the threshold. Equation (1.110) can be integrated and one obtains

$$\left(\frac{\partial U(\phi)}{\partial \phi} p_{\mathrm{st}}\right) + D\partial p_{\mathrm{st}} = -rH(\phi). \tag{1.111}$$

$H(\phi)$ is the Heaviside step function. The homogenous solution of eq. (1.111) reads

$$p_{\mathrm{st}}(\phi) = Be^{-\frac{U(\phi)}{D}}, \tag{1.112}$$

with the integration constant B. Using the variation of constants method, the latter can be varied $B \to B(\phi)$, to obtain a general solution of eq. (1.111). This results in

$$B(\phi) = -\frac{r}{D} \int^{\phi} dx\ e^{-\frac{U(x)}{D}} H(x). \tag{1.113}$$

Finally, the boundary conditions, eqs. (1.82) and (1.83) are fulfilled, by the solution

$$p_{\mathrm{st}}(\phi) = \frac{r}{D} e^{-\frac{U(\phi)}{D}} \int_{\phi}^{2\pi} dx\ e^{\frac{U(x)}{D}} H(x). \tag{1.114}$$

In particular, the asymptotic firing rate r can be calculated from the normalization condition $1 = \int_{-\infty}^{2\pi} dx\ p_{\mathrm{st}}(x)$, which yields

$$r = \frac{D}{\int_{-\infty}^{2\pi} dx\ e^{-\frac{U(x)}{D}} \int_{x}^{2\pi} dx'\ e^{\frac{U(x)}{D}} H(x')}. \tag{1.115}$$

Note that this result can be easily transformed into the inverse mean ISI $1/\langle \Delta t \rangle$, eq. (1.106), by changing the order of integrations and considering eq. (1.105) and is, therefore, consistent with the relation between asymptotic firing rate and mean ISI, eq. (1.72). The stationary probability distribution $p_{\mathrm{st}}(\phi)$ for one set of parameters in the excitable regime is depicted in fig. 1.8B.

2 Simulation techniques

Throughout this thesis we study the spiking statistics of several neuron models using numerical simulations. To estimate the statistics, we integrate the respective differential equations numerically. Corresponding algorithms are presented in the sections 2.1 and 2.2. In chapter 3, we consider the stationary probability distribution of system variables. The latter are obtained from a specialized simulation method that is introduced in section 2.4 and has been published in ref. [142]. Furthermore, we perform a numerical bifurcation analysis of the reduced Morris-Lecar model eq. (1.14), using the program AUTO-07P [61]. Details of this analysis are given in section 2.5.

2.1 Integration of ordinary differential equations

We first consider ordinary differential equations of the form

$$\dot{\mathbf{x}} = \mathbf{f}(\mathbf{x}(t), t), \tag{2.1}$$

with $\mathbf{x}$ being the vector of state variables and $\mathbf{f}(\mathbf{x}, t)$ the deterministic drift. For a given inital condition $\mathbf{x}_0 = \mathbf{x}(t_0)$ eq. (2.1) can be integrated formally to obtain $\mathbf{x}(t)$, which leads to

$$\mathbf{x}(t) = \mathbf{x}_0 + \int_{t_0}^{t} dt' \; \mathbf{f}(\mathbf{x}(t'), t'). \tag{2.2}$$

This yields for $t = t_0 + h$,

$$\mathbf{x}(t_0 + h) = \mathbf{x}(t_0) + \int_{t_0}^{t_0+h} dt' \; \mathbf{f}(\mathbf{x}(t'), t'). \tag{2.3}$$

Thus, good approximations for the integral are needed.

Runge-Kutta methods

A very simple approximation for the integral is

$$\int_{t_0}^{t_0+h} dt' \; \mathbf{f}(\mathbf{x}(t'), t') \approx \mathbf{f}(\mathbf{x}(t_0), t_0)h. \tag{2.4}$$

Using this in eq. (2.3), one can approximate $\mathbf{x}(t)$ by the sequence $\mathbf{x}_n$, which follows from an iteration of

$$\mathbf{x}_{n+1} = \mathbf{x}_n + \mathbf{f}(\mathbf{x}_n, t_n)h, \tag{2.5}$$

with $t_n = t_0 + nh$. This method is called *Euler method* and has been published by Leonard Euler in the 18th century [72]. The approximation of $\mathbf{x}_{n+1}$ is exact up to first order in h. Therefore, very small time steps h are required.

Higher accuracy can be achieved if other methods are used. For instance in the *Heun* method [109] two supporting points $\mathbf{x}$ and $\tilde{\mathbf{x}}$ are used, i.e.

$$\int_{t_0}^{t_0+h} dt'\ \mathbf{f}(\mathbf{x}(t'), t') \approx \frac{\mathbf{f}(\mathbf{x}(t_0), t_0) + \mathbf{f}(\tilde{\mathbf{x}}(t_0), t_0 + h)}{2} h, \tag{2.6}$$

with

$$\tilde{\mathbf{x}}(t_0) = \mathbf{x}(t_0) + \mathbf{f}(\mathbf{x}(t_0), t_0)h. \tag{2.7}$$

$\mathbf{x}_n$ follows from

$$\begin{aligned} \mathbf{x}_{n+1} &= \mathbf{x}_n + \frac{\mathbf{f}(\mathbf{x}_n, t_n) + \mathbf{f}(\tilde{\mathbf{x}}_n, t_n + h)}{2} h, \\ \tilde{\mathbf{x}}_n &= \mathbf{x}_n + \mathbf{f}(\mathbf{x}_n, t_n)h. \end{aligned} \tag{2.8}$$

This concept can be generalized to the class of *Runge-Kutta methods* [41]. In particular, in the sth-order Runge-Kutta method, the function $\mathbf{f}(\mathbf{x}(t), t)$ is evaluated at s different supporting points in order to approximate the integral. Thus, the Heun method is a second-order Runge-Kutta method and the Euler-method a first order Runge-Kutta method. In this thesis, we use the popular fourth-order Runge-Kutta method [219, 149] in which the value of the integral is approximated by

$$\int_{t_0}^{t_0+h} dt'\ \mathbf{f}(\mathbf{x}(t'), t') \approx \frac{\mathbf{k}_1(\mathbf{x}, t_0) + 2\mathbf{k}_2(\mathbf{x}, t_0) + 2\mathbf{k}_3(\mathbf{x}, t_0) + \mathbf{k}_4(\mathbf{x}, t_0)}{6} h, \tag{2.9}$$

with

$$\begin{aligned} \mathbf{k}_1(\mathbf{x}, t_0) &= \mathbf{f}(\mathbf{x}, t_0) \\ \mathbf{k}_2(\mathbf{x}, t_0) &= \mathbf{f}\left(\mathbf{x} + \frac{h}{2}\mathbf{k}_1(\mathbf{x}, t_0), t_0 + \frac{h}{2}\right) \\ \mathbf{k}_3(\mathbf{x}, t_0) &= \mathbf{f}\left(\mathbf{x} + \frac{h}{2}\mathbf{k}_2(\mathbf{x}, t_0), t_0 + \frac{h}{2}\right) \\ \mathbf{k}_4(\mathbf{x}, t_0) &= \mathbf{f}\left(\mathbf{x} + h\mathbf{k}_3(\mathbf{x}, t_0), t_0 + h\right) \end{aligned}$$

and $\mathbf{x}_n$ follows from

$$\mathbf{x}_{n+1} = \mathbf{x}_n + \frac{\mathbf{k}_1(\mathbf{x}_n, t_n) + 2\mathbf{k}_2(\mathbf{x}_n, t_n) + 2\mathbf{k}_3(\mathbf{x}_n, t_n) + \mathbf{k}_4(\mathbf{x}_n, t_n)}{6} h. \tag{2.10}$$

This approximation is used in fig. 5.6 of chapter 5 with integration time step $h = 0.00005$, in order to simulate the irregular burster with sufficiently high accuracy.

2.2 Integration of stochastic differential equations

Most models in the present thesis account for the influence of noise. This leads to stochastic differential equations of the form

$$\dot{\mathbf{x}} = \mathbf{f}(\mathbf{x}, t) + \mathbf{G}\boldsymbol{\xi}(t), \tag{2.11}$$

with $\mathbf{x}$ being the vector of d stochastic state variables, $\mathbf{f}(\mathbf{x})$ a deterministic drift, and $\mathbf{G}$ a constant $d \times d$ matrix of noise intensities. We restrict on white Gaussian noises for which the components of $\boldsymbol{\xi}(t)$ have zero mean and are delta correlated, i.e. $\langle \xi_i(t) \rangle = 0$ and $\langle \xi_i(t)\xi_j(t') \rangle = \delta(t - t')\delta_{ij}$. δ_{ij} is the Kronecker delta.

For a given initial condition $\mathbf{x}_0 = \mathbf{x}(t_0)$, eq. (2.11) can be integrated formally and one obtains

$$\mathbf{x}(t) = \mathbf{x}(t_0) + \int_{t_0}^{t} dt' \ \mathbf{f}(\mathbf{x}(t'), t') + \int_{t_0}^{t} dt' \mathbf{G}\boldsymbol{\xi}(t'). \tag{2.12}$$

The second integral is a stochastic integral and the components of the white Gaussian noise $\boldsymbol{\xi}(t)$ can attain infinitely-large values at fixed times t. Therefore, the integral cannot be interpreted as a Riemann integral. In order to interpret the second integral it is convenient to consider the white noise $\boldsymbol{\xi}(t)$ as a increment $\boldsymbol{dW}(t)$ of a Wiener process $\boldsymbol{W}(t)$, which yields

$$\mathbf{x}(t) = \mathbf{x}(t_0) + \int_{t_0}^{t} dt' \ \mathbf{f}(\mathbf{x}(t'), t') + \int_{t_0}^{t} \mathbf{G} \ \mathbf{dW}(t'). \tag{2.13}$$

In particular, since we restrict on constant noise-intensity matrizes $\mathbf{G}$, the equation for the kth component of $\mathbf{x}(t)$ is

$$x_k(t) = x_k(t_0) + \int_{t_0}^{t} dt' \ f_k(\mathbf{x}(t'), t') + \sum_{j=1}^{d} G_{kj} \int_{t_0}^{t} dW_j(t'). \tag{2.14}$$

f_n the nth component of $\mathbf{f}$ and G_{ij} the (i, j)th entry of $\mathbf{G}$. In general, the occurring

stochastic integrals are defined as [137]

$$\int_{t_0}^{t} dW_j(t') := \lim_{n\to\infty} \sum_{l=1}^{n} \left(W_j(t_{l+1}^{(n)}) - W_j(t_l^{(n)}) \right) = W_j(t) - W_j(t_0), \tag{2.15}$$

$t_0 = t_1^{(n)} < t_2^{(n)} < ... < t_{n+1}^{(n)} = t$ are arbitrary supporting points in the interval $[t_0, t]$, which become infinitely dense in the limit $n \to \infty$. Since $W_j(t)$ is a Wiener process, it fulfills $W_j(t_0) = 0$. Furthermore, its increments $\Delta W_j(t - t') := W_j(t) - W_j(t')$ are independent normal-distributed random numbers with zero mean and variance $t - t'$. Note that stochastic integration of time-dependent deterministic or stochastic functions is more complicate and requires the consideration of a certain interpretation of the stochastic integral[1].

Euler-Maruyama method

The Euler-Maruyama method is the most basic algorithm to integrate stochastic differential equations numerically and is based on the Euler method for ordinary differential equations, eq. (2.5). The latter has been extended to the *Euler-Maruyama method* – also called Euler method – for stochastic differential equations in the 20th century. In particular its convergence was shown by Gisiro Maruyama [177]. Applying the Euler-Maruyama method with a small integration time step h to equation, eq. (2.14), the approximation for the components of $\mathbf{x}(t)$ is given by

$$x_k(t_0 + h) \approx x_k(t_0) + f_k(\mathbf{x}(t_0), t_0)h + \sum_{j=1}^{d} G_{kj} \Delta W_j(h). \tag{2.17}$$

Thus, the integrals over the deterministic drifts, which are now evaluated at the respective realizations of the stochastic values of $\mathbf{x}(t)$, are approximated by eq. (2.4) and the contributions of the stochastic integrals are described by independent normal distributed random numbers $\Delta W_j(h)$ with zero mean and variance h. In particular, it holds that $\Delta W_j(h) = \sqrt{h} \Delta W_j(1)$. Thus, the lowest order contribution of the noise is of order $\sqrt{h}$.

[1] In more detail, the stochastic integral of a stochastic process $z(t')$ is defined as

$$\int_{t_0}^{t} z(t')\, dW_j(t') := \lim_{n\to\infty} \sum_{l=1}^{n} z(\tau_l^{(n)}) \left(W_j(t_{l+1}^{(n)}) - W_j(t_l^{(n)}) \right). \tag{2.16}$$

$\tau_l^{(n)} \in [t_l^{(n)}, t_{l+1}^{(n)}]$ is the evaluation point and defines the value of z that is used to approximate $z(t)$ in the interval. In contrast to the deterministic case in which the limit is independent of the particular choice of $\tau_l^{(n)}$, the choice of $\tau_l^{(n)}$ influence the value of the stochastic integral. Therefore, each choice of $\tau_l^{(n)}$ yields a certain interpretation of stochastic integrals. The most popular choices are: $\tau_l^{(n)} = t_l^{(n)}$ (Itô [119, 120, 103, 137]), $\tau_l^{(n)} = \frac{1}{2}(t_{l+1}^{(n)} + t_l^{(n)})$ (Stratonovich [245, 103, 137]), and $\tau_l^{(n)} = t_{l+1}^{(n)}$ (Hänggi-Klimontovich [103, 136]).

This yields for the full state vector

$$\mathbf{x}(t_0 + h) \approx \mathbf{x}(t_0) + \mathbf{f}(\mathbf{x}(t_0), t_0)h + \sqrt{h}\mathbf{G}\boldsymbol{\Delta W}(1). \tag{2.18}$$

$\boldsymbol{\Delta W}(1)$ is a vector with components $\Delta W_j(1)$. Iteratively applying eq. (2.18) yields $\mathbf{x}_{n+1} \approx \mathbf{x}(t_{n+1})$ from $\mathbf{x}_0$ and the realizations of the vector $\boldsymbol{\Delta W}_n(h)$ from the sequence

$$\mathbf{x}_{n+1} = \mathbf{x}_n + \mathbf{f}(\mathbf{x}_n, t_n)h + \sqrt{h}\mathbf{G}\boldsymbol{\Delta W}_n(1). \tag{2.19}$$

Numerically, the vector of random variables $\boldsymbol{\Delta W}_n(1)$ is realized using the pseudo-random number generator *Mersenne twister* [178]. Throughout this thesis, the Euler-Maruyama method is used, if not stated otherwise.

In order to approximate the spiking statistics for a neuron model, we integrate the corresponding stochastic differential equation numerically and start the recording of the spike times after a relaxation time T_{rel}. Then, simulations are stopped if either N_{spike} spike times have been recorded, or after t_{n+1} has reached a maximum time $T_{\max}$. The integration time step h has to be chosen small to guarantee that $\mathbf{f}(\mathbf{x}(t), t)$ varies only slightly between subsequent steps. On the other hand, large time steps are valuable in order to allow for the detection of a sufficient number of spike times, even if the firing rate is low. In order to chose a proper h, we have performed several test runs of the simulations and reduced h until the statistics has become independent of h. The final values used in the simulations are given in tab. 2.1. The time step h is either fixed or dynamic. In the later case, h is updated before the next Euler-Maruyama step is done and $t_n = t_0 + \sum_{k=1}^{n} h_k$ with h_k being the length of the kth time step. This allows for larger values of h in regions in which the components of $\mathbf{f}(\mathbf{x}(t), t)$ are small.

Stochastic Heun method

The generalization of higher order Runge-Kutta methods to stochastic differential can be done, but it has been found that higher-order schemes do often not improve the accuracy [218].

Therefore, we consider only one higher-order scheme, which can be seen as the generalization of the Heun method, eq. (2.8), to stochastic differential equations [28, 179]. In the stochastic version of the Heun scheme, the solution of the stochastic differential equation is approximated by the sequence

$$\mathbf{x}_{n+1} = \mathbf{x}_n + \frac{\mathbf{f}(\mathbf{x}_n, t_n) + \mathbf{f}(\tilde{\mathbf{x}}_n, t_n + h)}{2}h + \sqrt{h}\mathbf{G}\boldsymbol{\Delta W}_n(1), \tag{2.20}$$

with

$$\tilde{\mathbf{x}}_n = \mathbf{x}_n + \mathbf{f}(\mathbf{x}_n, t_n)h + \sqrt{h}\mathbf{G}\boldsymbol{\Delta W}_n(1). \tag{2.21}$$

Note that both, $\tilde{\mathbf{x}}_n$ and $\mathbf{x}_{n+1}$ contain the same realization of the Wiener process.

figure	h	T_{rel}	N_{spike}	$T_{\max}$
3.9	$2\pi\min(0.1, \frac{1}{100\lvert f(\phi)\rvert})$; (**d**)	0		10^5
3.11	$0.0001/D$; (**f**)	$100\tau/\sqrt{D}$	10^6	
3.12, 3.13, 3.14, 3.15	10^{-4} ($D < 1$) and 10^{-6} ($D \geq 1$); (**f**)	100τ	10^5	
3.15B	10^{-4}; (**f**)	100τ	10^5	
3.16, 3.20	$2\pi\min(0.1, \frac{1}{10000\lvert f(\phi)\rvert})$ if $D < 0.02$ and $\omega_0 \geq 0.85$, else $2\pi\min(0.1, \frac{1}{100\lvert f(\phi)\rvert})$; (**d**)	0	10^7	
3.19	$2\pi\min(0.1, \frac{1}{10000\lvert f(\phi)\rvert})$; (**d**)	0	10^7	
3.20	$2\pi\min(0.1, \frac{1}{10000\lvert f(\phi)\rvert})$ if $D > 0.01$, else $2\pi\min(0.1, \frac{1}{100\lvert f(\phi)\rvert})$; (**d**)	0	10^7 if $D > 0.01$, else 10^8	
3.21	$2\pi\min(0.1, \frac{1}{10000\lvert f(\phi)\rvert})$; (**d**)	0	10^7	
4.4 4.8, 4.7	$\min(\frac{10^{-3}}{\max(D_\theta, D_\phi)*\max(\kappa_\theta, \kappa_\phi)}, 5*10^{-3})$; (**f**)	0	10^5 (per node)	10^7
4.5	$\min(\frac{0.5*10^{-3}}{\max(D_\theta, D_\phi)*\max(\kappa_\theta, \kappa_\phi)}, 5*10^{-3})$; (**f**)	0	10^5	10^8
4.9	$\min(0.001/(D_\phi \max(\kappa_\phi, \kappa_\theta), 5*10^{-3})$; (**f**)		10^6 (per node)	10^8
4.10	$\min(0.01/(D_\phi \max(\kappa_\phi, \kappa_\theta)), 0.01)$; (**f**) and 0.01 for $\kappa_\theta < 0.3$	0	10^9 (per node) 10^7 (per node)	10^{11}
5.8 5.10, 5.11	10^{-4}; (**f**)	0		10^6

Table 2.1: Details of the simulations with Euler-Maruyama method for the respective figures. Fixed time steps are marked by (**f**) and dynamic time steps by (**d**).

2.3 Implementation of the reset

In most models, the differential equation is complemented by a spike-triggered feedback mechanism and/or a reset condition. These are implemented by comparing the components of $\mathbf{x}_{n+1}$ with the reset condition. If the reset condition applies, t_{n+1} has been detected as the spike time and $\mathbf{x}_{n+1}$ is set to its reset value. With this procedure, individual interspike intervals are at maximum h too long, but one accounts for differences of the contributions of the deterministic drift between reset and threshold properly. Note that the errors in the recorded interspike intervals do add up, i.e. nth order intervals are at maximum nh too long. In contrast, in simulations of the active rotator model in the absence of feedback, which were performed in the chapters 3 and 4, the phase reset, eq. (3.2), is implemented by reducing ϕ by 2π after each crossing of 2π. In this model the deterministic drift is 2π periodic and its contribution to $\dot{\mathbf{x}}$ is not influenced by the

reset. Thus, in these simulations individual interspike intervals are at maximum h too long, but this error does not add up to higher order intervals.

2.4 Weighted-ensemble Brownian dynamics simulation

In addition to the spiking statistics, we study the stationary probability distribution of system variables in section 3.3. Since all considered neuron models are ergodic, the stationary probability density can be estimated from simulations of long trajectories in the stationary regime. However, this method results into problems if transitions between particular regions of the phase space are rare or if the system variables evolve on different time scales. In order to simulated such systems more efficiently, several specialized algorithms have been developed in the past decades. Some of them are presented in the references [23, 91, 60]. The general idea of these algorithms is to decouple the probability for a transition in the simulation – determined by the so-called *sampling distribution* – from the corresponding transition probability. A general concept, which allows to sample arbitrary, but known probability distributions with an unphysical, at best, flat sampling distribution, has been published in the late seventies and is known as *umbrella sampling* [253]. In the last decades *umbrella sampling* has originated several efficient simulation algorithms for equilibrium systems. One of which is *weighted-ensemble Brownian dynamics simulation* [116, 25, 278, 24]. This method aims at realizing a flat sampling distribution by dividing the phase space in several equally sampled simulation boxes. Consequently, the finer the grid of boxes the more flat is the sampling distribution used for the simulation.

In chapter 3 we use a simplified version of this simulation technique, which we have published in ref. [142]. In order to explain this simulation technique in more detail, we consider the basic example of one-dimensional overdamped Brownian motion in the potential $U(x)$. The time evolution of the position x of the Brownian particle is then given by

$$\dot{x} = -\frac{\partial}{\partial x}U(x) + \sqrt{2D}\xi(t). \tag{2.22}$$

$\xi(t)$ fulfills the conditions of white Gaussian noise introduced above. We further divide the region of interest, given by the interval $[x_L, x_R]$ with $x_L < x_R$ into M equally sized boxes. Thus, the coordinates $x \in [x_L + i\Delta x, x_L + (i+1)\Delta x)$, $i = 0, 1, ..., M-1$ belong to the ith box. The size of one box is given by $\Delta x = (x_R - x_L)/M$. Furthermore, each box is given a probability $P_i(t)$, which describes the probability to find x at time t in that box. Initially, we start with a uniform distribution of probability among the boxes, which is approximated best by setting all P_i to $P_i(t_0) = 1/M$.

In order to approximate the stationary probability distribution $p_{\mathrm{st}}(x)$ the following time-evolution steps are performed [142].

1. At first, we perform a *redistribution step* in which N walkers – copies of the system – are uniformly distributed in the individual boxes. Besides their individual positions

$x_i^k(t)$, where $i = 0, ..., M-1$ denotes the particular box and $k = 1, ..., N$ the individual walkers, each walker possesses a given amount of weight $q_i^k(t)$. This is nothing but the present probability in the ith box distributed to the N walkers, i.e.

$$q_i^k(t) = \frac{P_i(t)}{N}. \tag{2.23}$$

Note that one does not need to introduce walkers in boxes with $P_i(t) = 0$.

2. At second, we perform N_{int} *integration steps*. In this step, eq. (2.22) is integrated N_{int} times for all walkers, by applying one of the integration schemes introduced in section 2.2 to eq. (2.22). One *integration step* realizes the time evolution $x_i^k(t) \to x_i^k(t+h)$ for the walkers and, therefore, leads to a transport of weights between the boxes. Note that walkers are independent and, therefore, explore the region around each box with different paths. Furthermore, if the equation of motion, eq. (2.22), is complemented by a reset condition

$$\text{if } x > x_{\text{thres}}, \text{ then } x \to x_{\text{res}}, \tag{2.24}$$

with threshold x_{thres} and reset x_{res}, it has to be applied to the individual walkers.

3. At third, an *updating step* is performed in which the new box probabilities $P_i(t + N_{\text{int}}h)$ are calculated by summing up the weights of all walkers that are in box i after the N_{int} *integration steps*,

$$P_i(t + N_{\text{int}}h) = \sum_{i',k|x_{i'}^k(t+N_{\text{int}}h)\in[x_L+i\Delta x, x_L+(i+1)\Delta x)} q_{i'}^k(t). \tag{2.25}$$

In the following, we refer to a sequence of a redistribution step, N_{int} integration steps, and an updating step as a *running step*. After an equilibration time T_{therm}, the set $\mathbf{P}(t) = (P_0(t), P_1(t), ..., P_{M-1}(t))^T$ reaches a stationary regime in which the individual $P_i(t)$s fluctuate around some constant values. Then, the stationary probability density $p_{\text{st}}(x)$ can be approximated by time-averaging the components of the sets $\mathbf{P}(t)$. These sets are recorded at N_{av} times $t_\ell = T_{\text{therm}} + (\ell - 1)n_{\text{av}}N_{\text{int}}h$, $l = 1, 2, ..., N_{\text{av}}$, i.e. every n_{av} running steps. Finally, the stationary probability $P_{i,\text{st}}$ of finding a particle in box i can be approximated by

$$P_{i,\text{st}} \approx \langle P_i \rangle = \frac{1}{N_{\text{av}}} \sum_{l=1}^{N_{\text{av}}} P_i(t_l). \tag{2.26}$$

Furthermore, we approximate the stationary probability distribution $p_{\text{st}}(x)$ by the set $\mathbf{p}_{\text{st}} = (p_{\text{st}}(X_0), p_{\text{st}}(X_1), ..., p_{\text{st}}(X_{M-1})))$ with $p_{\text{st}}(X_i) = P_{i,\text{st}}/\Delta x$, where X_i is the center of box i.

In addition to the specification of all system parameters, a run of the weighted-ensemble Brownian dynamics algorithm for a one-dimensional system requires a speci-

fig. 3.8A			fig. 3.8B			fig. 3.8C		
ω_0	D	T_{therm}	ω_0	D	T_{therm}	ω_0	D	T_{therm}
0.81	0.075	50000	0.865	0.01	300000	0.87	0.01	400000
0.81	0.1093	50000	0.865	0.03	50000	0.87	0.03	50000
0.81	0.125	50000	0.865	0.05	10000	0.87	0.05	50000

Table 2.2: Equilibration times used for simulations in fig. 3.8.

fication of the values of x_L, x_R, N, Δx, h, N_{int}, n_{av}, N_{av}, T_{therm}. The full simulation box, bordered by x_L and x_R should span the region with finite stationary probability density. The number of walkers per box N can be set to an arbitrary value $N \geq 2$ – at least two walkers per box are required to allow the $P_i(t)$ to split. As already stated in ref. [142] even $N = 2$ produces satisfying results for many systems and is, therefore, used in the simulations. The choices of the parameters Δx, h, and N_{int} are restricted to criteria that are caused by the uniform distribution of walkers in the redistribution step, which is rather unphysical and causes a slightly flatter stationary probability distribution, since walkers can escape deep potential minima or reach high maxima more easy. To minimize the resulting imprecisions, the size of the individual boxes Δx will be chosen small compared to the distance the walkers pass during the N_{int} integration steps. For noise-dominated regions, this relates the box size to the contribution of the noise term during one integration step. Applying the Euler-Maruyama method, eq. (2.18), this yields

$$\Delta x \ll 2\sqrt{Dh}. \tag{2.27}$$

In contrast, if the motion is dominated by the deterministic drift, one obtains from eqs. (2.18) and (2.22)

$$\Delta x \ll |\frac{\partial}{\partial x} U(x)|h. \tag{2.28}$$

In most systems the region of physical interest lies in a deep potential well and $p_{\text{st}}(x)$ attains small values at the borders. In order to simulate the border regions properly, small time steps h are required. The parameter N_{av} should be chosen as large as possible and n_{av} should be chosen large enough to ensure that the different sets $\mathbf{P}(t_l)$ are uncorrelated. Next, T_{therm} is obtained from test runs of the algorithm in which we check the equilibration time T_{therm} of the firing rate. Estimates of the firing rate can be easily obtained by summing up the weights of all walkers that are reset in a certain time interval and normalization by the length of the interval.

Finally, we provide the parameter values that are used in the weighted-ensemble Brownian dynamics simulation that were performed in chapter 3. In particular, this method is used for the distribution $p_{\text{st}}(\omega)$ in fig. 3.8. The corresponding parameter region is given by $\phi \in [-\pi/4, 2\pi]$ and $\omega \in [-0.05, 1.5]$ and divided into rectangular boxes with

side lengths $\Delta\phi = 0.01\sqrt{2Dh}$ and $\Delta\omega = 0.5h/\tau$ and $N = 2$ walkers per box. The walkers were redistribution every $N_{\text{int}} = 1$ steps, and $N_{\text{av}} = 10^4$ sets of $\mathbf{P}_{\text{st}}$ have been recorded every $n_{\text{av}} = 5$ redistribution steps in order to get an approximation $\mathbf{p}$ of the stationary probability distribution $p_{\text{st}}(\phi, \omega)$. The time evolution of the individual walkers has been performed using the stochastic Heun scheme, eq. (2.20), with time step $h = 0.1$. Finally, $p_{\text{st}}(\phi, \omega)$ was integrated over the full ϕ-range in order to obtain the stationary probability distribution of ω, i.e.

$$p_{\text{st}}(\omega) = \int_{-\pi/4}^{2\pi} d\phi \; p_{\text{st}}(\phi, \omega). \tag{2.29}$$

The reset condition has been implemented according to eq. (3.5). The parameter T_{therm} has been obtained by checking the saturation time of the firing rate. This resulted in the values of T_{therm} summarized in tab. 2.2.

2.5 Numerical bifurcation analysis

In chapter 5 we perform a numerical bifurcation analysis of the reduced Morris-Lecar model eq. (5.5) with respect to the three parameters I_{eff}, g_{eff}, and $V_{\text{K},1}$. All other parameters are fixed to the values given in tab. 1.1. The bifurcation analysis is performed with the program AUTO-07P [61] and the included HomCont package. In order to analyze the system we perform the following steps.

1. *Find the stable fixed point*: For fixed $V_{\text{K},1}$ and g_{eff} a high value of I_{eff} is chosen ($I_{\text{ext}} = 1000$). Then the high-voltage fixed point is approached by integrating the system eq. (5.5).

2. *Continuation of the fixed point*: In the next step continuation of the fixed point is performed for decreasing values of I_{ext} and all bifurcations are recorded.

3. *Continuation of Hopf and saddle-node bifurcations*: Next, continuation of the recorded Hopf and saddle-node bifurcations is performed by adding g_{eff} as a continuation parameter. With these procedure the location of the Bogdanov-Taken and Cusp bifurcation in fig. 5.3 are obtained. Repeating this procedure for different values of $V_{\text{K},1}$, leads to the corresponding lines in fig. 5.3B.

4. *Continuation of the limit cycle*: Now, continuation of the limit cycle is performed. To this end we start at the high-current Hopf bifurcation in region a in fig. 5.3, and follow the cycle for decreasing I_{eff}. If the limit cycle becomes a homoclinic orbit to a saddle point it undergoes a saddle homoclinic orbit bifurcation.

5. *Continuation of the homoclinic orbit*: The homoclinic orbit is followed using the HomCont package. For the results in fig. 5.3A, this is performed by adding g_{eff} and I_{eff} as continuation parameters. Furthermore to obtain the results presented

in fig. 5.3B, we used $V_{\mathrm{K},1}$ instead of g_{eff} as a bifurcation parameter in order to detect parts of codimension-two bifurcation lines that are almost parallel to the g_{eff}-axis. Following the homoclinic orbit, bifurcations can be detected with help of the test functions ψ_i, which are included in the HomCont package. In particular, for the detection of the saddle-node homoclinic orbit bifurcation, we evaluate the test function ψ_{15} (zero if non-central homoclinic orbit to saddle-node) and ψ_{10} (zero if number of eigenvalues with negative real part decreases). The former test function changes sign and latter becomes zero at the saddle-node homoclinic orbit bifurcation, which yields a point on the border line between region a and b coming from low values of g_{eff} or high values of $V_{\mathrm{K},1}$ in fig. 5.3B. Then, in region b, following the invariant circle to the saddle-node (same continuation parameters as before) the second saddle-node homoclinic orbit bifurcation can be found similarly. This yields another point on the border line. Further following the homoclinic orbit and recording the highest value of g_{eff} for which the homoclinic orbit exist yields the border between region a and c, which is marked by HH in fig. 5.3.

Note that AUTO-07P cannot follow codimension-two bifurcation lines of homoclinic orbits, thus, the described procedure has to be repeated for different initial values of g_{eff} and $V_{\mathrm{K},1}$ in order to obtain enough points on the codimension-two lines in fig. 5.3B.

3 Slow spike-triggered feedback in excitable systems

In the present chapter, we investigate the influence of spike-triggered feedback on the spike generation in a noisy excitable systems. In particular, we consider negative and positive feedback mechanisms, which can cause spike-frequency adapation or reverse spike-frequency adaptation, respectively. The general setup is illustrated in fig. 3.1. The excitable system is subject to a slow feedback mechanism, which is controlled by the spike generation and feeds back on the excitable system on a slow time scale, i.e. slow compared to individual interspike intervals (ISI). Parts of this chapter have been published in the refs. [143] and [144].

3.1 Active rotator model with spike-triggered feedback

In order to model the system, we use an *active rotator model*. In particular, we consider the noisy dimensionless active rotator model, eq. (1.38). In the following, we drop the tildes in eq. (1.38) in order to simplify the notation, which yields

$$\dot{\phi} = \omega_0 - \sin\phi + \sqrt{2D}\xi(t). \tag{3.1}$$

ω_0 is the positive driving parameter and the last term accounts for white Gaussian noise, i.e. $\langle \xi(t) \rangle = 0$ and $\langle \xi(t)\xi(t') \rangle = \delta(t-t')$, with noise intensity D. The system's state is given by the phase-like variable ϕ, which runs from zero to 2π within one ISI, i.e. when ϕ reaches 2π we postulate the occurrence of a spike. Spike times are recorded in order to evaluate the resulting spike train, count, and ISI statistics, see section 1.7. Note that ϕ can in principle attain all values between $-\infty$ and 2π, however, since $\dot{\phi}$ is usually positive at $\phi = 0$, negative values are rare.

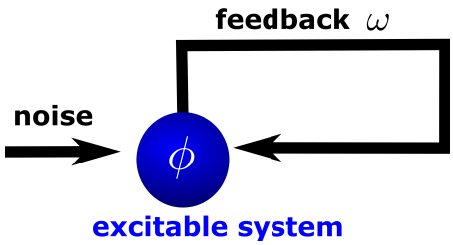

Figure 3.1: Basic setup in the present chapter. The excitable system is described by a single phase variable ϕ and is subject to a spike-triggered feedback ω and noise.

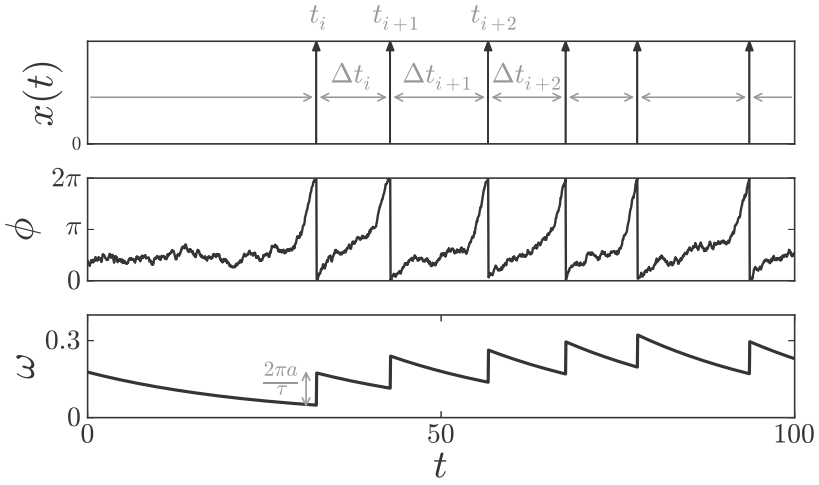

Figure 3.2: Representative trajectory of the noisy active rotator model eq. (3.1) with positive feedback eq. (3.4). Parameters: $\omega_0 = 0.9$, $a = 0.5$, $\tau = 25$, and $D = 0.05$.

For simplicity, we perform an instantaneous phase reset

$$\text{if } \phi \geq 2\pi, \quad \text{then } \phi \to 0, \tag{3.2}$$

after each spike, which does not affect the dynamics due to the periodicity of the sinus term but allows for a straightforward implementation of the spike-triggered feedback mechanism. The latter will be introduced later on.

At first, we briefly recapitulate the dynamics of the system, eq. (3.1), hence, in the absence of feedback, which was already presented in section 1.3.3 and summarized in fig. 1.5. Furthermore, we will refer to eq. (3.1) as *original system* in the following. The dynamics of the original system is controlled by the positive driving parameter ω_0. In particular, we distinguish between subthreshold driving ($0 < \omega_0 < 1$), and superthreshold driving ($\omega_0 > 1$). For subthreshold driving the deterministic system has a stable fixed point and the system is in excitable mode in which spikes can only occur due to noisy excitations. In contrast, for superthreshold driving the deterministic system has a limit cycle and the active rotator model is in oscillatory mode, which yields a regular (or tonic) spike generation. Note that the spiking is perfectly periodic in the absence of noise ($D = 0$). The bifurcation between both regimes is a *saddle-node on invariant circle bifurcation*. Thus, the active rotator model has Class 1 excitability, see sec. 1.4.

In order to implement the spike-triggered feedback dynamics, we introduce a time-dependent offset ω to the driving ω_0. Thus, the full system reads

$$\dot{\phi} = \omega_0 + \omega(t) - \sin\phi + \sqrt{2D}\xi(t). \tag{3.3}$$

In the following, we will refer to ω as feedback. Its dynamics is given by

$$\tau\dot{\omega} = -\omega + 2\pi a x(t). \tag{3.4}$$

τ scales the time scale separation between phase and feedback dynamics and is assumed to be large, i.e. $\tau \gg 1$ (slow feedback), if not mentioned otherwise. While the first term leads to an exponential decay of ω, the second term realizes the spike-triggered nature of the feedback and couples ω to the spike generation. The strength of this coupling is scaled by the parameter a, which determines how strong ω is affected by the individual spikes. This implementation of the feedback is motivated by biological mechanisms that lead to spike-frequency adaptation and reverse spike-frequency adaptation, which have been presented in section 1.5. In particular, it is a simplified variant from the adapting Θ-neuron, which can be derived from neurons with Class 1 excitability that contain biologically-plausible adaptation currents, see ref. [18]. In their model, the feedback – as well as the noise, see [68, 100, 165] – enters the ϕ dynamics with a phase-dependent prefactor, which we neglect for simplicity.

Furthermore, a representative trajectory, the definition of the spike times t_i, and that of the interspike intervals Δt_i are illustrated in fig. 3.2 for a positive a. An equivalent implementation for such feedback can be achieved by a modification of the reset condition, eq. (3.2), to

$$\text{if } \phi = 2\pi, \text{ then } \phi \to 0 \text{ and } \omega \to \omega + 2\pi a/\tau, \tag{3.5}$$

instead of coupling the feedback to the spike train. Note that ω attains the sign of a for large times $t \gg \tau$. Considering the sign of the parameter a, we can distinguish between *positive* feedback ($a > 0$), i.e. the total driving $\omega_0 + \omega$ is effectively increased after each spike, and *negative* feedback ($a < 0$), i.e. the total driving is effectively reduces after each spike.

3.2 Deterministic dynamics in the presence of feedback

First, we focus on the deterministic dynamics ($D = 0$). We first demonstrate that the transient dynamics in response to an instantaneous increase of the driving parameter resembles the phenomenon of spike-frequency adaptation for negative feedback and that of reverse spike-frequency adaptation for positive feedback. At second, we consider the influence of feedback on the asymptotic dynamics.

3.2.1 Transient dynamics

Since the investigation of negative and positive feedback has been motivated by the phenomena of spike-frequency and reverse spike-frequency adaptation, see section 1.5, we briefly demonstrate that these phenomena can be observed in the active rotator model with sufficiently strong negative and positive feedback, respectively. To this end we consider the response of the system to a step-like increase of the driving parameter

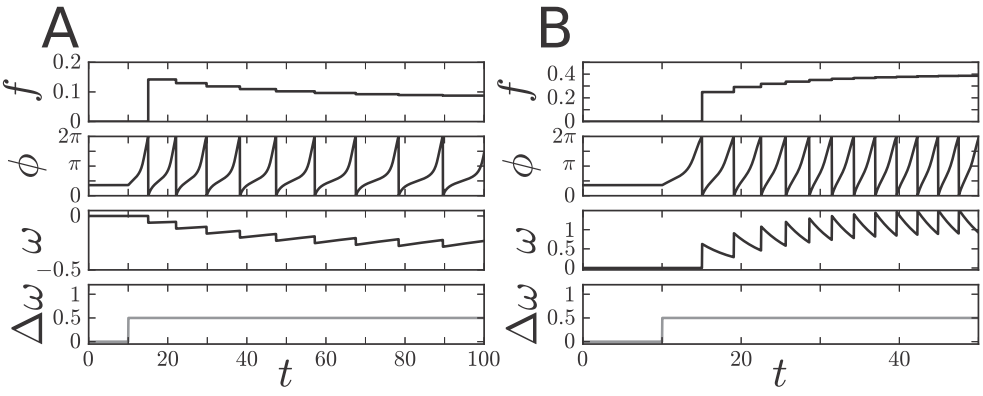

Figure 3.3: Spike-frequency adaptation for negative feedback (A) and reverse spike-frequency adaptation for positive feedback (B). Parameters: $\omega_0 = 0.9$, $\Delta\omega = 0.5$, $t_{\text{on}} = 10$, $D = 0$, $a = 0.5$, $\tau = 50$ (A) and $\tau = 5$ (B).

$\omega_0 \to \omega_0 + \Delta\omega$ at t_{on}, which resembles the application of a positive current to a neuron. In particular, both phenomena are related to the shape of the spike-frequency, i.e. the inverse lengths of the interspike intervals. In order to visualize the latter, we consider the function

$$f(t) := \begin{cases} 1/\Delta t_i & t_i < t < t_{i+1} \\ 0 & \text{else} \end{cases} \tag{3.6}$$

As demonstrated in fig. 3.3 negative feedback causes a decrease and positive feedback and increase of $f(t)$, and thereby the spike frequency, within the first ISIs in response to a step-like excitation. These phenomena are known as spike-frequency and reverse spike-frequency adaptation in neurons.

3.2.2 Asymptotic dynamics

Next, we aim at deriving approximations for the asymptotic firing rate of the system in the case of slow feedback ($\tau \gg \langle \Delta t \rangle$) and at understanding the feedback-induced modification of the dynamics. In case of slow feedback, we can consider the dynamics of ω as a small perturbation and apply averaging methods [221, 238]. To this end, we formulate the active rotator system with spike-triggered feedback as the initial value problem

$$\begin{pmatrix} \dot{\phi} \\ \dot{\omega} \end{pmatrix} = \begin{pmatrix} \omega_0 + \omega - \sin(\phi) \\ 0 \end{pmatrix} + \frac{1}{\tau} \begin{pmatrix} 0 \\ -\omega + 2\pi a x(t) \end{pmatrix}, \qquad \begin{pmatrix} \phi(0) \\ \omega(0) \end{pmatrix} = \begin{pmatrix} \Phi \\ \Omega \end{pmatrix}, \tag{3.7}$$

which is complemented by the reset condition

$$\text{if } \phi = 2\pi, \text{ then } \phi \to 0. \tag{3.8}$$

The first term on the right-hand side of eq. (3.7) is the unperturbed system and the second term corresponds to the small perturbation. The initial conditions are given by $\phi(0) = \Phi$ and $\omega(0) = \Omega$. Furthermore, the solutions of the unperturbed problem ($1/\tau \to 0$) are periodic in time for initial conditions $\Omega > 1 - \omega_0$ and their period T corresponds to the ISIs of the system. By separation of variables and integration over ϕ one gets

$$T(\omega_0, \Omega) = \frac{2\pi}{\sqrt{(\omega_0 + \Omega)^2 - 1}}, \ \tau \to \infty, \tag{3.9}$$

for $\Phi = 0$. Thus, positive feedback ($\Omega > 0$) leads to smaller ISIs, whereas negative feedback ($\Omega < 0$) increases the ISIs.

In order to deal with the perturbed system, we consider the dynamics of ω during one ISI. Given the initial condition $\Phi = \phi(t_i) = 0$ and $\Omega = \omega(t_i) = \omega_i$ at the beginning of the ith ISI, the dynamics of ω according to eq. (3.7) is given by

$$\omega(t) = \omega_i \ e^{-\frac{t-t_i}{\tau}}, \quad t \in [t_i, t_{i+1}). \tag{3.10}$$

At the end of the interval ω receives an offset of $2\pi a/\tau$ and ϕ is reset, which yields the initial condition at the beginning of the next interval as $\phi(t_{i+1}) = 0$ and $\omega(t_{i+1}) = \omega_{i+1}$, with

$$\omega_{i+1} = \omega(t_{i+1}) = \omega_i \ e^{-\frac{\Delta t_i}{\tau}} + \frac{2\pi a}{\tau}. \tag{3.11}$$

In order to obtain results for the ith ISI Δt_i, we apply the concept of averaging, see ref. [221], in which the influence of the small perturbation on the unperturbed dynamics is approximated by considering only the time-averaged perturbation. For the chosen initial conditions, this corresponds to considering the time-averaged driving parameter $\overline{\omega}_i$,

$$\overline{\omega}_i = \frac{1}{\Delta t_i} \int_{t_i}^{t_{i+1}} dt \ \omega(t) = \frac{\tau}{\Delta t_i} \omega_i \left(1 - e^{-\frac{\Delta t_i}{\tau}}\right), \tag{3.12}$$

in the unperturbed system. This yields the averaged-system:

$$\dot{\phi} = \omega_0 + \overline{\omega}_i - \sin(\phi), \quad t \in (t_i, t_{i+1}), \tag{3.13}$$

which approximates the perturbed system during the ith ISI. Considering the resulting length of the ith ISI according to eq. (3.9), we obtain the self-consistent equation

$$\Delta t_i \approx T(\omega_0, \overline{\omega}_i(\omega_i)) = \frac{2\pi}{\sqrt{(\omega_0 + \overline{\omega}_i)^2 - 1}}. \tag{3.14}$$

It is self-consistent, since $\overline{\omega}_i$ depends on Δt_i, see eq. (3.12).

Since we are mainly interested in the asymptotic behavior, we consider the asymptotic limit $i \to \infty$ and search for fixed points of eq. (3.11), i.e. for solutions $\omega^{\mathrm{fp}} = \omega_i = \omega_{i+1}$.

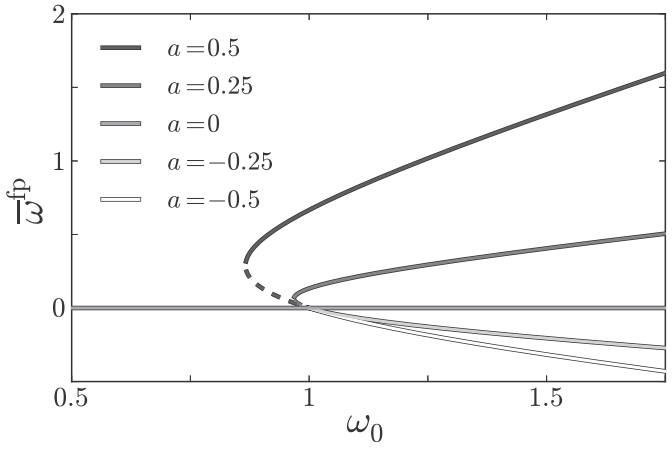

Figure 3.4: Solutions for the averaged feedback, eq. (3.18), that correspond to stable limit cycles (straight lines) and unstable limit cycles (dashed lines).

This accounts for the condition that the exponential decay of the feedback is balanced by the after spike offset $2\pi a/\tau$. Solving eq. (3.11) one immediately finds that

$$\omega^{\mathrm{fp}} \approx \frac{\frac{2\pi a}{\tau}}{1-\exp\left(-\frac{T(\omega_0,\overline{\omega}^{\mathrm{fp}})}{\tau}\right)}. \tag{3.15}$$

The resulting average feedback strength $\overline{\omega}^{\mathrm{fp}}$ has to fulfill eq. (3.12) with $\omega_i = \omega^{\mathrm{fp}}$ and $\Delta t_i = T(\omega_0, \overline{\omega}^{\mathrm{fp}})$, which yields

$$\overline{\omega}^{\mathrm{fp}} \approx \frac{2\pi a}{T(\omega_0, \overline{\omega}^{\mathrm{fp}})}. \tag{3.16}$$

Note that $T(\omega_0, \overline{\omega}^{\mathrm{fp}})$ is only defined for $\overline{\omega}^{\mathrm{fp}} \in (1-\omega_0, \infty)$. Furthermore, ω^{fp} approaches $\overline{\omega}^{\mathrm{fp}}$ in the limit of large τ and eq. (3.16) becomes exact. Dynamically, the fixed points ω^{fp} correspond the initial feedback value of limit cycle solutions. On the limit cycle, the phase and feedback dynamics is given by the eq. (3.7) with inital conditions $\phi(0) = 0$ and $\omega(0) = \omega^{\mathrm{fp}}$ and can be approximated by the averaged system eq. (3.13) with $\overline{\omega}_i = \overline{\omega}^{\mathrm{fp}}$ for large $\tau \gg 1$. In both case the phase reset, eq. (3.5) has to be considered.

Interestingly, eq. (3.16) relates the averaged feedback on the limit cycle $\overline{\omega}^{\mathrm{fp}}$ to the cycle period $T(\omega_0, \overline{\omega}^{\mathrm{fp}})$, which yields the asymptotic ISI and can be used to eliminate Ω in eq. (3.9) (with $\Omega = \overline{\omega}^{\mathrm{fp}}$). It results in a quadratic equation that has up to two solutions T_1 and T_2

$$T_{1,2} \approx \frac{2\pi}{\omega_0^2-1}(\pm\sqrt{\omega_0^2+(a^2-1)} - a\omega_0),\ \langle\Delta t\rangle \ll \tau. \tag{3.17}$$

Alternatively, using eq. (3.16) to eliminate T in eq. (3.9) yields the corresponding

averaged feedback values $\overline{\omega}_1^{\mathrm{fp}}$ and $\overline{\omega}_2^{\mathrm{fp}}$ on the limit cycle

$$\overline{\omega}_{1,2}^{\mathrm{fp}} \approx \frac{a}{1-a^2}(a\omega_0 \pm \sqrt{\omega_0^2 + (a^2-1)}),\ \langle \Delta t \rangle \ll \tau. \tag{3.18}$$

Note that in order to fulfill eq. (3.16) only solutions with $\mathrm{sgn}(\overline{\omega}^{\mathrm{fp}}) = \mathrm{sgn}(a)$ are allowed. $\mathrm{sgn}(x)$ denotes the sign of x.

The stability of these limit cycles can be analyzed by investigating how small perturbations $\delta\omega_i$ from the initial feedback value at the limic cycle ω^{fp} at the beginning of the ith ISI evolve. From eq. (3.11), we find for the perturbation at the beginning of the $(i+1)$th ISI $\delta\omega_{i+1}$:

$$\omega^{\mathrm{fp}} + \delta\omega_{i+1} = (\omega^{\mathrm{fp}} + \delta\omega_i) \exp\left(-\frac{T(\omega_0, \overline{\omega}_i)}{\tau}\right) + \frac{2\pi a}{\tau}. \tag{3.19}$$

$\overline{\omega}_i$ marks the time-average feedback for the perturbed ith ISI. Furthermore, for small perturbations $\delta\omega_i \ll \omega^{\mathrm{fp}}$, we can use the first-order Taylor expansion for the period of the perturbed cycle. This yields

$$T(\omega_0, \overline{\omega}_i) \approx T(\omega_0, \overline{\omega}^{\mathrm{fp}}) + \frac{\partial T}{\partial \overline{\omega}^{\mathrm{fp}}} \frac{\partial \overline{\omega}^{\mathrm{fp}}}{\partial \omega^{\mathrm{fp}}} \delta\omega_i. \tag{3.20}$$

Here and in the following, we suppress the arguments of $T(\omega_0, \overline{\omega}^{\mathrm{fp}})$. Considering only first-order terms in the perturbations in eq. (3.19), using the Taylor expansion eq. (3.20), and substituting the unperturbed equation, we find

$$\delta\omega_{i+1} \approx e^{-\frac{T}{\tau}} \left(1 - \frac{\omega_{\mathrm{fp}}}{\tau} \frac{\partial T}{\partial \overline{\omega}^{\mathrm{fp}}} \frac{\partial \overline{\omega}^{\mathrm{fp}}}{\partial \omega^{\mathrm{fp}}}\right) \delta\omega_i. \tag{3.21}$$

For $\tau \gg T(\omega_0, \overline{\omega}^{\mathrm{fp}})$, we can use that $e^{-\frac{T(\omega_0, \overline{\omega}^{\mathrm{fp}})}{\tau}} \approx 1 - T(\omega_0, \overline{\omega}^{\mathrm{fp}})/\tau$ and obtain

$$\delta\omega_{i+1} \approx \left(1 - \frac{1}{\tau} \frac{\partial}{\partial \omega^{\mathrm{fp}}} \left(\omega^{\mathrm{fp}} T\right)\right) \delta\omega_i. \tag{3.22}$$

Here, we have neglected terms of order $1/\tau^2$ and applied the chain rule. τ is positive, therefore perturbations grow if $\frac{\partial}{\partial \omega^{\mathrm{fp}}}(-\omega^{\mathrm{fp}} T(\omega_0, \overline{\omega}^{\mathrm{fp}}))$ is positive in the vicinity of $\omega = \omega^{\mathrm{fp}}$ and ω^{fp} describes an unstable limit cycle. In contrast, negative values indicate a stable limit cycle at ω^{fp}.

Solutions of eq. (3.18) are illustrated in fig. 3.4 for different feedback strengths. Furthermore, the dynamical regimes, which result from the evaluation of the number of stable and unstable solutions of eq. (3.18), are shown in fig. 3.5. In the following, we discuss the different regimes in more detail.

- *Excitable*: For $\omega_0 < 1$, the original system has one stable fixed point at $\phi = \arcsin(\omega_0)$. In the presence of negative or weak positive feedback ($a < \sqrt{1-\omega_0^2}$) no finite solution for $\overline{\omega}^{\mathrm{fp}}$ exists and the system relaxes to the fixed point at $(\phi, \omega) =$

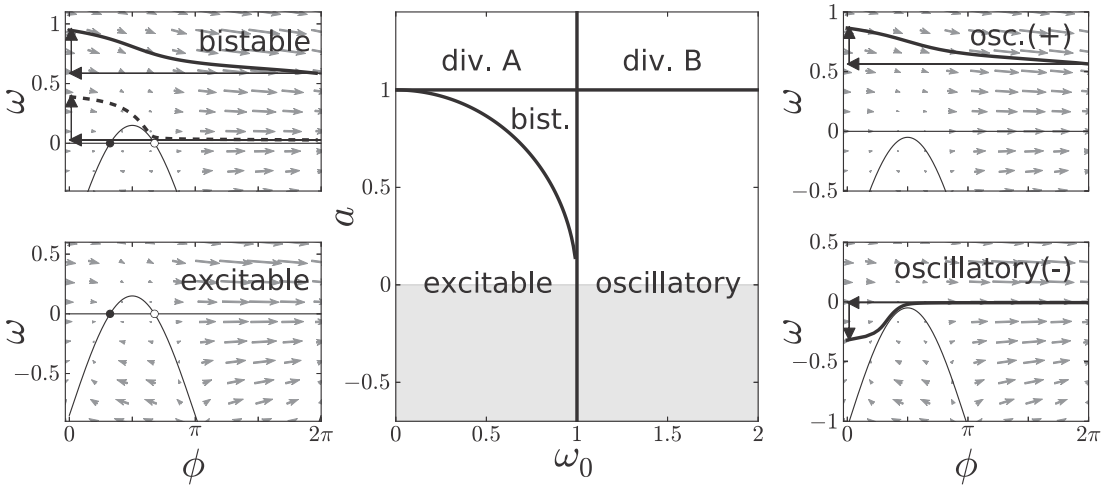

Figure 3.5: Dynamical regimes in the (ω_0, a)-parameter space in the slow-feedback limit ($\tau \to \infty$) (center) and phase portraits in the physically-relevant regions of bistable (bist. ,top left), excitable (left bottom), and oscillatory (osc.) behavior with positive (+) and negative (-) feedback (right) for $\tau = 10$. Center: black lines illustrate bifurcations between dynamical regimes. Phase portraits: limit cycles are indicated by thick black lines and arrows, which illustrate the reset. Nullclines and fixed points are marked by thin black lines and black points for stable and white points for unstable fixed points, respectively. Gray arrows illustrate the velocity field $(\dot{\phi}, \dot{\omega})$. Parameters left: $\omega_0 = 0.8$, $a = 0.6$ (bistable) and $a = 0$ (excitable); right: $\omega_0 = 1.05$ and $a = 0.5$ (osc.(+)) and $a = -0.5$ (osc.(-)).

$(\arcsin(\omega_0), 0)$ from any initial condition. Furthermore, once it has reached this fixed point, spikes can only occur due to noisy excitations (see next section).

- *Oscillatory*: For $\omega_0 > 1$ the original system has a stable limit cycle that remains in the presence of feedback. In this regime, we find two solutions for $\overline{\omega}^{\text{fp}}$. However, since $\overline{\omega}^{\text{fp}}$ and a must have the same sign in order to fulfill eq. (3.16), only $\overline{\omega}_1^{\text{fp}}$ is a reasonable solution. Furthermore, it describes the averaged-feedback value on the limit cycle with period T_1 (eq. (3.17)), corresponding to the ISIs.

- *Bistable*: This regime exists for strong positive feedback ($\sqrt{1-\omega_0^2} < a < 1$) and strong, but subthreshold driving ($\sqrt{1-a^2} < \omega_0 < 1$). Besides the stable fixed point of the original system, the feedback creates one stable and one unstable limit cycle at $\omega \approx \overline{\omega}_1^{\text{fp}}$ and $\omega \approx \overline{\omega}_2^{\text{fp}}$, respectively. The corresponding ISIs are given by the solution T_1 and T_2 of eq. (3.17), respectively.

- *Divergent*: For $a > 1$ the feedback is so strong that the exponential decay of ω during the ISIs cannot balance the after-spike offset and no stable solution exist for $\omega_0 > 1$ (div. B in fig. 3.5). However, subthreshold driving ($\omega_0 < 1$) still causes the existence of the stable fixed point from the original system (div. A in fig. 3.5). The separatrix between initial conditions that are attracted by the fixed point and

those that diverge to infinite ω is described by the unstable limit cycle solution $\omega \approx \overline{\omega}_2^{\mathrm{fp}}$ with corresponding period T_2.

Solutions for the asymptotic firing rate are studied in section 3.4.1 in more detail.

3.3 Dynamics in the presence of noise and feedback

Since most biological systems operate in a noisy environment, we consider finite noise intensities $D \neq 0$ in the following. Thus, noisy perturbations enable the system to escape the stable fixed point, which exists for weak driving $\omega_0 < 1$, and, thus, allow for the generation of spikes.

In order to apply the concept of averaging that was used in the previous section, we first assume that τ is large compared to a long sequences of ISI. In this case, we can time-average the feedback dynamics eq. (3.4) over time intervals T_{av} of length $\langle \Delta t \rangle \ll T_{\mathrm{av}} \ll \tau$ and introduce the time-resolved average feedback

$$\overline{\omega}_t := \frac{1}{T_{\mathrm{av}}} \int_t^{t+T_{\mathrm{av}}} dt' \; \omega(t'). \tag{3.23}$$

In order to find stationary solutions, we consider its time derivative

$$\dot{\overline{\omega}}_t := \lim_{\Delta t \to 0} \frac{\overline{\omega}_{t+dt} - \overline{\omega}_t}{dt}. \tag{3.24}$$

The latter can be related to $\dot{\omega}$ and we find for long intervals that $T_{\mathrm{av}} \gg \langle \Delta t \rangle$:

$$\tau \dot{\overline{\omega}}_t \;\; = -\tfrac{1}{T_{\mathrm{av}}} \int_t^{t+T_{\mathrm{av}}} dt' \, (\omega + 2\pi a \; x(t)) = \overline{\omega}_t + 2\pi a \tfrac{N(t,T_{\mathrm{av}})}{T_{\mathrm{av}}}. \tag{3.25}$$

This yields for long intervals $T_{\mathrm{av}} \gg \langle \Delta t \rangle$

$$\tau \dot{\overline{\omega}}_t \approx -\overline{\omega}_t + 2\pi a \; r \approx -\overline{\omega}_t + \frac{2\pi a}{\langle \Delta t \rangle}. \tag{3.26}$$

The second relations follows from eq. (1.72). Thus, stationary solutions for $\overline{\omega}_t$ fulfill

$$\dot{\overline{\omega}}^{\mathrm{fp}} = 0 \quad \rightarrow \quad \overline{\omega}^{\mathrm{fp}} \approx 2\pi a r \approx \frac{2\pi a}{\langle \Delta t \rangle}. \tag{3.27}$$

We denoted solutions of $\dot{\overline{\omega}}_t = 0$ by $\overline{\omega}^{\mathrm{fp}}$, since eq. (3.27) becomes exact for $T_{\mathrm{av}} \to \infty$ and yields the same conditions as eq. (3.16) for the deterministic solutions.

We are now interested in calculating $\overline{\omega}^{\mathrm{fp}}$ in the presence of noise. To this end, we assume that $\omega \approx \overline{\omega}^{\mathrm{fp}}$ and that ω is approximately constant on time scales of order T_{av}.

In this case, ϕ is approximately given by the one-dimensional dynamics

$$\dot{\phi} \approx \omega_0 + \overline{\omega}^{\mathrm{fp}} - \sin\phi + \sqrt{2D}\xi(t) = -\frac{\partial}{\partial\phi}U(\phi, \overline{\omega}^{\mathrm{fp}}) + \sqrt{2D}\xi(t). \tag{3.28}$$

For such systems, we have presented analytical results for the mean ISI in section 1.8. In particular, the application of eq. (1.106) to eq. (3.28) yields an approximation for the mean ISI, which reads

$$\langle \Delta t \rangle \approx \frac{\int_0^{2\pi} dx\; e^{\frac{U(x,\overline{\omega}^{\mathrm{fp}})}{D}} \int_{x-2\pi}^{x} dy\; e^{-\frac{U(y,\overline{\omega}^{\mathrm{fp}})}{D}}}{D\left(1 - e^{-\frac{2\pi(\omega_0+\overline{\omega}^{\mathrm{fp}})}{D}}\right)},\ \langle \Delta t \rangle \ll \tau. \tag{3.29}$$

Applying eq. (3.27), we end up with the following self-consistent equation for the stationary solutions for the average feedback $\overline{\omega}^{\mathrm{fp}}$:

$$\overline{\omega}^{\mathrm{fp}} = \frac{2\pi a D\left(1 - e^{-\frac{2\pi(\omega_0+\overline{\omega}^{\mathrm{fp}})}{D}}\right)}{\int_0^{2\pi} dx\; e^{\frac{U(x,\overline{\omega}^{\mathrm{fp}})}{D}} \int_{x-2\pi}^{x} dy\; e^{-\frac{U(y,\overline{\omega}^{\mathrm{fp}})}{D}}}. \tag{3.30}$$

Equation (3.30) allows for a numerical evaluation of $\overline{\omega}^{\mathrm{fp}}$ by searching for the intersections of the left-hand and right-hand side. Furthermore, a solution is stable if the slope of the right-hand side as a function of $\overline{\omega}^{\mathrm{fp}}$, evaluated at the solution, is smaller than one and unstable if it is larger than one.

Results for the self-consistent solutions of eq. (3.30) are illustrated in fig. 3.6A for a strong positive feedback and subthreshold driving ($\omega_0 < 1$), i.e. close to the bistable region, which we have found for the deterministic system before. Interestingly, in the noisy system up to two stable finite solutions for $\overline{\omega}^{\mathrm{fp}}$ can be found. One fulfills $\omega_0 + \overline{\omega}^{\mathrm{fp}} < 1$ and the other one $\omega_0 + \overline{\omega}^{\mathrm{fp}} > 1$. The former one will be referred to as low-feedback state (L), see fig. 3.7, and results in excitable behavior. The driving is on average smaller than one and the averaged system, eq. (3.28), has a stable fixed point (if D is formally set to zero). Consequently, ϕ relaxes to the stable branch of the ϕ-nullcline first and follows the branch while ω approaches zero. Spikes can only occur due to noisy excitations that enable ϕ to escape to pass the unstable branch. In contrast, in the high-feedback state (H) the driving is on average larger than one. Thus, the system is in an oscillatory state and the phase reset leads to a limit cycle in the averaged system eq. (3.28) (again, if D is formally set to zero). This causes a tonic spike generation. For illustration, representative trajectories are illustrated in fig. 3.7 in the parameter region were even the deterministic system is bistable. In general, we find that for negative feedback and for superthreshold driving, no additional stationary solutions $\overline{\omega}^{\mathrm{fp}}$ exist. Thus, we focus on strong positive feedback $a > 0$ in the region of subthreshold driving $\omega_0 < 1$ in the following.

Parameter regions for which the averaged system eq. (3.28) has qualitatively similar

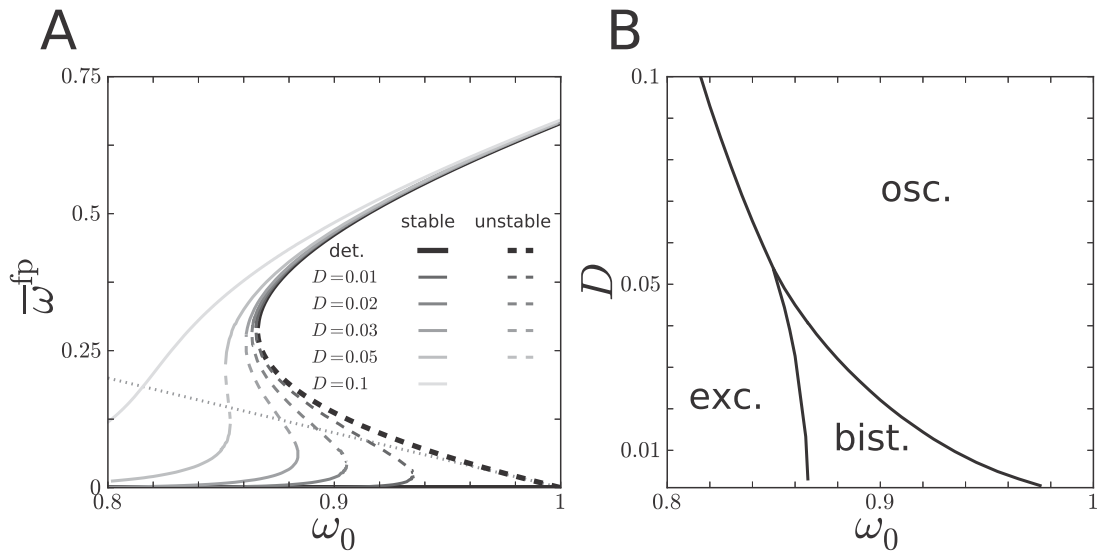

Figure 3.6: Self-consistent solutions of eq. (3.30) as a function of ω_0 (A) and regions of qualitatively similar solutions in the (ω_0, D) parameter space (B) for positive feedback. A: Solutions of eq. (3.30), the average feedback on the limit cycle for $D = 0$ (det.), and the fixed point solution $\overline{\omega}^{\mathrm{fp}} = 0$ are plotted. The dotted, straight gray line marks the border between regions with solutions that lead to excitable (exc.) behavior ($\omega_0 + \overline{\omega}^{\mathrm{fp}} < 1$) and those that cause oscillatory (osc.) behavior ($\omega_0 + \overline{\omega}^{\mathrm{fp}} > 1$) in eq. (3.28). If both solutions coexist the region is referred to as bistable (bist.). Parameters: $a = 0.5$.

stable states are illustrated in fig. 3.6B for strong positive feedback ($a = 0.5$). In the region of weak driving and weak noise, the averaged system is in the excitable regime ($\omega_0 + \overline{\omega}^{\mathrm{fp}} < 1$), while strong noise and strong driving lead to limit cycle oscillations and rather tonic spike generation ($\omega_0 + \overline{\omega}^{\mathrm{fp}} > 1$). In between, L and H-state coexist. We will refer to this region as bistable, since two stable solutions of eq. (3.30) coexists. Interestingly, the bistable region becomes smaller and extends towards weaker driving if the noise is strengthened. Consequently, fixing all parameters of the deterministic system (ω_0, a, $\tau \gg \langle \Delta t \rangle$), we find that the solutions for $\overline{\omega}^{\mathrm{fp}}$ change in three qualitatively different ways as a function of D. Those are illustrated in fig. 3.8A-C and will be studied in the following in more detail. Furthermore, the corresponding stationary probability distributions $p_{\mathrm{st}}(\omega)$, eq. (2.29), of ω are shown in the upper panels of fig. 3.8. In particular, $p_{\mathrm{st}}(\omega)dw$ yields the stationary probability to find the feedback in the interval $[\omega, \omega + d\omega)$. Note that due to the large time scale separation between the ϕ and ω-dynamics, long simulation times are required. Therefore, we used a weighted-ensemble Brownian dynamics simulation technique, which is described in section 2.4. Parameters related to the numerics are given in table 2.2.

The shape of $\overline{\omega}^{\mathrm{fp}}$ for weak driving is illustrated in fig. 3.8A. For such driving, one stable solution $\overline{\omega}^{\mathrm{fp}}$ exists for each noise intensity and $\overline{\omega}^{\mathrm{fp}}$ increases monotonically if D is increased. This is a consequence of eq. (3.27) and the fact that the mean ISI decreases

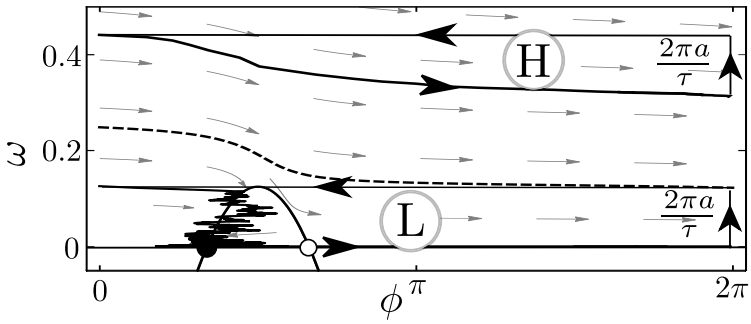

Figure 3.7: Trajectories during one ISI in the low-feedback state (L) and high-feedback state (H) obtained from simulations in the region where the deterministic system is bistable. The dashed line indicates the separating unstable periodic orbit in the deterministic system. Parameters: $a = 0.5$, $\omega_0 = 0.875$, $\tau = 25$, $D = 0.02$. Figure has been modified from ref. [144]

monotonically with the noise intensity, which has already been found by Stratonovich [246]. However, in the presence of positive feedback the reduction of the mean ISI causes an increase of the driving. This can even shift the system into the tonic firing mode ($\omega_0 + \overline{\omega}^{\mathrm{fp}} > 1$). However, the corresponding distribution $p_{\mathrm{st}}(\omega)$ of the feedback ω is unimodal for all noise intensities, see fig. 3.8A (top). The maximum of $p_{\mathrm{st}}(\omega)$ is well-approximated by the corresponding solutions of $\overline{\omega}^{\mathrm{fp}}$. Only for weak noise, we find higher values of $p_{\mathrm{st}}(\omega)$ below $\overline{\omega}^{\mathrm{fp}}$. This may be caused by the finite τ used in the simulations of $p_{\mathrm{st}}(\omega)$.

Another type of behavior occurs for a strong but still subthreshold driving $\sqrt{1-a^2} < \omega_0 < 1$. Here, even the deterministic system is bistable and two stable solutions of eq. (3.30) coexist for weak noise, marked gray in fig. 3.8C. Then, an increase of the noise intensity leads to the annihilation of the stable low-feedback solution with the unstable one and only the high-feedback solution remains for strong noise. We find a bimodal shape of $p_{\mathrm{st}}(\omega)$ in the weak-noise region. Increasing the noise intensity shifts probability into the high-feedback maximum of $p_{\mathrm{st}}(\omega)$ and, finally, the distribution becomes unimodal for strong noise.

Most interestingly, for intermediate subthreshold driving, we find a limited noise range, marked as gray in fig. 3.8B, in which two stable solutions for $\overline{\omega}^{\mathrm{fp}}$ coexists. Traces of $\omega(t)$ in this regime, as illustrated in figures 3.9B, show long time intervals, long compared to the feedback time scale, in which $\omega(t)$ is close to the high-feedback solution. These intervals are followed by long intervals in which $\omega(t)$ is close to the low-feedback solution. This is reminiscent of noise-induced switching between two minima in a bistable potential. However, in marked contrast to Brownian motion in a bistable potential the existence of stable solutions for $\overline{\omega}^{\mathrm{fp}}$ significantly depends on the noise intensity. As illustrated in fig. 3.8B, an increase of the noise intensity first leads to one solution causing excitable behavior. Then, for intermediate noise, we find two coexisting stable solutions and finally, for strong noise, only one solution that causes limit cycle oscillations exists. We will call this type of behavior *noise-controlled bistability*. The corresponding station-

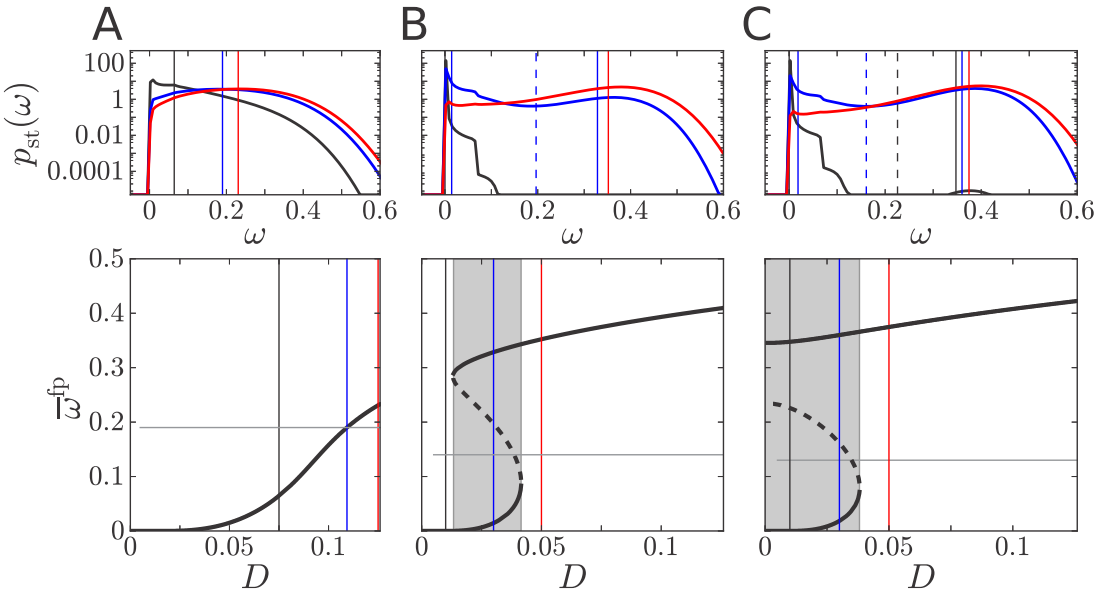

Figure 3.8: Solutions $\overline{\omega}^{\rm fp}$ as a function of noise intensity D (bottom). For weak driving ($\omega_0 = 0.81$) (A), intermediate driving ($\omega_0 = 0.865$) (B), and strong, subthreshold driving $\sqrt{1-a^2} < \omega_0 < 1$ ($\omega_0 = 0.87$) (C). Corresponding stationary probability distributions $p_{\rm st}(\omega)$ for the feedback values and the noise intensities, which are marked by vertical colored lines in the bottom figures, are plotted in upper figures. In the upper figures vertical lines mark stable (straight) and unstable (dashed) solutions for $\overline{\omega}^{\rm fp}$ obtained for the noise intensities: $D = 0.075$, 0.1093, 0.125 (A) and $D = 0.01$, 0.03, 0.05 (B and C). Parameters: $a = 0.5$ (both) and $\tau = 50$ (top).

ary probability distribution $p_{\rm st}(\omega)$ is either unimodal, with a maximum at low ω (weak noise) or high ω (strong noise), respectively, or bimodal (intermediate noise). In any case the maxima can be approximated by the stable solutions of $\overline{\omega}^{\rm fp}$, while the unstable solution can serve as an approximant for the position of the local minimum, which is present in the bimodal distribution. Such qualitative changes in probability distributions are typically referred to as *stochastic phenomenological bifurcations* [8]. Recently, similar changes of modality have been observed in the distribution of oscillation amplitudes close to a bistable regime near a subcritical Hopf bifurcation [275, 273, 276]. However, in these systems the oscillation frequency is rather independent of the amplitude and no transition from excitable to oscillatory behavior occurs. In contrast, in the active rotator model with spike-triggered feedback noise controls the occupation of two states with qualitatively different spiking statistics. The latter will be discussed in the next sections in more detail.

Interestingly, the phenomenon of noise-controlled bistability stays in marked contrast to the influence of noise in other bistable systems. Considering for instance the bistable

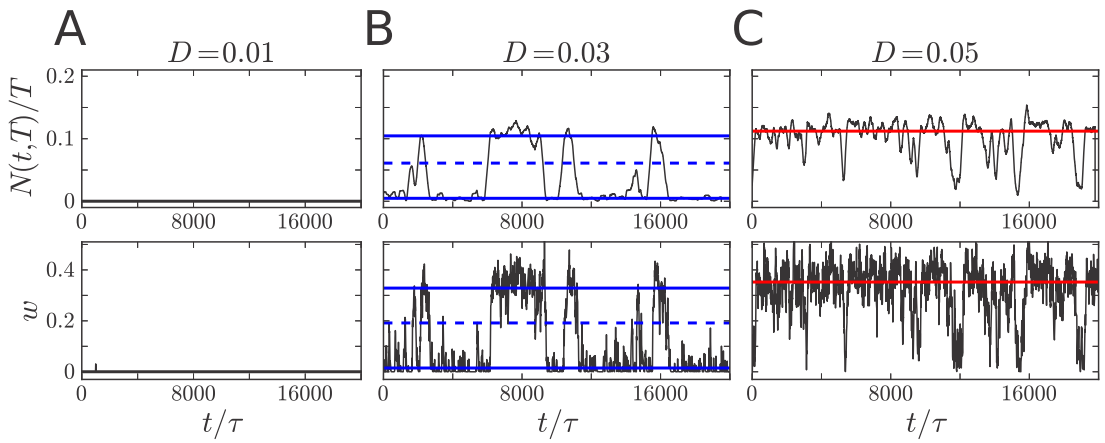

Figure 3.9: Traces of $\omega(t)$ (bottom) and normalized time-resolved spike count $N(t,T)/T$ for $T = \tau/D$ (top) from simulations for noise intensities marked in fig. 3.8B and corresponding parameters of the deterministic system. Colors indicate solutions for $\overline{\omega}^{\text{fp}}$ (bottom) and corresponding firing rates according to eq. (3.27).

potential

$$U(x) = -\frac{x^2}{2} + \frac{x^4}{4}, \tag{3.31}$$

with stationary probability distribution given by $p_{\text{st}}(x) \propto e^{-U(x)/D}$, which follows from eq. (1.77). Due to the symmetry, the two minima at $x^{\pm}_{\text{min}}$ are equally-occupied for all noise intensities ($\int_{-\infty}^{0} p_{\text{st}}(x)dx \approx \int_{0}^{\infty} p_{\text{st}}(x)dx$). Now, breaking the symmetry, e.g. by deepen the minimum at negative x-values x^{-}_{min}, only the lower minimum is occupied in the weak-noise limit ($\int_{-\infty}^{0} p_{\text{st}}(x)dx \approx 1$). Increasing the noise intensity shifts probability into the second minimum. But, in contrast to the observed probability distributions in the region of noise-controlled bistability, even in the strong-noise limit both minima are at most equally occupied ($\int_{-\infty}^{0} p_{\text{st}}(x)dx \approx \int_{0}^{\infty} p_{\text{st}}(x)dx$). Thus, there is no way to choose the noise intensity such that the probability to find the system in the minimum at x^{+}_{min} is higher than that of finding it in the minimum at x^{-}_{min}, i.e. to fulfill the inequality ($\int_{-\infty}^{0} p_{\text{st}}(x)dx < \int_{0}^{\infty} p_{\text{st}}(x)dx$). In case of noise-controlled bistability, however, only the low-feedback state is occupied in the weak-noise limit, while only the high-feedback state is occupied in the strong-noise limit. In between, both states are occupied with finite probability.

Time traces of the feedback in the region of noise-controlled bistability are illustrated in fig. 3.9A-C for the noise intensities marked in fig. 3.8B. Furthermore, in order to compare the firing rates associated with the corresponding solutions $\overline{\omega}^{\text{fp}}$, see eq. (3.27), the normalized time-resolved spike count $N(t,T)/T$, see eq. (1.57) in section 1.7, is plotted in the upper panel. It yields the number of spikes per unit time in a time interval T starting at time t. First, at weak noise intensities, ω decays to zero before

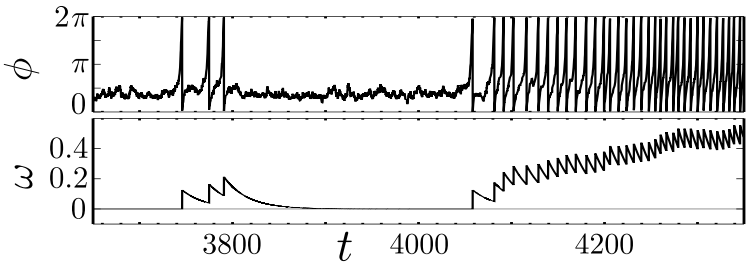

Figure 3.10: Trace of ϕ and ω during a LH-transition obtained from simulations. Parameters: $a = 0.5$, $\omega_0 = 0.875$, $\tau = 25$, $D = 0.02$. Figure has been modified from ref. [144]

the next spike occurs. Due to the resulting low firing rates, $N(t,T)/T$ is close to zero. However, if D is increased the system enters the regime of coexisting L and H-states and, as has been described before, the trace of $\omega(t)$ resembles that of a Brownian particle in a bistable potential. While ω remains in the vicinity of the stable solutions for times that are long compared to the feedback time scale τ, transitions between L and H-states occur on time scales of order τ. Finally, for strong noise only the H-state remains. Interestingly, the traces of $\omega(t)$ in the H-state look quite different from that in the L-state. First, much stronger fluctuations are present and, second, we find fast excursions towards very low values of ω even if only the H-state solution exists. This is reminiscent of power dropouts of light intensity observed in laser systems with optical feedback, which have been studied in [92, 188].

In order to understand this, we investigate the transition dynamics from L to H-state (LH-transition) and the opposite transition from H to L-state (HL-transition). Remarkably, these transitions are highly asymmetric at large τ. This results from the fact that the feedback can decay to zero within long intervals, whereas even the shortest ISI can only cause an increase of $2\pi a/\tau$. Thus, in order to perform a LH-transition, a sequence of short ISIs is required that leads to a slow increase of ω. A time series of ϕ and ω during a LH-transition is shown in fig. 3.10. In the L-state the increase of ω due to the after-spike offset typically decays until the next spike occurs. However, if noisy fluctuations lead to a sequence of short ISIs the feedback can build up and, finally, stabilizes in the vicinity of the high-feedback solution. In contrast, the HL-transition can occur within a single, long ISI. The fact that such ISIs are even possible when only one oscillatory solution of $\overline{\omega}^{\mathrm{fp}}$ exists leads to the escapes towards low feedback values observed in fig. 3.9C, which are reminiscent of an excitable system with downward spikes.

3.4 Effect of feedback on ISI statistics in excitable and oscillatory regime

In the following, we study the influence of feedback on the ISI statistics in the excitable and oscillator regime. During our investigations we focus on two measures. The first

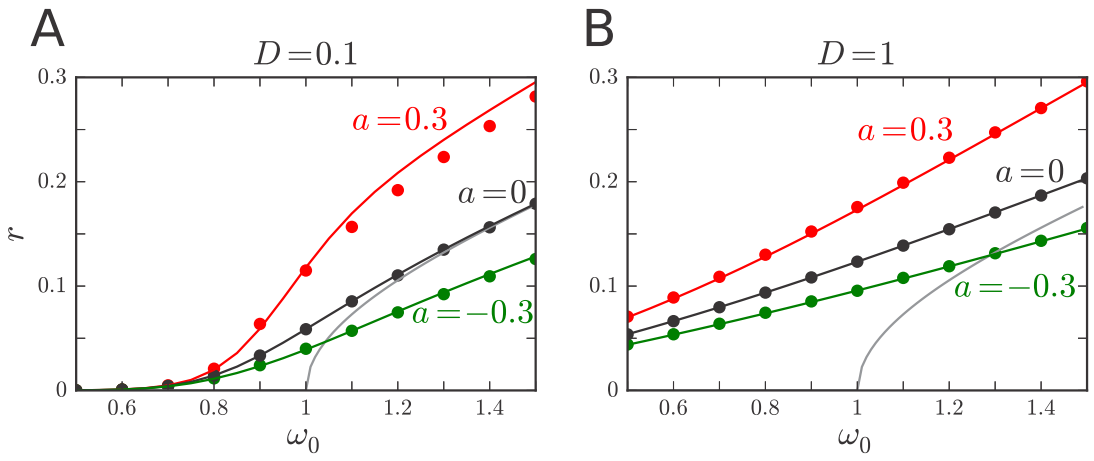

Figure 3.11: Asymptotic firing rate $1/\langle\Delta t\rangle$ from simulations (dots) compared to the weak-feedback approximation eq. (3.33) (lines). For $a = 0$ we used eq. (3.29) with $\overline{\omega}^{\mathrm{fp}} = 0$. The sum in the function $B(D, \omega_0)$ has been truncated after 600 summands. In addition, the deterministic firing rate, i.e. the inverse of the mean ISI given by eq. (3.9) ($\Omega = 0$), is plotted gray. Parameters: $\tau = 50$.

one is the asymptotic firing rate r, which is one of the most basic statistical measures in neuroscience, and the second one is the coefficient of variation (CV), which quantifies the degree of variability in the series of ISIs. Furthermore, we distinguish between the two qualitatively different cases of excitable behavior ($\omega_0 + \overline{\omega}^{\mathrm{fp}} < 1$) and tonic spiking behavior ($\omega_0 + \overline{\omega}^{\mathrm{fp}} > 1$).

3.4.1 Firing rate

Results for the firing rate for large $\tau \gg \langle\Delta t\rangle$, can be obtained from the self-consistent eq. (3.29). One way to deal with the double integral is a series expansion of the exponential terms, which reads

$$\langle\Delta t\rangle \approx \frac{2\pi}{\omega_0 + \overline{\omega}^{\mathrm{fp}}} \sum_{k=0}^{\infty} \left(\frac{1}{2D}\right)^k \sum_{m=0}^{k} \frac{1}{m!(k-m)!} \frac{I_{|k-2m|}\left(-\frac{1}{D}\right)}{1 + \frac{D^2(k-2m)^2}{(\omega_0+\overline{\omega}^{\mathrm{fp}})^2}}, \quad \langle\Delta t\rangle \ll \tau. \tag{3.32}$$

More details on this are given in appendix A.2.1. Note that the series expansion is exact, hence, the only assumption we use up to this point is that ω is close to $\overline{\omega}^{\mathrm{fp}}$.

While analytical results can be derived in the absence of feedback $\overline{\omega}^{\mathrm{fp}} = 0$ [246], we investigate small deviations from this case ($\overline{\omega}^{\mathrm{fp}} \ll \omega_0$) in the following. To this end, we perform a weak-feedback approximation of eq. (3.32). Due to the connection between $\overline{\omega}^{\mathrm{fp}}$ and the mean ISI, which presented in eq. (3.27), this approximation becomes valid in different cases. In more detail, each parameter combination that leads to $2\pi a/\langle\Delta t\rangle \ll \omega_0$ can in principle be treated in terms of the weak-feedback approximation. For such

parameter sets, we can expand eq. (3.32) in a Taylor series, which results into

$$\langle \Delta t \rangle \approx \langle \Delta t \rangle_{\overline{\omega}^{\mathrm{fp}}=0} - \frac{2\pi a}{\omega_0} + \frac{4\pi^2 a}{\omega_0^2 \langle \Delta t \rangle_{\overline{\omega}^{\mathrm{fp}}=0}} B(D, \omega_0), \quad \overline{\omega}^{\mathrm{fp}} \ll \omega_0, \quad \langle \Delta t \rangle \ll \tau. \tag{3.33}$$

The function $B(D, \omega_0)$ is an infinite series and given in eq (A.41) in appendix A.2.2. Furthermore, $\langle \Delta t \rangle_{\overline{\omega}^{\mathrm{fp}}=0}$ denotes the mean ISI in the absence of feedback, given by eq. (3.29) with $\overline{\omega}^{\mathrm{fp}} = 0$. The weak-feedback approximation eq. (3.33) compared to results from computer simulations is shown in fig. 3.11A and B. While the simulation results are well-approximated for strong noise, see fig. 3.11B, and subthreshold driving, we find deviations for weak noise and superthreshold driving, see fig. 3.11A. For the latter, the weak-feedback approximation produces deviations, because it treats $2\pi a/(\omega_0 \langle \Delta t \rangle)$ as a small parameter. However, for superthreshold driving positive feedback leads to quite high firing rates and, therefore, to moderate contributions of higher order terms. In addition, weak noise leads to stronger contributions of higher order terms. For instance, the first order in $2\pi a/(\omega_0 \langle \Delta t \rangle)$ contains the function $B(D, \omega_0)$, which becomes large for small noise intensities. This leads to stronger contributions of higher order terms at weak noise intensities, high firing rates, and strong feedback.

Equation (3.33) can be further simplified for high noise intensities. In particular, the last term in eq. (3.33) can be neglected for $D \gg 1$, see appendix A.2.2. Then the influence of feedback on the mean ISI can be approximated by

$$\langle \Delta t \rangle \approx \langle \Delta t \rangle_{\overline{\omega}^{\mathrm{fp}}=0} - \frac{2\pi a}{\omega_0}, \quad D \gg 1, \ \overline{\omega}^{\mathrm{fp}} \ll \omega_0, \quad \langle \Delta t \rangle \ll \tau. \tag{3.34}$$

Thus, positive feedback reduces the mean ISI, i.e. increases the asymptotic firing rate, while negative feedback acts in the opposite way.

The investigation for weak noise requires a discrimination between the cases of excitable behavior ($\omega_0 + \overline{\omega}^{\mathrm{fp}} < 1$) and tonic spiking ($\omega_0 + \overline{\omega}^{\mathrm{fp}} > 1$). In case of excitable behavior, the potential $U(\phi, \overline{\omega}^{\mathrm{fp}})$ in eq. (3.28) has one local minimum at $\phi = \arcsin(\omega_0 + \overline{\omega}^{\mathrm{fp}})$ and one local maximum at $\phi = \pi - \arcsin(\omega_0 + \overline{\omega}^{\mathrm{fp}})$. The mean ISI is approximately given by the inverse rate to pass the potential barrier and can be obtained from Kramers rate theory [140, 104]. This yields for the firing rate:

$$r = \frac{1}{\langle \Delta t \rangle} \approx \frac{\sqrt{1 - (\omega_0 + \overline{\omega}^{\mathrm{fp}})^2}}{2\pi} e^{-\frac{\Delta U}{D}}, \ D \ll 1, \quad \langle \Delta t \rangle \ll \tau. \tag{3.35}$$

While the prefactor can be obtained from the second derivatives of the potential at the local minimum and the local maximum, ΔU describes the height of the potential barrier $\Delta U = 2\sqrt{1 - (\omega_0 + \overline{\omega}^{\mathrm{fp}})^2} - 2(\omega_0 + \overline{\omega}^{\mathrm{fp}}) \arccos(\omega_0 + \overline{\omega}^{\mathrm{fp}})$. In case of weak feedback we

can expand the right-hand side of eq. (3.35) in a Taylor series and obtain

$$r \approx r_{\overline{\omega}^{\mathrm{fp}}=0}\left(1 - 2\pi a r_{\overline{\omega}^{\mathrm{fp}}=0}\left(\frac{\omega_0}{1-\omega_0^2} - \frac{2}{D}\arccos(\omega_0)\right)\right), \quad D \ll 1, \ \ \langle\Delta t\rangle \ll \tau, \tag{3.36}$$

up to first order in $\overline{\omega}^{\mathrm{fp}} = 2\pi a r_{\overline{\omega}^{\mathrm{fp}}=0}$. Thus, for sufficiently small noise intensities, the correction has the same sign as a. Alternatively, considering the inverse of the right-hand side of eq. (3.35) yields the first order approximation of the mean ISI:

$$\langle\Delta t\rangle \approx \langle\Delta t\rangle_{\overline{\omega}^{\mathrm{fp}}=0}\left(1 + \frac{2\pi a}{\langle\Delta t\rangle_{\overline{\omega}^{\mathrm{fp}}=0}}\left(\frac{\omega_0}{1-\omega_0^2} - 2\arccos(\omega_0)\right)\right), \quad D \ll 1, \ \ \langle\Delta t\rangle \ll \tau. \tag{3.37}$$

Consequently, the influence of feedback on the mean ISI and the firing rate is qualitatively similar to that in the strong noise region.

In the tonic spiking regime the potential $U(\phi, \overline{\omega}^{\mathrm{fp}})$ has no local minimum and, when reset to $\phi = 0$, the system follows the potential's gradient until $\phi = 2\pi$. For such problems, weak-noise approximations have been derived by Arecchi and Politi in ref. [6][1]. In particular, the mean ISI up to first order in D is given by

$$\langle\Delta t\rangle \approx \langle\Delta t\rangle_{D=0} + D\int_0^{2\pi} dy \frac{\frac{\partial K_1^{\mathrm{av}}}{\partial y}}{K_1^{\mathrm{av}}(y)^3}, \quad D \ll 1, \ \langle\Delta t\rangle \ll \tau, \tag{3.38}$$

where $K_1^{\mathrm{av}}(\phi)$ denotes the first kinetic coefficient, eq. (1.78), for the averaged system, eq. (3.28), i.e. $K_1^{\mathrm{av}}(\phi) = \omega_0 + \overline{\omega}^{\mathrm{fp}} - \sin(\phi)$. However, the first order term is zero and, hence, $\langle\Delta t\rangle$ is approximated up to first order by the deterministic limit, which has been derived before, see eq. (3.17). Thus, as we observed for the deterministic limit before, the firing rate increases for positive and decreases for negative feedback for weak noise in the oscillatory regime, too.

Results of the different approximations compared to simulations are shown in fig. 3.12 for the excitable regime (fig. 3.12A) and oscillatory regime (fig. 3.12B), respectively. While the strong-noise approximation eq. (3.34) yields good results for $D > 1$, the series expansion eq. (3.33) deviates from the simulation results for positive feedback and superthreshold driving. The infinite sum in the function $B(D, \omega_0)$ has been evaluated for the first 500 summands with high numerical precision. Evaluations up to more summands indicate that the break down is not due to the evaluation of the infinite sum, but due to the assumption that $\overline{\omega}^{\mathrm{fp}} \ll \omega_0$ used in the weak-feedback approximation. Breakdowns of the latter have been discussed before. Finally, triangles in fig. 3.12 indicate the deterministic limit, which produces satisfying results up to $D \approx 0.01$.

[1] They expanded the moments of the waiting time density in a series in the second kinetic coefficient, eq. (1.78), i.e. in the noise intensity, and used this in the iterative scheme, eq. (1.93). Solving the scheme for the zeroth and first order terms yields eq. (3.38) for the first moment, i.e. the mean ISI.

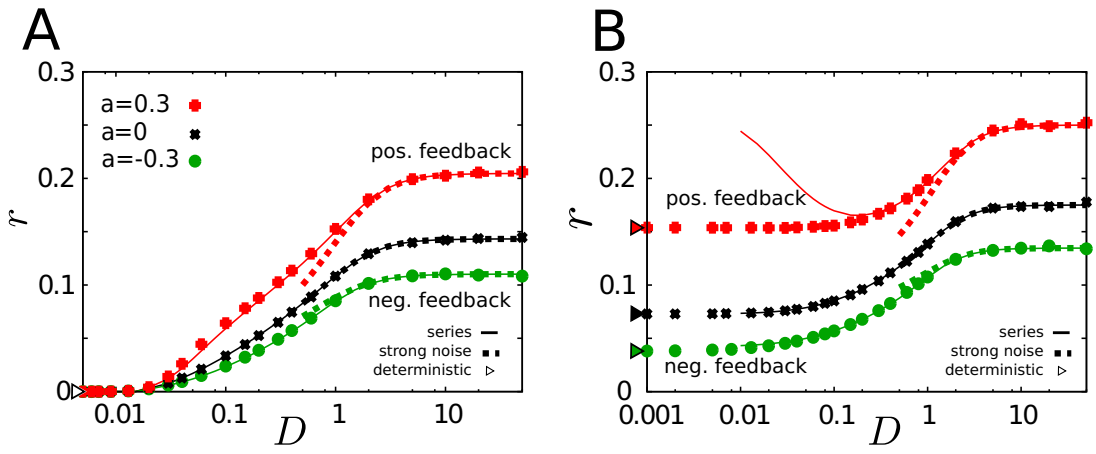

Figure 3.12: Asymptotic firing rate r for moderate positive ($a = 0.3$), negative feedback ($a = -0.3$), and in the absence of feedback ($a = 0$) as a function of noise intensity in the excitable (A) and in the oscillatory regime (B). Symbols mark results from simulations, triangles the deterministic limits obtained from the inverse of T_1 in eq. (3.17), straight lines the series expansion eq. (3.33), and dashed lines the strong-noise approximation eq. (3.34). Parameters: $\tau = 100$, $\omega_0 = 0.9$ (A) and $\omega_0 = 1.1$ (B). This figure has been modified from ref. [143]

3.4.2 ISI variability

In the following, we apply similar approaches to derive analytical approximations for the CV, eq. (1.64), for which, besides the mean ISI, the ISI variance eq. (1.63) is needed. A simplified formula for the latter is eq. (1.108), which has been derived in ref. [212]. If it is applied to the averaged systems eq. (3.28) it reads

$$\mathrm{Var}(\Delta t) \approx \frac{2\int_0^{2\pi} dx\; e^{\frac{U(x,\overline{\omega}^{\mathrm{fp}})}{D}} \left(\int_{x-2\pi}^{x} dy\; e^{-\frac{U(y,\overline{\omega}^{\mathrm{fp}})}{D}}\right)^2 \int_x^{x+2\pi} dz\; e^{\frac{U(z,\overline{\omega}^{\mathrm{fp}})}{D}}}{D^2\left(1-e^{-\frac{2\pi(\omega_0+\overline{\omega}^{\mathrm{fp}})}{D}}\right)^3}, \quad \langle\Delta t\rangle \ll \tau. \tag{3.39}$$

In order to obtain a weak-feedback approximation, we proceed by performing a series expansion of the exponential functions. The details of this calculation are given in appendix A.2.1. Considering $\overline{\omega}^{\mathrm{fp}} \ll \omega_0$ and performing the corresponding Taylor expansion, the terms up to first order read

$$\mathrm{Var}(\Delta t) \approx \mathrm{Var}(\Delta t)_{\overline{\omega}^{\mathrm{fp}}=0}\left(1+\frac{2\pi a}{\langle\Delta t\rangle_{\overline{\omega}^{\mathrm{fp}}=0}}\left(-\frac{3}{\omega_0}+\frac{2D^2}{\omega_0^3\mathrm{Var}(\Delta t)_{\overline{\omega}^{\mathrm{fp}}=0}}C(D,\omega_0)\right)\right), \quad \overline{\omega}^{\mathrm{fp}} \ll \omega_0, \quad \langle\Delta t\rangle \ll \tau. \tag{3.40}$$

The function $C(D,\omega_0)$ is a infinite series and given in eq. (A.50) in appendix A.2.2. We are now interested in approximations for strong and weak noise.

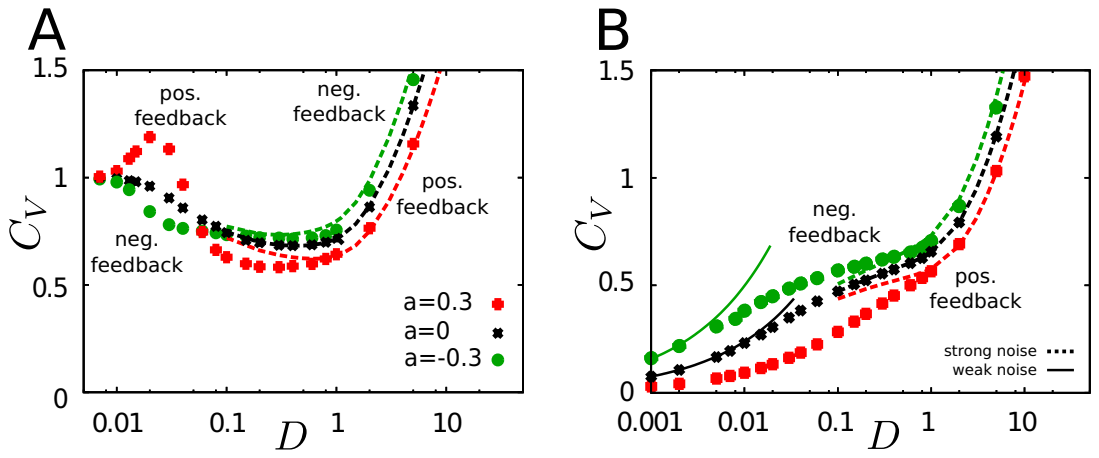

Figure 3.13: Coefficient of variation C_V for moderate positive ($a = 0.3$) and negative feedback ($a = -0.3$) and in the absence of feedback ($a = 0$) as a function of noise intensity in the excitable regime ($\omega_0 < 1$) (A) and in the oscillatory regime ($\omega_0 > 1$)(B). Symbols mark results from simulations, dashed lines mark the strong-noise approximation eq. (3.42) and solid lines the weak-noise approximation eq. (3.45) for super-threshold driving ($\omega_0 > 1$). Parameters: $\tau = 100$, $\omega_0 = 0.9$ (A) and $\omega_0 = 1.1$ (B). This figure has been modified from ref. [143].

At first, in case of a strong noise $D \gg 1$, the series $C(D, \omega_0)$ can be neglected, see appendix A.2.2. Then eq. (3.40) becomes

$$\mathrm{Var}(\Delta t) \approx \mathrm{Var}(\Delta t)_{\overline{\omega}^{\mathrm{fp}}=0} \left(1 - \frac{6\pi a}{\omega_0 \langle \Delta t \rangle_{\overline{\omega}^{\mathrm{fp}}=0}}\right), \quad D \gg 1, \quad \overline{\omega}^{\mathrm{fp}} \ll \omega_0, \quad \langle \Delta t \rangle \ll \tau. \quad (3.41)$$

Consequently, positive feedback reduces the variance, whereas, negative feedback increases the variance in the strong noise regime. By combining eq. (3.41) with our previous results for the mean ISI eq. (3.34), we obtain an estimate for the CV for strong noise and weak feedback

$$C_V = \frac{\sqrt{\mathrm{Var}(\Delta t)}}{\langle \Delta t \rangle} \approx C_{V,\overline{\omega}^{\mathrm{fp}}=0} \left(1 - \frac{\pi a}{\omega_0 \langle \Delta t \rangle_{\overline{\omega}^{\mathrm{fp}}=0}}\right), \quad D \gg 1, \quad \overline{\omega}^{\mathrm{fp}} \ll \omega_0, \quad \langle \Delta t \rangle \ll \tau. \quad (3.42)$$

Thus, as we found for the variance, positive feedback reduces the ISI variability, whereas negative feedback increases the CV for high noise intensities.

For small noise intensities, analytical approximations can be derived in the tonic firing regime. As for the mean ISI, see eq. (3.38), we can apply the results of ref. [6] to obtain

approximations for the variance. In case of weak noise this yields

$$\mathrm{Var}(\Delta t) \approx 2\int_0^{2\pi} dy \frac{D}{K_1^{\mathrm{av}}(y)^3} \approx \frac{2\pi D(1+2(\omega_0+\overline{\omega}^{\mathrm{fp}})^2)}{((\omega_0+\overline{\omega}^{\mathrm{fp}})^2-1)^{\frac{5}{2}}},\ D \ll 1,\ \langle \Delta t\rangle \ll \tau, \tag{3.43}$$

with $K_1^{\mathrm{av}}(\phi) = \omega_0 + \overline{\omega}^{\mathrm{fp}} - \sin(\phi)$. Using this and the weak noise approximation for the mean ISI, i.e. eq. (3.17) with $\Omega = \overline{\omega}^{\mathrm{fp}}$, for the CV, we obtain

$$C_V = \frac{\sqrt{\mathrm{Var}(\Delta t)}}{\langle \Delta t\rangle} \approx \sqrt{\frac{D}{2\pi}}\sqrt{\frac{1+2(\omega_0+\overline{\omega}^{\mathrm{fp}})^2}{((\omega_0+\overline{\omega}^{\mathrm{fp}})^2-1)^{\frac{3}{2}}}},\ D \ll 1,\ \langle \Delta t\rangle \ll \tau. \tag{3.44}$$

In case of a weak feedback, we can expand this in a Taylor series and find

$$C_V \approx C_{V,\overline{\omega}^{\mathrm{fp}}=0}\left(1 - \frac{\pi a}{\langle \Delta t\rangle_{\overline{\omega}^{\mathrm{fp}}=0}} \frac{\omega_0^2(7+2\omega_0^2)}{(\omega_0^2-1)(1+2\omega_0^2)}\right),\ D \ll 1,\ \overline{\omega}^{\mathrm{fp}} \ll \omega_0,\ \langle \Delta t\rangle \ll \tau. \tag{3.45}$$

Approximations for strong noise, eq. (3.42), and for weak noise in the superthreshold regime, eq. (3.45), in accordance with results from simulations are shown in fig. 3.13. As can be seen in the figure, the strong-noise approximation well-approximates the CV for $D \geq 1$, while the weak-noise approximation produces satisfying results for $D \leq 0.01$. However, for strong positive feedback the weak-noise approximation produces negative CVs and cannot be applied. As has been observed for the firing rate before, the weak-feedback approximation produces large deviations.

Considering the qualitative effect of positive and negative feedback on the CV, we find that negative feedback increases the variability, whereas positive feedback reduces ISI variability in the oscillatory regime and for strong noise in the excitable regime, compare fig. 3.13B and 3.13A, respectively. Furthermore, we find that positive feedback deepens the minimum of the CV observed for subthreshold driving. Such a global minimum of variability as a function of noise intensity is called *coherence resonance* and has been predicted by Pikovsky and Kurths [202] as a consequence of at least two time scales with fluctuations that scale differently with the noise intensity. In recent years, coherence resonance has been investigated in several theoretical [191, 154, 102, 115, 161, 209, 195, 150, 141, 10] and experimental studies [205, 63, 90, 132, 222, 260, 274, 153]. Even more remarkable, at intermediate noise intensities the qualitative effect of feedback in the excitable regime changes. Then, positive feedback increases ISI variability, while negative feedback leads to more regular behavior. Interestingly, this can even cause a local maximum of the CV for positive feedback in the excitable regime fig. 3.13A, which is expressed by $C_V > 1$. Spiking with such high CVs is usually called bursting behavior. Furthermore, a maximum in the CV as a function of noise intensity is called *anticoherence resonance* or *incoherence resonance* – variability attains a maximum at a finite noise intensity. The latter has been studied theoretically as a consequence of damped subthreshold oscillations [150] or a finite refractory period [163]. Recently, anticoher-

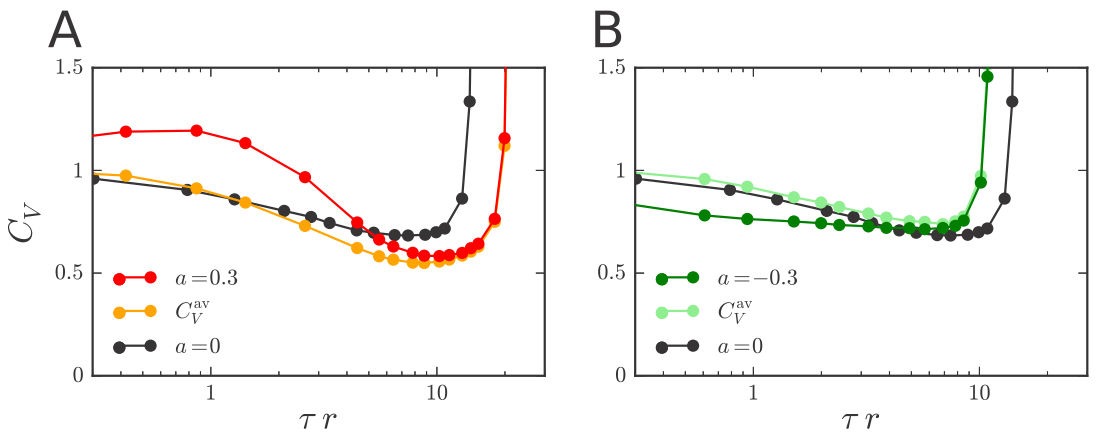

Figure 3.14: Coefficient of variation C_V and corresponding values of C_V^{av} from eq. (3.46) as a function of the average number of spikes per time interval τ for moderate positive (A) and negative feedback (B) and in the absence of feedback. Parameters: $\omega_0 = 0.9$, $\tau = 100$.

ence resonance has been verified experimentally in a laser system [233]. Finally, for weak noise intensities the spiking behavior becomes Poisson-like and the CV approaches one.

The qualitative change in the effect of feedback on the CV is caused by the fact that feedback acts in two different ways on the system. On the one hand, it leads on average to a stronger (positive feedback) or weaker (negative feedback) driving. This has been accounted for in the approximations given by eqs. (3.45) and (3.42), by considering its time average $\overline{\omega}^{\mathrm{fp}}$ in the respective formulas. On the other hand, the dynamics of ω leads to higher (positive feedback) or lower (negative feedback) values of $\omega_0 + \omega$ in the beginning of an ISI, which highly affects escapes from the fixed point in the excitable region. In order to find the mechanism that dominates the shaping of ISI variability in the excitable regime, we compare the simulation results presented in fig. 3.13 with the C_V that results for a system that feels only the time-averaged feedback $\overline{\omega}^{\mathrm{fp}}$. For such a system the CV reads

$$C_V^{\mathrm{av}} = \frac{\sqrt{\mathrm{Var}(\Delta t)}}{\langle \Delta t \rangle}, \tag{3.46}$$

where the variance is exactly given by eq. (3.39). Here $\overline{\omega}^{\mathrm{fp}}$ is calculated from the mean ISI obtained from simulations by eq. (3.27). As can be seen in fig. 3.14, the effect of the average feedback dominates for high firing rates $r \gg 1/\tau$, which correspond to high noise intensities as we have seen in fig. 3.12. In this regime, individual ISIs are short compared to τ and ω is approximately constant during individual ISIs. In this regime, positive feedback reduces the ISI variability and negative feedback increases the variability, if compared to the original system at the same firing rates. However, the same CV can be achieved if ω_0 is changed appropriately ($\omega_0 \to \omega_0 + \overline{\omega}^{\mathrm{fp}}$). In contrast, at low rates $r \approx 1/\tau$ the feedback dynamics dominates the shaping of the CV. Interestingly, it modulates the

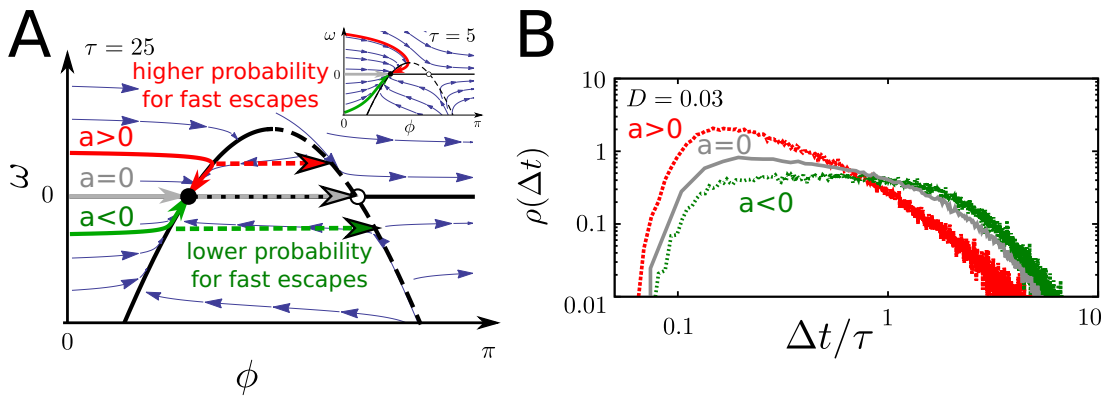

Figure 3.15: Schematic dynamics close to the stable fixed point for $\tau = 25$ and $\tau = 5$ (inset) (A) and shapes of the ISI density in the corresponding parameter region (B). A: nullclines (black line), stable (black dot) and unstable nodes (white dot), the deterministic velocity field (arrows), and deterministic trajectories (solid colored lines) are shown. Escapes from the stable branch are indicated as colored arrows. B. ISI densities are shown for positive feedback (red), negative feedback (green), and in the absence of feedback (gray). Parameters A: $\omega_0 = 0.8$, $a = -0.5, 0, 0.5$; B: $\tau = 100$, $a = -0.3, 0, 0.3$. This figure has been modified from ref. [143].

CV in the opposite way as the effective increase of the driving. The reason for this is that ω decreases during individual ISIs for positive feedback, which leads to higher ISI variability at similar rates compared to the original system, while ω increases during individual ISIs when negative feedback is applied. This leads to less variability at similar firing rates compared to the original system. This is illustrated in fig. 3.15A. For positive feedback, trajectories reach the ϕ-nullcline at positive ω and, thus, short ISIs $\Delta t < \tau$ caused by fast escapes from the stable branch are more likely than in the original system. However, if no short escapes occur, ω approaches zero. Consequently, the statistics of long ISIs becomes similar to that in the original system. Thus, as shown in fig. 3.15B, ISI distribution for positive feedback possess higher probability at short ISIs, i.e. far away from the mean ISI, than those of the original system. This leads to higher CVs and causes the anticoherence resonance phenomenon. In contrast, for negative feedback, short ISIs $\Delta t < \tau$ are suppressed since the system approaches the stable branch of the nullcline with negative ω. However, as ω approaches zero the statistics of long ISIs becomes similar to that in the original system. Thus, the corresponding ISI distribution possesses less probability at short ISIs and is more narrowed around the mean ISI. This leads to smaller CVs than in the original system, compare fig. 3.15B.

3.5 Spike train variability in excitable systems with strong positive feedback

Finally, we investigate the spike train variability close to the bistable region, i.e. in the regime where a low-feedback (L) state and a high-feedback (H) state coexist. To this

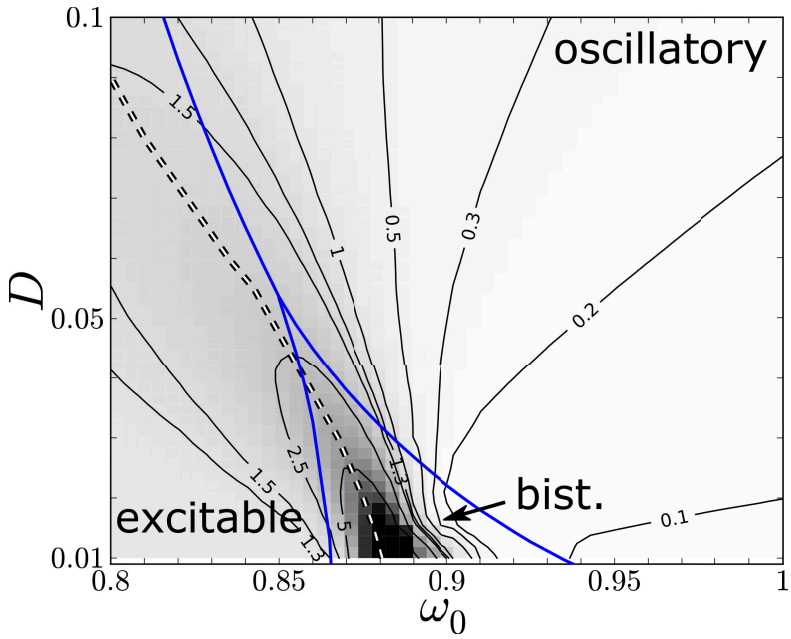

Figure 3.16: Coefficient of variation in the vicinity of the bistable region (bist.). Borders are obtained from fig. 3.6B and marked blue. Contour lines and gray levels illustrate C_V values. Furthermore, the dashed white line marks the maximum of the CV as a function of ω_0 for fixed D.

end, we focus on two measures of variability: first, the coefficient of variation C_V, which quantifies the spike train variability on the time scale of individual ISIs, and second, the Fano factor $F(T)$, which quantifies the variability in the spike count on time scales of order T.

3.5.1 Interspike interval variability

At first investigate the shape of the CV in the regime of coexisting states. Results obtained from simulations are shown in fig. 3.16. The weak noise limits $C_V \to 1$ for $\omega_0 \approx 0.8$ and $C_V \to 0$ for $\omega_0 \approx 1$ correspond to those obtained for pure excitable and pure oscillatory behavior, respectively. Interestingly, in the bistable region the CV attains giant values. In that regime, the system switches between two states of spike generation, compare section 3.3.

In order to investigate the CV in the region of coexisting stable solutions for $\overline{\omega}^{\mathrm{fp}}$, we use a two state approach similar to the one presented in ref. [229]. Following ref. [229] spiking in the H-state is assumed to occur at firing rate r^H and in the L-state at the rate r^L. Furthermore, we assume that ISIs either correspond to the H-state or to the L-state and, thereby, neglect the influence of transitions between both states on the ISI statistics. The respective ISIs will be denoted as Δt^H and Δt^L. Then, we can define the means of ISIs in the respective states as $\langle \Delta t^H \rangle$ and $\langle \Delta t^L \rangle$ via eq. (1.72). Additionally, we denote the corresponding CVs as C_V^L and C_V^H. In the following, we assume uncorrelated,

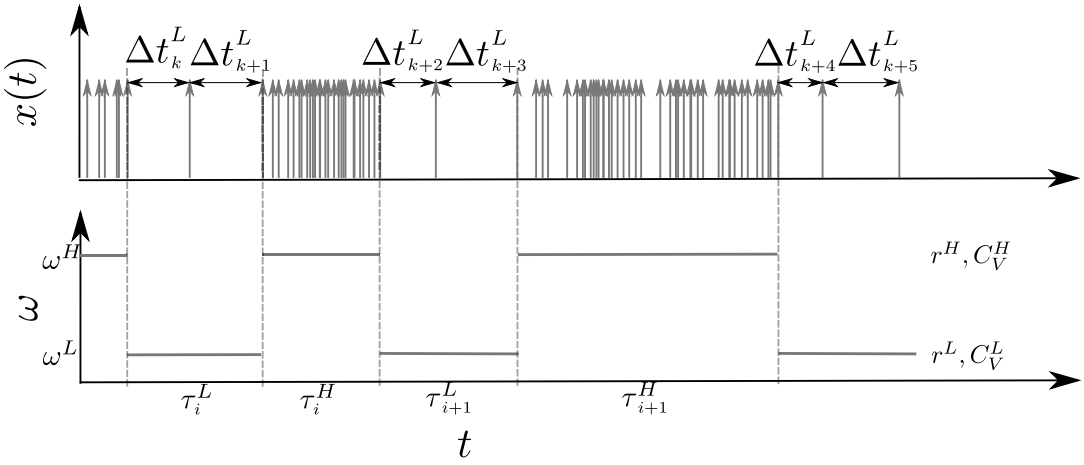

Figure 3.17: Schematic of the two-state approximation. In the bottom panel two-state switching between two feedback values is shown. Spiking in the states occurs at different rates, as is illustrated in the upper panel. Note that only the sequence of ISI in the L-state is shown.

exponentially-distributed waiting times τ_i^H and τ_i^L for both states with mean waiting times $\langle\tau^L\rangle$ and $\langle\tau^H\rangle$. Then, the corresponding transition rate from $L \to H$ is given by $1/\langle\tau^L\rangle$ and that from $H \to L$ reads $1/\langle\tau^H\rangle$. The introduced notation is illustrated in fig. 3.17. It follows, that the mean number of spikes before the next switching in either state is given by $r^L\langle\tau^L\rangle$ and $r^H\langle\tau^H\rangle$, respectively. Consequently, the stationary probability to pick an ISI from the H-state $p_{\rm st}^H$ and from the L-state $p_{\rm st}^L$ from the ISI sequence is given by

$$\begin{aligned} p_{\rm st}^H &= \frac{r^H\tau^H}{r^H\tau^H + r^L\tau^L} = \frac{\alpha\gamma}{1+\alpha\gamma} \\ p_{\rm st}^L &= 1 - p_{\rm st}^H = \frac{1}{1+\alpha\gamma}. \end{aligned} \tag{3.47}$$

Here, we introduced the ratio of firing rates γ and that of the mean waiting times α as

$$\begin{aligned} \gamma &= \tfrac{r^H}{r^L} = \tfrac{\langle\Delta t^L\rangle}{\langle\Delta t^H\rangle} \\ \alpha &= \tfrac{\tau^H}{\tau^L}. \end{aligned} \tag{3.48}$$

In this setup, the ISI statistics follows from two averages. One over the realizations of waiting times in the respective states, marked as $\langle x\rangle_{\rm HL}$ in the following, and a second average over the actual realization of ISIs for each realization of waiting times, marked by $\langle x\rangle$. We assume that both realizations are independent. Then, the nth moment of

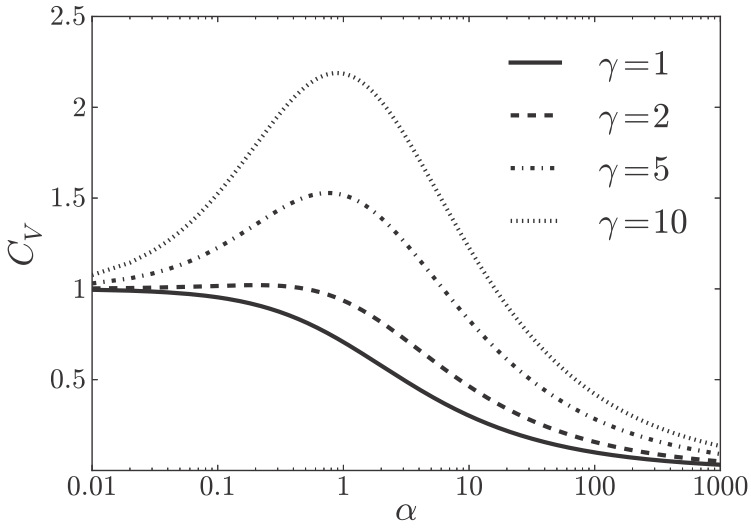

Figure 3.18: Two state approximation eq. (3.51) for different γ. Parameters: $C_V^H = 0$ and $C_V^L = 1$.

the ISIs can be calculated according to

$$\begin{aligned}\langle\langle\Delta t^n\rangle\rangle_{\mathrm{HL}} &= \langle\frac{1}{M}\sum_{k=1}^{M}(\Delta t_k)^n\rangle_{\mathrm{HL}} = \langle\frac{1}{M}(\sum_{k=1}^{M_H}(\Delta t_k^H)^n + \sum_{k=1}^{M_L}(\Delta t_k^L)^n)\rangle_{\mathrm{HL}} \\ &= \langle\frac{M_H}{M}\langle(\Delta t^H)^n\rangle + \frac{M_L}{M}\langle(\Delta t^L)^n\rangle\rangle_{\mathrm{HL}} = p_{st}^H\langle(\Delta t^H)^n\rangle + p_{st}^L\langle(\Delta t^L)^n\rangle.\end{aligned} \tag{3.49}$$

M denotes the total number of ISIs in the ISI sequence. Furthermore, we assume a large number of ISIs in the H-state M^H and L-state M^L for the respective realizations of waiting times. Using these results, we obtain for the CV:[2]

$$C_V = \sqrt{\frac{p_{st}^H(\langle(\Delta t^H)^2\rangle - \langle\Delta t^H\rangle^2 + \langle\Delta t^H\rangle^2)}{(p_{st}^H\langle\Delta t^H\rangle + p_{st}^L\langle\Delta t^L\rangle)^2} + \frac{p_{st}^L(\langle(\Delta t^L)^2\rangle - \langle\Delta t^L\rangle^2 + \langle\Delta t^L\rangle^2)}{(p_{st}^H\langle\Delta t^H\rangle + p_{st}^L\langle\Delta t^L\rangle)^2}} - 1. \tag{3.50}$$

Furthermore, we can use eqs. (3.47) and (3.48) to express the CV of the full system by

[2] This can be obtained by evaluating the average over all realizations of the waiting times first, i.e.

$$\begin{aligned}C_V &= \sqrt{\frac{\langle\langle(\Delta t - \langle\langle\Delta t\rangle\rangle_{\mathrm{HL}})^2\rangle\rangle_{\mathrm{HL}}}{\langle\langle\Delta t\rangle\rangle_{\mathrm{HL}}^2}} = \sqrt{\frac{\langle\langle\Delta t^2\rangle\rangle_{\mathrm{HL}} - \langle\langle\Delta t\rangle\rangle_{\mathrm{HL}}^2}{\langle\langle\Delta t\rangle\rangle_{\mathrm{HL}}^2}} \\ &= \sqrt{\frac{p_{st}^H\langle(\Delta t^H)^2\rangle + p_{st}^L\langle(\Delta t^L)^2\rangle}{(p_{st}^H\langle\Delta t^H\rangle + p_{st}^L\langle\Delta t^L\rangle)^2} - 1}.\end{aligned}$$

the CVs in the respective states, which yields

$$C_V = \sqrt{\frac{1+\alpha\gamma}{(1+\alpha)^2}\left(\frac{\alpha}{\gamma}\left((C_V^H)^2+1\right)+(C_V^L)^2+1\right)-1}. \tag{3.51}$$

In order to proceed, we make some assumptions for the respective states. First of all, the region of two coexisting stable solutions for $\overline{\omega}^{\mathrm{fp}}$ is mainly locate in the weak and intermediate noise region, as can be seen in fig. 3.16. Then, the CV in the excitable state is close to one due to the Poisson-like spike generation, therefore, we set $C_V^L = 1$. However, in the H-state, the CV approaches zero, $C_V^H \to 0$. Furthermore, the firing rate in the H-state is much higher than that in the L-state, which will cause large values of γ, i.e. $\gamma \gg 1$.

Figure 3.18 shows the two-state approximation eq. (3.51) of the CV for different γ. Interestingly, for large γ the CV possesses a maximum with respect to the ratio of mean waiting times α. For constant $\gamma \gg 1$, the local maximum of C_V can be easily obtained. The lowest order terms in $1/\gamma$ for $\alpha_{\max}$, i.e. the value of α for which the maximum CV is attained, read:

$$\alpha_{\max} \approx 1 + \frac{2}{\gamma}\frac{(C_V^H)^2-(C_V^L)^2}{1+(C_V^L)^2}. \tag{3.52}$$

The corresponding dominating order term for the maximum C_V reads

$$C_{V,\max} \approx \frac{1}{2}\sqrt{\gamma(1+(C_V^L)^2)}. \tag{3.53}$$

Considering the weak-noise limits of the firing rates $r^H \to$ const. and $r^L \to 0$, we find that γ diverges as D approaches zero. Consequently, the maximum ISI variability attains giant values for weak noise intensities.

In the active rotator model with positive spike-triggered feedback, the main difficulty that arises when it is compared with the two state system is the lack of a theory for α as a function of the system parameters ω_0 and D. In order to compensate for that, we first consider the system for a constant noise intensity. For fixed D, the shape of the CV as a function of ω_0 is presented in fig. 3.19A for different values of τ. Remarkably, the shape is qualitatively similar to that of the CV in the two-state system as a function of α, which has been presented in fig. 3.18 before. In particular, we find a maximum of the CV. In the following, the CV at the maximum will be denoted as $C_{V,\max}(D)$. This is illustrated in fig. 3.19A for different values of τ. For each τ we can find a maximum value of the CV. Interestingly, the CV attains even higher values for smaller τ. Moreover, the corresponding maximum is attained at smaller values of ω_0 and it is brighten. Unfortunately, we have no information about the shape of α except that deep inside the excitable region only the L-state exists and α approaches zero, while for strong drivings only the H-state exists and α runs to infinity. For some ω_0 in between, however, α has to attain one. In the following, we make use of the assumption that $\alpha = 1$ is attained for the value of ω_0 for which the maximum CV $C_{V,\max}(D)$ is obtained

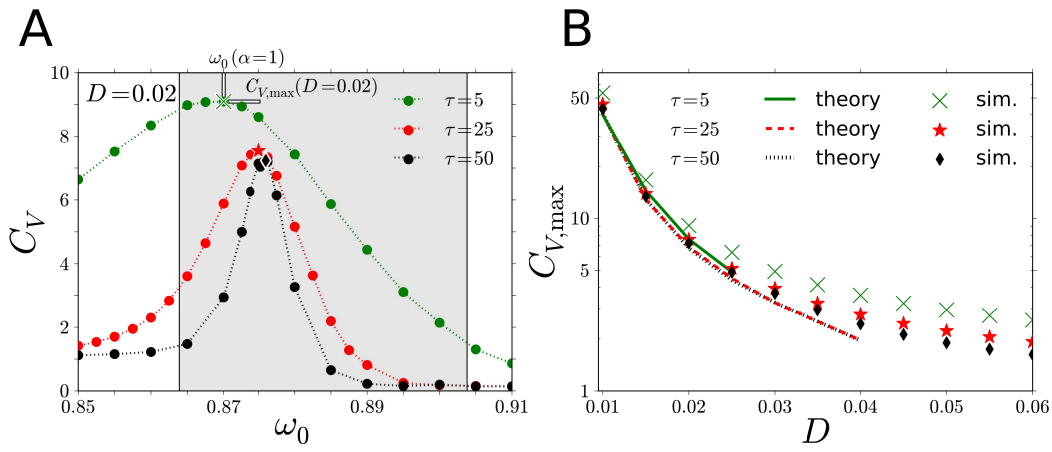

Figure 3.19: CV for fixed $D = 0.02$ (A) and $C_{V,\max}$ as a function of noise intensity for different τ compared to the solution of eq. (3.53) (B). A: the region of coexisting solutions for $\overline{\omega}^{\text{fp}}$ is marked gray, values for $C_{V,\max}$ are marked by the symbols used in B. Figure B has been modified from ref. [144]. Parameters: $a = 0.5$.

in simulations. Thus, we can get $\omega_0(\alpha = 1)$ from simulations. Corresponding values of $C_{V,\max}(D)$ and $\omega_0(\alpha = 1)$ are marked in fig. 3.19A for $\tau = 5$ and $D = 0.02$. Next, in order to get the corresponding value of γ – in the active rotator model, γ is in general a function of ω_0 – we use the solutions for the firing rate that follow from the average-feedback approximation eq. (3.29). The ratio of the high-rate solution (short mean ISI) and low-rate solution (long mean ISI) for the fixed D value and $\omega_0 = \omega_0(\alpha = 1)$ will serve us as an approximation for $\gamma(\alpha = 1)$. Repeating this procedure for different D and τ leads to the results depicted in fig. 3.19B. Since the maximum CV for different τ is attained at different ω_0, we find different values of $\gamma(\alpha = 1)$ for each τ. These result in other solutions of eq. (3.53), which are marked as 'theory' in fig. 3.19B. As shown in the figure, the two-state approximation eq. (3.53) fits the simulation results remarkably well for weak noise. Furthermore, we find that the theory underestimates numerical results for small τ and strong noise. One reason for the higher CV values for small τ is that the maximum CV is attained at smaller values of ω_0. Considering the solutions of eq. (3.29), this results in higher values of γ and thereby leads to higher $C_{V,\max}$ values in eq. (3.53). However, this can only qualitatively account for the increase of the maximum CV in simulations. Possible sources for the differences are our estimates of γ from the solutions of the average-feedback approximation eq. (3.29). The latter produces best results for large τ.

3.5.2 Spike count variability

While the CV measures the variability of the system's output on times scales of the order of individual ISIs, variability of the spike count on arbitrary time scales T is measured

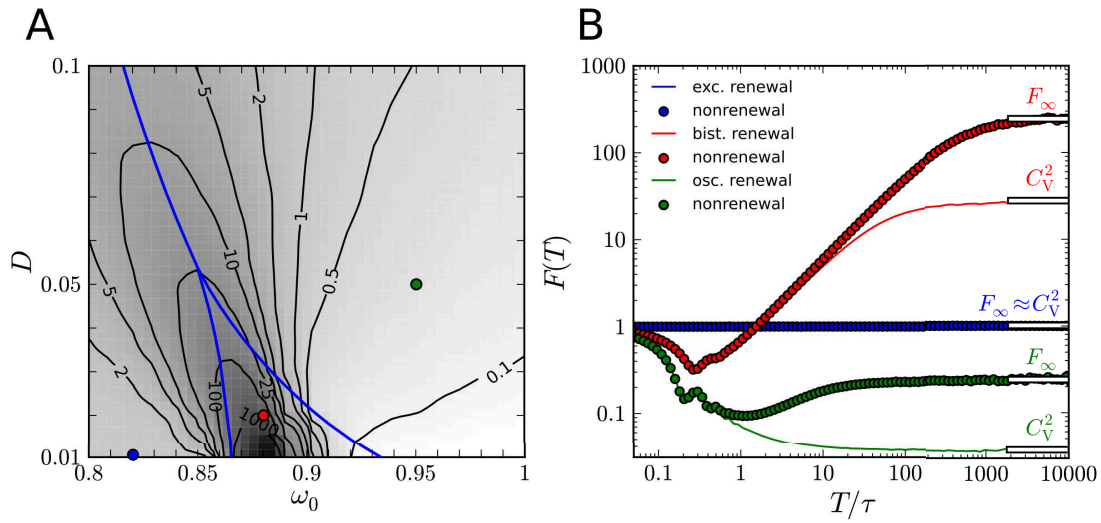

Figure 3.20: Contour plot of F_∞ as a function of (ω_0, D) (A) and Fano factor $F(T)$ (B) for parameter combinations marked by colored dots in A. A: light regions indicate low values and dark regions high values of F_∞, black lines illustrate contour levels and blue lines the borders of excitable (lower left) oscillatory (upper right), and bistable (in between) regions presented in fig. 3.6B in section 3.3. B: Fano factors obtained from simulations (nonrenewal) and from shuffled ISI sequences (renewal). Parameters: $\tau = 25$, $a = 0.5$, and $(\omega_0 = 0.82, D = 0.01)$ (excitable), $(\omega_0 = 0.88, D = 0.02)$ (bistable), $(\omega_0 = 0.95, D = 0.05)$ (oscillatory).

by the Fano factor $F(T)$, which has been introduced in eq. (1.60) in section 1.7. Of particular interest, is the variability on asymptotically long time scales $T \to \infty$. This can be quantified by the asymptotic Fano factor F_∞ given in eq. (1.73).

F_∞ for different noise intensities and drivings and $F(T)$ for representative sets of parameters in the excitable, bistable, and oscillatory region, respectively, are shown in the figs. 3.20A and B. First, the shape of F_∞ is qualitatively similar to that of the CV, shown in fig. 3.18. In particular, highest values are attained in the bistable region. Outside the bistable region, highest values are observed along the border between excitable and oscillatory region. Furthermore, the well-known weak-noise limits of F_∞ are $F_\infty \to 1$ (excitable), which is approached in the lower left corner of fig. 3.20A, and $F_\infty \to 0$ (oscillatory), which is approached for high subthreshold driving ($\omega_0 \to 1$). Considering the Fano factor $F(T)$ as a function of the length of the time window T, see fig. 3.20B, we find the limits $F(T) \to 1$ for $T \to 0$ (rare-event statistics) and a saturation $(F(T) \to F_\infty)$ for $T \to \infty$. The long-time limit F_∞ can be related to the CV and the sum of the serial correlation coefficients ρ_n according to eq. (1.74). However, at time intervals of order τ the Fano factor possesses a global minimum in the oscillatory region. This minimum also exists in the bistable region, but is shifted to shorter time intervals. Furthermore, we find small-amplitude oscillations at time intervals of order $\langle \Delta t \rangle$. These oscillations result from limit cycle oscillations and an analytical approximation for the Fano factor in that region has been presented in ref. [183] for the perfect integrate-

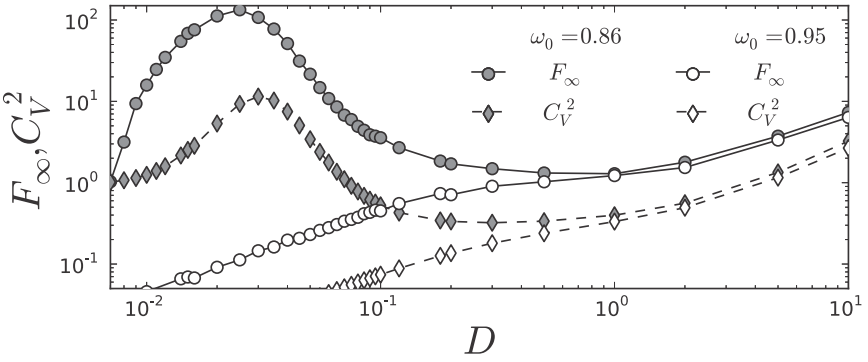

Figure 3.21: Shape of the asymptotic Fano factor F_∞ (circles) compared to that of C_V^2 (diamonds) as functions of noise intensity in the regime of noise-controlled bistability (gray) and close to the oscillatory regime (white). Parameters: $a = 0.5$, $\tau = 25$. Figure has been modified from ref. [144].

and-fire model driven by a colored noise. The minimum indicates that the spiking is most regular at respective time scales. The reason for these oscillations is that if the spike generation occurs due to limit cycle oscillations, the firing becomes almost periodic for weak noise and thus, the time window T used in the calculation of the spike count contains a fixed number of spikes if T is a multiple of the mean ISI. This leads to small values of $F(T)$ at such time scales and results in a global minimum in $F(T)$ regimes where limit cycle oscillations occur, i.e. in the oscillatory and bistable regime.

As presented in section 1.7, see eq. (1.73), F_∞ is strongly affected by ISI correlations, see also refs. [47, 183, 227]. In order to exclude the influence of these correlations, we have shuffled the ISI sequences. Fano factors from the shuffled ISI sequences are marked by 'renewal' in fig. 3.20B. Remarkably, besides the effect of ISI correlations on F_∞, they also cause the vanishing of the global minimum in the oscillatory regime, which is in accordance with previous results presented in refs. [47, 227, 67]. However, in the bistable regime, the minimum remains even after the ISI sequence has been shuffled. The reason for that is the high ISI variability ($C_V > 1$), which results in $F_\infty > 1$ for long time intervals, while the rare-event statistics at short time intervals causes $F(T \to 0) = 1$. In between, however, we find more regular behavior when T is comparable to the mean ISI of limit cycle oscillations that occur in the H-state. This remains even after a shuffling of the ISI sequence since, due to the high differences in the states' firing rates, most ISIs are related to the oscillatory state. Consequently, we find long sequences of short ISIs in the shuffled ISI sequence even by chance. For weak noise these sequence resemble a periodic spiking and thereby cause the minimum in the Fano factor.

Interestingly, the different long-time limits, which are related to the excitable ($F_\infty = 1$), bistable ($F_\infty > 1$), and oscillatory regime ($F_\infty < 1$) for weak and intermediate noise intensities, respectively, result in a local maximum of F_∞ and C_V^2 as a function of noise intensity, in the regime of *noise-controlled bistability*. This is shown in fig. 3.21. In this regime, noise provides full control of the probability to find the system in the respective states and, thereby, determines the characteristics of the output statistics. Therefore,

F_∞ and C_V are determined by the excitable dynamics for weak noise. In contrast, for strong noise, these measures are determined by the oscillatory dynamics. In between, both measures attain local maxima. Here, as our investigation of the C_V of a two-state system showed before, ISI variability is a result of two-state switching between states of highly different firing rates. However, as illustrated in fig. 3.21, the asymptotic Fano factor attains higher values than C_V^2, which indicates the presents of strong positive ISI correlations. The latter have been found to be present in two-state systems over several lags, see ref. [229].

3.6 Discussion and outlook

We have intensively studied the influence of noise and a spike-triggered feedback mechanism on the spike generation in an excitable system with Class 1 excitability. For our investigations, we complemented a popular active rotator model by a feedback mechanism. The feedback has been implemented in a similar way as adaptation currents are added to integrate-and-fire neuron models. Thus, the driving is temporally increased (positive) or decreased (negative feedback) after each spike, which pushes the system towards the oscillatory or the excitable regime, respectively.

First, we studied the deterministic system and found analytical expressions for the asymptotic feedback solutions. Our results well-describe the existence of a bistable regime for strong positive feedback and high, but subthreshold, driving. In that regime, an excitable and an oscillatory state coexist. This is reminiscent of the arise of an additional limit cycle solution in the presence of positive feedback due to autaptic coupling, which has been observed in terms of numerical investigations of a Hodgkin Huxley neuron [107] and yields a possible explanation for persistent activity in neurons with slow excitatory autapses [171, 220, 16].

In the presence of noise, we used an average-feedback approach, which relates the time-averaged contribution of the feedback to the firing rate. Furthermore, we were able to derive analytical approximations for the firing rate and the ISI variability in the presence of feedback. In particular, we found that the feedback acts like a constant modification of the driving parameter, corresponding to a constant inward (positive) or outward (negative) current in a neuron, for strong noise or at high firing rates, and, consequently, reduces (positive) or increases (negative) ISI variability. However, for small firing rates in the excitable regime, the dynamics of the feedback leads to a manipulation of ISI variability in the opposite way. In particular, positive feedback leads to bursting behavior, which results into high ISI variability. The results for negative feedback are in accordance with previous studies on the influence of adapation currents on the variability of ISIs [167].

Interestingly, close to the bistable region, the interplay of noise and strong positive feedback leads to a remarkable effect, which we named *noise-controlled bistability*. It describes the fact that, by solely varying the noise intensity, one is able to shift the system from excitable behavior, for weak noise, into oscillatory behavior, for strong noise. For intermediate noise intensities, both states coexists and the system switches between time

periods of rare spike generation (excitable) and periods of fast and more regular spiking (oscillatory). *Noise-controlled bistability* would enable a neuron to adjust its operation mode to an external or internal noise source. Furthermore, the behavior at intermediate noise intensities is reminiscent of the switching between high- and low-activity states in cortical networks [113, 110, 96]. In these networks positive feedback arises from excitatory synaptic coupling rather than from intrinsic spike-triggered feedback mechanisms. However, the total excitation due to the synaptic coupling is controlled by the firing rate of the network. This is similar to positive spike-triggered feedback for which we have shown in section 3.3 that its average contribution to the driving is proportional to the firing rate. Therefore, both mechanisms may lead to similar effects. Another consequence of *noise-controlled bistability* is that it enables one to tune several statistical measures. Most noteworthy, it allows one to fine-tune the noise intensity to obtain giant ISI variability and asymptotic spike count variability.

Our results provide a deeper understanding of spike-triggered feedback in neural systems. Especially, the case of positive feedback has been investigated only rarely. Furthermore, as we have presented in the previous paragraphs, the active rotator model with spike-triggered feedback is capable of describing various effects that have been observed in neurons with intrinsic feedback mechanisms. However, in contrast to many neuron models it allows for an analytical treatment of slow feedback mechanisms and their influence on statistical measures like the firing rate or the CV.

For further studies, several things might be of interest. First, the active rotator model, which we used for our investigations, is restricted to neurons with Class 1 excitability. A generalization to Class 2 excitability could result in several new phenomena. In such systems, the firing rate is much weaker affected by the driving current, therefore, the feedback may have much less influence on the dynamics. Furthermore, it is not clear whether *noise-controlled bistability* is also present in systems with Class 2 excitability. To this end, detailed studies of positive spike-triggered feedback in other neuron models, such as the FitzHugh-Nagumo-Model [79, 80] could be done. Moreover, in many neurons multiple spike-triggered feedback mechanisms are present. In this context it would be interesting to study a single neuron model with a set of two or more feedback mechanisms. This would provide evidence to the open question whether *noise-controlled bistability* is observable in real neurons or whether it is suppressed as soon as multiple feedback mechanisms are present. Finally, in the context of neural networks, a generalization of our theory to excitatory coupling between neurons would provide a new framework to study the existence of states of different activity in neural networks.

4 Spike generation in coupled noisy active rotators

In the present chapter, we consider the spike generation in coupled active rotators. In particular, we are interested in how the spike generation of the individual rotators changes when they are coupled to other rotators. In contrast to most prior studies, which focused on the collective dynamics of huge populations of active rotators, see for instance refs. [237, 277, 250, 139, 242, 243], by using different versions of a mean field theory, we consider star networks with rather small numbers of nodes. In a star network a population of peripheral nodes is connected indirectly via a hub or central node, see fig. 4.1 (center). This topology is of particular interest, since it occurs as a motif in other types of networks, for instance in scale-free networks.

In scale-free networks the number of connections per node – the degree of the node– is distributed according to a power law among the nodes and, therefore, typically hubs – nodes with high degree – are connected to nodes with very low degree, see schematic in fig. 4.1 (right). In scale-free neuronal networks the spiking of hub neurons has been found to have a great influence on collective phenomena [29]. Interestingly, these hubs also emerge and control collective behavior in network models with synaptic plasticity, i.e. in neuronal networks were synaptic conductances evolve in time [169]. Of particular interest is also the phenomenon of remote synchronization, which allows neurons to synchronize via indirect connections [22]. Star networks of deterministic nodes have been

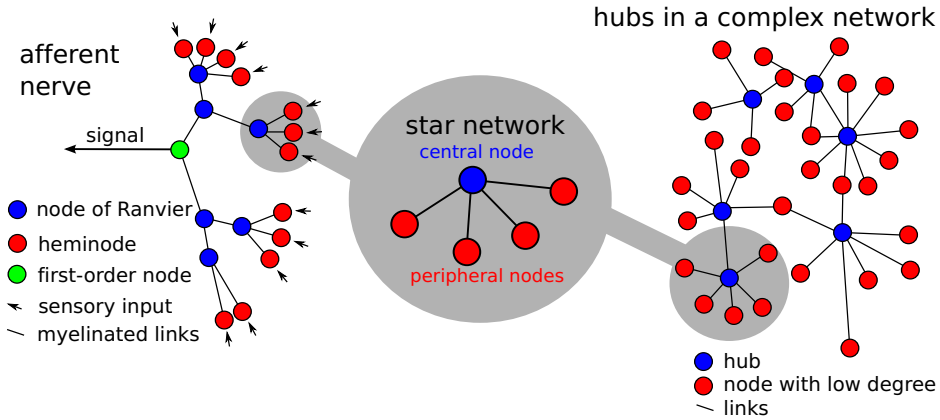

Figure 4.1: Schematics of an afferent nerve (left), hubs in a complex network (right), and a star network (center).

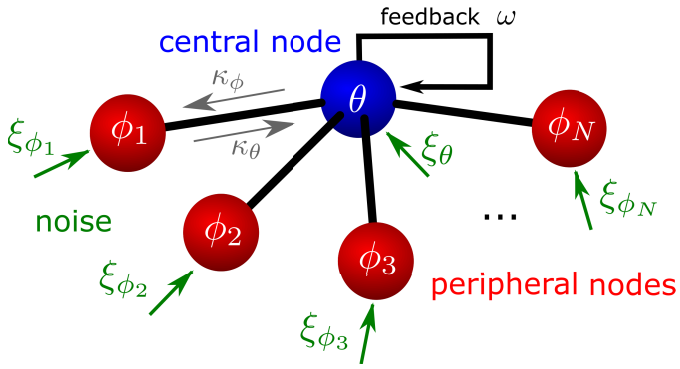

Figure 4.2: Schematic of the star network studied throughout this chapter.

studied intensively in recent years [133, 134, 40, 128]. However, most systems operate in noisy environments and, thereby, we focus on star networks of noisy elements, which can be either excitable or oscillator.

In addition to star motifs in large complex networks, structures of similar topology are also observed in primary sensory neurons, so-called afferents. A popular example is for instance the muscle spindle afferent, which has been studied, for instance, in cats [14]. These neurons have branched myelinated axons that form a tree-like structure in which the nodes are excitable elements called nodes of Ranvier [210], see fig. 4.1 (left). The nodes at the 'roots' of the tree-like structure are called heminodes and receive noisy sensory input. This initiates spikes at the nodes that propagate through the myelinated links. Finally, the spiking of the first-order node encodes information about the sensory input. Interestingly, it has been found that intrinsic noise at the nodes of Ranvier can enhance the propagation of spikes through the axon branches [194]. Furthermore, it has been shown by using deterministic cable equations for the myelinated links that the coupling between individual nodes has to be strong in order to ensure the propagation of action potentials [129]. Therefore, we put the focus on strongly-coupled star networks. In this context, our investigation of the star network structure is a first step in order to study tree-like structures of noisy excitable elements. Then, the star network would correspond to a set of N heminodes (peripherals) that are connected to the remaining part of the tree (central node), as illustrated in fig. 4.1(left).

Parts of the chapter are destined for publication in ref. [146].

4.1 Star network model

In star networks, a central node is coupled to N peripheral nodes. Throughout this chapter we denote the phase of the central node by θ and those of the N peripheral nodes by ϕ_i, $i = 1, 2, ..., N$, respectively. This is illustrated in fig. 4.2. Furthermore, we consider a situation in which the central node is subject to a spike-triggered feedback ω. Coupling between the nodes is realized by a coupling between their phases, as it is often used in phase oscillator models, see section 1.3.3. This yields the following phase

and feedback dynamics

$$\begin{aligned}\dot{\theta} &= \omega_\theta + \omega - \sin(\theta) + \kappa_\theta \sum_{i=1}^{N} \sin(\phi_i - \theta) + \sqrt{2D_\theta}\xi_\theta(t) \\ \tau\dot{\omega} &= -\omega + 2\pi a x_\theta(t) \\ \dot{\phi}_i &= \omega_{\phi_i} - \sin(\phi_i) + \kappa_\phi \sin(\theta - \phi_i) + \sqrt{2D_{\phi_i}}\xi_{\phi_i}(t). \end{aligned} \tag{4.1}$$

ω_θ and ω_{ϕ_i} are the individual driving parameters of the θ and the N ϕ-oscillators, respectively, κ_θ and κ_ϕ are the coupling strengths, that quantify the influence of the peripheral nodes on the θ-oscillator and that of the central node on the ϕ-oscillators, respectively, and τ and a are the feedback parameters that quantify the time scale separation between the θ and ω dynamics and scale the offset to ω after each spike of the central node, respectively. Note that the coupling strengths are not rescaled with the number of connections.

As in the previous chapter, spikes are associated with the 2π crossings of the respective phases and the corresponding spike times t_k^θ and $t_k^{\phi_i}$ and interspike intervals (ISI)s $\Delta t_k^\theta = t_{k+1}^\theta - t_k^\theta$ and $\Delta t_k^{\phi_i} = t_{k+1}^{\phi_i}$ are recorded. Thus, we can define the spike trains of the θ and ith ϕ-oscillator by

$$x_\theta(t) = \sum_{k=1}^{M_\theta} \delta(t - t_k^\theta) \tag{4.2}$$

and

$$x_{\phi_i}(t) = \sum_{k=1}^{M_{\phi_i}} \delta(t - t_k^{\phi_i}). \tag{4.3}$$

M_θ and M_{ϕ_i} are the total numbers of spikes for the respective nodes. Furthermore, we reset the phases θ and ϕ_i to zero after each 2π crossing. Additionally, each active rotator is subject to independent white Gaussian noise input, i.e. $\langle \xi_j(t) \rangle = 0$ and $\langle \xi_j(t)\xi_k(t') \rangle = \delta_{jk}\delta(t - t')$, with $j, k = \theta, \phi_1, \phi_2, ..., \phi_N$. Here, δ_{ij} is the Kronecker delta and $\delta(t - t')$ the Dirac delta function.

Of particular interest in networks of phase oscillators is the degree of synchronization. A frequently-used measure in this context is the time-dependent Kuramoto order parameter:

$$\rho(t)\ e^{I\Psi(t)} := \frac{1}{N} \sum_{i=1}^{N} e^{I\phi_i}. \tag{4.4}$$

$\rho(t) \in [0, 1]$ quantifies the actual degree of synchronization and $\Psi(t)$ the mean field phase $\Psi(t) \in [0, 2\pi)$ of the peripheral nodes. Note that we apply this measure only to the peripheral nodes. Thus, in case of perfectly-synchronized peripheral nodes, all ϕ_i are equal and $\rho(t) = 1$. On the other hand asynchronous peripherals cause small values of $\rho(t)$. In the following, we suppress the arguments of $\rho(t)$ and $\Psi(t)$.

The θ-dynamics can be simplified rigorously if the Kuramoto order parameter is used

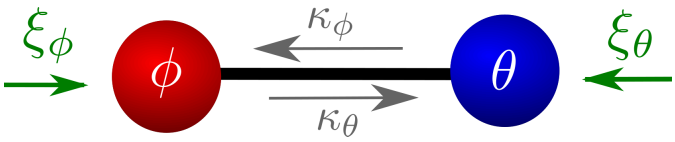

Figure 4.3: Schematic of two coupled active rotators.

in eq. (4.1). Then, the θ-dynamics becomes

$$\dot{\theta} = \omega_\theta + \omega - \sin(\theta) + N\kappa_\theta\rho\sin(\Psi - \theta) + \sqrt{2D_\theta}\xi_\theta(t). \tag{4.5}$$

Thus, θ couples solely to the mean field phase Ψ and is most affected if the peripherals are synchronized.

4.2 Spike generation in the absence of feedback

We first investigate how the parameters κ_θ, κ_ϕ, and N influence the spike generation in the absence of spike-triggered feedback and set ω in eq. (4.5) to zero – alternatively one can put $a = 0$ and restrict on the dynamics in the stationary regime. Then, eq. (4.5) becomes

$$\dot{\theta} = \omega_\theta - \sin(\theta) + N\kappa_\theta\rho\sin(\Psi - \theta) + \sqrt{2D_\theta}\xi_\theta(t). \tag{4.6}$$

Thus, for $\omega_\theta + N\kappa_\theta < 1$, θ can only reach 2π due to noisy excitations. In the next sections we study the spike generation by considering the firing rates $r^\theta = \overline{x_\theta(t)}$ and $r^{\phi_i} = \overline{x_{\phi_i}(t)}$ and the coefficients of variation (CV)s C_V^θ and $C_V^{\phi_i}$, which can be obtained by applying eq. (1.64) to the respective rotator's ISI sequences.

4.2.1 Two coupled rotators

At first, we focus on the simplest case $N = 1$ for which the θ-node is coupled to a single ϕ-node, see fig. 4.3. The latter's phase will be denoted by ϕ in the following. Thus, the full dynamics of the two coupled active rotators reads

$$\begin{aligned} \dot{\theta} &= \omega_\theta - \sin(\theta) + \kappa_\theta\sin(\phi - \theta) + \sqrt{2D_\theta}\xi_\theta(t) \\ \dot{\phi} &= \omega_\phi - \sin(\phi) + \kappa_\phi\sin(\theta - \phi) + \sqrt{2D_\phi}\xi_\phi(t). \end{aligned} \tag{4.7}$$

Recently, the statistics of two coupled nonidentical noisy Kuramoto oscillator has been studied [4], however, in eq. (4.7) a much richer dynamics is considered since, in contrast to the Kuramoto model, the active rotator model can describe excitable and oscillatory behavior of the individual nodes.

Firing rates r^ϕ and r^θ and CVs C_V^ϕ and C_V^θ obtained from simulations of eq. (4.7) are shown in fig. 4.4. In the figure, both rotators possess similar deterministic dynamics but, noise is applied solely to the ϕ-node. Interestingly, if one of the coupling strengths

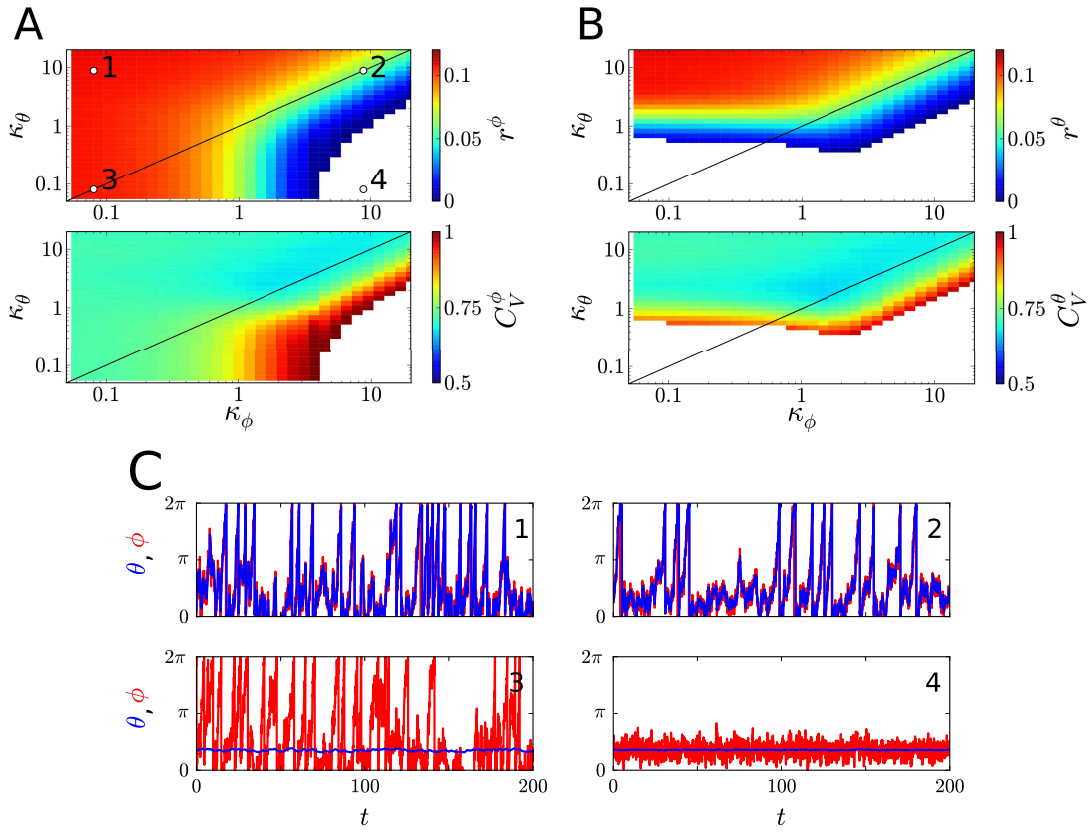

Figure 4.4: Firing rate and CV for the ϕ-node (A) and θ-node (B) obtained from simulations and time traces of θ (blue) and ϕ (red) (C) for the parameters that are marked by white dots in A. Black lines in A and B mark the diagonal for which the coupling is symmetric ($\kappa_\theta = \kappa_\phi$). Parameters: $D_\phi = 1.0$, $D_\theta = 0$, $\omega_\theta = \omega_\phi = 0.9$. Pairs of the coupling strengths $(\kappa_\phi, \kappa_\theta)$ for the traces in C are: $(0.08, 8.79609)$ (1), $(8.79609, 8.79609)$ (2), $(0.08, 0.08)$ (3), and $(8.79609, 0.08)$ (4). Regions with firing rates below 10^{-5} are marked white in A and B. In these regions, an insufficient number of spikes has been recorded, in order to produce a meaningful statistics.

is much larger than the other one, the system behaves like the rotator that is subject to weaker input. More precisely, if $\kappa_\theta \gg \kappa_\phi$ and $\kappa_\theta \gg \max(1, \omega_\theta, D_\theta)$, the θ-dynamics is dominated by the coupling term and θ approaches ϕ almost instantaneously. The function $\max(x, y, ...)$ returns its largest argument. For such constellations of the coupling strengths the coupling term in the ϕ-dynamics can be neglected and both rotators behave like the isolated ϕ-rotator. On the other hand, for $\kappa_\phi \gg \kappa_\theta$ and $\kappa_\phi \gg \max(1, \omega_\phi, D_\phi)$, the ϕ-dynamics is dominated by the coupling term and ϕ approaches θ almost instantaneously. In this case, the coupling term in the θ-dynamics can be neglected and both rotators behave like the isolated θ-rotator. Furthermore, for weak coupling ($\kappa_\phi \ll 1$ or $\kappa_\theta \ll 1$) the respective rotator is hardly affected by the other one and acts like in isolation. In particular, for the parameters considered in fig. 4.4, small values of κ_θ cause the situation that no θ-spikes are produced. Thus, the θ-node acts like in isolation.

Firing rate and CV for a single active rotator were presented in figs. 3.12A and 3.13A in chapter 3. Traces of θ and ϕ for $\kappa_\phi \ll \kappa_\theta$ (1), $\kappa_\phi \gg \kappa_\theta$ (4), and $\kappa_\phi = \kappa_\theta$ (2,3) are illustrated in fig. 4.4C.

In order to investigate the spiking statistics in two coupled active rotators, eq. (4.7) analytically, we follow the standard approach for coupled oscillators and switch to the variables $\beta = \theta + \phi$, capturing the sum of phases, and $\delta = \theta - \phi$, which accounts for the phase difference. Since the coupling function solely depends on the phase difference, we focus on the dynamics of δ. Subtracting the equations for the individual phases in eq. (4.7), we find

$$\dot{\delta} = \omega_- - \sin\left(\frac{\beta+\delta}{2}\right) + \sin\left(\frac{\beta-\delta}{2}\right) - \kappa_+ \sin(\delta) + \sqrt{2D_-}\xi_-(t). \tag{4.8}$$

$\omega_- = \omega_\theta - \omega_\phi$ is the difference of the driving parameters and $\kappa_+ = \kappa_\theta + \kappa_\phi$ the sum of coupling strengths. Furthermore, we set

$$\sqrt{2D_-}\xi_-(t) = \sqrt{2D_\theta}\xi_\theta(t) - \sqrt{2D_\phi}\xi_\phi(t). \tag{4.9}$$

Since the sum of two independent white Gaussian noises is Gaussian and has a variance that is the sum of both variances, it follows that $\langle \xi_-(t) \rangle = 0$, $\langle \xi_-(t), \xi_-(t') \rangle = \delta(t-t')$, and $D_- = D_\theta + D_\phi$.

Next, we study the case of strong coupling

$$\kappa_+ \gg \max(1, \omega_\theta, \omega_\phi, D_\theta, D_\phi). \tag{4.10}$$

In that case, both oscillators tend to synchronize and δ becomes a small parameter. Note that synchronization can be achieved if at least one of the phase dynamics is dominated by the coupling term, see fig. 4.4C (1,2,4). Using a Taylor expansion for eq. (4.8) up to first order in δ leads to

$$\dot{\delta} \approx \omega_- - \cos\left(\frac{\beta}{2}\right)\delta - \kappa_+\delta + \sqrt{2D_-}\xi_-(t). \tag{4.11}$$

Furthermore, we can neglect the cosine since it is bounded and $\kappa_+ \gg 1$. Thus, the δ-dynamics is approximately given by

$$\dot{\delta} \approx \omega_- - \kappa_+\delta + \sqrt{2D_-}\xi_-(t), \tag{4.12}$$

which is an *Ornstein-Uhlenbeck process*. Consequently, δ is approximately Gaussian distributed with time-dependent mean and variance, see appendix A.3.1 for more details.

The idea is now to consider δ as a noise in the respective equations for the phases, eq. (4.7). To this end, we consider the solution of eq. (4.12) in the stationary limit. This

yields

$$\delta(t) \approx \frac{\omega_-}{\kappa_+} + \int_{-\infty}^{t} dt' \; e^{\kappa_+(t'-t)} \sqrt{2D_-}\xi_-(t'), \tag{4.13}$$

which can be obtained by an integration of the homogenous system and an application of the method of variation of constants. Note that the actual value of δ depends on the realization of the noise in the past. Next, we use eq. (4.13) in the equations for θ and ϕ of the system (4.7). First, we consider the θ-dynamics, which becomes

$$\dot{\theta} \approx \frac{1}{2}\left(\omega_+ - \frac{\kappa_-}{\kappa_+}\omega_-\right) - \sin(\theta) + \eta(t), \tag{4.14}$$

after a Taylor expansion of the coupling term. $\omega_+ = \omega_\theta + \omega_\phi$ is the sum of the driving parameters and $\kappa_- = \kappa_\theta - \kappa_\phi$ the difference of the coupling parameters. Moreover, $\eta(t)$ accounts for the influence of the white Gaussian noises and is given by

$$\eta(t) = \sqrt{2D_\theta}\xi_\theta(t) - \kappa_\theta \int_{-\infty}^{t} dt' \; e^{\kappa_+(t'-t)} \sqrt{2D_-}\xi_-(t'). \tag{4.15}$$

If $\eta(t)$ would be a white Gaussian noise, eq. (4.14) would be qualitatively similar to a single noisy active rotator. Then, the influence of the second rotator on the θ-dynamics is captured by a change of the driving and noise parameters. In order to check under which conditions $\eta(t)$ becomes a white Gaussian noise, we have to calculate its mean and correlation function. For the former, it follows immediately from eq. (4.15) that $\langle\eta(t)\rangle = 0$. Furthermore, the calculation of the correlation function yields

$$\langle\eta(t)\eta(t')\rangle = 2D_\theta\delta(t-t') + \left(D_\theta\left(\frac{\kappa_\theta^2}{\kappa_+} - 2\kappa_\theta\right) + D_\theta\frac{\kappa_\theta^2}{\kappa_+}\right)e^{-\kappa_+|t-t'|}. \tag{4.16}$$

More details on this are given in appendix A.3.2. Since we assume κ_+ to be large, the exponential term can be represented by a Dirac delta function. In particular it holds in the limit of strong coupling that

$$\lim_{\kappa_+\to\infty} e^{-\kappa_+|t-t'|} = \frac{2}{\kappa_+}\delta(t-t'). \tag{4.17}$$

Thus, for strong coupling, eq. (4.10), we obtain

$$\langle\eta(t)\eta(t')\rangle \approx 2\left(D_\theta\frac{\kappa_\phi^2}{\kappa_+^2} + D_\theta\frac{\kappa_\theta^2}{\kappa_+^2}\right)\delta(t-t') =: 2D_{\mathrm{mod}}\langle\xi(t)\xi(t')\rangle. \tag{4.18}$$

$\xi(t)$ is a white Gaussian noise with $\langle\xi(t)\rangle = 0$ and $\langle\xi(t)\xi(t')\rangle = \delta(t-t')$ and $D_{\mathrm{mod}} = D_\theta\frac{\kappa_\phi^2}{\kappa_+^2} + D_\phi\frac{\kappa_\theta^2}{\kappa_+^2}$ the noise intensity. Considering this in eq. (4.14) allows for the represen-

tation of $\eta(t)$ by a white Gaussian noise and yields a single-node representation for the system of two synchronized active rotators

$$\dot{\theta} \;=\; \omega_{\mathrm{mod}} - \sin(\theta) + \sqrt{2D_{\mathrm{mod}}}\xi(t), \quad \kappa_+ \gg \max(1, \omega_\theta, \omega_\phi, D_\theta, D_\phi). \tag{4.19}$$

This is complemented by the instantaneous phase reset at each 2π crossing of θ. Remarkably, the influence of the coupling strengths and the individual rotators' parameters on the θ-dynamics is completely captured by the modified driving parameter ω_{mod} and the modified noise intensity D_{mod}, which are given by

$$\begin{aligned}
\omega_{\mathrm{mod}} &= \omega_\phi + \frac{\kappa_\phi}{\kappa_+}(\omega_\theta - \omega_\phi) = \frac{1}{2}\left(\omega_+ - \frac{\kappa_-}{\kappa_+}\omega_-\right), \\
D_{\mathrm{mod}} &= D_\theta \frac{\kappa_\phi^2}{\kappa_+^2} + D_\phi \frac{\kappa_\theta^2}{\kappa_+^2} \\
&= \frac{1}{4}\left(D_\theta \left(\frac{\kappa_-}{\kappa_+} - 1\right)^2 + D_\phi \left(\frac{\kappa_-}{\kappa_+} + 1\right)^2\right).
\end{aligned} \tag{4.20}$$

Performing a similar calculation for the ϕ-dynamics, we find that ϕ obeys the same dynamics, i.e.

$$\dot{\phi} \;=\; \omega_{\mathrm{mod}} - \sin(\phi) + \sqrt{2D_{\mathrm{mod}}}\xi(t), \quad \kappa_+ \gg \max(1, \omega_\theta, \omega_\phi, D_\theta, D_\phi), \tag{4.21}$$

which is consistent with the assumption that $\theta \approx \phi$. Thus, as a first result, we find that the two strongly-coupled active rotators can be described by a single active rotator with driving parameter ω_{mod} and noise intensity D_{mod} in the regime of synchronous oscillations. Consequently, parameter sets that cause $\omega_{\mathrm{mod}} < 1$ lead to excitable behavior and those that cause $\omega_{\mathrm{mod}} > 1$ to oscillatory behavior for strong coupling. Note that eq. (4.20) includes our previous results, i.e. $D_{\mathrm{mod}} \to D_\theta$ and $\omega_{\mathrm{mod}} \to \omega_\theta$ for $\kappa_\theta \ll \kappa_\phi$. Thus, the two coupled rotators act like the isolated θ rotator. In contrast, if $\kappa_\theta \gg \kappa_\phi$ they act like the isolate ϕ-rotator, i.e. $D_{\mathrm{mod}} \to D_\phi$ and $\omega_{\mathrm{mod}} \to \omega_\phi$. Finally, the case $\kappa_\theta = \kappa_\phi$ results into $D_{\mathrm{mod}} = (D_\theta + D_\phi)/4$ and $\omega_{\mathrm{mod}} = \omega_+/2$.

Since eq. (4.19) and (4.21) are one-dimensional systems, strong-coupling approximations for the firing rate and the CV can be obtained by applying the respective results for a single active rotator, which were presented in section 1.8.1. In more detail the firing rate can be obtained from the inverse of eq. (1.106) and the CV can be obtained from the ISI variance, eq. (1.108), and the firing rate. In both formulas, one should replace $U(x)$ by

$$U_{\cos}(x) = -\omega_{\mathrm{mod}} x - \cos(x). \tag{4.22}$$

A contour plot of both measures as functions of ω_{mod} and D_{mod} in the vicinity of the transition between excitable and oscillatory behavior is presented in fig. 4.5A. In the figure, the characteristic noise-dependence of both measures in the excitable and oscillatory regime can be seen. In particular, in the excitable regime $\omega_{\mathrm{mod}} < 1$ the coherence

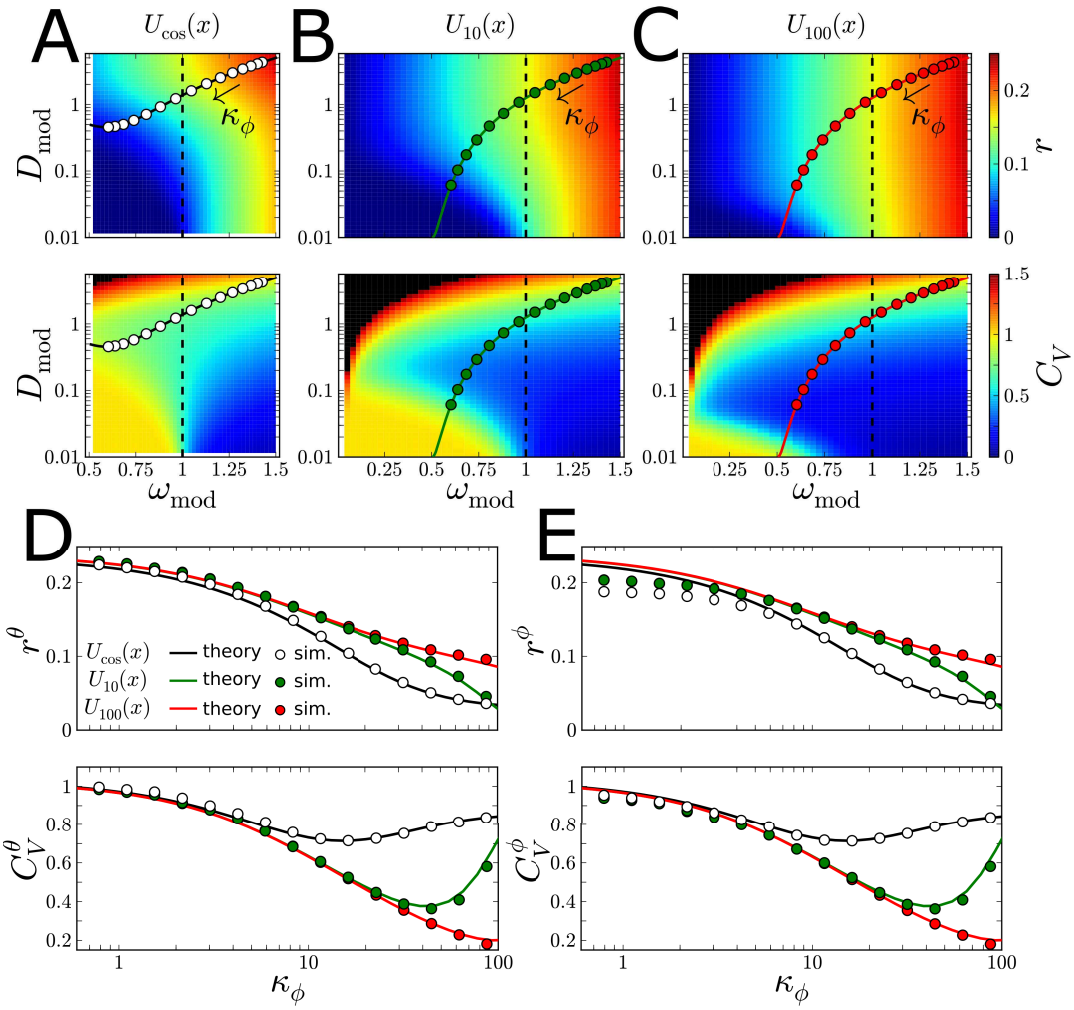

Figure 4.5: Firing rate (top) and CV (bottom) for the eqs. (4.19) (A) and (4.25) (B-C), with $U_G(x) = U_\epsilon(x)$, see eq. (4.27), for $\epsilon = 10$ (B), and for $\epsilon = 100$ (C), and of the two coupled oscillators (D-E). In the latter case the statistics of θ (D) and ϕ spikes (E) obtained from simulations of eq. (4.23) with $h(x) = \sin(x)$ (green and red dots) is compared to that for eq. (4.19) and (4.25) with $U_G(x) = U_\epsilon(x)$, respectively. Black regions mark CVs that are higher than 1.5. The curves in A-C illustrate the traces of $(\omega_{\text{mod}}, D_{\text{mod}})$ for the parameters $\omega_\phi = 1.5$, $\omega_\theta = 0.5$, $\kappa_\theta = 10$, $D_\phi = 5$ and $D_\theta = 0.5$ (A) and $D_\theta = 0.01$ (B,C). Dots mark the points $(\omega_{\text{mod}}, D_{\text{mod}})$ for the coupling strengths used in the simulations and presented in D and E. Vertical dashed lines in A-C mark the border between excitable and oscillatory behavior.

resonance phenomenon [202] is expressed by a global minimum of the CV for fixed ω_{mod}. The ISI statistics in the strong-coupling limit obtained from applying the formulas for firing rate and CV are compared to results for θ and ϕ spikes from simulations in fig. 4.5D and 4.5E, respectively. For strong coupling, eq. (4.10), the theory fits the data points very well. However, for weaker coupling we find deviations between the strong-coupling approximation and the simulation results, which indicate that both oscillators are not completely synchronized. Note that a high difference between the drivings and noise intensities of the oscillators is used in fig. 4.5, which hinders synchronization.

In order to understand how the choice of the coupling strengths influences the ISI statistics of the synchronized oscillators, we study the shape of ω_{mod} and D_{mod}, see eq. (4.20), as functions of κ_θ and κ_ϕ in more detail. Most interestingly, while ω_{mod} scales linearly with κ_-/κ_+, the modified noise intensity possesses a local minimum at $(D_\theta - D_\phi)/(D_\theta + D_\phi) = \kappa_-/\kappa_+$ with $D_{\mathrm{mod,min}} = D_\theta D_\phi/(D_\theta + D_\phi)$ and, consequently, D_{mod} can become smaller than the noise intensities of the isolated active rotators. A representative shape of ω_{mod} and D_{mod} is presented in fig. 4.5A. The shape of ω_{mod} and D_{mod} then yields that of the firing rate and the CV. Note that the firing rate increases monotonically with both parameters, while the CV possesses a local minimum at finite noise intensities for fixed ω_{mod} in the excitable regime $\omega_{\mathrm{mod}} < 1$. This allows for different shapes of the firing rate $r = 1/\langle \Delta t \rangle$ and CV $C_V = \sqrt{\mathrm{Var}(\Delta t)}/\langle \Delta t \rangle$ as functions of the coupling strengths.

Most interestingly in terms of the reduction of spike train variability is the fact that, minimization of the CV for particular combinations of coupling strengths can be achieved by considering two active rotators, one subject to strong noise and the other one to weak noise, respectively, with the latter one operating in the excitable regime. In that case the curve $(\omega_{\mathrm{mod}}, D_{\mathrm{mod}})$ passes regions with lower CVs, which are caused by the coherence resonance effect, than those of the isolated rotators, as can be seen in fig. 4.5A. Thus, if one coupling strength is fixed, the CV possesses a global minimum at some finite value of the other coupling strength. This is illustrated in fig. 4.5A, 4.5D, and 4.5E.

4.2.2 Influence of node dynamics

Next, we consider the influence of the deterministic phase-dependent force on the ISI statistics. To this end, we generalize the system of two coupled active rotators, eq. (4.7), to

$$\begin{aligned} \dot{\theta} =& \omega_\theta + G(\theta) + \kappa_\theta h(\phi - \theta) + \sqrt{2D_\theta}\xi_\theta(t) \\ \dot{\phi} =& \omega_\phi + G(\phi) + \kappa_\phi h(\theta - \phi) + \sqrt{2D_\phi}\xi_\phi(t). \end{aligned} \tag{4.23}$$

$G(x)$ is a phase-dependent force and $h(x)$ an attractive, odd coupling function, i.e. $h(x) = -h(-x)$, such that the phases approach for strong coupling. The other parameters have been introduced in section 4.1 before. Furthermore, we keep the phase reset. Next, we proceed as in the previous section and consider the dynamics of the phase

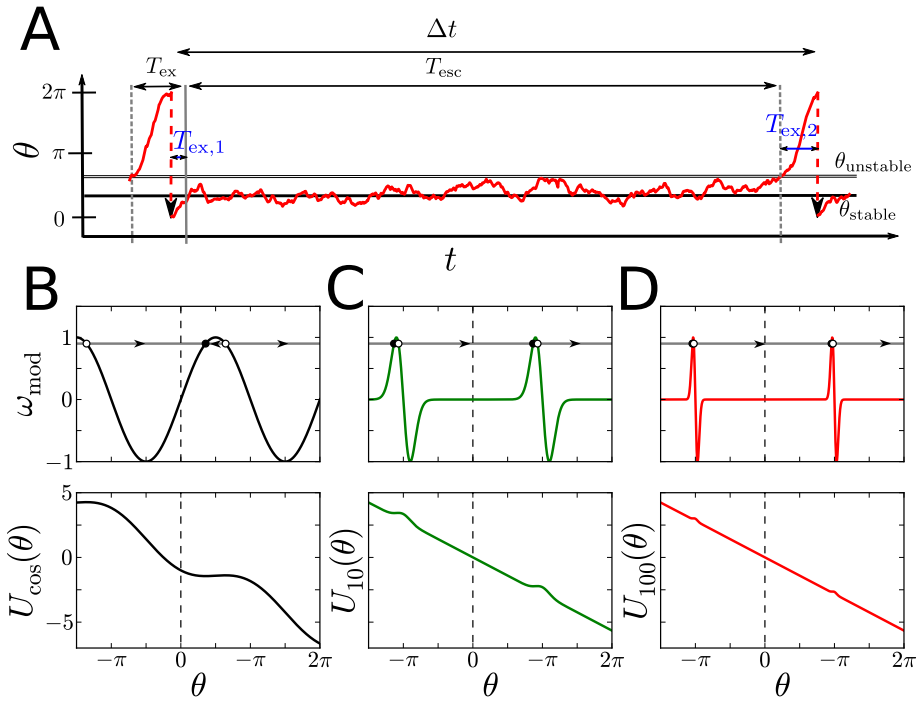

Figure 4.6: Illustration of T_{ex}, $T_{\mathrm{ex},1}$, $T_{\mathrm{ex},2}$, and the escape time T_{esc} on a simulated interspike interval of eq. (4.19) (A) and plots of the negative phase dependent forces of eq. (4.19) ($-\sin(x)$) (B) and of eq. (4.25) ($-G(x)$) with $U_G(x) = U_\epsilon(x)$ for $\epsilon = 10$ (C) and $\epsilon = 100$ (D). Shapes of the corresponding potentials are illustrated for $\omega_{\mathrm{mod}} = 0.9$ (see gray horizontal line) in the bottom figures. Vertical lines in A mark crossings of the unstable fixed point $\theta_{\mathrm{unstable}}$ (dashed) and the first subsequent crossing of the stable one θ_{stable} (straight) in the deterministic system. The values of $\theta_{\mathrm{unstable}}$ and θ_{stable} are marked by horizontal lines in A and corresponding fixed points by white and black dots in figs. B-D, respectively. Furthermore, right arrows in B-D mark positive $\dot{\theta}$ and left ones negative $\dot{\theta}$. Parameters in A are $\omega_{\mathrm{mod}} = 0.9$, $D_{\mathrm{mod}} = 0.01$.

difference $\delta = \theta - \phi$. Considering only terms of first order in δ, we find

$$\dot{\delta} \approx \omega_- - (\kappa_+ h'(0) - G'(\theta))\,\delta + \sqrt{2D_-}\xi_-(t). \tag{4.24}$$

$f'(x)$ denotes the first derivative of $f(x)$ evaluated at x. For strong coupling similar steps as in section 4.2.1, can be performed, which result in the strong-coupling approximation for the θ-dynamics

$$\dot{\theta} = \omega_{\mathrm{mod}} + G(\theta) + \sqrt{2D_{\mathrm{mod}}}\xi(t) \tag{4.25}$$

and a similar equation for the ϕ-dynamics. The parameters ω_{mod} and D_{mod} are given by eq. (4.20). Equation (4.25) is complemented by an instantaneous phase reset. The resulting values of the firing rate and the CV are strongly influenced by the shape of the

function $G(x)$, or, equivalently, by the shape of the potential

$$U_G(x) = -\omega_{\mathrm{mod}} x - \int^x dy\; G(y). \tag{4.26}$$

As we have observed in the section 4.2.1, the minimization of the CV for particular coupling strengths is strongly related to the coherence resonance phenomenon in the excitable regime. In the latter, $\omega_{\mathrm{mod}} + G(y)$ has zeros, which correspond to local extrema of $U_G(x)$. Accordingly, the deterministic part of eq. (4.25) has stable and unstable fixed points.

The coherence resonance phenomenon results from the fact that an ISI consists of two time intervals. The escape time T_{esc}, which measures the time between the first reaching of the stable fixed point and a crossing of the unstable fixed point in our model, and, the excursion time T_{ex}, which is needed to reach the stable fixed point again – in our setup through a crossing of the threshold 2π and application of the phase reset. These intervals are illustrated in fig. 4.6A. More precisely, T_{ex} can be divided into $T_{\mathrm{ex},1}$, which is the time the system needs to reach the stable fixed point θ_{stable} after it has been reset, and $T_{\mathrm{ex},2}$, which is the time between the crossing of the unstable fixed point and the next reset, see fig. 4.6A. Thus, $\Delta t = T_{\mathrm{es}} + T_{\mathrm{ex},1} + T_{\mathrm{ex},2}$ and the sum $T_{\mathrm{ex},1} + T_{\mathrm{ex},2}$ has the same mean and variance as T_{ex} if subsequent ISIs are uncorrelated, see statistics of higher order intervals in section 1.7.2. However, T_{ex} and T_{esc} and their fluctuations possess different noise dependences, which leads to a local minimum of the CV at a finite noise intensity. This is known as coherence resonance [202]. In particular, the escape time becomes long for weak noise and its variance is of order $\langle T_{\mathrm{esc}} \rangle$ [217, 104], while the excursion time dominates for strong noise. For weak noise, however, T_{ex} has only a weak noise dependence but its variance grows as D is increased [201]. The coherence resonance phenomenon occurs, when ISIs are dominated by the excursion time T_{ex}, but the noise is weak enough to ensure that fluctuations of T_{ex} are weak.

Considering these observations, the minimum CV in the excitable regime can be reduced if the shape of $U_G(x)$ causes long excursion times T_{ex} compared to the escape time. In the tilted cosine potential eq. (4.22), which has been used in the previous section and results into $G(x) = -\sin(x)$, both times are of comparable lengths in the noise range of coherence resonance. In order to enhance the effect of coherence resonance, a potential in which the excursion time can be controlled by a parameter ϵ has been presented by Lindner et al. in ref. [162]. We use a similar potential, which is given by

$$U_\epsilon(x) = -\omega_{\mathrm{mod}} x + \frac{\Delta}{\epsilon} \exp\left(\epsilon(1 - \cos(\theta))\right). \tag{4.27}$$

While the parameter ϵ alters the shape of $U_\epsilon(x)$ in order to increase the contribution of the excursion time to the ISIs and, thereby, enhances the effect of coherence resonance,

the parameter Δ scales the height of the potential barrier. In the following, we set

$$\Delta = \left(\exp\left(\epsilon - \frac{1}{2} + \sqrt{\epsilon^2 + \frac{1}{4}} \right) \sqrt{1 - \frac{1}{\epsilon^2}\left(\frac{1}{2} - \sqrt{\epsilon^2 + \frac{1}{4}} \right)^2} \right)^{-1}, \tag{4.28}$$

which ensures that the transition between excitable ($U_\epsilon(x)$ has a local minimum) and oscillatory behavior ($U_\epsilon(x)$ has no local minimum) occurs at $\omega_{\mathrm{mod}} = 1$, as in the cosine potential eq. (4.22). Representative shapes of $U_\epsilon(x)$ and the corresponding dynamics is illustrated in fig. 4.6C-D. In particular, in the limit $\epsilon \to 0$, $-\partial_x U_\epsilon(x)$ attains $\omega_{\mathrm{mod}} - \sin(x)$, which yields the active rotator model, we have studied before. However, in order to enhance the effect of the coherence resonance, high values of ϵ are most interesting. As can be seen in fig. 4.6C-D, the stable and unstable fixed point are relatively close to each other for high ϵ and the potential barrier is reduced. This reduces the escape time and, thereby, leads to a stronger contribution of T_{ex} to the ISIs. Shapes of the resulting firing rate and CV, obtained from the equations for the mean ISI, eq. (1.106), and ISI variance, eq. (1.108), by substituting $U(x)$ by $U_\epsilon(x)$, are plotted in fig. 4.5B,C. As can be seen in the figure, much lower CVs than for the potential $U_{\cos}(x)$, eq. (4.22), are possible. Furthermore, simulation results for two coupled rotators, eq. (4.23), with $U_G(x) \to U_{10}(x)$ and $U_G(x) \to U_{100}(x)$ are shown in fig. 4.5D and E for fixed $\kappa_\theta = 10$. The statistics obtained from eq. (4.25) with corresponding functions $G(x)$ fits the simulation results well for $\kappa_\phi > 2$. In particular, as predicted by the strong-coupling approximations, the CV values can be reduced by increasing ϵ.

4.2.3 Star network of active rotators

Next, we consider star networks with $N > 1$ peripheral nodes. Coupling strengths between central and peripheral nodes are chosen according to fig. 4.2. First, we study the firing rates and CVs for the different rotators by simulating the system (4.1) with $\omega = 0$. Results are illustrated in fig. 4.7B and C for $N = 2$ and in fig. 4.7D and E, for $N = 4$. Interestingly, and in marked contrast to the two coupled active rotators, we find a global maximum of the firing rate of the θ-node and, in the same range of coupling strengths, a minimum of the CV. Thus, for some optimal constellation of the coupling strengths the system spikes most regular and the central node has the highest firing rate. Furthermore, for the presented set of parameters, both extrema occur in the range of intermediate coupling strengths above the diagonal, i.e. for $\kappa_\theta > \kappa_\phi$. In addition to the presence of local extrema, we find that the θ-spiking becomes rare-event-like for small $\kappa_\theta < 1$ and for high values of N and small κ_ϕ, i.e. $C_V^\theta \to 1$ and $r^\theta \to 0$. Moreover, trajectories of the phases for an intermediate value of κ_θ, $N = 2$, and three different values of κ_ϕ are presented in fig. 4.7A. In particular traces for a small value of κ_ϕ, for one value close to the extrema of r^θ and C_V^θ, and for one high value of κ_ϕ are shown. In the most-left panel, the peripheral nodes are only weakly-coupled via the central node. Thus, the individual ϕ-nodes spike rather randomly. However, since their influence on the θ-dynamics is proportional to the degree of synchronization ρ. Spikes of

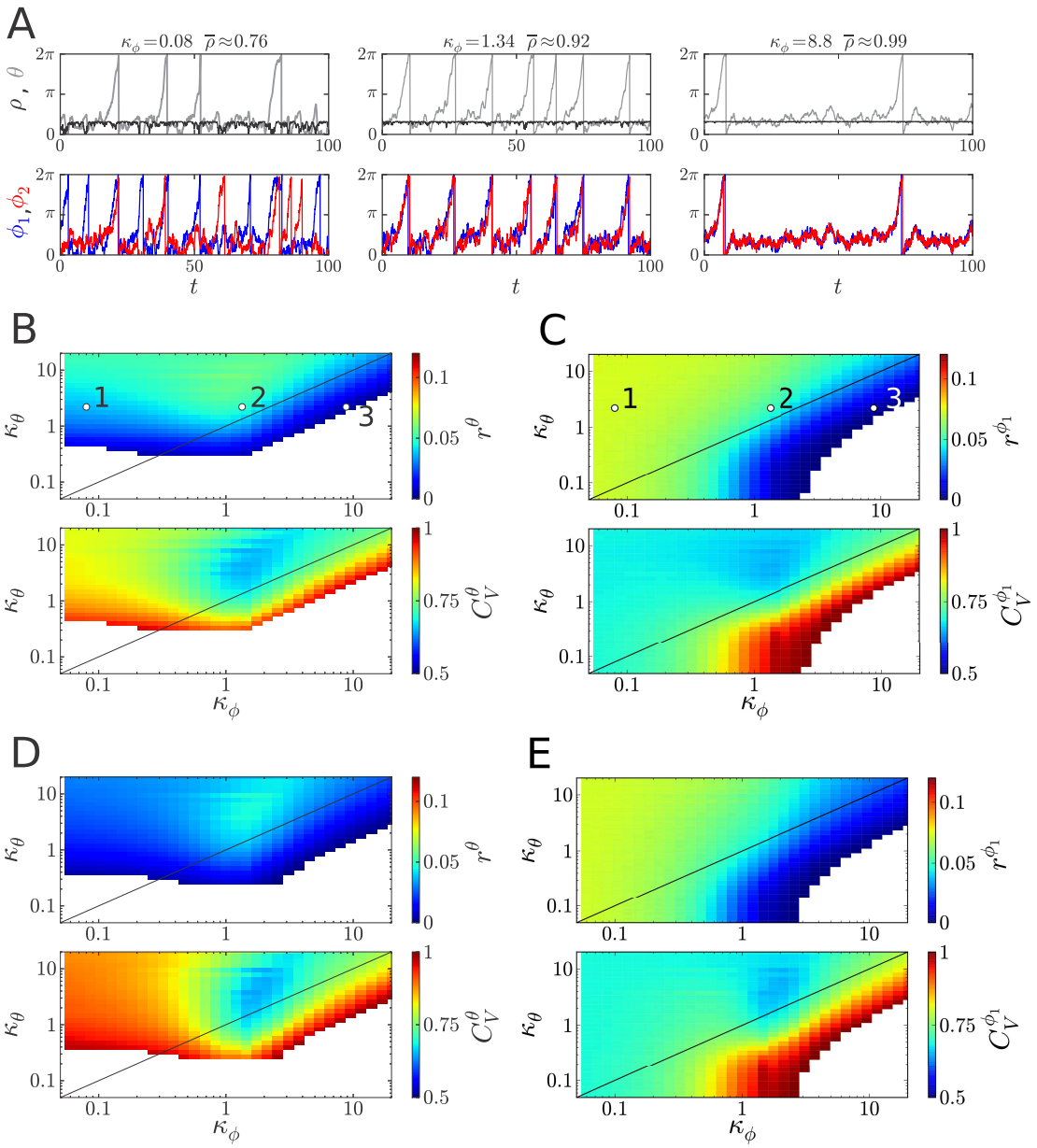

Figure 4.7: Traces of phases and the Kuramoto order parameter ρ (black) for $N = 2$ and $\kappa_\theta = 2.2$ (A), and firing rate and CV for $N = 2$ (B, C) and $N = 4$ (D, E) for the central node (B, D) and one of the N peripheral nodes (C, E), respectively. Regions with firing rates below 10^{-5} are marked white in B-E. Parameters: $D_\theta = 0$, $D_{\phi_i} = 0.4$, $\omega_\theta = \omega_{\phi_i} = 0.9$.

the θ-nodes are preferentially observed during synchronized spikes of the ϕ-oscillators, see fig. 4.7A (most-left panel). If κ_ϕ is increased, the peripheral nodes synchronize via the central node and ρ becomes almost constant. Note that spikes of the peripherals are synchronized for intermediate values of κ_ϕ, but individual fluctuations of the phases between spikes are not. This leads to deviations of ρ below one, see time-averaged ρ-values from simulations that are given for the respective panels in fig. 4.7A. Finally, for high values of κ_ϕ all oscillator phases become synchronized and $\rho \approx \overline{\rho} \to 1$. $\overline{\rho}$ is the time average of ρ over some long time interval T, i.e.

$$\overline{\rho} = \frac{1}{T} \int_0^T dt' \rho(t'). \tag{4.29}$$

For such strong coupling $\overline{\rho}$ approaches one and spiking occurs at a very low firing rate.

Next, we investigate the region of strong coupling analytically. As presented in eq. (4.6), the central node is coupled to the mean field phase Ψ of the peripheral nodes with a time-dependent 'coupling strength' $N\rho\kappa_\theta$. Thus, the system can be considered as two coupled active rotators, where the phase of the second rotator is given by the mean field phase Ψ. The idea is now to derive equations for the Ψ dynamics and the dynamics of ρ and, then, apply the results of section 4.2.1. To this end, we follow the approach presented by Tessone et al. in ref. [250] and consider the time-derivative of the Kuramoto order parameter, eq. (4.4), which yields

$$\frac{d}{dt}\left(\rho e^{I\Psi}\right) = \dot{\rho} e^{I\Psi} + I\dot{\Psi}\rho e^{I\Psi} \quad = \quad \frac{I}{N}\sum_{i=1}^{N} \dot{\phi}_i e^{I\phi_i}. \tag{4.30}$$

Dividing both sides by $e^{I\Psi}$ and evaluating the imaginary part, yields

$$\rho\dot{\Psi} \quad = \quad \frac{1}{N}\sum_{i=1}^{N} \dot{\phi}_i \cos\left(\delta_i\right). \tag{4.31}$$

Note that the phase differences $\delta_i := \phi_i - \Psi$ between the individual phases of peripheral nodes and the mean field phase occur. Note that δ_i can be represented by the phase difference between the phase of the central node and the mean field phase of the peripherals $\delta^{\theta,\Psi} = \theta - \Psi$ and the phase differences between θ and the individual peripheral nodes' phases ϕ_i, denoted as $\delta^{\theta,i} = \theta - \phi_i$. This yields

$$\rho\dot{\Psi} \quad = \quad \frac{1}{N}\sum_{i=1}^{N} \dot{\phi}_i \cos\left(-\delta^{\theta,i} + \delta^{\theta,\Psi}\right). \tag{4.32}$$

Both phase differences become small in case of strong coupling. In particular, for $\kappa_\theta \gg \max(1, \omega_\theta, D_\theta)$ the phase of the central node approaches the mean field phase, i.e. $\delta^{\theta,\Psi} \ll 1$ and for $\kappa_\phi \gg \max(1, \omega_{\phi_i}, D_{\phi_i})$ the phase difference $\delta^{\theta,i}$ becomes a small parameter. Consequently, if both coupling strengths are high we can consider the Taylor expansion

of eq. (4.32) and obtain

$$\rho\dot{\Psi} \approx \frac{1}{N}\sum_{i=1}^{N}\dot{\phi}_i(1+\mathcal{O}((\delta^{\theta,\Psi})^2)+\mathcal{O}((\delta^{\theta,i})^2)). \tag{4.33}$$

Using eq. (4.1) for $\dot{\phi}_i$ and the definition of the Kuramoto order parameter, eq. (4.4), we end up with an approximated dynamics for Ψ, which is exact up to second order in the phase differences

$$\rho\dot{\Psi} \approx \langle\omega_\phi\rangle - \rho\sin(\Psi)+\kappa_\phi\rho\sin(\theta-\Psi)+\sqrt{\frac{2\langle D_\phi\rangle}{N}}\xi(t), \quad \delta^{\theta,\Psi}\ll 1, \quad \delta^{\theta,i}\ll 1. \tag{4.34}$$

Here, we introduced the average driving of the peripheral nodes $\langle\omega_\phi\rangle = 1/N\sum_{i=1}^{N}\omega_{\phi_i}$ and the average of their noise intensities $\langle D_\phi\rangle = 1/N\sum_{i=1}^{N}D_{\phi_i}$. Note that ρ is still a time-dependent parameter. In order to investigate the dynamics of ρ, we first represent ρ by its time average $\overline{\rho}$ and a time-dependent deviation from the average $\delta\rho$, i.e.

$$\rho = \overline{\rho}+\delta\rho. \tag{4.35}$$

Considering the definition of ρ in eq. (4.4), we find for its time-dependent part

$$\delta\rho = \rho-\overline{\rho} = \frac{1}{N}\sum_{i=1}^{N}e^{I\delta_i}-\overline{e^{I\delta_i}} \approx \mathcal{O}((\delta^{\theta,\Psi})^2)+\mathcal{O}((\delta^{\theta,i})^2). \tag{4.36}$$

The last relation follows from the definition of δ_i, which yields real values of $\delta\rho$. Thus, as already stated in ref. [250], $\delta\rho$ is of second order in the phase differences and ρ can be approximated by its time average in eq. (4.34). Finally, we end up with the following *strong-coupling approximation* for the dynamics of the mean field phase:

$$\dot{\Psi} \approx \frac{\langle\omega_\phi\rangle}{\overline{\rho}}-\sin(\Psi)+\kappa_\phi\sin(\theta-\Psi)+\sqrt{\frac{2\langle D_\phi\rangle}{\overline{\rho}^2 N}}\xi(t). \tag{4.37}$$

Note that in case of perfectly-synchronized peripheral nodes ($\rho=\overline{\rho}=1$), the dynamics of Ψ is similar to that of a single ϕ-rotator with a reduced noise intensity $\langle D_\phi\rangle/N$ and the average driving of the peripheral nodes $\langle\omega_\phi\rangle$. Finally, we represent ρ by $\overline{\rho}$ in eq. (4.5), with $\omega=0$, and can approximate the dynamics of the synchronized star network by a system of two coupled active rotators

$$\begin{aligned}\dot{\theta} &\approx \omega_\theta-\sin(\theta)+N\kappa_\theta\overline{\rho}\sin(\Psi-\theta)+\sqrt{2D_\theta}\xi_\theta(t)\\ \dot{\Psi} &\approx \frac{\langle\omega_\phi\rangle}{\overline{\rho}}-\sin(\Psi)+\kappa_\phi\sin(\theta-\Psi)+\sqrt{\frac{2\langle D_\phi\rangle}{\overline{\rho}^2 N}}\xi(t)\end{aligned} \tag{4.38}$$

Next, we apply the results for two coupled rotators and identify the parameters of eq.

(4.7) with those of eq. (4.38), i.e.

$$\begin{aligned}\kappa_\theta \to \kappa'_\theta &:= N\kappa_\theta\overline{\rho}\\ \omega_\phi \to \omega'_\phi &:= \frac{\langle\omega_\phi\rangle}{\overline{\rho}}\\ D_\phi \to D'_\phi &:= \frac{\langle D_\phi\rangle}{N\overline{\rho}^2}.\end{aligned} \tag{4.39}$$

Now, we can use the resulting strong-coupling approximation for the phase dynamics, eqs. (4.19) and (4.21), and, obtain the following results for the parameters ω_{mod} and D_{mod} from eq. (4.20):

$$\begin{aligned}\omega_{\mathrm{mod}} &= \frac{\langle\omega_\phi\rangle}{\overline{\rho}} + \frac{\kappa_\phi(\omega_\theta - \frac{\langle\omega_\phi\rangle}{\overline{\rho}})}{\kappa_\phi + N\overline{\rho}\kappa_\theta} \approx \langle\omega_\phi\rangle + \frac{\kappa_\phi(\omega_\theta - \langle\omega_\phi\rangle)}{\kappa_\phi + N\kappa_\theta} + \frac{N\kappa_\theta(N\kappa_\theta\omega_\phi + \kappa_\phi\omega_\theta)}{(\kappa_\phi + N\kappa_\theta)^2}(1-\overline{\rho})\\ D_{\mathrm{mod}} &= \frac{D_\theta\kappa_\phi^2 + N\langle D_\phi\rangle\kappa_\theta^2}{(\kappa_\phi + N\overline{\rho}\kappa_\theta)^2} \approx \frac{D_\theta\kappa_\phi^2 + N\langle D_\phi\rangle\kappa_\theta^2}{(\kappa_\phi + N\kappa_\theta)^2} + 2N\kappa_\theta\frac{D_\theta\kappa_\phi^2 + N\langle D_\phi\rangle\kappa_\theta^2}{(\kappa_\phi + N\kappa_\theta)^2}(1-\overline{\rho}).\end{aligned} \tag{4.40}$$

Thus, the dynamics in the regime of synchronized oscillators can be expressed by a single active rotator with driving parameter ω_{mod} and noise intensity D_{mod}. Both depend on the degree of synchronization of the peripheral nodes. For a better illustration of this dependency, a Taylor expansion with respect to deviations of $\overline{\rho}$ from one is shown on the right-hand side. We find that a slight desynchronization of the peripherals nodes leads to an increase of the noise intensity D_{mod} and the driving ω_{mod} in the single-node representation. Considering the influence of these parameters on the firing rate, see contour plots in fig. 4.5A, the first order terms cause an increase of the firing rate for all sets of parameters. Furthermore, the driving ω_{mod} approaches the values ω_θ and $\langle\omega_\phi\rangle/\overline{\rho}$ and the noise intensity D_{mod} the values D_θ and $\langle D_\phi\rangle/\overline{\rho}^2 N$ in the limits $\kappa_\theta/\kappa_\phi \to 0$ and $\kappa_\theta/\kappa_\phi \to \infty$, respectively.

In order to compare theses results with simulations an approximation for $\overline{\rho}$, eq. (4.29), is needed. To this end, we follow the approach of Tessone et. al. [250] and evaluate the time average of the Kuramoto order parameter

$$\overline{\rho} = \frac{1}{T}\int_0^T dt'\rho(t') \approx \frac{1}{N}\overline{\sum_{i=1}^{N} e^{I(\phi_i-\Psi)}} = \frac{1}{N}\overline{\sum_{i=1}^{N}\cos(\phi_i-\Psi)}. \tag{4.41}$$

The second relation becomes exact in the limit of $T \to \infty$. Moreover, the last relation follows from the definition of the mean field phase Ψ, which causes a vanishing of the imaginary part of the sum. It has been discussed before, that the phase of the central node θ approaches the mean field phase of the peripheral nodes Ψ in case of strong coupling $\kappa_\theta \gg \max(1, \omega_\theta, D_\theta)$. In that case, $\delta^{\theta,\Psi} = \theta - \Psi$ becomes a small parameter.

Considering a Taylor expansion of eq. (4.41) with respect to $\delta^{\theta,\Psi}$, we find[1]

$$\overline{\rho} \approx \frac{1}{N}\overline{\sum_{i=1}^{N} \cos(\phi_i - \theta)} + \mathcal{O}((\delta^{\theta,\Psi})^2). \tag{4.42}$$

Furthermore, by introducing the stationary conditional probability distribution $p(\theta|\overline{\rho})$ of θ for a given $\overline{\rho}$ and that of the phases ϕ_i for a given phase of the θ-node $p_i(\phi_i|\theta)$, we can represent the time average in eq. (4.42) by integrals over the probability densities. This yields the self-consistent equation for $\overline{\rho}$

$$\overline{\rho} \approx \frac{1}{N}\int_0^{2\pi} d\theta\ p(\theta|\overline{\rho}) \sum_{i=1}^{N} \int_0^{2\pi} d\phi_i\ \cos(\phi_i - \theta) p_i(\phi_i|\theta). \tag{4.43}$$

Finally, the stationary probability densities $p_i(\phi_i|\theta)$ and $p(\theta|\overline{\rho})$ follow from the application of eq. (1.114) to the equation for $\dot{\phi}_i$ in eq. (4.1) with fixed θ, and to the strong-coupling approximation for $\dot{\theta}$, eq. (4.38), with ω_{mod} and D_{mod} given by eq. (4.40). Thus, eq. (1.114) has to be evaluated for $U(x) \to -\omega_{\phi_i} x - \cos(x) - \kappa_\phi \cos(\theta - x)$ and $D = D_{\phi_i}$, which yields $p_i(\phi_i|\theta)$, and for $U(x) \to -\omega_{\mathrm{mod}} x - \cos(x)$ and $D = D_{\mathrm{mod}}$, which yields $p(\theta|\overline{\rho})$. In both cases the respective firing rates can be obtained from the normalization condition eq. (1.115).

Using the results for $p_i(\phi_i|\theta)$ and $p(\theta|\overline{\rho})$, we can calculate the self-consistent solutions of eq. (4.43) numerically by searching for the intersection of the left-hand and right-hand side. For all considered parameter sets, we find only one solution for $\overline{\rho}$, which fulfills the stability condition $\partial_{\overline{\rho}} f^{\mathrm{RHS}}(\overline{\rho}) < 1$, with $\partial_{\overline{\rho}} f^{\mathrm{RHS}}(\overline{\rho})$ denoting the slope of the right-hand side of eq. (4.43) as a function of $\overline{\rho}$. The solutions for $\overline{\rho}$ yield the modified driving and noise intensity in eq. (4.40). Considering the latter in eqs. (4.19) and (4.21) results into a strong-coupling approximation for the θ and ϕ-dynamics, respectively. Finally, the respective approximations for the firing rate and the CV follow from the application of the formulas for the mean ISI eq. (1.106) and the ISI variance eq.(1.108) to eq. (4.19) and (4.21) with modified parameters given by eq. (4.40), respectively.

The resulting values for $\overline{\rho}$, the strong-coupling approximations for the firing rate and CV, and r^θ and C_V^θ obtained from simulations are plotted in fig. 4.8 for different values of N and symmetric coupling $\kappa_\phi = \kappa_\theta = \kappa$. In the weak-coupling limit the active rotators become isolated and their spiking statistics is solely determined by their individual parameters and, therefore, independent of N. However, for strong coupling the spiking statistics is strongly shaped by the number of peripherals. This shaping will be investigated in more detail in the next paragraph. Most remarkably, in fig. 4.8, both,

[1] $\overline{\rho} = \frac{1}{N}\overline{\sum_{i=1}^{N} \cos(\phi_i - \Psi)} = \frac{1}{N}\overline{\sum_{i=1}^{N} \cos(\phi_i - \theta + \delta^{\theta,\Psi})} \approx \frac{1}{N}\overline{\sum_{i=1}^{N} \cos(\phi_i - \theta) - \sin(\phi_i - \theta)\delta^{\theta,\Psi}} + \mathcal{O}((\delta^{\theta,\Psi})^2)$
Now, applying the definition of the Kuramoto order parameter eq. (4.4), one finds
$\overline{\rho} \approx \overline{\left(-\delta^{\theta,\Psi}\rho\sin(\delta^{\theta,\Psi}) + \frac{1}{N}\sum_{i=1}^{N}\cos(\phi_i - \theta)\right)} + \mathcal{O}((\delta^{\theta,\Psi})^2)$.
Finally, a Taylor expansion of the sinus leads to the result in eq. (4.42).

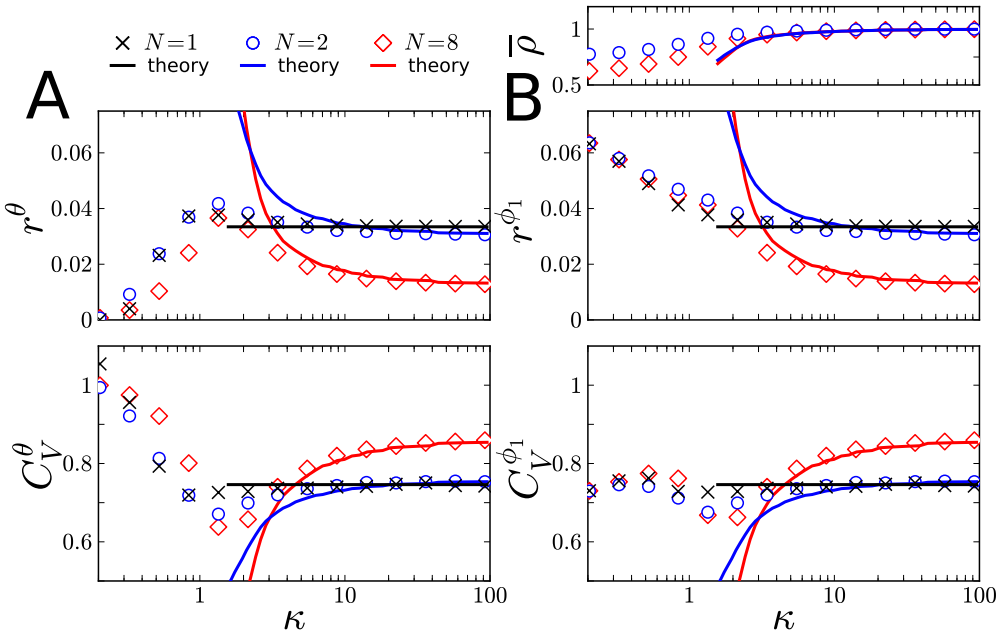

Figure 4.8: Statistics of the central node (A) and one peripheral node (B) for different values of N and symmetric coupling $\kappa_\phi = \kappa_\theta = \kappa$. In addition, the time-averaged Kuramoto order parameter eq. (4.29) is shown in the top right panel. Symbols show results from simulation and lines the strong-coupling approximations and the self-consistent solutions of eq. (4.43), respectively. Parameters: $D_\theta = 0$, $D_\phi = 0.4$, $\omega_\theta = \omega_\phi = 0.9$.

the firing rate and the CV of the central node possess global extrema at finite values of κ. In particular the qualitative shape of both measures on the right-hand side of the extrema is well-described by the strong-coupling approximation and results from deviations of $\overline{\rho}$ from one. These deviations cause an increase of ω_{mod} and D_{mod}, as we have discussed before. This causes an increase of the firing rate when leaving the regime of perfectly-synchronized oscillations ($\overline{\rho} = 1$) and, thereby, leads to a global maximum of the firing rate of the individual oscillators whenever the firing rate in the strong-coupling limit equals or is higher than that of the respective oscillator in isolation. The shaping of ω_{mod} and D_{mod}, however, does not necessarily result in a global minimum of the CV, even if the CV of the isolated oscillator is higher than the strong-coupling limit. The reason for this is that an increase of ω_{mod} and D_{mod} does not always reduce the CV, as can be seen in fig. 4.5A. Quantitatively, the strong-coupling approximation yields sufficient results for $\kappa > 10$.

4.2.4 Influence of number of peripheral nodes on spiking statistics

Of particular interest in many studies of complex networks is the influence of the topology or the number nodes and connections on the dynamics. Therefore, we investigate the influence of the parameter N on the spiking statistics next. In particular, we focus

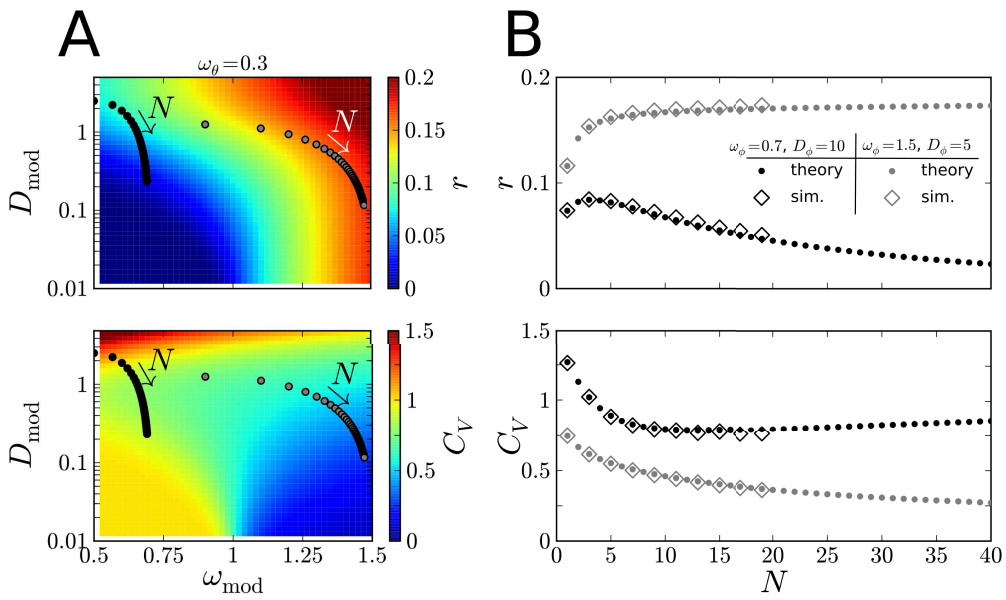

Figure 4.9: Values for $\omega_{\rm mod}$ and $D_{\rm mod}$ for different N on the contour plot of the firing rate and CV (A) and the resulting firing rate and CV as functions of N (B) obtained from the strong-coupling approximation for symmetric coupling (dots) and r^θ and C_V^θ from simulations of eq. (4.1) with $\kappa_\theta = \kappa_\phi = 100$ (diamonds). Parameters: $D_\theta = 0$. Traces in A indicate the values of $(\omega_{\rm mod}, D_{\rm mod})$ for the values of N for which r and C_V are shown in B.

on the case of strong, symmetric coupling $\kappa_\phi = \kappa_\theta = \kappa \gg \max(\omega_\theta, \omega_{\phi_i}, D_\theta, D_{\phi_i})$, with $i = 1, 2, .., N$. In this case, peripheral nodes synchronize via their indirect connections through the central node and, hence, $\overline{\rho} \approx 1$. Consequently, we can approximate the node dynamics by the eqs. (4.19) and (4.21), respectively, with modified parameters given by eq. (4.40). Applying theses restrictions yields

$$\begin{aligned} \omega_{\rm mod} &= \langle\omega_\phi\rangle + \frac{\omega_\theta - \langle\omega_\phi\rangle}{1+N}, \\ D_{\rm mod} &= \frac{D_\theta + N\langle D_\phi\rangle}{(1+N)^2}. \end{aligned} \tag{4.44}$$

As described in the previous sections, a strong-coupling approximation for the firing rate and the CV can be obtained when considering the corresponding formulas for the mean ISI and ISI variance eqs. (1.106) and (1.108), respectively. Results are illustrated in fig. 4.9 in accordance with results obtained from simulations of eq. (4.1) with $\omega = 0$ for a strong symmetric coupling $\kappa = 100$. For the parameters considered in the figure the central node operates deep in the excitable regime and does not receive noisy input, while the peripheral nodes are considered either excitable (black) or oscillatory (gray), respectively. In both cases peripherals are subject to strong noise. Interestingly, the statistics in the regime of synchronized spiking is strongly shaped by the number of

peripherals N. In particular if peripherals are considered excitable, the firing rate attains a global maximum and the CV a global minimum at a finite N. In that case, the trace of $(\omega_{\mathrm{mod}}, D_{\mathrm{mod}})$ passes the region of low CVs, see fig. 4.9A. Furthermore, the limits of two coupled oscillators $N = 1$ and of infinitely many peripherals $N \to \infty$ from eq. (4.44) are

$$\omega_{\mathrm{mod}} = \begin{cases} \frac{\omega_\theta + \langle \omega_\phi \rangle}{2}, & N = 1 \\ \langle \omega_\phi \rangle, & N \to \infty \end{cases}, \quad D_{\mathrm{mod}} = \begin{cases} \frac{D_\theta + \langle D_\phi \rangle}{4}, & N = 1 \\ 0, & N \to \infty \end{cases}. \tag{4.45}$$

These limits illustrate that the influence of noise reduces in the limit $N \to \infty$. This is in accordance with results from prior studies of globally-coupled oscillators [250]. However, due to the coherence resonance phenomonen in isolated active rotators, the lowest ISI variability is not always observed for the weakest noise D_{mod} if $\langle \omega_\phi \rangle < 1$. This results in an optimal network size for which synchronized spiking becomes most coherent.

4.3 Spike generation in the presence of feedback

Finally, we consider the influence of spike-triggered feedback in the central node ($\omega \neq 0$) on the spiking statistics in the regime of perfectly-synchronized oscillations $\overline{\rho} = 1$. Note that we have intensively studied the influence of feedback in an isolated active rotator in chapter 3. Remarkably, our investigations of the dynamics in the regime of synchronous oscillations, in particular the derivation of the single-node description eq. (4.19) can be directly extended to the presence of feedback, by substituting $\omega_\theta \to \omega_\theta + \omega$. Applying eq. (4.40), this yields for the total modified driving $\omega_{\mathrm{mod}}^{\mathrm{tot}}$

$$\begin{aligned} \omega_{\mathrm{mod}}^{\mathrm{tot}} &= \frac{\langle \omega_\phi \rangle}{\overline{\rho}} + \frac{\kappa_\phi}{\kappa_\phi + N\overline{\rho}\kappa_\theta}(\omega_\theta + \omega(t) - \frac{\langle \omega_\phi \rangle}{\overline{\rho}}), \\ &= \frac{\langle \omega_\phi \rangle}{\overline{\rho}} + \frac{\kappa_\phi}{\kappa_\phi + N\overline{\rho}\kappa_\theta}(\omega_\theta - \frac{\langle \omega_\phi \rangle}{\overline{\rho}}) + \frac{\kappa_\phi}{\kappa_\phi + N\overline{\rho}\kappa_\theta}\omega(t), \\ &= \omega_{\mathrm{mod}} + \omega_{\mathrm{mod}}^{\mathrm{feed}}(t). \end{aligned} \tag{4.46}$$

We denote the time-dependent contribution of the feedback to the total driving by $\omega_{\mathrm{mod}}^{\mathrm{feed}}(t) = \kappa_\phi/(\kappa_\phi + N\overline{\rho}\kappa_\theta)\omega(t)$. Thus, the contribution of the feedback to the dynamics of the synchronized system is shaped by the coupling strengths and the degree of synchronization of the peripheral nodes and the dynamics is given by that of a single active rotator with spike-triggered feedback, i.e. the strong-coupling approximation for the θ-dynamics in the regime of synchronized oscillations reads

$$\dot{\theta} = \omega_{\mathrm{mod}} + \omega_{\mathrm{mod}}^{\mathrm{feed}}(t) - \sin(\theta) + \sqrt{2D_{\mathrm{mod}}}\xi(t), \tag{4.47}$$

with the spike-triggered feedback dynamics

$$\tau\dot{\omega} = -\omega + 2\pi a x_\theta(t). \tag{4.48}$$

This is complemented by the instantaneous phase reset at $\theta = 2\pi$. However, this dynamics is similar to the one we have intensively studied in chapter 3. Thus, we can apply the methods from the previous chapter.

4.3.1 Spike generation in two coupled active rotators with positive feedback

We restrict the discussion on the influence of positive feedback $a > 0$ in two coupled active rotators. We will demonstrate how the phenomenon of noise-controlled bistability, which we have presented in section 3.3, influences the spike generation in strongly-coupled active rotators. For such coupling and slow feedback $\tau \gg 1/r^\theta$, the spiking statistics can be investigated by applying the approach, we used to study the stationary solutions for the time-averaged feedback strength $\overline{\omega}^{\rm fp}$ in section 3.3, to the strong-coupling approximation of the θ-dynamics, eq. (4.47), and the feedback dynamics eq. (4.48). Time averaging of eq. (4.48) and considering stationary solutions ($\dot{\overline{\omega}}^{\rm fp} = 0$) yields

$$\overline{\omega}^{\rm fp} = 2\pi a r^\theta \tag{4.49}$$

and allows for approximating $\omega_{\rm mod}^{\rm feed}(t)$ by

$$\omega_{\rm mod}^{\rm feed}(t) \approx \overline{\omega_{\rm mod}^{\rm feed}}^{\rm fp} = \frac{\kappa_\phi \overline{\omega}^{\rm fp}}{\kappa_\phi + N\overline{\rho}\kappa_\theta} = 2\pi \frac{\kappa_\phi a}{\kappa_\phi + N\overline{\rho}\kappa_\theta} r^\theta, \tag{4.50}$$

for a slow feedback timescale, $\tau \gg 1/r^\theta$. Thus, the stationary solutions $\overline{\omega_{\rm mod}^{\rm feed}}^{\rm fp}$ correspond to those in a single active rotator with a rescaled parameter $a \to a_{\rm mod}$, given by

$$a_{\rm mod} = \frac{\kappa_\phi a}{\kappa_\phi + N\overline{\rho}\kappa_\theta}. \tag{4.51}$$

In case of perfectly-synchronized peripheral oscillators $\overline{\rho} = 1$, we can directly apply the self-consistent approach used section 3.3. Thus, we consider eq. (3.30), set $\overline{\omega}^{\rm fp} \to \overline{\omega_{\rm mod}^{\rm feed}}^{\rm fp}$, $\omega_0 \to \omega_{\rm mod}$, $D \to D_{\rm mod}$, and investigate the number of solutions for combinations of the coupling strengths that fulfill $\kappa_\theta \gg \max(1, \omega_\theta, D_\theta)$ and $\kappa_\phi \gg \max(1, \omega_{\phi_i}, D_{\phi_i})$ for $i = 1, 2, .., N$. Thus, we search for self-consistent solutions of

$$\overline{\omega}^{\rm fp} = 2\pi a D \left(1 - \exp\left(-\frac{2\pi(\omega_0 + \omega_{\rm mod} + \overline{\omega_{\rm mod}^{\rm feed}}^{\rm fp})}{D}\right)\right) \left(\int_0^{2\pi} dx\; e^{\frac{U_{\rm mod}(x)}{D}} \int_{x-2\pi}^{x} dy\; e^{-\frac{U_{\rm mod}(y)}{D}}\right)^{-1}. \tag{4.52}$$

Here, we set

$$U_{\rm mod}(x) = -\left(\omega_{\rm mod} + \overline{\omega_{\rm mod}^{\rm feed}}^{\rm fp}\right) x - \cos(x). \tag{4.53}$$

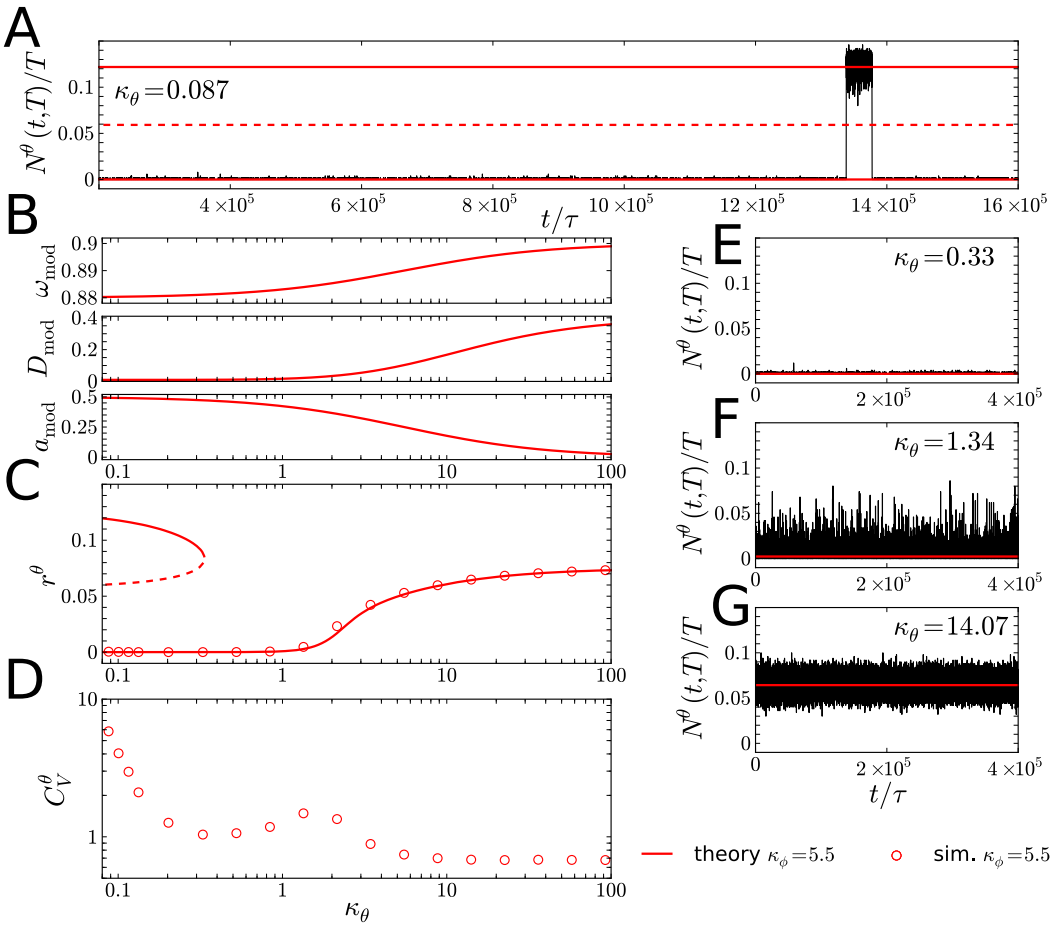

Figure 4.10: Traces of the normalized time-resolved spike count for the θ-rotator $N^\theta(t,T)/T$ for several values of κ_θ (A,E-G), the modified parameters (B), and firing rate and CV as functions of κ_θ (C and D), respectively. In subfigures A,C-G we plot only the measures for the θ-rotator, since those for the ϕ-rotator have almost identical values. Firing rates that result from self-consistent solutions of eq. (4.52) and eq. (4.49) are marked by 'theory'. Parameters: $N = 1$, $D_\theta = 0.01$, $D_\phi = 0.4$, $\omega_\phi = 0.9$, $\omega_\theta = 0.88$, $a = 0.5$, $\tau = 50$, and $T = 500$.

Considering previous results from section 3.3, multiple stable solutions for $\overline{\omega}^{\mathrm{fp}}$ are possible if ω_{mod} is close to, but smaller than one, a is high, and D_{mod} is low. Furthermore, self-consistent solutions of eq. (4.52) can be related to the firing rate by eq. (4.49).

Representative results for the firing rate for fixed κ_ϕ are shown in fig. 4.10C. For the presented set of parameters, two stable solutions coexist for small κ_θ and the synchronized system behaves like the θ-node in isolation, which we tuned to be inside the region of giant variability by choosing a proper set of parameters, compare fig. 3.16. Consequently the synchronized rotators switch between an excitable and an oscillatory state, see fig. 4.10A. The firing rate in each state is approximately given by the self-consistent solutions for the firing rate. Switching between these states leads to giant ISI variability, see fig. 4.10D. As for a single active rotator with positive feedback, the bistable region is bounded by an oscillatory regime ($\omega_{\mathrm{mod}} + \overline{\omega_{\mathrm{mod}}^{\mathrm{feed}}}^{\mathrm{fp}} > 1$) at high D_{mod} and ω_{mod} and by an excitable regime ($\omega_{\mathrm{mod}} + \overline{\omega_{\mathrm{mod}}^{\mathrm{feed}}}^{\mathrm{fp}} < 1$) at low D_{mod} and ω_{mod}, see results for the single active rotator in fig. 3.16. Furthermore, a decrease of a_{mod} shifts the bistable region towards higher ω_{mod}, compare fig. 3.5 (center). If κ_θ is increased, the parameter a_{mod} is reduced and D_{mod} and ω_{mod} increase. The reduction of a_{mod}causes a shift of the bistable region higher ω_{mod}. This effect dominates for small κ_θ and leads to the leaving of the bistable region and the entering of the excitable regime. Then, the CV approaches one and spiking occurs at a low firing rate, see fig. 4.10E. Now, in the excitable regime the shaping of the firing rate and the CV is controlled by two effects: first the increase of D_{mod} and ω_{mod} brings the system closer to the transition to oscillatory behavior and leads to an increase of the firing rate and the CV, compare results for a single active rotator in fig. 3.16, and, second the decrease of a_{mod} shifts the system deeper into the excitable regime, which mainly reduces the CV. For the set of parameters shown in fig. 4.10C the interplay of both leads to a second maximum in the CV at intermediate coupling strengths. Furthermore, we find strong fluctuations in the time-resolved spike count, fig. 4.10F, which lead to bursting behavior and CVs above one. Finally, at high κ_θ the system behaves like the ϕ-oscillator in isolation. For the latter parameters were chosen according to the coherence resonance minimum of the single active rotator in the absence of feedback, compare fig. 3.13. Corresponding traces of the time-resolved spike count are depicted in fig. 4.10G.

4.4 Discussion and outlook

In the present chapter, we studied the spike generation in star networks of noisy active rotators. In particular, we considered phase coupling between a central node and N peripheral nodes. The coupling is described by two coupling strengths, one for each direction. We focused on the influence of the coupling strengths and the number of peripheral nodes on the spiking statistics of the individual nodes.

One of our most remarkable results is that, for particular choices of the coupling strengths, spike train variability is reduced and the firing rate of the central node is increased. In particular, we found that both measures attain global extrema for particular

choices of the coupling strengths and numbers of peripheral nodes. These results can be applied to predict the optimal number of peripherals, with respect to high firing rates and low spike train variability, for fixed sets of parameters and noise intensities of the individual nodes.

Furthermore, we derived analytical approximations for the case of strong coupling, which causes synchronized spiking of the central and the peripheral nodes. Remarkably, our results for the regime of synchronized spiking provide the possibility to account for the influence of the coupling strengths and the number of peripheral nodes on the spike generation in the individual nodes by a rescaling of their parameters. This can also be applied when spike-triggered feedback is present and, therefore, allows for a direct application of the results from the previous chapter. In particular, the coupling between active rotators can be fine-tuned in order to obtain giant spike train variability in the presence of strong positive feedback. This has been demonstrated for two coupled rotators in section 4.3 and can be applied in the strong-coupling limit of star networks, too. An interesting question in this context is how deviations from the perfectly-synchronized state influence these results. In particular, combining the self-consistent approach for the degree of synchronization, which we have used in section 4.2.3, with the one we have used for the stationary solutions of the feedback strengths in section 4.3 may lead to additional self-consistent solutions. Those could correspond to regimes in which the central node can switch between an oscillatory state and an excitable state, but coupling is only strong enough to synchronize the nodes in one of the states.

Our results point out how firing rates and spike-train variability can be influenced by either changing coupling strengths or the number of connections between the nodes. This is important in biological systems, like the myelinated axon, which typically operate in noisy environments. In particular, while the system cannot directly influence its environment or reduce the strengths of noisy inputs to regularize the spike generation, it can develop more connections or change their lengths, which directly influences the related coupling strengths [258]. As we showed in this chapter, these two mechanisms allow for a tuning of its spike train statistics in order to realize its biological function best. For instance, by changing lengths and numbers of connections it can tune its firing rate and spike train variability to become optimal for particular strengths of an external input (in the active rotator model similar to an increase of the driving parameter) or a particular noise intensity.

An interesting topic for further studies would be the extension of our strong-coupling approximation to more complex network structures. In particular for the afferent nerve, see schematic in fig. 4.1 (left), the strong-coupling regime is most interesting since it allows for the propagation of action potentials along the axon branches. In order to provide a deeper understanding of the spiking statistics at the first-order node, our results should be extended to tree-like structures. As a further step, one could also consider delay or phase lags in the phase coupling, which would account for the finite time the action potential needs to travel along the connections.

5 Influence of noise and strong coupling on the intraburst spike pattern of bursting neurons

In the present chapter, we study noise in isolated and strongly-coupled bursting neurons. In particular, we focus on slow-wave bursters in which the bursting occurs due to autonomous slow oscillations that periodically switch a fast spike-generating subsystem between a spiking state and a resting state. In order to motivate our studies, we consider a bursting neuron in the pyloric central pattern generator (CPG) of *crustaceans*, which is subject to strong electrical coupling. CPGs can be found in many animals and are typically involved in locomotion [117]. In general, when activated, they produce rhythmic motor patterns, which control processes like walking, breathing, heartbeating, and swimming [173]. Since the regularity of the rhythm is often critical for survival, it is highly valuable to reduce noise-induced variability in the system.

Parts of the chapter are destined for publication in ref. [145].

5.1 Bursting neurons in the pyloric central pattern generator

The pyloric CPG generates a bursting rhythm that operates muscles that dilate and constrict the pyloric part of the stomach of *crustaceans*. The rhythm is mainly controlled by a *pacemaker* group, see fig. 5.1, consisting of the *anterior burster* (AB) neuron – whose membrane potential performs slow-wave oscillations – and two *pyloric dilator* (PD) neurons. The AB and PD neurons are coupled by a strong electrical synapse[1]. In the network, both burst in synchrony and inhibit the follower neurons via inhibitory synaptic connections, see fig. 5.1. This suppresses bursting of the follower neurons during bursts of the pacemaker neurons. However, when inhibition from the pacemakers stops the follower neurons start to burst immediately. Thus, the rhythm is generated via an interplay of *reciprocal inhibition and postinhibitory rebound*, which is a general mechanism in many CPGs [223, 97, 43, 174, 232, 114] and has been found to ensure a reliable network rhythm [35, 235]. Furthermore, the pyloric rhythm serves as a models system for various studies of bursting rhythms, see for instance refs. [184, 230, 232, 270, 213].

We are mainly interested in a specific neuron in the pacemaker group, the PD neuron, and how its spike generation is influenced by the strong coupling to the slow-wave driving

[1] Professor Reynaldo Daniel Pinto (Instituto de Física de São Carlos, University of São Paulo, São Carlos, Brazil), private communication

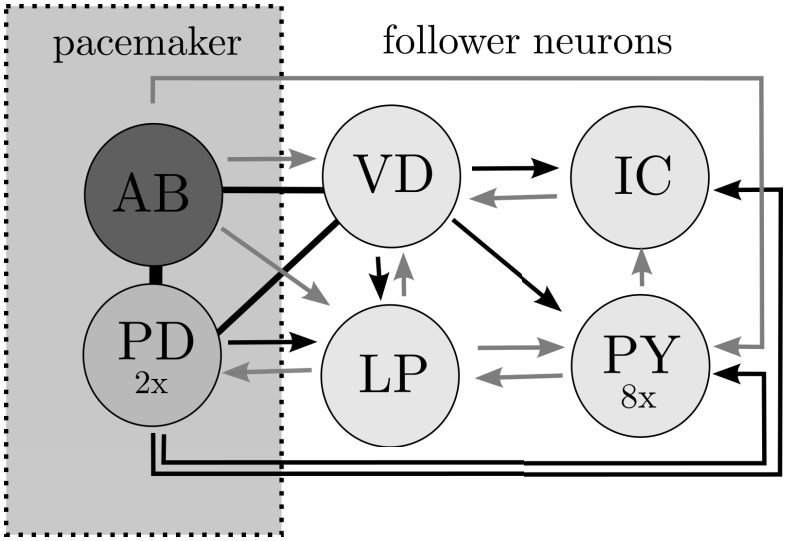

Figure 5.1: Network topology of the pyloric central pattern generator according to ref. [13]. Connections are marked as follows: electrical coupling (solid black line), glutamatergic inhibitory chemical synapses (gray arrow), and cholinergic inhibitory synapses (black arrow). Neurons are: anterior burster (AB), pyloric dilator (PD), lateral pyloric (LP), ventricular dilator (VD), pyloric (PY), and inferior cardiac (IC) neuron.

of the AB neuron. To this end, we compare its bursting dynamics in two setups, first the PD neuron in the intact circuit, see schematic of the pacemaker group in fig. 5.2A, and, second the isolated[2] PD neuron (fig. 5.2B). While bursting of the isolated PD neuron is caused by its intrinsic dynamics, it is strongly influenced by the coupling to other neurons, most dominant the strong electrical coupling to the AB's slow-wave oscillations, when connected to the circuit.

[2]In order to isolate the neuron in an experimental setup, other neurons in the networks are photoinactivated, deeply hyperpolarized, or their synaptic inputs have to be blocked pharmacologically, see ref. [184, 13].

[3]Data for the isolated neuron are obtained from ref. [176], this data is for the PD neuron in the *spiny lobster*. For the connected neuron, we use data for the *blue crab* from ref. [33]. In the former case, data includes recordings of the membrane potential with time resolution of 0.2 ms. In order to detect spike times, we calculated the time derivative of the membrane potential. If the derivative exceeded 4 V/s, we recorded the corresponding time as the spike time and waited at least 10 ms until the next spike time was recorded. This procedure turned out to be more precise than using a threshold voltage, since individual spikes differ in their peak voltages. Recordings contain 163 bursts of the isolated and 6106 bursts of the connected neuron. In order to distinguish interburst from intraburst intervals, we introduced thresholds of 0.4s (isolated) and 0.3s (connected). All ISIs longer than these thresholds were considered as interburst intervals.

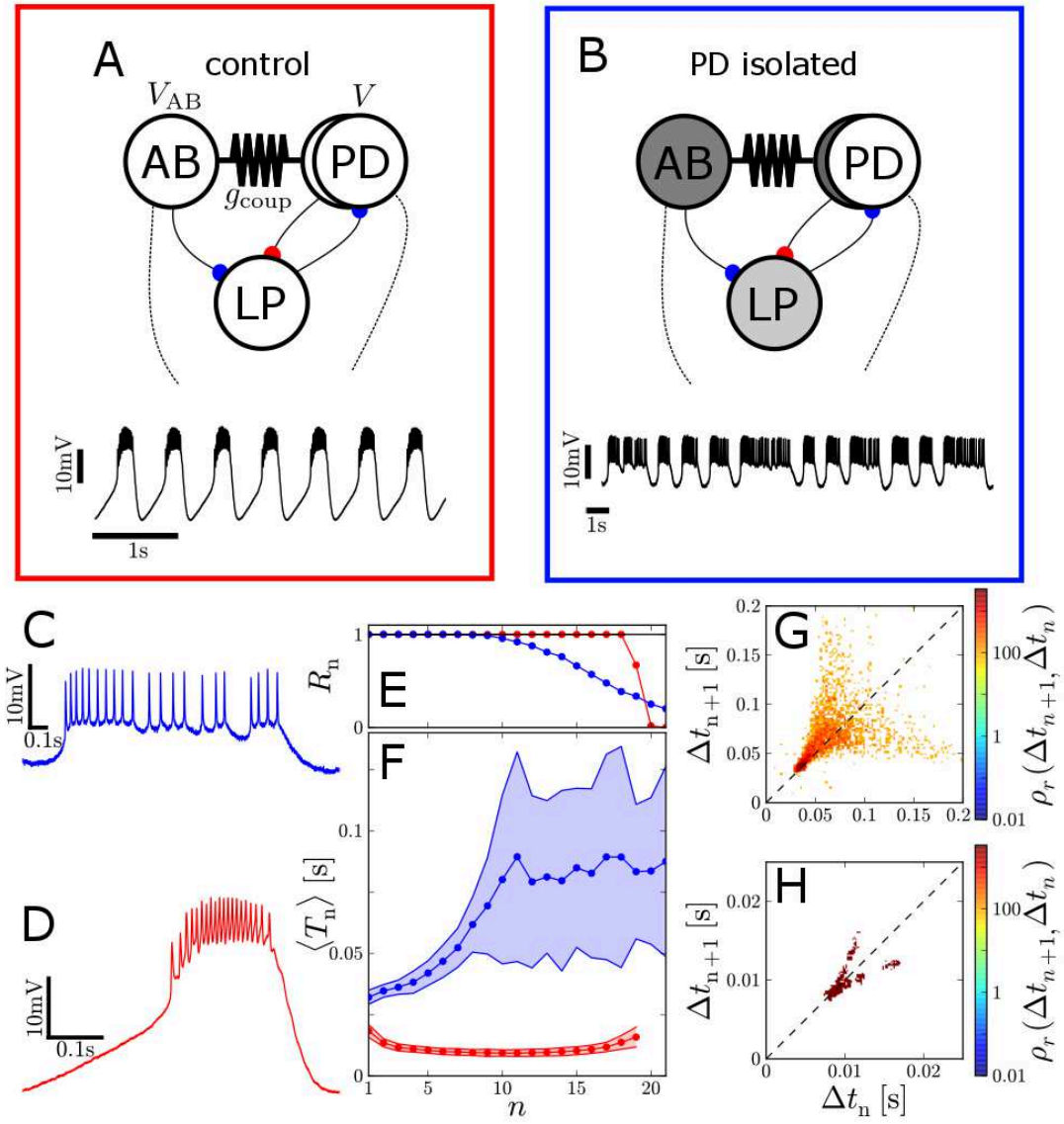

Figure 5.2: Schematics of the pacemaker group and one follower neuron in the intact network (A) and the isolated PD neuron (B). Dark gray colors indicates photoinactivated neurons and light gray deeply hyperpolarized neurons. Accordingly, voltage time series of the PD in the respective scenarios are shown. Basic statistics of the isolated PD (blue) and the connected PD (red)[3]are shown in C-H. In particular, the voltage time series during single bursts (C-D), the ratio of bursts R_n with at least n ISIs (E), average nth ISI within a burst (dot) and the range of one standard deviation from the average (colored region) (F), and intraburst part of the ISI return maps for the isolated (G) and the connected neuron (H), note the different scaling.

5.1.1 Influence of electrical coupling on intraburst spike pattern of the pyloric dilator neuron

When synaptically isolated, the PD neuron and other neurons in the network exhibit irregular bursting behavior [231, 13, 232, 74, 46], i.e. bursts with high variability in the numbers of spikes per burst and burst durations. We refer by burst duration to the time between the first spikes of two subsequent bursts. Recordings of the membrane potential for the isolated PD neuron are shown in fig. 5.2B. However, connection to the circuit leads to regular bursting, i.e. all bursts have similar numbers of spikes per bursts and similar burst durations, see voltage time series in fig. 5.2A. Thus, the electrical coupling between the PD and AB neuron regularizes the bursting rhythm of the pacemaker neurons, see also refs. [1].

In the following, we compare the intraburst spike patterns – the sequence of interspike intervals (ISI) within individual bursts – of the isolated PD neuron and of the PD neuron in the intact network. First, we consider the regularity of the bursting. To this end, we evaluate the relative number of bursts R_n with at least n ISIs per burst. Thus, regular bursting is expressed by a step-like shape of R_n, i.e. if each burst has exactly N ISIs $R_n = 1$ for $n \leq N$ and $R_n = 0$ for $n > N$. In contrast, a slow decrease of R_n indicates strong fluctuations of the number of ISIs per burst. As can be seen in fig. 5.2E, the isolated PD neuron exhibits bursts with strongly-varying numbers of ISIs. Furthermore, $R_n \approx 1$ for $n \leq 9$ and decreases slowly for larger n. Thus, we will refer to the first 9 ISIs of a burst as *regular part* of a burst and to the remaining part as *irregular part*. In contrast, synaptic connection regularizes the behavior as can be seen in the shape of R_n for the connected neuron, fig. 5.2E. The latter illustrates that all recorded bursts of the connected PD neuron possess either 18 or 19 ISIs.

In order to study other qualitative changes in the intraburst spike pattern, we denote the nth ISI in the mth burst as $T_{\mathrm{n}}^{\mathrm{m}}$, $n = 1, 2, ..., N^{\mathrm{m}}$ and $m = 1, 2, ..., M$, with N^{m} the number of ISIs in the mth burst and M the total number of bursts. In fig. 5.2F the statistics of $T_{\mathrm{n}}^{\mathrm{m}}$ is illustrated. In particular, dots indicate the average nth ISI within a burst $\langle T_{\mathrm{n}} \rangle$ and the colored region the range of one standard deviation $\sigma(T_{\mathrm{n}})$ from $\langle T_{\mathrm{n}} \rangle$. These measures are calculated according to

$$\langle T_{\mathrm{n}} \rangle = \frac{1}{M_n} \sum_{\substack{m=1 \\ N^m \geq n}}^{M} T_{\mathrm{n}}^{\mathrm{m}} \tag{5.1}$$

and

$$\sigma(T_{\mathrm{n}}) = \sqrt{\frac{1}{M_n} \sum_{\substack{m=1 \\ N^m \geq n}}^{M} (T_{\mathrm{n}}^{\mathrm{m}} - \langle T_{\mathrm{n}} \rangle)^2} \tag{5.2}$$

from experimental data. M_n is the number of bursts with at least n ISIs and the remark $N^m \geq n$ indicates that the summation is only performed over bursts that include at least

n ISIs. In fig. 5.2F, we can clearly distinguish between the regular and irregular part in the bursts of the isolated neuron. In the former part $\langle T_\mathrm{n} \rangle$ and $\sigma(T_\mathrm{n})$ grow monotonically as functions of n. In contrast, in the irregular part they are approximately constant. Since $\sigma(T_\mathrm{n})$ amounts almost half of $\langle T_\mathrm{n} \rangle$, the nth ISI varies strongly among different bursts. In the connected neuron, $\langle T_\mathrm{n} \rangle$ and $\sigma(T_\mathrm{n})$ become much smaller in the entire burst. Here, we can distinguish between a part of decreasing $\langle T_\mathrm{n} \rangle$ in the beginning of a burst and a part of increasing $\langle T_\mathrm{n} \rangle$ in the bursts' tails.

These properties of the intraburst spike pattern lead to characteristic shapes of the ISI signature, or ISI return map, which is given by the joint probability density $\rho_r(\Delta t_n, \Delta t_{n+1})$ to find a combination of subsequent ISIs. In order to estimate $\rho_r(\Delta t_n, \Delta t_{n+1})$, a normalized histogram of combinations Δt_n and Δt_{n+1} is depicted in figs. 5.2G and 5.2H for the data of the isolated and the connected PD neuron, respectively. Bursts of the isolated neuron start with rather small ISIs, which leads to the red-colored region in fig. 5.2G. In the regular part of the burst ISIs increase, which causes the dark-orange region above the diagonal. In the irregular part, ISIs strongly fluctuate among individual bursts. This part is mapped to the widely-spread orange-colored region. When the PD neuron is connected to the circuit, the ISI signature attains a v-like shape, which is illustrated in fig. 5.2H. The lower branch in the signature is caused by the decrease of ISIs in the beginning of the burst. In the center of the burst ISIs have almost equal lengths. This leads to the region on the diagonal. Finally, the increase of ISIs in the second half of the burst causes the upper branch of the v-like shape. Note that experimental studies have shown that these shapes of the ISI signatures are independent of the particular species of crustaceans [248].

As previously described in section 1.6, many bursters can be modeled as fast-slow bursters. In such bursters, the fast spike-generating subsystem is switched between spiking and resting state by oscillations of a slow dynamics. Applying this approach, characteristics of the intraburst spike pattern in the beginning and in the end of a burst are closely related to the set of bifurcations the fast subsystem undergoes when it switches between the states. Considering all possible bifurcations with codimension one, 16 classes of bursting neurons are possible [125]. In case of the PD neuron, the qualitative differences between the intraburst spiking patterns of the isolated and the connected neuron, presented in the last paragraphs, indicate that the coupling to the circuit causes a change of the bifurcation structure in the fast subsystem. For the isolated PD neuron, it has been found that its ISI signature, shown in fig. 5.2G, can be reproduced by using a fast-slow burster of *Fold-Homoclinic* type [176]. In such bursters the resting-state equilibrium of the fast subsystem vanishes via saddle-node bifurcation (Fold), while the spiking-state disappears via saddle homoclinic orbit bifurcation (Homoclinic). Furthermore, the spike amplitude remains approximately constant during the whole burst and ISIs are almost constant in the beginning of a burst. However, ISIs increase in the burst's tail, when the system approaches the saddle homoclinic orbit bifurcation. The latter can cause highly variable ISIs and other dynamical phenomena presented in ref. [176]. In contrast, in the connected neuron the intraburst spike pattern displays qualitatively different characteristics. Most important, ISIs in the connected neuron decrease

in the beginning of a burst and ISI variability in the burst's tail is reduced. In particular, the decrease of ISIs in the beginning of a burst stays in marked contrast to the ISI statistics in the isolated neuron and indicates a change in the bifurcation structure of the fast subsystem. Applying the classification scheme, presented in section 1.6, only two types of bursters possess comparable characteristics, the *Circle-Circle* burster and the *Circle-Homoclinic* burster, see ref. [125]. *Circle* marks a saddle-node on invariant circle bifurcation leading either to the vanishing of the resting state equilibrium (if stated as first) or to the vanishing of the spiking state limit cycle (if stated as second). In order to switch from *Fold-Homoclinic* bursting to *Circle-Circle* or *Circle-Homoclinic* bursting, due to the connection to the circuit, the PD neuron's fast spike-generating subsystem has to operate in a region of its parameter space, where the bifurcations involved are relatively close to each other.

5.2 Strong electrical coupling in the Morris-Lecar model

The strongest synaptic connection of the PD neuron to the circuit is the electrical coupling between PD and AB. In order to investigate the influence of strong electrical coupling on the bifurcation structure of the fast-spike generating dynamics, we have to go beyond the scope of active rotator models and phase coupling. The reason for this is that these models typically assume that the input from other systems is just a small perturbation to the intrinsic dynamics and, thus, do not account for situations in which the coupling causes significant changes of the dynamics. Therefore, we study electrical coupling in a more-realistic conductance-based neuron model in the following. In particular, we use the Morris-Lecar model as a representative of the fast subsystem in a bursting neuron. However, our qualitative results do not depend on that choice.

The Morris-Lecar model has been introduced in eq. (1.14) in section 1.1. In the presence of electrical coupling to a second neuron, in our case the AB neuron with membrane potential V_{AB}, the Morris-Lecar model becomes

$$\begin{aligned} C\dot{V} &= I - g_L(V - V_{\mathrm{L}}) - g^*_{\mathrm{Ca}} m^{\infty}_{\mathrm{Ca}}(V)(V - V_{\mathrm{Ca}}) - g^*_{\mathrm{K}} m_{\mathrm{K}}(V - V_{\mathrm{K}}) \\ &\quad + g_{\mathrm{coup}}(V_{\mathrm{AB}} - V) \\ \tau_{\mathrm{K}}(V)\dot{m}_{\mathrm{K}} &= m^{\infty}_{\mathrm{K}}(V) - m_{\mathrm{K}}, \end{aligned} \tag{5.3}$$

compare eq. (1.10). V is the membrane potential of the PD neuron and g_{coup} the coupling conductance between the neurons, see fig. 5.2A. All other quantities have been introduced in section 1.1. In particular, in order to reproduce the situation in the AB-PD pacemaker group, we will consider V_{AB} as slow-wave oscillations

$$V_{\mathrm{AB}}(t) = V^0_{\mathrm{AB}} - V^{\mathrm{Amp}}_{\mathrm{AB}} \cos(2\pi\omega_{\mathrm{AB}} t). \tag{5.4}$$

V^0_{AB} is the baseline voltage, $V^{\mathrm{Amp}}_{\mathrm{AB}}$ the amplitude, and ω_{AB} the frequency of the slow-wave oscillations.

Considering eq. (5.3) as the fast subsystem of a bursting neuron, we are mainly interested in the differences between the bifurcation structure of the isolated system

($g_{\text{coup}} = 0$) and that of the system when coupled with coupling strength g_{coup} to the slow wave. For a more detailed analysis, we rewrite eq. (5.3) and obtain a single-neuron description, which accounts for the influence of the coupling by a rescaling of the leak conductance g_{eff} and the applied external current I_{eff}, i.e.

$$\begin{aligned} C\dot{V} &= I_{\text{eff}} - g_{\text{eff}}(V - V_{\text{L}}) - g^*_{\text{Ca}} m^{\infty}_{\text{Ca}}(V)(V - V_{\text{Ca}}) - g^*_{\text{K}} m_{\text{K}}(V - V_{\text{K}}) \\ \tau_{\text{K}}(V)\dot{m}_{\text{K}} &= m^{\infty}_{\text{K}}(V) - m_{\text{K}}. \end{aligned} \tag{5.5}$$

We set $g_{\text{eff}} = g_L + g_{\text{coup}}$ and $I_{\text{eff}} = I - g_{\text{coup}}(V_L - V_{\text{AB}})$. Thus, the electrically-coupled neuron can be interpreted as an isolated neuron with a higher leak conductance g_{eff}, which is subject to an external current I_{eff}. Furthermore, we distinguish between weak coupling $g_{\text{eff}}/g_L \approx 1$, for which the influence of coupling is mainly given by the modulation of the current, and the case of strong coupling, in which g_{coup} contributes significantly to g_{eff}. At this point we should mention that no information about the influence of the coupling on the AB neuron is provided by this approach. $V_{\text{AB}}(t)$ is simply the trace of the second neurons' membrane potential in the connected system and, in case of the AB-PD pacemaker group can be recorded in experiments.

Next, we perform a fast-slow analysis of eq. (5.5) complemented by the slow-wave oscillation, eq. (5.4). Thus, we first consider the dynamics of eq. (5.5) for fixed values of g_{eff} and I_{eff}, i.e. fixed V_{AB}. To this end, we perform a numerical bifurcation analysis of eq. (5.5) using the software AUTO-07p and the included HomCont package [61]. Furthermore, we choose the parameters of the Morris-Lecar model according to ref. [257], which are presented in table 1.1 and consider g_{eff} and I_{eff} as bifurcation parameters. More details on this are given in section 2.5. Later on, we allow for slow oscillations of I_{eff} which give rise to slow-wave bursting.

Results of the bifurcation analysis are illustrated in fig. 5.3A and 5.3B. We have defined parameter regions in which sufficiently-strong oscillations of the slow-wave, eq. (5.4), cause similar types of bursting, as *a*,*b*,*c*, and *d*. For low values of g_{eff} the Morris-Lecar model operates in regime *a*. For small values of I_{eff}, the system possesses one stable equilibrium (equ.) at low membrane potentials, which corresponds to the resting state. Increasing I_{eff} leads to a saddle-node bifurcation at high membrane potentials, which causes the birth of an unstable node and a saddle. These are illustrated in phase portrait I in fig. 5.4A. For sufficiently high I_{eff} the spiking state periodic orbit is born via saddle homoclinic orbit bifurcation and coexists with the resting state for a limited rage of I_{eff}, see fig. 5.4A (IV). A further increase of I_{eff} leads to another saddle-node bifurcation in which the resting state equilibrium annihilates with one of the two other equilibria and the system relaxes to the periodic orbit, which corresponds to the spiking state, see fig. 5.4 (II). As discussed in section 1.4 this bifurcation structure leads to *integrator*-neuron-like behavior with Class 2 excitability. Moreover, if we consider slow oscillations of $V_{\text{AB}}(t)$ as described in eq. (5.4), we obtain slow oscillations of I_{eff} such that

$$I_{\text{eff}} = I_0 - I_{\text{amp}} \cos(2\pi\omega t), \tag{5.6}$$

with $I_0 = I - g_{\text{coup}}(V_{\text{L}} - V^0_{\text{AB}})$, $I_{\text{Amp}} = g_{\text{coup}} V^{\text{Amp}}_{\text{AB}}$, and $\omega = \omega_{\text{AB}}$. If I_{eff} drives the system

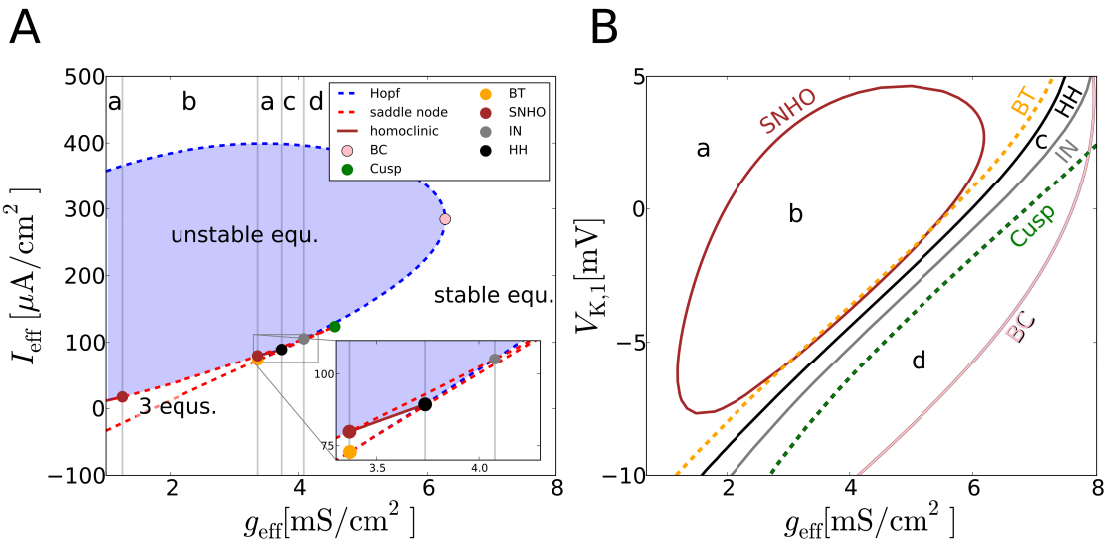

Figure 5.3: Bifurcation structure in the $(g_{\mathrm{eff}}, I_{\mathrm{eff}})$-plane for fixed $V_{\mathrm{K},1} = -5$ mV (A) and the projection of codimension-two bifurcations for different values of I_{eff} on the $(g_{\mathrm{eff}}, V_{\mathrm{K},1})$-plane (B). A: Codimension-one lines and respective codimension-two bifurcations (dots) are shown. Codimension two bifurcation points: saddle-node homoclinic orbit (SNHO, brown), Bogdanov-Takens (BT, orange), and Cusp (green). The points BC and HH mark upper-bounds of g_{eff} for which a spiking state and the homoclinic orbit exist, respectively. The point IN marks the intersection of the Hopf and saddle-node curve. Vertical lines separate regions with different types of bifurcations for the quiescence-spiking and spiking-quiescence transitions, respectively. Those regions are labeled by lower-case letters. Parameter combinations for which the spiking state periodic orbit exists are shown in blue. B: projections of curves of codimension-two bifurcations are shown and indicated by the same colors as dots in A. Dashed lines indicate codimension-two bifurcations that do not separate regions of different combinations of bifurcations.

across the latter saddle-node bifurcation and the saddle homoclinic orbit bifurcation, the Morris-Lecar model will exhibit bursting of Fold-Homoclinic type, see section 1.6. This is illustrated in fig. 5.4A.

Interestingly, the bifurcation structure changes if g_{eff} is increased, for instance because the application of an electrical synapse leads to positive values of g_{coup}. That the coupling of an excitable system to a slow wave can lead to bursting behavior has been found in ref. [69] before, however, as illustrated in fig. 5.3 several codimension-two bifurcations are possible. In the following, we focus on the one that allows for the switching from a Fold-Homoclinic into a Circle-Circle or Circle-Homoclinic burster, since this transition will help us to model the PD neuron. More information on the other changes in the bifurcation structure are given in appendix A.4.1.

Starting in region a, an increase of g_{eff} leads to a *saddle-node homoclinic orbit bifurcation* (SNHO) in which the saddle point of the saddle homoclinic orbit bifurcation, which causes the transition from spiking to resting state, meets the stable resting state equilibrium and undergoes a saddle-node bifurcation. On the right-hand side of the

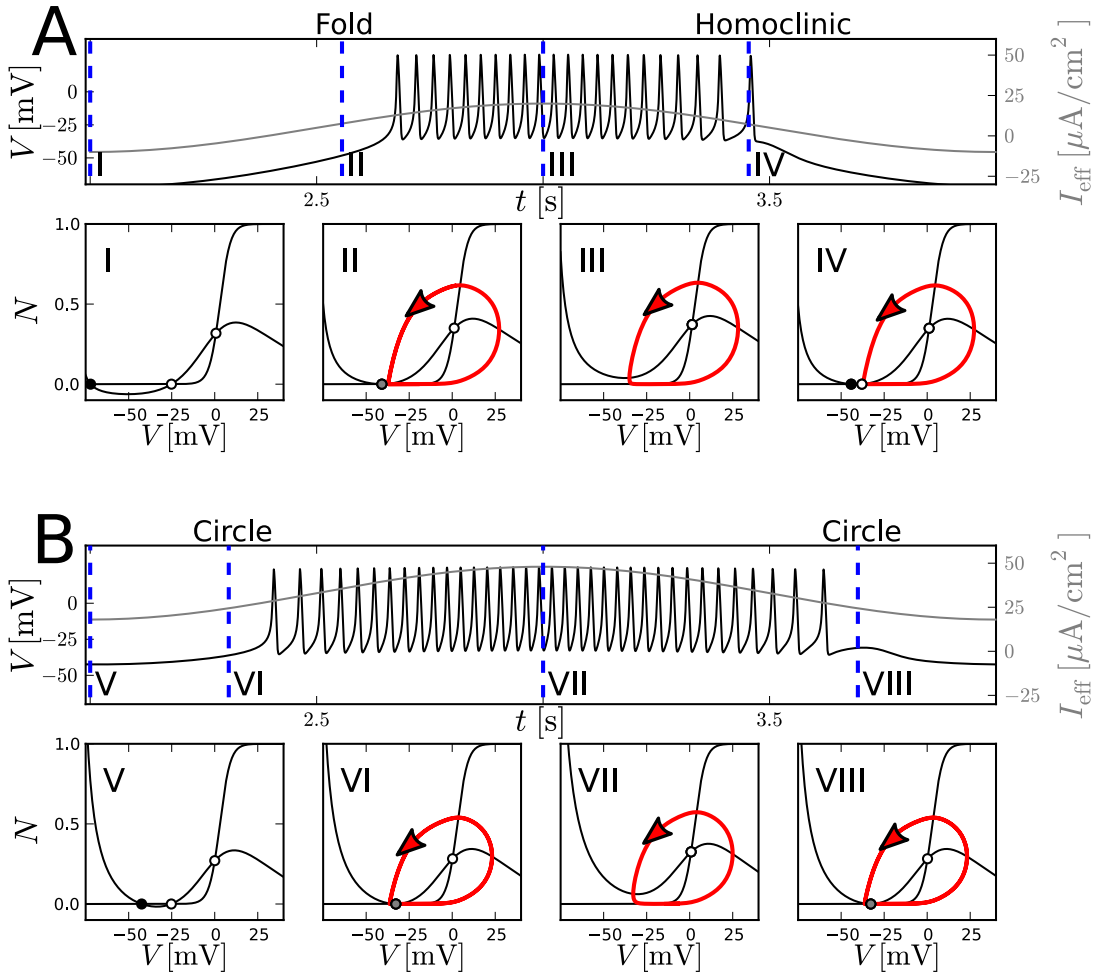

Figure 5.4: Transition from region a to region b in fig. 5.3. Voltage time series for the Fold-Homoclinic burster (A) and the Circle-Circle burster (B) and illustrations of the phase space for fixed external current (I-VIII) that are realized by the oscillating I_{eff} at corresponding times (blue dashed lines) are shown. The phase portraits show stable fixed points (black), unstable fixed points (white), saddle-nodes (gray), periodic orbits (red lines) (in VI and VIII it is an invariant cycle with infinite period), and nullclines (black lines). Directions of motion on the limit cycle are illustrated by red arrows. Values of I_{eff} for the phase portraits (I-VIII) in μA/cm^2: -10, 7.6, 20, 7.17, 18, 24.4, 48, and 24.4. Parameters: $V_{\text{K},1} = -5$ mV, $\omega = 0.5$ Hz, $I_{\text{amp}} = 15$ μA/cm^2; (A): $I_0 = 5$ μA/cm^2, $g_{\text{eff}} = 0.8$ mS/cm^2 and (B): $I_0 = 33$ μA/cm^2, $g_{\text{eff}} = 1.8$ mS/cm^2.

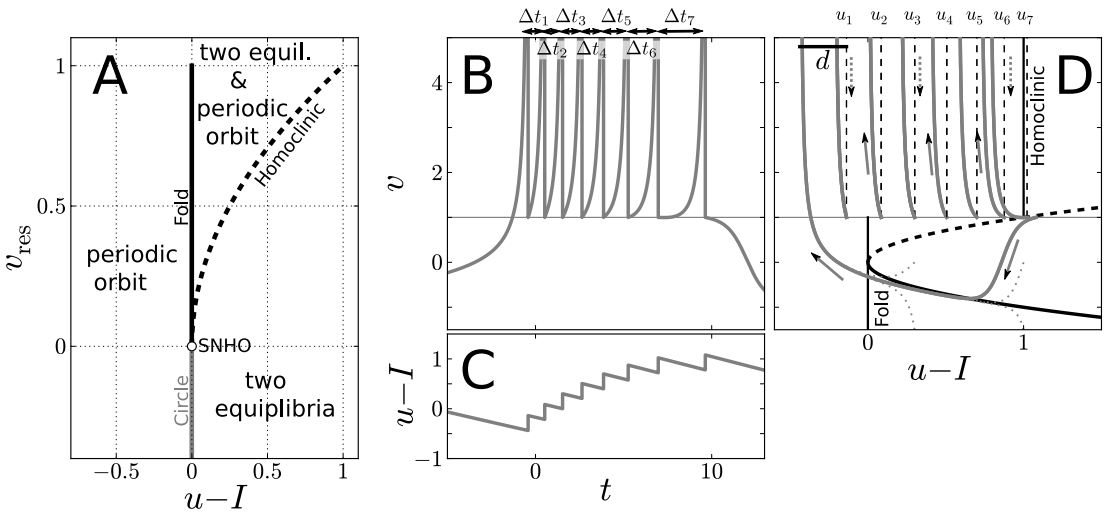

Figure 5.5: Bifurcation diagram of the fast subsystem of eq. (5.7) (A) combined with the reset condition eq. (5.8) and time trace for Fold-Homoclinic bursting (B-D). In particular, time traces of the rescaled membrane potential v (B), the slow variable u (C), and the corresponding trajectory in the phase space (D) are shown. Furthermore, straight arrows indicate the direction of motion and dashed arrows the reset. ISIs and u values at their beginnings are marked as Δt_n and u_n. Dotted lines in D show trajectories for alternative initial conditions to illustrate that the main trajectory (thick gray) is an attractor. Parameters: $I = 10$, $\tau = 120$, $d = 0.3$, $v_{\mathrm{cut}} = 100$ (A-D), and $v_{\mathrm{res}} = 1$ (B-D).

SNHO bifurcation, the system is in region *b*, see fig. 5.3A. In that region, both, the transition from resting to spiking state and the transition from spiking to resting state occur via a saddle-node on invariant circle bifurcation in the Morris-Lecar model, see fig. 5.4 (V-VIII) for corresponding phase portraits. Interestingly, the difference between the phase portraits fig. 5.4 II and fig. 5.4 VI, which show the entering of the spiking state, is mainly the position of the saddle node and the high voltage region of the limit cycle. Thus, the transition from Fold to Circle bifurcation occurs due to a shift of the saddle node to higher voltages. As described in section 1.4, the entering of the spiking state via Circle bifurcation yields an *integrator*-neuron with Class 1 excitability or, for sufficiently-strong oscillating I_{eff}, a Circle-Circle burster. Thus, strong electrical coupling can switch the Morris-Lecar model from Class 2 into Class 1 excitability and, if periodically driven, from a Fold-Homoclinic into a Circle-Circle burster.

These results demonstrate how the class of excitability and type of bursting are affected by strong electrical coupling. Furthermore, in fig. 5.3B we investigate the influence of an additional parameter, $V_{\mathrm{K},1}$, on the observed regions and find that a similar behavior can be observed for a broad range of $V_{\mathrm{K},1}$ values, which indicates the robustness of our results.

5.3 Geometrical modeling of the pyloric dilator neuron

In the vicinity of a SNHO bifurcation we find Fold, Circle, and Homoclinic bifurcations for close sets of parameters. Since these bifurcations cause qualitative shapes in the intraburst spike pattern that are similar to those we have observed in the PD neuron, see section 5.1.1, we now assume that the PD neuron's fast subsystem operates in the vicinity of a SNHO bifurcation. In order to verify this hypothesis, we will investigate the spiking dynamics close to that bifurcation and compare the results with data for the PD neuron.

In order to obtain general results for neurons with fast subsystems that are close to a SNHO bifurcation, we apply the concept of *topological equivalence* [247], which allows for the mapping of any *Fold-Homoclinic* burster with a fast subsystem close to a SNHO bifurcation to the *canonical model* for Fold-Homoclinic bursting:

$$\begin{aligned} \dot{v} &= I + v^2 - u \\ \tau\dot{u} &= -u, \end{aligned} \tag{5.7}$$

with the after-spike reset condition

$$\text{if } v = v_{\text{cut}}, \text{ then } v \to v_{\text{res}} \text{ and } u \to u + d, \tag{5.8}$$

see discussion of such bursters in ref. [125]. All parameters are in dimensionless units. In particular, v is the rescaled membrane potential, u a reduced slow variable, which accounts for a negative spike-triggered feedback current, and I a constant current acting as a bifurcation parameter and, therefore, as an experimentally-applied external current. Furthermore, the slow feedback dynamics is characterized by the time scale separation $\tau \gg 1$ between v and u and $d > 0$, which describes the change of the feedback variable u during one spike. Note that the slow, negative spike-triggered feedback u acts in a similar way on the dynamics, as the negative feedback in the active rotator model, we studied in chapter 3. The voltage cutoff v_{cut} should be set to $+\infty$ for the canonical model, while the reset value v_{res} can be set to one for any positive value of v_{res} by a proper rescaling of the parameters, system variables and time. In simulations any large $v_{\text{cut}} \gg 1$ is appropriate since v runs to infinity in a finite time due to the quadratic term in the voltage dynamics. We set $v_{\text{cut}} = 100$ in all simulations. However, for a better illustration, we show only the range of low v values in the figs. 5.6, 5.8, 5.9, and 5.10.

The first line of eq. (5.7) is the fast subsystem and follows from the geometric reduction in the vicinity of the saddle-node point $(v, u) = (0, I)$, as described section 1.3. This, in combination with the reset condition eq. (5.8), yields the *topological normal form* of the SNHO bifurcation [125]. Since the SNHO bifurcation has codimension two, two bifurcation parameters are required. The first on is the parameter I, in eq. (5.7) $I - u$, and the second one is the reset value of the membrane potential v_{res}. The resulting bifurcation diagram of the fast subsystem ($u = const$) is illustrated in fig. 5.5A. For positive values of $u - I$, two equilibria exist, one stable node and one saddle. Those annihilate for negative v_{res} in a Circle bifurcation, which leads to the emergence of a

stable periodic orbit for negative values of $u - I$. Thus, for negative v_{res}, the system, eqs. (5.7) and (5.8), possesses similar dynamics as the active rotator model with negative feedback, see chapter 3. We will, therefore, focus on positive v_{res}. Then, two equilibria coexist with a stable periodic orbit for $0 < u - I < v_{\mathrm{res}}^2$. The latter appears via a saddle homoclinic orbit bifurcation at $u - I = v_{\mathrm{res}}^2$. At $u - I = 0$ the two equilibria annihilate in a Fold bifurcation. Finally, the SNHO bifurcation occurs for the parameter values $u - I = 0$ and $v_{\mathrm{res}} = 0$.

5.3.1 Deterministic dynamics

Due to the combination of the fast subsystem in eq. (5.7) with the negative spike-triggered feedback u, the canonical model is able to perform Fold-Homoclinic bursting for positive v_{res} and I. A representative trajectory for one burst in the Fold-Homoclinic bursting regime is depicted in fig. 5.5B-D. In the resting state ($u - I > 0$ and $v < v_{\mathrm{res}}$), the system evolves along the stable branch of the v-nullcline, while u relaxes towards zero. Finally, at $u - I = 0$ the stable equilibrium of the fast subsystem vanishes via a Fold bifurcation and v becomes positive. Due to the v^2 term in eq. (5.7), v reaches the cutoff voltage v_{cut} in a finite time. This leads to a spike, which is then followed by the reset $v \to v_{\mathrm{res}}$. Additionally, u is increased by d, which causes positive values of $u - I$ after the first few spikes and the reappearance of the two equilibria in the fast subsystem at $u - I = 0$. For sufficiently large d, the increase of $u - I$ cannot be balanced by the relaxation of u and $u - I$ reaches v_{res}^2. This leads to a saddle homoclinic orbit bifurcation in the fast subsystem and the disappearance of the periodic orbit. Now, right after the reset, the unstable branch of the v-nullcline is crossed, $\dot{v}$ becomes negative and v relaxes to the stable branch of the v-nullcline. This pushes the system back into the quiescence regime.

In order to test whether the canonical model, eqs. (5.7) and (5.8), is able to reproduce the experimentally-observed behavior of the PD neuron, we compare traces of v for different values of the external current parameter I with recordings of the membrane potential of the PD neuron for different strengths of experimentally-applied currents. Figure 5.6 shows trajectories of the canonical model and recordings of the isolated PD neuron. First, for low values of I the canonical model performs regular bursting, i.e. all bursts have similar durations and numbers of spikes. This is illustrated in figs. 5.6A1-4. Similar bursting of the PD neuron is obtained if a negative directed current is applied. Corresponding recordings of the membrane potential are depicted in fig. 5.6A3. Next, for sufficiently high values of I, irregular bursting is observed, see figs. 5.6B1-4. For such bursting, high variations in the duration of bursts and in the number of spikes per burst are present. Similar behavior is found in the isolated PD neuron in the absence of external currents, see statistics in fig. 5.2 and traces of the membrane potential in fig. 5.6B3. Phase space trajectories of the canonical model in fig. 5.6B1-2 show that the irregular bursting arises due to so-called *burstlets*, which can occur when the reset

[4] Data are for experiments on the isolated PD neurons in the Lobster stomatogastric ganglion, which have been performed by Professor Robert C. Elson (Institute for Nonlinear Science, University of California, San Diego, USA). A3: unpublished data; B3: data published in ref. [176].

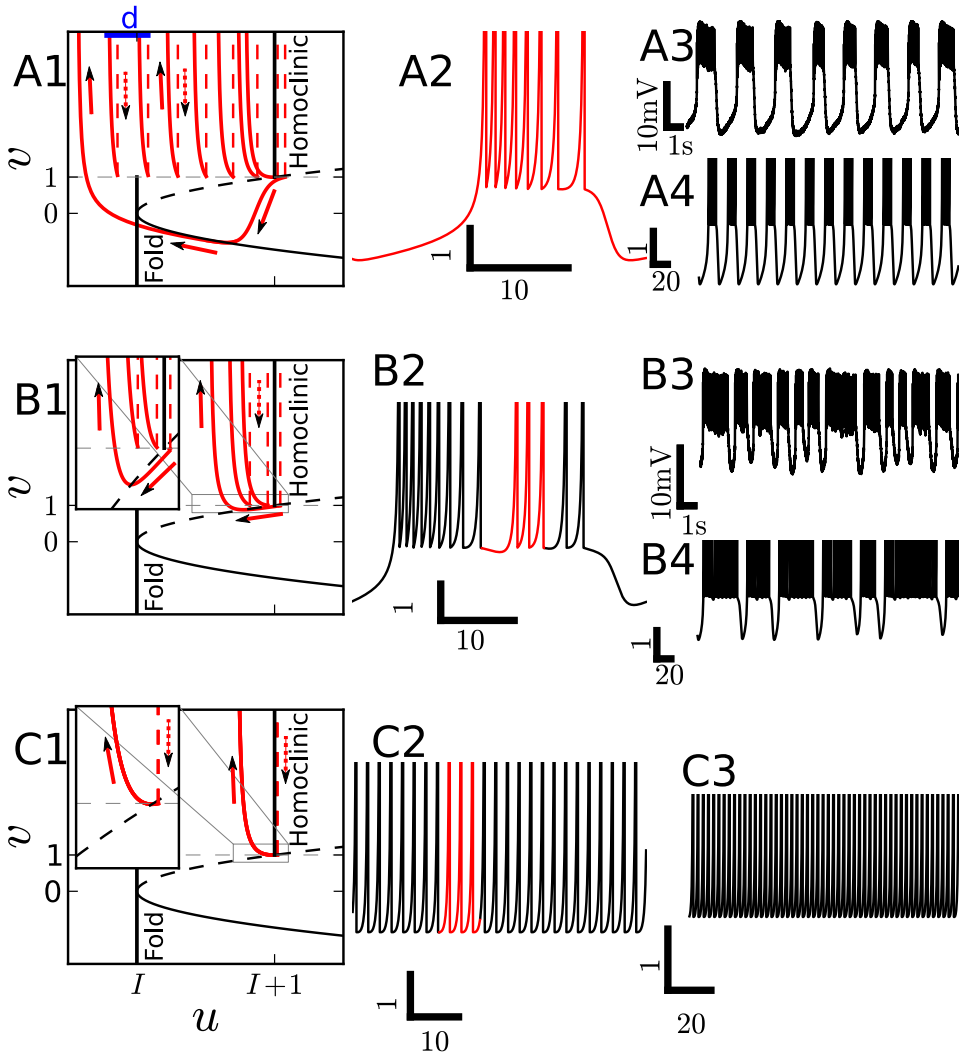

Figure 5.6: Dynamics of the canonical model for different I values compared to experimental data. We find regular busting (A1-A4) ($I = 10$), irregular bursting (B1-B4) ($I = 12.05$), and tonic spiking (C1-C3) ($I = 14$). Similar behavior can be observed experimentally in the isolated PD neuron, when it is subject to a directed current of $I = -2$ nA (A3) or $I = 0$ nA (B3). Furthermore, tonic spiking has been observed in the presence of a positive current, see fig. 3 in ref. [65]. Data for A3 and B3 are obtained from Robert C. Elson [4]. In the phase portraits (A1,B1,C1) straight arrows indicate the direction of motion and dashed arrows the reset. Parts of the voltage time series (A2, B2, C2) that correspond to the trajectories in the phase space (A1,B1,B2) are marked red. Parameters in the canonical model are $d = 0.3$ and $\tau = 120$.

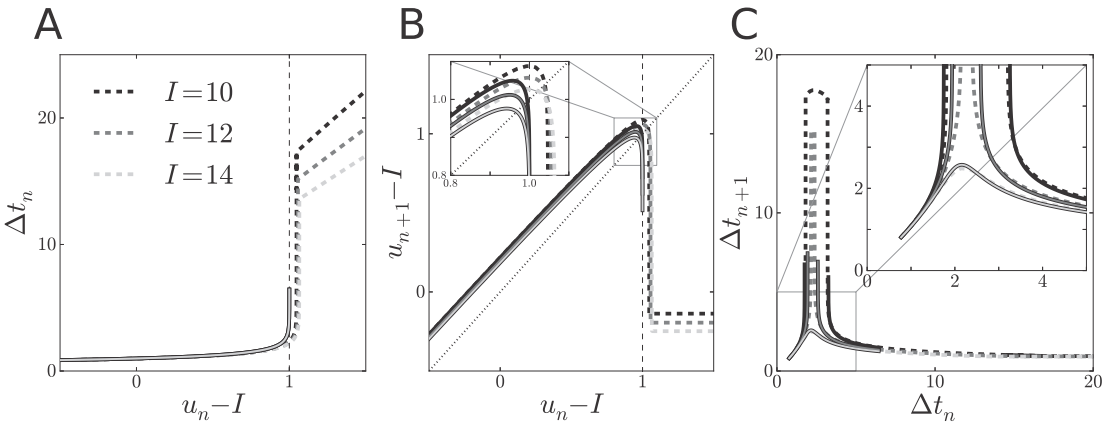

Figure 5.7: $\Delta t_n(u_n)$ (A) and $u_{n+1}(u_n)$ (B) obtained from numerical integration (dashed lines) of eq. (5.7) with Euler integration time step $10^{-9}\tau$ and resulting ISI signature (C). The analytical approximation, eqs. (5.9) and (5.10), are indicated by solid lines for different values of I (grayscale). Parameters: $d = 0.3$, $\tau = 120$.

brings the system close to the unstable branch of the v-nullcline. After the reset, $|\dot{v}|$ and $|\dot{u}|$ are of comparable size. Therefore, the system evolves on trajectories, which follow the unstable branch of the v-nullcline, see fig. 5.6B1 (inset). Finally, the v-nullcline is crossed again and the system reenters the spiking state and produces a short sequence of spikes – a *burstlet* – until it crosses the v-nullcline again due to the reset condition. Burstlets occur preferentially for high values of I. Those shift the saddle homoclinic orbit bifurcation, which occurs at $u = I + 1$, to higher u values. Consequently, since $\dot{u}$ is proportional to u but $\dot{v}$ depends only on $I - u$, the region of $|\dot{u}| \approx |\dot{v}|$ is enlarged and more u values lead to burstlets after the reset. Thus, burstlets occur more often and the bursting becomes more irregular. For even higher values of I the exponential decay of u during a spike can balance the after-spike offset d and the system remains in the spiking state, see fig. 5.6C1-3. All three types of behavior have been observed in the biological PD neuron, see fig. 5.6A3, B3, and fig. 3 in ref. [65] for the spiking state. This indicates that the canonical model for Fold-Homoclinic bursting is able to reproduce the very complex behavior of the biological PD neuron and, thereby, creates some evidence that the PD neuron's fast subsystem indeed operates close to a SNHO bifurcation.

In contrast to complex conductance-based neuron models, the great advantage of the canonical model is that it has only three free parameters[5]: I, τ, and d. Furthermore, it allows for analytical approximations of the interspike intervals. In particular, exact analytical results for the intraburst intervals can be obtained for a slightly different choice of the slow dynamics, which has been intensively studied in refs. [279, 238] and is known as the 'quadratic integrate-and-fire model with recovery variable'. In general, the nth ISI Δt_n solely depends on the value of u at its beginning u_n, see fig. 5.5B and 5.5D.

[5] v_{res} can be set to $v_{\mathrm{res}} = 1$ by rescaling all other parameters and the time and v_{cut} should be set to ∞

Furthermore, due to the reset condition the system is at the point $(v, u) = (v_{\mathrm{res}}, u_n)$ at the beginning of the nth interval. Thus, given the time $T(u)$ the system needs to reach v_{cut} when starting at (v_{res}, u), the nth ISI is given by $\Delta t_n = T(u_n)$ and the full ISI sequence can be constructed from the map

$$\begin{aligned} \Delta t_n &= T(u_n) \\ u_{n+1} &= u_n e^{-\frac{\Delta t_n}{\tau}} + d, \end{aligned} \tag{5.9}$$

for an initial condition $(v(t=0), u(t=0)) = (v_{\mathrm{res}}, u_0)$. The equation for u_{n+1} follows from the integration of the second line of eq. (5.7) and the reset condition eq. (5.8). Note that this approach can be applied to other models of fast-slow bursters too, see refs. [180, 49, 176].

Both, $\Delta t_n(u_n)$ and $u_{n+1}(u_n)$ for different values of the external current are shown in fig. 5.7. The shape of both functions is characteristic for Fold-Homoclinic bursters and consists of three qualitatively different regions, compare with refs. [180, 49, 176]. The first regime, $u_n - I < 1$ represents the regular part of the burst – the part where no burstlets are observed and Δt_n increases monotonically for sufficiently-small values of I. In that part, the slow feedback u builds up. At $u_n - I = 1$ the saddle homoclinic orbit bifurcation occurs in the fast subsystem. Afterwards, in the second regime, $u_n - I \geq 1$, solutions from all initial conditions (v_{res}, u_n) start with negative $\dot{v}$ and, consequently, first evolve along the unstable branch of the nullcline and causes a burstlet or relax towards its stable branch. This leads to rapidly increasing Δt_n and decreasing u_{n+1}. Thus, small variations in u_n can result in highly different Δt_n and u_{n+1}. Furthermore, a fixed point of the map $u_n \to u_{n+1}$ can be observed. A corresponding burstlet is illustrated in fig. 5.6B. In the third regime, Δt_n increases approximately linear with $u_n - I$ while u_{n+1} is approximately constant. All initial conditions in this regime lead to interburst intervals. It is noteworthy that all trajectories in this regime approach the same u_{n+1}, which indicates the presence of an attractor for such trajectories.

Additionally, fig. 5.7 shows the functions $\Delta t_n(u_n)$ and $u_{n+1}(u_n)$ for different values of the external current I. Remarkably, variations of I hardly affect Δt_n in the regular part and decrease u_{n+1} only slightly. In contrast, the decrease is highly pronounced for $u_{n+1} - I \approx 1$ and in the regime of burstlet generation. Furthermore, an increase of I leads to a shift of the fixed point $u_{n+1} = u_n$ towards smaller values of u_n and enlarges the fixed point's basin of attraction. Finally, for sufficiently large values of I, the fixed point attracts trajectories from all initial conditions, which leads to the appearance of the spiking state illustrated in fig. 5.6C1-3. Note that for very high values of I the fixed point can even cross $u_{n+1} - I = 1$.

Plotting $\Delta t_{n+1} = T(u_{n+1})$ as a function of $\Delta t_n = T(u_n)$ for all possible initial values u_n yields all possible points in the deterministic ISI return map. They follow the curve $(T(u_n), T(u_{n+1}(u_n)))^T$ with $u_n \in [u_{\mathrm{Min}}, u_{\mathrm{Max}}]$. Corresponding curves for $u_{\mathrm{Min}} = I - 1$ and $u_{\mathrm{Max}} = I + 2$ and $T(u_n)$ obtained from numerical integration of the system with initial conditions $v(t=0) = v_{\mathrm{res}}$ and $u(t=0) = u_n$ are depicted in fig. 5.7C. Additionally, analytical approximations for the function $T(u)$ in the spiking state can

be obtained from the results presented in ref. [238]. In the reference, the function $T(u)$ has been calculated in the limit $\tau \to \infty$, by integrating the equation for $\dot{v}$ in eq. (5.7) from v_{res} to v_{cut}. This yields

$$T(u) = \begin{cases} \frac{1}{\sqrt{I-u}} \arctan\left(\frac{\sqrt{I-u}(v_{\mathrm{cut}}-v_{\mathrm{res}})}{I-u+v_{\mathrm{res}}v_{\mathrm{cut}}}\right), & u \leq I \\ \frac{1}{2\sqrt{|I-u|}} \log\left(\frac{(v_{\mathrm{cut}}-\sqrt{|I-u|})(v_{\mathrm{res}}+\sqrt{|I-u|})}{(v_{\mathrm{cut}}+\sqrt{|I-u|})(v_{\mathrm{res}}-\sqrt{|I-u|})}\right), & I < u < I + v_{\mathrm{res}}^2 \end{cases}, \quad \tau \to \infty. \tag{5.10}$$

Note that this approach only applies in the regular part of a burst and can be used to approximate u_{n+1} by using eq. (5.10) in eq. (5.9). The resulting approximation of the return map curve $(\Delta t_n, \Delta t_{n+1})^T = (T(u_n), T(u_{n+1}(u_n)))^T$ with $u_n \in [I-1, I+2]$ is shown in fig. 5.7C. Additionally, resulting approximations for Δt_n and u_{n+1} are shown in figs. 5.7A and 5.7B, respectively. The analytical approximation describes the results from simulations well for $u_n - I < 1$. Close to the homoclinic orbit $u_n - I \approx 1$ the analytical $T(u)$ runs to infinity since it does not account for the u dynamics. This leads to deviations from the simulation results. In the deterministic return map curve in fig. 5.7C, we find a large vertical antinode for small values of I, which expresses the observed irregular bursting behavior, since, due to the previously-presented mechanism of burstlet generation, small variations in Δt_n, and thereby small deviations of u_{n+1}, close to the homoclinic orbit can lead to values of Δt_{n+1} of highly different lengths. Note that the approximation, eq. (5.10), does not apply to $u_n > 1$ or, in case of the return map curve, to $u_{n+1} > 1$, which causes the discontinuities in the analytical approximation in fig. 5.7C.

5.3.2 Influence of noise on the intraburst spike pattern

As discussed in the previous section, the canonical model, eqs. (5.7) and (5.8), is capable of describing the different types of spiking behavior observed in the biological PD neuron, i.e. regular bursting, irregular bursting, and tonic spiking. However, the ISI return map shown in fig. 5.2 displays much higher variability of individual ISIs then the deterministic curve in fig. 5.7C, which indicates the presence of noise in the system. In ref. [176] return maps obtained from simulations of noisy conductance-based models were compared to experimental data. Furthermore, possible noise sources were discussed in sec. 1.2. In the following, we add noise to the canonical model eqs. (5.7) and (5.8) and aim at deriving approximations for the ISI statistics. The noisy model reads:

$$\begin{aligned} \dot{v} &= I + v^2 - u \\ \tau \dot{u} &= -u + \sqrt{2D}\xi(t). \end{aligned} \tag{5.11}$$

Furthermore, the after-spike reset condition is given by eq. (5.8). $\xi(t)$ obeys the criteria of white Gaussian noise, i.e. $\langle \xi(t) \rangle = 0$ and $\langle \xi(t)\xi(t') \rangle = \delta(t-t')$. Note that white Gaussian noise is just the simplest way to consider noise in the model and, due to the normal form reduction, cannot be related directly to the biologically-motivated noise terms in conductance-based neuron models. Moreover, we restrict the discussion to

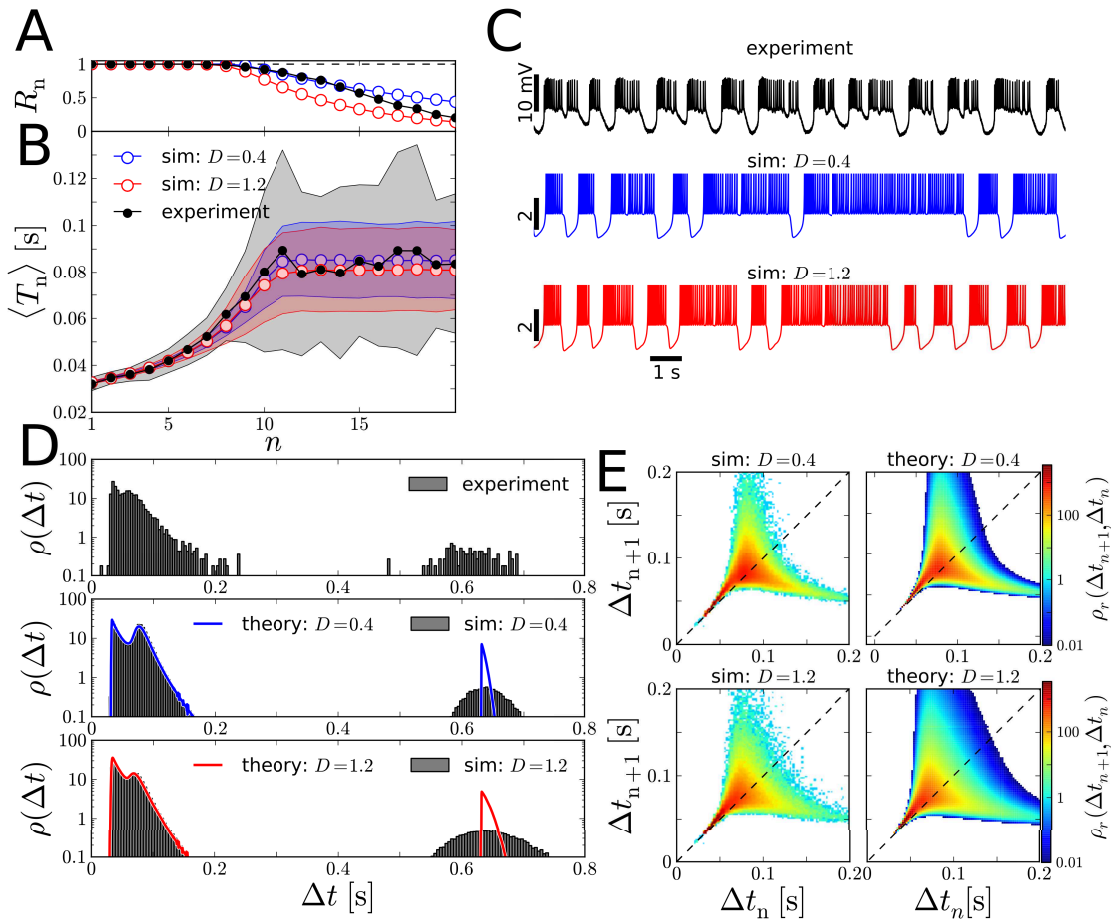

Figure 5.8: Ratio R_n of bursts with at least n ISIs (A), shape of $\langle T_n \rangle$ (B), traces of the (rescaled) membrane potential (C), ISI density (D), and intraburst part of the ISI return maps (E) in logscale obtained from experimental data, simulations and eqs. (5.17) (D) and (5.20) (E), respectively. Parameters of the deterministic system, which are used in simulations and the theory are presented in tab. A.1 and noise intensities are $D = 0.4$ (blue) and $D = 1.2$ (red). Furthermore, the time scale of all simulation results has been rescaled by t_0 in order to fit the time scale of the biological PD neuron, see tab. A.1. Experimental data is the same as for the isolated PD neuron in fig. 5.2. In order to evaluate eqs. (5.17) and (5.20), we discretizes the interval $[I-1, I+2]$ of u_n and u_{n+1} values such that the difference between subsequent u_n, $T(u_n)$, u_{n+1}, and $T(u_{n+1})$ values is smaller than 0.025 (dimensionless units). Then, the transition probability distribution, the stationary probability distribution, the ISI density, $p(\Delta t_{n+1}|\Delta t_n)$, and $\rho_r(\Delta t_{n+1}, \Delta t_n)$ were calculated for the corresponding bins from the discretized versions of eq. (5.13), (5.15), (5.17), (5.19), and (5.20).

white Gaussian noise in the slow variable. In principle, noise can also be added to the v-dynamics, however, such noise is often motivated by massive synaptic input, see sec. 1.2, which is not very plausible in a small neuronal network like the pyloric central pattern generator.

Statistical measures obtained from simulations of the noisy model compared to experimental data are shown in fig. 5.8A and 5.8B. In order to obtain the set of I, d, and τ that fits the data best, we applied the optimization scheme described in appendix A.4.2. This scheme searches for the parameter combinations for which the ISIs of the deterministic model fit the $\langle T_n \rangle$ best. In the absence of noise this choice of parameters pushes the system into the spiking state. However, in the presence of noise the system can cross the unstable branch of the v-nullcline, which leads to irregular bursting behavior comparable to that observed in experiments. Therefore, the noise D strongly affects the shape of R_n, i.e. the ratio of bursts with at least n spikes. In fig. 5.8, we considered two noise intensities, $D = 0.4$ and $D = 1.2$. For $D = 0.4$, we find that the shape of R_n resulting from the data is well-reproduced for the first ≈ 14 ISIs. However, bursts with more ISIs are observed more often than in the experimental data. If the noise intensity is increased, bursts become on average shorter, which results in lower values of R_n in the irregular part, see fig. 5.8A. In both cases, we observe regular and irregular parts in the bursts and corresponding values of $\langle T_\mathrm{n} \rangle$ are close to those observed in simulations, see fig. 5.8B. However, ISIs in the biological neuron show higher variability than that observed in the model neuron, as can be seen in fig. 5.8B. In order to increase the variability in the model, a state-dependent noise may lead to better results. Nevertheless, the model is capable of reproducing both parts of the bursts well.

Next, we investigate the influence of noise in terms of analytical approximations. To this end, we consider the dynamics of the slow variable u first. In the noisy model, u diffuses during individual ISI, which leads to deviations of the actual u_{n+1} from that given by the deterministic map eq. (5.9). In more detail, the dynamics of u during the nth ISI is given by the *Ornstein-Uhlenbeck process*

$$\tau \dot{u} \quad = \quad -u + \sqrt{2D}\xi(t), \quad u(0) = u_n. \tag{5.12}$$

In particular, for large $\tau \gg 1$ the slow variable u changes only slightly during a single ISI and we can assume that individual ISIs Δt_n are still given by the deterministic function $T(u_n)$, which has been illustrated in fig. 5.7A. This assumption is known as a quasistatic approximation and has been used, for instance, in refs. [183, 185, 227] before. In order to investigate the deviations of u_{n+1} from the deterministic value, we consider the transition probability density $p(u, t|u_n, 0)$ to find the value u at time $t > 0$ given u_n at time $t = 0$. For an *Ornstein-Uhlenbeck process* $p(u, t|u_n, 0)$ is a Gaussian distribution with time-dependent mean $M(t, u_n)$ and variance $\sigma^2(t, u_n)$, see appendix A.3.1. Using the results for the transition probability density, presented in eqs. (A.58) and (A.59),

one finds

$$\begin{aligned} p(u,t|u_n,0) &= \frac{1}{\sqrt{2\pi}\sigma(t)} \exp\left(-\frac{(u-M(t,u_n))^2}{2\sigma(t)^2}\right) \\ M(t,u_n) &= u_n\ e^{-\frac{t}{\tau}} \\ \sigma^2(t) &= \frac{D}{\tau}\left(1-e^{-\frac{2t}{\tau}}\right). \end{aligned} \tag{5.13}$$

Thus, including the reset and given the initial state at the beginning of the first ISI $(v,u)=(v_{\mathrm{res}},u_1)$, the distribution of u at the beginning of the nth ISI $p_n(u_n|u_1)$ follows from

$$p_n(u_n|u_1) \approx \int_0^\infty du'\ p(u_n-d,T(u')|u',0)\ p_{n-1}(u'|u_1), \quad p_1(u|u_1)=\delta(u-u_1). \tag{5.14}$$

Furthermore, we can calculate the stationary probability density $p_{\mathrm{eq}}(u)$ from the integral equation:

$$p_{\mathrm{eq}}(u) = \int_0^\infty du'\ p(u-d,T(u')|u',0)\ p_{\mathrm{eq}}(u'). \tag{5.15}$$

Thus, by using the quasistatic approximation, the ISI density $\rho(\Delta t)$ can be approximated, by

$$\rho(\Delta t) \approx \int_0^\infty du' \delta(\Delta t - T(u'))\ p_{\mathrm{eq}}(u'), \tag{5.16}$$

which, after a transformation of the Dirac delta function, leads to

$$\rho(\Delta t) \approx \int_0^\infty du' \frac{\delta(u'-T^{-1}(\Delta t))}{|\partial_u T(T^{-1}(\Delta t))|}\ p_{\mathrm{eq}}(u'). \tag{5.17}$$

$T^{-1}(\Delta t)$ denotes the inverse of the function $T(u)$ evaluated at Δt. Note that for the set of parameters considered, $T(u)$ is strictly increasing, compare fig. 5.7, and, thus, the denominator is larger than zero. $\rho(\Delta t)$ obtained from eq. (5.17) is illustrated in fig. 5.8D. For the theory, we calculated the deterministic ISI $T(u_n)$ from numerical integrations of the deterministic system[6]. In addition, the ISI distribution of the biological neuron and the ISI distribution of the model neuron obtained from simulations are depicted fig. 5.8D. For the latter, we used the parameters obtained from the optimization procedure described in appendix A.4.2. Although, the irregular-bursting PD neuron is described

[6]Initial conditions are (u_n, v_{res}) and integration has been performed until v_{cut} has been crossed. For the numerical integration we used an Euler step of $dt = 10^{-8}\tau$. Afterwards, the results were rescale by t_0, which is given in tab. A.1.

by a very simple model with only one white noise source, its ISI distribution can be reproduced remarkably well. In more detail, the distribution is tri-modal. Its first maximum results from several short ISIs in the beginning of a burst. These ISIs display low variability, which leads to a sharp maximum at short ISIs. During the following ISIs the fluctuations increase and cause the tail, which ends at the second maximum in the distribution. The latter results from ISIs close to, but before, the homoclinic orbit. They occur more often than other ISIs since each burstlet ends with such ISIs. Next, longer intraburst intervals result from the first ISIs of the burstlets and lead to the long tail in the distribution. Finally, the maximum at the right-hand side of the distribution is caused by interburst intervals. The theory, eq. (5.17), well-approximates the intraburst part of the distribution. In particular, we find a remarkable coincidence between simulations of the model and the theory. This indicates that the quasistatic approximation produces only slight deviations for intraburst intervals. However, the lengths of interburst intervals are affected by the diffusion of u. The reason for this is that interburst intervals are comparable to the slow time scale τ and, thus, the diffusion of u has a stronger effect on interburst intervals. In the experimental data, however, we find a larger number of long intervals in the beginning of the burstlets than in the simulations of the model.

Next we consider the ISI return map, see section (1.7.1). In the presence of noise, the ISI return map is given by the joint probability distribution $\rho_r(\Delta t_{n+1}, \Delta t_n)$ and follows from the conditional probability distribution $p(\Delta t_{n+1}|\Delta t_n)$ to find an ISI of length $\Delta t_{n+1} = T(u_{n+1})$ given the length of the previous ISI $\Delta t_n = T(u_n)$ and the ISI density $\rho(\Delta t_n)$. Since ISIs for given u are assumed to be delta distributed, $p(\Delta t_{n+1}|\Delta t_n)$ can be obtained from the inverse $T^{-1}(\Delta t_n)$ of the function $T(u_n)$ by

$$p(\Delta t_{n+1}|\Delta t_n) \approx \int_0^\infty du'' \delta(\Delta t_{n+1} - T(u'')) \int_0^\infty du' \; p(u'', \Delta t_n|u', 0)\delta(u' - T^{-1}(\Delta t_n)). \tag{5.18}$$

Using the definition of Dirac the delta function, transforming the first delta function, and applying eq. (5.13), we immediately get

$$p(\Delta t_{n+1}|\Delta t_n) \approx \frac{\exp\left(-\frac{(T^{-1}(\Delta t_{n+1}) - d - M(\Delta t_n, T^{-1}(\Delta t_n)))^2}{2\sigma(\Delta t_n)^2}\right)}{\sqrt{2\pi}\sigma(\Delta t_n)|\partial_u T(T^{-1}(\Delta t_{n+1}))|}. \tag{5.19}$$

Finally, the ISI return map $\rho_r(\Delta t_{n+1}, \Delta t_n)$ can be approximated as

$$\rho_r(\Delta t_{n+1}, \Delta t_n) \approx p(\Delta t_{n+1}|\Delta t_n)\rho(\Delta t_n). \tag{5.20}$$

Results for the ISI return map are depicted in fig. 5.8E (theory) and compared to estimates of $\rho_r(\Delta t_{n+1}, \Delta t_n)$ obtained from simulations (sim). Here, we find great coincidence between the theory and simulations. Unfortunately for a quantitative comparison with the biological PD neuron, the experimental data does not include enough

spikes (163 bursts with 3007 spikes have been recorded). However, the return maps in fig. 5.8E qualitatively reproduce that of the isolated PD neuron shown in fig. 5.2G.

5.3.3 Influence of slow-wave driving

In the intact circuit, the PD neuron is strongly coupled to the AB neuron, which performs slow-wave oscillations. In order to describe the qualitative influence of electrical coupling on the ISI statistics, we add a coupling term to the noisy model, eq. (5.11). This yields

$$\begin{aligned} \dot{v} &= I + v^2 - u + g_{\mathrm{coup}}(v_{\mathrm{AB}} - v) \\ \tau\dot{u} &= -u + \sqrt{2D}\xi(t). \end{aligned} \tag{5.21}$$

Furthermore, we keep the reset condition eq. (5.8) unaffected. Note that since the coupling is added to the canonical model, we only account for its influence on the dynamics close to the saddle node. However, as we have found before for the Morris-Lecar model in section 5.1.1, the effect of coupling on that region is mainly responsible for the change in the bifurcation structure. In particular, we have observed that the coupling leads to a shift of the saddle node to higher membrane potentials and lets the low-voltage end of the limit cycle almost unaffected, see phase portraits II and VI in fig. 5.4. Therefore, we can neglect its influence on the limit cycle. If the latter would be considered, the values of v_{res} and v_{cut} would become functions of g_{coup}.

In order to understand the influence of the electrical coupling on the dynamics, we can rewrite the first line of eq. (5.21) into

$$\dot{v} = I - u + g_{\mathrm{coup}}(v_{\mathrm{AB}} - \frac{g_{\mathrm{coup}}}{4}) + (v - \frac{g_{\mathrm{coup}}}{2})^2. \tag{5.22}$$

Consequently, the electrical coupling can be described by a change of the external current $I \to I_{\mathrm{eff}} := I + g_{\mathrm{coup}}(v_{\mathrm{AB}} - \frac{g_{\mathrm{coup}}}{4})$, where v_{AB} is the rescaled membrane potential of the AB neuron, and a shift of the saddle-node point to $v_{\mathrm{sn}} = g_{\mathrm{coup}}/2$ and, hence, towards the after-spike reset v_{res}. Considering the bifurcation diagram of the isolated PD neuron, fig. 5.5, this shifts the SNHO bifurcation to the point $g_{\mathrm{coup}}/2 = v_{\mathrm{res}}$ and $I_{\mathrm{eff}} - u = 0$. Thus, g_{coup} acts like a bifurcation parameter and sufficiently strong electrical coupling, i.e. $g_{\mathrm{coup}} > 2v_{\mathrm{res}}$, and strong oscillations of I_{eff} switch the Fold-Homoclinic burster into a Circle-Circle burster. Note that v in the model corresponds to a rescaled membrane potential, thus, the introduction of a linear coupling term is just an approximation of the electrical coupling between both neurons.

In order to account for the slow-wave oscillations of the AB neuron, we consider a slowly-oscillating rescaled membrane potential of the AB neuron, similar to that considered in the Morris-Lecar model before. In particular we use

$$v_{\mathrm{AB}}(t) = v_{\mathrm{AB}}^0 - v_{\mathrm{AB}}^{\mathrm{Amp}} \cos(2\pi\omega_{\mathrm{AB}} t). \tag{5.23}$$

v_{AB}^0 is the baseline voltage $v_{\mathrm{AB}}(t)$, $v_{\mathrm{AB}}^{\mathrm{Amp}}$ the amplitude, and ω_{AB} the frequency of slow-

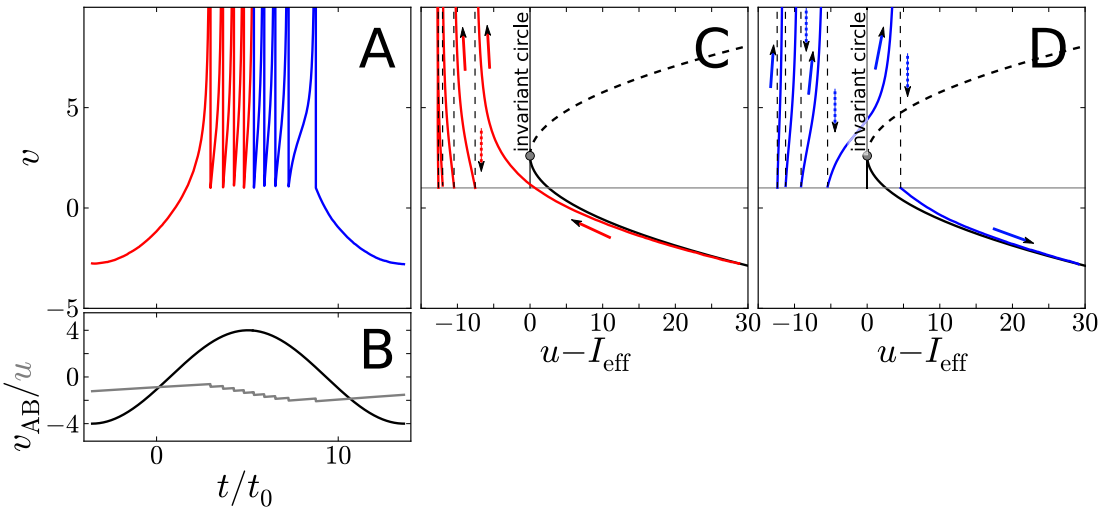

Figure 5.9: Trajectory of the model eq. (5.21) in the regime of Circle-Circle bursting. Voltage-time series (A), time series of u (gray) and v_{AB} (black) (B), and trajectories in phase space during the first (red, (C)) and second part (blue, (D)) are shown. Colors in A indicate the part of the voltage time series corresponding to the trajectories in phase space depicted in C and D, respectively. In the phase portraits (C and D) straight arrows indicate the direction of motion and dashed arrows the reset. Parameters: $g_{coup} = 5.2$, $v_{AB}^{Amp} = 4$, $\omega_{AB} = t_0/6s^2$, and v_{AB}^0. Other parameters are given in tab. A.1.

wave oscillations. Since the membrane-potential oscillations of the biological AB neuron in the intact circuit have higher amplitudes than those of the isolated PD neuron, see for instance ref. [13], we consider $v_{AB}^{Amp} > 1$. A representative trajectory during one burst in the regime of Circle-Circle bursting is illustrated in fig. 5.9A-D. While the decrease of ISIs in the first part of the burst and the increase in the second part can be easily seen in the voltage time series fig. 5.9A, subfigure B shows that the main contribution to oscillations of I_{eff} comes from v_{AB}. Thus, in contrast to the isolated neuron in which the burst duration was controlled by the intrinsic spike-triggered feedback mechanism, the model for the connected neuron in the regime of Circle-Circle bursting is mainly driven by slow-wave oscillations of v_{AB}. Additionally, trajectories in the phase space are illustrated in fig. 5.9C (first part of a burst) and D (second part). As can be seen in the figure, oscillations of I_{eff} drive the system from the resting state ($u - I_{eff} > 0$) to the spiking state ($u - I_{eff} < 0$) and through the saddle-node on invariant circle bifurcation ($u - I_{eff} = 0$)

In the following, we fix the parameters of the isolated PD neuron to the values we obtained from the optimization scheme, see tab. A.1, and the noise intensity to $D = 0.4$, see in fig. 5.8, and study the influence of v_{AB}^{Amp} and g_{coup} on the bursting behavior for fixed $v_{AB}^0 = 0$. This value of v_{AB}^0 corresponds to a scenario in which $v_{AB}(t)$ oscillates around the bifurcation point v_{sn} of the isolated PD neuron. To this end, we investigate several measures of the bursting statistics. In more detail, we study the mean number

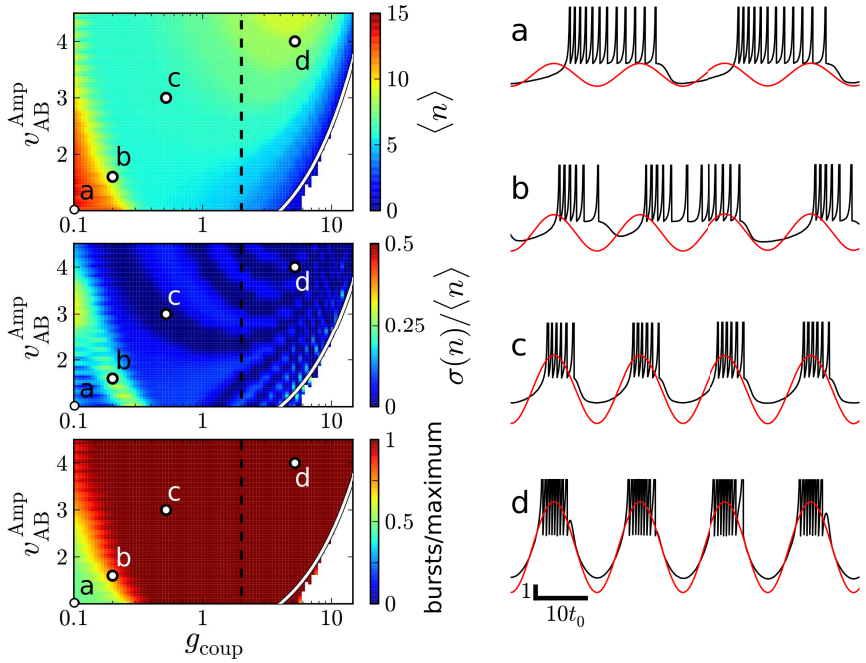

Figure 5.10: Basic burst statistics (left) and voltage time series (right) of the model for the connected neuron. Mean $\langle n \rangle$ and normalized standard deviation $\sigma(n)/\langle n \rangle$ of the number of spikes per burst n and average number of bursts per maximum of slow-wave driving $v_{\mathrm{AB}}(t)$ are shown left. The SNHO bifurcation line (black dashed) and the line of vanishing effective driving at the threshold (white line), see eq. (5.25), are marked. On the right-hand side time series of v (black) and $v_{\mathrm{AB}}(t)$ (red) for parameters $(g_{\mathrm{coup}}, v_{\mathrm{AB}}^{\mathrm{Amp}}) = (0.1, 1)$ (a), $(0.2, 1.6)$ (b), $(0.52, 3)$ (c), and $(5.2, 4)$ (d) are shown. Other parameters are $D = 0.4$, $v_{\mathrm{AB}}^{0} = 0$, $\omega_{\mathrm{AB}} = t_0/6s^2$ and those given in tab. A.1.

of spikes per burst $\langle n \rangle$, the normalized standard deviation of the number of spikes per burst $\sigma(n)/\langle n \rangle$, and the average number of bursts per maximum of the slow-wave driving $v_{\mathrm{AB}}(t)$. Theses statistics for different values of g_{coup} and $v_{\mathrm{AB}}^{\mathrm{Amp}}$ are illustrated in fig. 5.10 (left). Interestingly, several types of qualitatively different behavior can be distinguished. First, for weak coupling and small amplitudes of the slow-wave driving, we find a regime in which bursts of the canonical model and slow-wave oscillations are $2:1$ synchronized, i.e. the burst frequency is half the frequency of the slow-wave driving, see refs. [199, 5]. A corresponding voltage time series is depicted in fig. 5.10a. The dynamics during the spiking state is mainly controlled by the spike-triggered feedback mechanism and even the most-negative value of the slow-wave driving is only able to stop the bursting when the fast dynamics is close to the homoclinic orbit. At the first minimum of the slow-wave driving the system is still far from the homoclinic orbit. However, when the second minimum appears, the feedback has build up and the system is close to the homoclinic orbit and, thus, inhibition during the second minimum of the slow wave is able to end the burst. Increasing the coupling and/or the amplitude of the slow-wave driving leads to a transition to $1:1$ synchronization and the model performs either

regular Fold-Homoclinic bursting, see voltage time series in fig. 5.10c, or Circle-Circle bursting, fig. 5.10d. In both cases, the end of the burst is solely controlled by the slow-wave driving. However, while the negative spike-triggered feedback can be neglected in the Circle-Circle bursting regime, it still determines the length of individual ISIs in case of Fold-Homoclinic bursting. In between the regimes of $2:1$ and $1:1$ synchronization, we find high variability in the number of spikes per burst, i.e. high values of $\sigma(n)/\langle n\rangle$. This results from a stochastic switching between $2:1$ and $1:1$ synchronization and the related numbers of spike per burst, see voltage time series in fig. 5.10b. Interestingly, we find an optimal coupling strength with respect to the number of spikes per burst for fixed $v_{\mathrm{AB}}^{\mathrm{Amp}}$. Furthermore, for high amplitudes of the slow-wave oscillations the optimal coupling strength is beyond that of the SNHO bifurcation ($g_{\mathrm{coup}} = v_{\mathrm{res}}/2$). A further increase of the coupling strength results in less spikes per burst. Finally, the neuron model cannot even generate a single spike per burst in the strong-coupling limit. For such strong coupling, the v-dynamics is dominated by the coupling term and the v^2 term is not able to drive the system towards the cutoff v_{cut}. In order to investigate the end of spiking quantitatively, we study the equation for $\dot{v}$ in eq. (5.22). In order to enter the spiking state, v has to pass the line $v = g_{\mathrm{coup}}/2$. At this line, we find

$$\dot{v} = I + g_{\mathrm{coup}}\left(v_{\mathrm{AB}} - \frac{g_{\mathrm{coup}}}{4}\right) - u\Big|_{v=g_{\mathrm{coup}}/2}. \tag{5.24}$$

The term $I - u$ increases on the slow timescale τ and is close to zero when entering the spiking state. Thus, for a rough estimate of the point at which the system cannot enter the spiking state anymore, we consider the case where the term $g_{\mathrm{coup}}(v_{\mathrm{AB}} - \frac{g_{\mathrm{coup}}}{4})$ vanishes for the maximum driving $v_{\mathrm{AB}}(t) = v_{\mathrm{AB}}^0 + v_{\mathrm{AB}}^{\mathrm{Amp}}$. This yields

$$v_{\mathrm{AB}}^0 + v_{\mathrm{AB}}^{\mathrm{Amp}} = \frac{g_{\mathrm{coup}}}{4}. \tag{5.25}$$

This line is plotted white in fig. 5.10 and well-approximates the strong-coupling limit of spike generation.

Next, we discuss the different bursting regimes with respect to network functionality, i.e. the realization of a robust network rhythm. To this end, the choice of the electrical coupling between AB and PD should ensure: first, that PD bursts are $1:1$ synchronized with those of the AB neuron (corresponding to the maxima of the slow-wave driving eq. (5.23)), second, that a large number of spikes in each burst is realized in order to enhance the synaptic inhibition of the follower neuron LP, see fig. 5.1 for circuit connectivity, and third, that PD bursts display small fluctuations in the number of spikes per burst. As can been seen on the left-hand side of fig. 5.10, all these features are realized in the vicinity of point d and, thus, in the regime of Circle-Circle bursting. Close to that point, the slow-wave driving dominates over both, the intrinsic spike-triggered feedback of the PD neuron, and the noise. Consequently, while the latter causes strong fluctuation of individual ISIs of the isolated neuron, ISIs in the connected neuron show much smaller fluctuations, compare fig. 5.2.

Finally, we investigate the influence of the electrical coupling on the ISI signature of

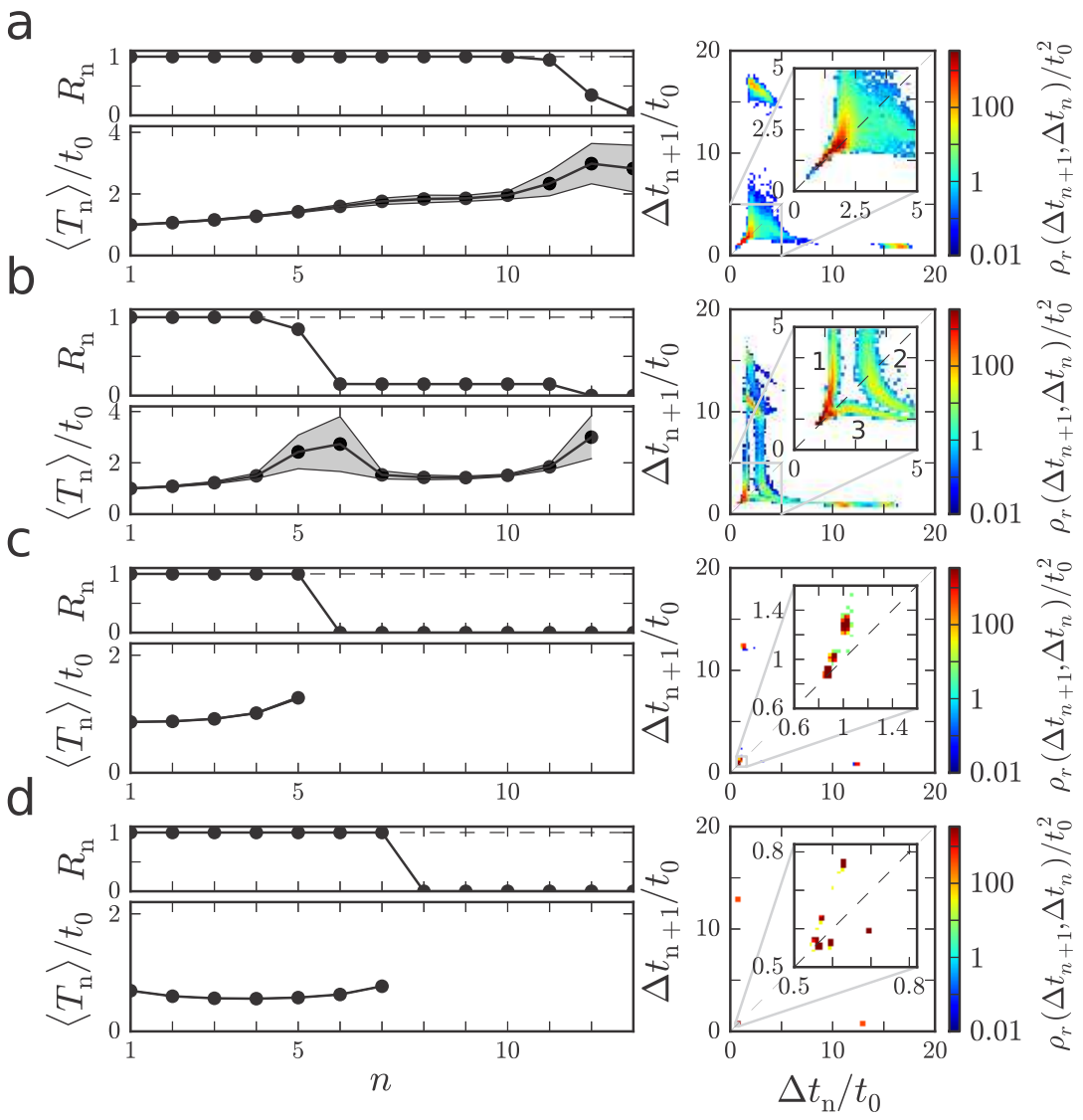

Figure 5.11: Similar statistics as in fig. 5.8A and 5.8B but for the connected neuron model eq. (5.21). For parameter combinations marked as (a-d) in fig. 5.10 obtained from simulations. Insets show the return map of intraburst intervals in higher resolution. Note the different scaling.

the model neuron. The latter is shown in fig. 5.11 together with the measures R_n (ratio of bursts with at least n ISIs) and the average nth ISI $\langle T_n \rangle$ within a burst for the four different types of behavior, which were described in the previous paragraph and marked by lower case letters in fig. 5.10. First, fig. 5.11a illustrates the statistics in the region of 2 : 1 synchronization. We find similar statistics in the first part of the burst as in the regular part of bursts of the isolated neuron, compare fig. 5.8A and 5.8B. In this regime, the slow-wave driving mainly affects the irregular part of the burst, where the system evolves close to the homoclinic orbit, and inhibition during the minima of the slow-wave driving ends the burst and prevents the system from the generation of burstlets.

Next, for the regime of stochastic switching between 2 : 1 and 1 : 1 synchronization, the statistics is illustrated in fig. 5.11b. Here, the statistics of the nth ISI is reminiscent of that of two regular parts of bursts of the isolated model neuron, each consisting of a monotonically increasing $\langle T_\mathrm{n} \rangle$ and increasing variability $\sigma(T_\mathrm{n})$. The shape of R_n shows that most bursts have at least $n \approx 5$ ISIs. At the first minimum of the slow-wave driving, a ratio of bursts ends, while the other bursts perform some long ISIs and stay in the spiking state until the next minimum of the slow-wave driving appears, see voltage-time series in fig. 5.10b. This leads to complex patterns in the ISI signature with several regions with high probability. In particular, the cluster at $\Delta t_\mathrm{n}/t_0 \approx 10$ and $\Delta t_{\mathrm{n}+1}/t_0 \approx 1.5$ and that at $\Delta t_\mathrm{n}/t_0 \approx 1$ and $\Delta t_{\mathrm{n}+1}/t_0 \approx 10$ correspond to the combination of the last ISI and the following interburst interval of bursts that end after the first maximum of the slow-wave driving. In contrast, the cluster at $\Delta t_\mathrm{n}/t_0 \approx 15$ and $\Delta t_{\mathrm{n}+1}/t_0 \approx 1.5$ and the one at $\Delta t_\mathrm{n}/t_0 \approx 1$ and $\Delta t_{\mathrm{n}+1}/t_0 \approx 15$ results from such combinations in bursts that last two maxima of the driving and end after eleven ISIs. Furthermore, there are several regions that possess high probability. Besides the cluster of regular ISIs close to the origin, three tail regions are marked in the inset of the ISI signature in fig. 5.10b. Region 1 corresponds to long ISIs that directly follow short regular ISIs. In that region, we preferentially find the combinations of ISIs (T_4^m, T_5^m) and (T_{11}^m, T_{12}^m) of the mth burst. The first combination is either followed by another long intraburst interval, which leads to a point in region 2, or, similar to the second combination, an interburst interval, which leads to a point above region 2, most likely a point at the right-hand side of the cluster at $\Delta t_\mathrm{n}/t_0 \approx 1$ and $\Delta t_{\mathrm{n}+1}/t_0 \approx 10$. Combinations of ISIs from region 2 are then followed by a regular, short ISI T_7^m. Combinations of long, irregular T_6^m and short, regular T_7^m can be found in region 3 of the ISI signature. For stronger coupling, we find either regular Fold-Homoclinic bursting, which leads to the characteristic increase of ISIs during the burst shown in fig. 5.10c and several clusters above the diagonal in the ISI signature, see fig. 5.11c. Or, similar to the coupled biological PD neuron (compare fig. 5.2H), regular Circle-Circle bursting with decreasing ISIs in the beginning of the burst, leading to clusters below the diagonal in the return map, and increasing ISIs in the bursts' tails, resulting in clusters above the diagonal in the signature, see fig. 5.11d.

5.4 Discussion and outlook

In this chapter, we investigated the isolated and strongly-coupled bursting neurons. In particular we focused on the PD neuron, a slow-wave burster in the pyloric central pattern generator of crustaceans. While its bursting is irregular when synaptic connections are cut, a regular bursting rhythm arises when the PD neuron is electrically-coupled to another neuron in the network, the AB neuron. The AB neuron's membrane potential performs slow-wave oscillations that drive the network rhythm.

By analyzing experimental data, we found that particular characteristics of the ISI sequence during individual bursts alter significantly when the neuron is connected to the circuit. Some of these have been studied in ref. [248]. This indicates that the intrinsic dynamics strongly interacts with input from other neurons in the network. In order to understand how electrical coupling affects the ISI sequence during a burst, we studied strong electrical coupling in a conductance-based neuron model and showed that it acts like a bifurcation parameter and, therefore, can cause qualitative changes in the dynamics. For instance, it can change the excitability class or the type of bursting, which can have serious consequences for the communication with other neurons via synaptic connections [166, 126]. This explains the change of the ISI sequence, which was observed in the data. On the other hand, it shows that strong electrical coupling can significantly alter the dynamics of individual neurons in a network, which may not be accounted for if rather simple models, for instance integrate-and-fire models, are used to describe the individual nodes. This topic is frequently discussed in the literature, see for instance [130, 50, 182, 181].

Our results on strong coupling in conductance-based models give rise to the hypothesis that the isolated PD neuron performs irregular Fold-Homoclinic bursting and that its fast subsystem operates in the vicinity of a codimension-two bifurcation. Vicinity to that bifurcation enabled us to describe the rather complex neuronal dynamics by a two-dimensional neuron model, which is based on the normal form of the bifurcation and, therefore, accounts for general dynamical properties of all neurons that operate close to the bifurcation. This rather geometric type of modeling can be applied to PD neurons in different species of crustaceans, since it is not restricted to a fine-tuned set of parameters. The model is capable of describing the ISI characteristics and dynamical regimes of the PD neuron, which supports our hypothesis. Furthermore, it reproduces the irregular bursting behavior by an interplay of an intrinsic negative spike-triggered feedback mechanism and noise in the vicinity of a homoclinic orbit, which is in accordance with simulation results for noisy conductance-based models [176], and allows for the derivation of analytical approximations for the ISI density and the ISI return map. In principle, these results can be applied to all neuron models with a fast subsystem that is close to the codimension-two bifurcation.

Considering the effect of electrical coupling in the model neuron, we were able to describe the change in the ISI return map and the change of the bursting behavior previously observed in experiments [13]. Furthermore, we investigated the influence of the coupling strength on the bursting characteristics and observed that strong coupling

does not only lead to 1 : 1 synchronization of the PD and AB neuron, but causes optimal bursting with respect to the generation of a robust bursting rhythm in the pyloric central pattern generator. In particular, it reduces the variability of ISIs in the bursts and supports the reciprocal inhibition mechanism, which is responsible for the generation of a robust network rhythm, see for instance [223, 174, 232], by realizing a large number of spikes per burst. These findings show that the presence of strong electrical coupling in the pacemaker group of the pyloric CPG supports network functionality, i.e. the generation of a robust rhythm.

Moreover, the model predicts that synchronization between the electrically-coupled neurons can switch to 2 : 1 synchronization, if the electrical coupling is weakened. This arises due to the interplay of the spike-triggered feedback, which dominates the neuron's behavior in isolation, and the strong coupling to the AB neuron's slow-wave oscillations, which dominates the dynamics in case of strong coupling.

An interesting subject for further research would be a detailed study of strong electrical coupling in two coupled conductance-based neuron models in which experimentally-observed ionic currents are considered. This would, first, allow for the identification of biological mechanisms that contribute to the spike-triggered negative feedback in the simplified model and second, verify our observation of an optimal coupling strength with respect to network functionality.

6 Conclusions

Neurons are excitable systems that are subject to permanent noisy perturbations. Nevertheless, their spike generation has to be most reliable in order to fulfill their biological function, which can be, for instance, the processing of sensory stimuli or the generation of robust rhythms that control muscle contraction. The realization of reliable output is a difficult task, especially, on the level of single neurons or small networks, and an understanding of the underlying mechanisms requires detailed studies of the interplay of noise, complex intrinsic dynamics, and synaptic input. In this thesis, we uncovered possible mechanisms that allow for an enhancement of particular statistical aspects of the spike generation, for instance, for a reduction of spike train variability or for an increase of the firing rate. In particular, we studied the influence of noise on the spike generation in three different setups. Results for the respective setups are given in the following paragraphs.

Noise in adaptive excitable systems

In chapter 3, we studied the influence of noise on the spike generation in an adaptive excitable system. In such systems, the spike generation is shaped by a slow feedback mechanism. The latter causes phenomena like spike-frequency adaptation (negative feedback) or reverse spike-frequency adaptation (positive feedback), which are observed in many neurons. To study the interplay of noise and feedback, we expanded a popular active rotator model by a spike-triggered feedback mechanism. For the resulting two-dimensional neuron model, we could derive analytical approximations for the firing rate and the coefficient of variation.

In section 3.4, we found that it depends significantly on the noise intensity and the type of feedback, whether the interplay of feedback and noise leads to an increase or a reduction of spike train variability. Our studies show that systems with positive feedback show less variability for strong noise, while negative feedback reduces the ISI variability in the presence of weak noise.

Another interesting result, which we obtained in section 3.2, is that strong positive feedback leads to the emergence of a stable limit cycle in the deterministic system and, thereby, causes a coexistence between an oscillatory and an excitable state. This yields a possible explanation for the occurrence of persistent-activity patterns in neurons that are subject to positive feedback due to autaptic coupling [171, 220, 16].

In section 3.3, we found that the interplay of strong positive feedback and noise causes the phenomenon of noise-controlled bistability, which enables an excitable system to change its operation mode from excitable, for weak noise, to oscillatory, for strong noise. For intermediate noise strengths, the system switches between both modes, which, as

we found in section 3.5, leads to giant spike train variability. This kind of behavior is reminiscent of the switching between high and low activity states in cortical networks [113, 105, 110, 96]. In such networks, excitatory coupling between neurons may provide a source of positive feedback that acts on average in a similar way as the positive spike-triggered feedback considered in chapter 3.

Coupled noisy excitable systems

In chapter 4, we studied star networks of noisy excitable systems. The star topology accounts for a situation in which a hub (or central) node is connected to several peripheral nodes. We first focused on the role of the coupling strengths and the number of peripheral nodes on the spike generation.

To this end, we considered coupled active rotator models and started with the simplest case of one central and one peripheral node, which are coupled by directed links. Interestingly, we observed that ISI variability in the system can be minimized by choosing strong coupling, which leads to synchronized spiking, and certain ratios of the respective links' coupling strengths. Furthermore, we derived a single-node representation, which reproduces the statistics of the synchronized spikes. We found that the reduction of variability works best if one node is subject to strong noise and the other one to weak noise. The derived single-node representation can be extended to the presence of spike-triggered feedback in one of the nodes. Moreover, it predicts that all results of chapter 4 can be observed in the strongly-coupled excitable systems for a proper choice of the coupling strengths. Thus, changing the coupling strengths provides the possibility to tune the spike train statistics in coupled neurons.

In section 4.2.3, we considered more peripheral nodes and found that a reduction of variability for strong coupling is still possible and can be described by an extended version of the single-node representation. Interestingly, a second mechanism appears that allows for a further reduction of variability for intermediate coupling strengths for which spikes of the nodes are synchronized, but small fluctuations of their phases are not. Finally, we investigated the influence of the number of peripheral nodes on the ISI statistics in section 4.2.4. We found that ISI variability is minimized for an optimal number of peripheral nodes if the peripherals are subject to strong noise and the central node is in an excitable mode and subject to weak noise. These results show how the structure of networks of excitable systems can be improved in order to reduce variability in the spiking of individual nodes.

Influence of noise and strong coupling on the intraburst spike pattern of bursting neurons

Finally, in chapter 5, we went beyond the active rotator model and consider strongly-coupled bursting neurons in the pyloric central pattern generator of crustaceans. Using experimental data for one of the neurons, the pyloric dilator neuron, we observed qualitative differences between the intraburst spike patterns of the isolate neuron, which performs irregular bursting, and that of the strongly-coupled neuron, which bursts reg-

ularly, in section 5.1. Since these changes are induced by the strong coupling to the circuit, we investigated such coupling in a conductance-based neuron model in section 5.2.

Our analysis showed that the coupling conductance acts like a bifurcation parameter in the model and strong coupling can change the bifurcation structure. Thereby, strong coupling can alter fundamental properties of the neuron, for instance, the excitability class or the type of bursting. Since the bifurcation structure is closely related to the ISI statistics, the application of strong coupling allows for a change of several aspects of the ISI statistics.

These results point out that electrical coupling between neurons can have a strong influence on the dynamics, which has to be accounted for in studies of electrically-coupled neurons. Furthermore, we used these finding to derive a minimal model for the pyloric dilator neuron, which we studied in section 5.3. With help of this model, we were able to identify an interplay of a negative spike-triggered feedback mechanism and noise as the source of the irregular bursting of the isolated pyloric dilator neuron. Moreover, we uncovered different possibilities to regularize the bursting. First, the application of a constant negative current and second, as it is realized in the biological circuit, strong electrical coupling to a slow-wave driving. By investigating the latter one in the minimal model, we found that strong electrical coupling does not only regularize the bursting, but also ensures a high number of spikes per burst, which supports the generation of a robust network rhythm in the central pattern generator. These results give some insight in the role of the strong electrical synapse in the pacemaker group of the pyloric CPG.

A Appendix

A.1 Supplement to chapter 1

A.1.1 Derivation of the relation between asymptotic Fano factor and ISI statistics

In order to derive eq. (1.74), we first relate the spike count variability, as quantified by the Fano factor, to the low frequency limit of the spike train power spectrum eq. (1.56)[1]. To this end, we first express the spike count variance

$$\mathrm{Var}(N(T)) = \langle (N(T) - \langle N(T) \rangle)^2 \rangle$$

by the spike train auto correlation function $c(t)$ eq. (1.54). Using the definition of the spike count eq. (1.57) and interchanging integration and averaging, we obtain for stationary spike trains

$$\begin{aligned} \mathrm{Var}(N(T)) &= \langle \int_{t_k}^{t_k+T} dt_1 \; (x(t_1) - \langle x(t) \rangle) \int_{t_l}^{t_l+T} dt_2 \; (x(t_2) - \langle x(t) \rangle) \rangle \\ &= \int_0^T dt_1 \int_0^T dt_2 \; c(t_2 - t_1) = \int_0^T dt_2 \int_{t_2-T}^{t_2} d\tau \; c(\tau). \end{aligned}$$

Here we set the starting point of the time intervals to zero and used that $c(\tau) = c(-\tau)$. Changing the parametrization of the integration area yields

$$\mathrm{Var}(N(T)) = \int_0^T d\tau \; c(\tau) \left(\int_\tau^T dt_2 - \int_0^{T+\tau} dt_2 \right) = 2T \int_0^T d\tau \; \left(c(\tau) - c(\tau) \frac{\tau}{T} \right).$$

Since the auto correlation function approaches zero for large τ, the integrand is dominated by the first term in the limit of long time windows $T \to \infty$. Thus, by applying eq. (1.56), the spike count variance can be related to the low frequency limit of the power spectrum,

$$\lim_{T\to\infty} \mathrm{Var}(N(T)) = \lim_{T\to\infty} 2T \int_0^T d\tau \; c(\tau) \left(1 - \frac{\tau}{T} \right) = \lim_{T\to\infty} 2T \int_0^T d\tau \; c(\tau) = TS(0).$$

[1] Professor Benjamin Lindner (Institut für Physik, Humboldt-Universität zu Berlin, Berlin, Germany), personal communication, April 17, 2012

This, in combination with the approximation of the spike count in long time windows eq. (1.58) yields the asymptotic Fano factor

$$F_\infty := \lim_{T\to\infty} F(T) = \lim_{T\to\infty} \frac{\mathrm{Var}(N(T))}{\langle N(T)\rangle} = \frac{S(0)}{r}. \tag{A.1}$$

In the next step, we derive a relation between $S(0)$ and the coefficient of variation. To this end, we first consider a renewal statistics, in which the serial correlation coefficients vanish, eq. (1.68), for all lags, i.e. $\rho_l = 0$, $l > 0$. In this case, the spike train power spectrum eq. (1.56) can be evaluated using the spike train autocorrelation function eq. (1.55) and eq. (1.67). Since the Fourier transformation of the Dirac delta distribution is a constant, one finds

$$S(f) = r\left(1 + \sum_{k=1}^{\infty} \tilde{\rho}_k(f) + \tilde{\rho}_k(f)^\dagger\right), \quad f > 0. \tag{A.2}$$

$\tilde{g}(f)$ denotes the Fourier transformation of a function $g(t)$ and $z^\dagger$ the complex conjugation of z. Furthermore, it follows from eq. (1.66) that $\tilde{\rho}_k(f) = \tilde{\rho}(f)^k$ for renewal processes. Since the ISI density is normalized and positive, $\tilde{\rho}(f) < \tilde{\rho}(0) = 1$ for $f > 0$, and the sum over $\tilde{\rho}(f)^k$ can be simplified using a geometric series. This yields

$$\begin{aligned} S(f) &= r\left(1 + \sum_{k=1}^{\infty} \tilde{\rho}(f)^k + \tilde{\rho}(f)^{k\dagger}\right) \\ &= r\left(-1 + \sum_{k=0}^{\infty} \tilde{\rho}(f)^k + \tilde{\rho}(f)^{k\dagger}\right) \\ &= r\left(-1 + \frac{1}{1-\tilde{\rho}(f)} + \left[\frac{1}{1-\tilde{\rho}(f)}\right]^\dagger\right) \\ &= r\frac{1-|\tilde{\rho}(f)|^2}{|1-\tilde{\rho}(f)^2|}, \quad f > 0, \text{ renewal.} \end{aligned} \tag{A.3}$$

Furthermore, in order to obtain the low frequency limit, we consider the Fourier transformation of the ISI density $\tilde{\rho}(f)$

$$\tilde{\rho}(f) = \int_{-\infty}^{\infty} dt\ \rho(t) e^{I2\pi f t}. \tag{A.4}$$

I is the imaginary unit. This implies for the moments of the ISI density that

$$\langle \Delta t^n \rangle = \frac{1}{(2\pi i)^n} \left.\frac{\partial^n \tilde{\rho}(f)}{\partial f^n}\right|_{f=0}. \tag{A.5}$$

Expanding $\tilde{\rho}(f)$ for low-frequencies $f \ll 1$ in a Taylor series up to second order, we can express the low-frequency limit by the moments of the ISI density. The resulting

low-frequency limit for the spike train power spectrum of a renewal process reads

$$\lim_{f\to 0} S(f) = rC_V, \quad \text{renewal.} \tag{A.6}$$

In order to generalize this result to nonrenewal processes, we use the connection of the low-frequency limit of the power spectrum to the asymptotic Fano factor, which was presented in eq. (A.1). In case of a renewal process, we can apply eq. (A.6) and obtain

$$F_\infty = C_V^2, \quad \text{renewal.} \tag{A.7}$$

However, in order to obtain the asymptotic Fano factor for a nonrenewal process, we introduce the counting process $N_k(T)$, which counts all sets of k subsequent spikes. Consequently, every kth order ISI, $N_k(T)$ is increased by one. Furthermore, the (single) spike count $N(T)$ can be related to $N_k(T)$ by

$$N(T) \approx kN_k(T) + \delta N, \quad 0 \le \delta N < k. \tag{A.8}$$

Next, we can calculate the mean spike count $\langle N(T)\rangle = k\langle N_k(T)\rangle$ and its variance $\mathrm{Var}(N(T)) = k^2\mathrm{Var}(N_k(T))$ in the limit $k \to \infty$. Thus, the Fano factor of $N_k(T)$ is given by

$$F_k(T) \approx \frac{1}{k}F(T) = \frac{\mathrm{Var}(N_k(T))}{\langle N_k(T)\rangle}, \quad k \gg 1. \tag{A.9}$$

The corresponding interspike interval statistics is that of the kth order ISIs from the original process. Assuming that correlations between the kth order ISIs vanish for large k, we can apply eq. (A.7) to the Fano factor of $N_k(T)$ and obtain

$$\lim_{T\to\infty} F_k(T) = \frac{1}{k}F_\infty = C_{V,k}^2 = \frac{\mathrm{Var}(\Delta_k t)}{\langle \Delta_k t\rangle^2}, \quad k \gg 1. \tag{A.10}$$

Applying eqs. (1.70) and (1.71), we can transform the asymptotic Fano factor of the kth-spike count into that of the single-spike count for a large k:

$$F_\infty = C_{V,k}^2 = \frac{k^2C_V^2\left(1 + 2\sum_{l=1}^{k-1}(1-\frac{l}{k})\rho_l\right)}{k^2}, \quad k \gg 1. \tag{A.11}$$

Finally, performing the limit of $k \to \infty$, which can be done since as T goes to infinity the number of spikes for finite firing rates goes to infinity as well, we obtain eq. (1.74).

A.1.2 Formular for the ISI variance in the active rotator model

In order to obtain the simplified result for the ISI variance, eq. (1.108), out of eq. (1.107), we follow appendix A of ref. [212] and define the 2π periodic function

$$\tilde{I}_+(x) := \frac{1}{D} e^{\frac{U(x)}{D}} \int_{-\infty}^{x} dy\; e^{-\frac{U(y)}{D}} = \frac{e^{\frac{U(x)}{D}} \int_{x-2\pi}^{x} dy\; e^{-\frac{U(y)}{D}}}{D(1 - e^{-\frac{2\pi\omega_0}{D}})}. \tag{A.12}$$

The second relation follows from eq. (1.105). This yields for the mean ISI

$$\langle \Delta t \rangle = \int_0^{2\pi} dx\; \tilde{I}_+(x). \tag{A.13}$$

For the second moment, eq. (1.107), one obtains

$$\langle \Delta t^2 \rangle = \frac{2}{D} \int_0^{2\pi} dx\; e^{\frac{U(x)}{D}} \int_{-\infty}^{x} dx'\; e^{-\frac{U(x')}{D}} \int_{x'}^{2\pi} dx''\; \tilde{I}_+(x''). \tag{A.14}$$

Next, splitting up the range of integration in the integral over x'' yields

$$\langle \Delta t^2 \rangle = \frac{2}{D} \int_0^{2\pi} dx\; e^{\frac{U(x)}{D}} \int_{-\infty}^{x} dx'\; e^{-\frac{U(x')}{D}} \int_{x'}^{x} dx''\; \tilde{I}_+(x'') + R, \tag{A.15}$$

with R given by

$$\begin{aligned} R &= \frac{2}{D} \int_0^{2\pi} dx\; e^{\frac{U(x)}{D}} \int_{-\infty}^{x} dx'\; e^{-\frac{U(x')}{D}} \int_{x}^{2\pi} dx''\; \tilde{I}_+(x'') \\ &= 2 \int_0^{2\pi} dx\; \tilde{I}_+(x) \int_x^{2\pi} dx''\; \tilde{I}_+(x''). \end{aligned} \tag{A.16}$$

Since $x \geq 0$, the last integral can be represented as an integral over $x'' \in [0, 2\pi]$ minus an integral over $x'' \in [0, x]$. The former yields the squared mean ISI. Thus, one finds for R:

$$\begin{aligned} R &= 2\langle \Delta t \rangle^2 - 2 \int_0^{2\pi} dx\; \tilde{I}_+(x) \int_0^{x} dx''\; \tilde{I}_+(x'') \\ &= 2\langle \Delta t \rangle^2 - \underbrace{2 \int_0^{2\pi} dx\; \tilde{I}_+(x'') \int_{x''}^{2\pi} dx\; \tilde{I}_+(x)}_{=R}. \end{aligned} \tag{A.17}$$

This yields

$$R = \langle \Delta t \rangle^2. \tag{A.18}$$

Using this in eq. (A.15), it follows for the ISI variance

$$\mathrm{Var}(\Delta t) = \langle \Delta t^2 \rangle - \langle \Delta t \rangle^2 = \frac{2}{D} \int_0^{2\pi} dx \; e^{\frac{U(x)}{D}} \int_{-\infty}^{x} dx' \; e^{-\frac{U(x')}{D}} \int_{x'}^{x} dx'' \; \tilde{I}_+(x''). \tag{A.19}$$

Next, one can interchange the order of the integrations over x' and x'' and obtain

$$\mathrm{Var}(\Delta t) = 2 \int_0^{2\pi} dx \int_{-\infty}^{x} dx'' \; e^{\frac{U(x)-U(x'')}{D}} (\tilde{I}_+(x''))^2. \tag{A.20}$$

Since $\tilde{I}(x'')$ is 2π periodic, a similar calculation as in eq. (1.105) yields

$$\mathrm{Var}(\Delta t) = \frac{2}{(1 - e^{-\frac{2\pi\omega_0}{D}})} \int_0^{2\pi} dx \int_{x-2\pi}^{x} dx'' \; e^{\frac{U(x)-U(x'')}{D}} (\tilde{I}_+(x''))^2. \tag{A.21}$$

Considering the integrand

$$f(x, x'') := e^{\frac{U(x)-U(x'')}{D}} (\tilde{I}_+(x''))^2 \tag{A.22}$$

and the fact that $U(x)$ is a tilted periodic potential, one finds that

$$f(x, x'') = f(x + 2\pi, x'' + 2\pi). \tag{A.23}$$

Next, we switch the order of the integration in eq. (A.21) and obtain

$$\mathrm{Var}(\Delta t) = 2 \frac{\int_0^{2\pi} dx \int_{x-2\pi}^{x} dx'' f(x, x'')}{(1 - e^{-\frac{2\pi\omega_0}{D}})} = 2 \frac{\int_0^{2\pi} dx'' \int_{x''}^{2\pi} dx \; f(x, x'') + \int_{-2\pi}^{0} dx'' \int_{0}^{2\pi+x''} dx \; f(x, x'')}{(1 - e^{-\frac{2\pi\omega_0}{D}})}. \tag{A.24}$$

Considering eq. (A.23), the integration region of the second integral can be shifted by 2π and one obtains

$$\mathrm{Var}(\Delta t) = 2 \frac{\int_0^{2\pi} dx \int_{x-2\pi}^{x} dx'' f(x, x'')}{(1 - e^{-\frac{2\pi\omega_0}{D}})} = 2 \frac{\int_0^{2\pi} dx'' \int_{x''}^{x''+2\pi} dx \; f(x, x'')}{(1 - e^{-\frac{2\pi\omega_0}{D}})}. \tag{A.25}$$

Finally, inserting eq. (A.22) and (A.12) yields the result presented in eq. (1.108).

A.2 Supplement to chapter 3

A.2.1 Series expansion for mean ISI and ISI variance

In order to derive a series expansion for eq. (3.29), we first set $w := \omega_0 + \overline{\omega}^{\mathrm{fp}}$ and consider the potential $U(x, w) = -wx - \cos(x)$. This yields

$$\langle \Delta t \rangle \approx \frac{\int_0^{2\pi} dx\ e^{-\frac{wx+\cos(x)}{D}} \int_{x-2\pi}^{x} dy\ e^{\frac{wy+\cos(y)}{D}}}{D\left(1 - e^{-\frac{2\pi\omega}{D}}\right)}. \tag{A.26}$$

In order to derive a series expansion for the integrals, we first consider integrals of the type

$$\int_a^b dx\ e^{\pm\frac{wx+\cos(x)}{D}}.$$

a and b are real numbers with $a < b$. Using a series for the exponential with the cosine argument, we obtain.

$$\int_a^b dx\ e^{\pm\frac{wx+\cos(x)}{D}} = \sum_{k=0}^{\infty} \frac{1}{k!} \left(\pm\frac{1}{D}\right)^k \int_a^b dx\ \cos^k(x) e^{\pm\frac{wx}{D}}. \tag{A.27}$$

Furthermore, the cosine can be rewritten using the trigonometric identity

$$\cos^k(\alpha) = \frac{1}{2^k} \sum_{m=0}^{k} \binom{k}{m} \cos(q_{km}\alpha), \tag{A.28}$$

which yields for the integral

$$\int_a^b dx\ e^{\pm\frac{wx+\cos(x)}{D}} = \sum_{k=0}^{\infty} \frac{1}{k!} \left(\pm\frac{1}{2D}\right)^k \sum_{m=0}^{k} \binom{k}{m} \int_a^b dx\ \cos(q_{km}x) e^{\pm\frac{wx}{D}}. \tag{A.29}$$

Here, we introduce $q_{km} := k - 2m$. In general, such integrals can be solved by using integration by parts and the solution reads

$$\int_a^b dy\ \cos(c(y-d)) e^{\pm\frac{wy}{D}} = \frac{D}{w^2 + c^2D^2} \left(e^{\pm\frac{bw}{D}} \left(\pm w \cos(c(d-b)) + cD \sin(c(b-d))\right) \right.$$
$$\left. - e^{\pm\frac{a\omega}{D}} \left(\pm w \cos(c(d-a)) + cD \sin(c(a-d))\right) \right). \tag{A.30}$$

Applying this to eq. (A.29) yields

$$\int_a^b dx\ e^{\pm\frac{wx+\cos(x)}{D}} = \sum_{k=0}^{\infty}\frac{1}{k!}\left(\pm\frac{1}{2D}\right)^k\sum_{m=0}^{k}\binom{k}{m}\frac{D}{w^2+q_{km}^2D^2}\times$$
$$\times\left(e^{\pm\frac{bw}{D}}\left(\pm w\cos(q_{km}b)+q_{km}D\sin(q_{km}b)\right)\right.$$
$$\left.-e^{\pm\frac{aw}{D}}\left(\pm w\cos(q_{km}a)+q_{km}D\sin(q_{km}a)\right)\right). \tag{A.31}$$

Thus, for the second integral in eq. (A.26), we find

$$\int_{x-2\pi}^{x} dy\ e^{\frac{wy+\cos(y)}{D}} = \sum_{k=0}^{\infty}\frac{1}{k!}\left(\frac{1}{2D}\right)^k\sum_{m=0}^{k}\binom{k}{m}\frac{D\left(1-e^{\frac{-2\pi w}{D}}\right)}{w^2+q_{km}^2D^2}\times$$
$$\times e^{\frac{wx}{D}}\left(w\cos(q_{km}x)+q_{km}D\sin(q_{km}x)\right). \tag{A.32}$$

Using this in the original integral equation for the mean ISI, eq. (A.26), we obtain

$$\langle\Delta t\rangle \approx \sum_{k=0}^{\infty}\frac{1}{k!}\left(\frac{1}{2D}\right)^k\sum_{m=0}^{k}\binom{k}{m}\frac{\int_0^{2\pi}dx\ e^{\frac{-\cos(x)}{D}}\left(w\cos(q_{km}x)+q_{km}D\sin(q_{km}x)\right)}{w^2+q_{km}^2D^2}. \tag{A.33}$$

While the integral over the sinus term vanishes, the integral over the cosine can be rewritten as a modified Bessel function of the first kind $I_n(x)$, by using the integral representation

$$I_n(z) = \frac{1}{\pi}\int_0^{\pi} dx\ e^{z\cos(x)}\cos(nx). \tag{A.34}$$

n is an integer and z an arbitrary, in general complex number. Using this in eq. (A.33), the periodicity of the cosine, and that the cosine is an even function, one obtains

$$\langle\Delta t\rangle \approx \sum_{k=0}^{\infty}\frac{1}{k!}\left(\frac{1}{2D}\right)^k\sum_{m=0}^{k}\binom{k}{m}\frac{2\pi w I_{q_{km}}\left(-\frac{1}{D}\right)}{w^2+q_{km}^2D^2}. \tag{A.35}$$

Finally, since $I_n(x) = I_{|n|}(x)$ for integer arguments and $\binom{k}{m} = k!/m!(k-m)!$ the series expansion eq. (3.32) follows from simple algebraic transformations.

Next, we consider the ISI variance eq. (3.39). Applying eq. (A.31) and (A.32), the three latter integrals in eq. (3.39) can be written in terms of coupled series, which leads

to

$$\begin{aligned}\mathrm{Var}(\Delta t) \;&\approx\; 2D\sum_{\substack{i=0\\j=0\\k=0}}^{\infty}\frac{(-1)^k}{i!j!k!}\sum_{l=0}^{i}\binom{i}{l}\sum_{m=0}^{j}\binom{j}{m}\sum_{n=0}^{k}\binom{k}{n}\int_0^{2\pi}dx\; e^{-\frac{\cos(x)}{D}}\\ &\times\quad\left(\frac{1}{2D}\right)^{i+j+k}\frac{\Big(\cos(q_{il}x)+q_{il}\frac{D}{w}\sin(q_{il}x)\Big)}{w^3(1+q_{il}^2\frac{D^2}{w^2})(1+q_{jm}^2\frac{D^2}{w^2})(1+q_{kn}^2\frac{D^2}{w^2})}\\ &\times\quad\left(\cos(q_{jm}x)+q_{jm}\frac{D}{w}\sin(q_{jm}x)\right)\left(\cos(q_{kn}x)-q_{kn}\frac{D}{w}\sin(q_{kn}x)\right)\end{aligned}$$

Expanding the last three factors results in cubic terms of sinus and cosine functions, which can be simplified to sums of simple cosine and sinus terms, using trigonometric identities. Then, as described before, the integrals of the sinus terms vanishe, while the others can be represented by modified Bessel functions, by using eq. (A.34). This results into

$$\begin{aligned}\mathrm{Var}(\Delta t) \approx{}& \frac{2\pi D}{w^3}\sum_{\substack{i=0\\j=0\\k=0}}^{\infty}\frac{(-1)^k}{i!j!k!}\left(\frac{1}{2D}\right)^{i+j+k}\sum_{l=0}^{i}\binom{i}{l}\sum_{m=0}^{j}\binom{j}{m}\sum_{n=0}^{k}\binom{k}{n}\times\\ &\times\frac{1}{2(1+q_{il}^2\frac{D^2}{w^2})(1+q_{jm}^2\frac{D^2}{w^2})(1+q_{kn}^2\frac{D^2}{w^2})}\times\\ &\left(\left(1+\frac{D^2}{w^2}(-q_{il}q_{jm}+q_{jm}q_{kn}-q_{il}q_{kn})\right)I_{(q_{il}+q_{jm}-q_{kn})}\left(-\frac{1}{D}\right)\right.\\ &+\left(1+\frac{D^2}{w^2}(q_{il}q_{jm}-q_{jm}q_{kn}+q_{il}q_{kn})\right)I_{(-q_{il}+q_{jm}+q_{kn})}\left(-\frac{1}{D}\right)\\ &+\left(1+\frac{D^2}{w^2}(q_{il}q_{jm}+q_{jm}q_{kn}-q_{il}q_{kn})\right)I_{(q_{il}-q_{jm}+q_{kn})}\left(-\frac{1}{D}\right)\\ &\left.+\left(1+\frac{D^2}{w^2}(-q_{il}q_{jm}-q_{jm}q_{kn}-q_{il}q_{kn})\right)I_{(q_{il}+q_{jm}+q_{kn})}\left(-\frac{1}{D}\right)\right).\end{aligned}\tag{A.36}$$

In particular, in the strong noise limit $D\to\infty$ only the summand $i=j=k=0$ survives and yields the strong noise behavior

$$\mathrm{Var}(\Delta t)\approx\frac{4\pi D}{w^3},\quad D\gg 1.\tag{A.37}$$

A.2.2 Weak-feedback approximation for mean ISI and ISI variance

Starting from eq. (A.35), or, alternatively from eq. (3.32), a weak feedback approximation can be derived by setting $w\to\omega_0(1+\epsilon)$. Here, $\epsilon:=\overline{\omega}^{\mathrm{fp}}/\omega_0\ll 1$ is a small parameter. As can be seen in eq. (A.35), the feedback dependence of the individual

summands is given by the factor

$$\frac{\omega}{w^2+q_{km}^2D^2} \approx \frac{\omega_0}{\omega_0^2+q_{km}^2D^2} + \left(\frac{\omega_0}{\omega_0^2+q_{km}^2D^2} - \frac{2\omega_0^3}{(\omega_0^2+q_{km}^2D^2)^2}\right)\epsilon. \tag{A.38}$$

The right-hand side shows a first order Taylor expansion with respect to the small parameter. Furthermore, adding the zero $+2\omega_0D^2q_{km}^2 - 2\omega_0D^2q_{km}^2$ in the nominator of the most-right term leads to

$$\frac{\omega}{w^2+q_{km}^2D^2} \approx \frac{\omega_0}{\omega_0^2+q_{km}^2D^2} + \left(-\frac{\omega_0}{\omega_0^2+q_{km}^2D^2} - \frac{2\omega_0D^2(k-2m)^2}{(\omega_0^2+q_{km}^2D^2)^2}\right)\epsilon. \tag{A.39}$$

The latter representation has the advantage that the second term is zero whenever $k=-2m$, in particular for $k=m=0$. Applying, this to eq. (A.35) leads to

$$\langle\Delta t\rangle \approx \langle\Delta t\rangle_{\epsilon=0} - \langle\Delta t\rangle_{\epsilon=0}\epsilon + \frac{2\pi}{\omega_0}B(D,\omega_0)\epsilon. \tag{A.40}$$

The function $B(D,\omega_0)$ is given by the infinite series

$$B(D,\omega_0) = \sum_{k=1}^{\infty}\left(\frac{1}{2D}\right)^k \sum_{m=0}^{k} \frac{2(k-2m)^2 I_{|k-2m|}\left(-\frac{1}{D}\right)}{m!(k-m)!\left(1+\frac{D^2}{\omega_0^2}(k-2m)^2\right)\left(\frac{\omega_0^2}{D^2}+(k-2m)^2\right)}. \tag{A.41}$$

Here, the summand with $k=0$ is zero. Using the relation between average feedback and mean ISI, eq. (3.27), one finds that $\epsilon = 2\pi a/\omega_0\langle\Delta t\rangle \approx 2\pi a/\omega_0\langle\Delta t\rangle_{\epsilon=0} + \mathcal{O}(\epsilon)$ and considering only first order terms, one , finally, arrives at the weak-feedback approximation given in eq. (3.33).

A similar approach can be applied for the variance eq. (A.36). In particular, setting $w \to \omega_0(1+\epsilon)$ the individual summands become

$$f_{iljmkn}(\epsilon) = \frac{\pi D}{\omega_0^3(1+\epsilon)^3} \frac{\sum_{p=1}^{4}\left(1+\frac{D^2}{\omega_0^2(1+\epsilon)^2}A_p^{iljmkn}\right) I_{B_p^{iljmkn}}\left(-\frac{1}{D}\right)}{Q^{il}(\epsilon,\omega_0)Q^{jm}(\epsilon,\omega_0)Q^{kn}(\epsilon,\omega_0)} \tag{A.42}$$

At this point, we introduced

$$\begin{aligned}
A_1^{iljmkn} &= -q_{il}q_{jm} + q_{jm}q_{kn} - q_{il}q_{kn} \\
A_2^{iljmkn} &= q_{il}q_{jm} - q_{jm}q_{kn} + q_{il}q_{kn} \\
A_3^{iljmkn} &= q_{il}q_{jm} + q_{jm}q_{kn} - q_{il}q_{kn} \\
A_4^{iljmkn} &= -q_{il}q_{jm} - q_{jm}q_{kn} - q_{il}q_{kn}
\end{aligned} \tag{A.43}$$

and

$$\begin{aligned} B_1^{iljmkn} &= q_{il} + q_{jm} - q_{kn} \\ B_2^{iljmkn} &= -q_{il} + q_{jm} + q_{kn} \\ B_3^{iljmkn} &= q_{il} - q_{jm} + q_{kn} \\ B_4^{iljmkn} &= q_{il} + q_{jm} + q_{kn}. \end{aligned} \tag{A.44}$$

Furthermore, we set

$$Q^{ab}(\epsilon, \omega_0) = \left(1 + q_{ab}^2 \frac{D^2}{\omega_0^2 (1+\epsilon)^2}\right). \tag{A.45}$$

Next, we perform a Taylor expansion of the individual summands in eq. (A.42) with respect to ϵ. Then, the terms up to first order read

$$f_{iljmkn}(\epsilon) \approx f_{iljmkn}(0) + \left(-3 f_{iljmkn}(0) + \frac{2D^2}{\omega_0^2} G_{iljmkn}(\omega_0, D)\right)\epsilon, \tag{A.46}$$

with

$$\begin{aligned} G_{iljmkn}(\omega_0, D) = \frac{\pi D}{\omega_0^3} (& \frac{\sum_{p=1}^{4} \left(-A_p^{iljmkn}\right) I_{B_p^{iljmkn}}\left(-\frac{1}{D}\right) \left(Q^{il}(0,\omega_0) Q^{jm}(0,\omega_0) Q^{kn}(0,\omega_0)\right)}{\left(Q^{il}(0,\omega_0) Q^{jm}(0,\omega_0) Q^{kn}(0,\omega_0)\right)^2} \\ & + \frac{\sum_{p=1}^{4} \left(1 + \frac{D^2}{\omega_0^2} A_p^{iljmkn}\right) I_{B_p^{iljmkn}}\left(-\frac{1}{D}\right)}{\left(Q^{il}(0,\omega_0) Q^{jm}(0,\omega_0) Q^{kn}(0,\omega_0)\right)^2} \times \\ & \times \Big(q_{il}^2 (0,\omega_0) Q^{jm}(0,\omega_0) Q^{kn}(0,\omega_0) + q_{jm}^2 Q^{il}(0,\omega_0) Q^{kn}(0,\omega_0) + q_{kn}^2 Q^{il}(0,\omega_0) Q^{jm}(0,\omega_0) \Big)). \end{aligned} \tag{A.47}$$

In particular, on finds that $G_{000000}(\omega_0, D) = 0$, since $A_p^{000000} = 0$, $q_{00} = 0$, and $Q^{00}(0, \omega_0) = 1$. Furthermore, in order to study the strong noise behavior of $G_{iljmkn}(\omega_0, D)$, we introduce

$$\tilde{Q}^{ab}(\omega_0) = \left(\frac{1}{D^2} + \frac{q_{ab}^2}{\omega_0^2}\right), \tag{A.48}$$

which has a well defined strong noise limit of $\lim_{D\to\infty} \tilde{Q}^{ab}(\omega_0) = \frac{q_{ab}^2}{\omega_0^2}$. This yields

$$G_{iljmkn}(\omega_0, D) = \frac{\pi}{\omega_0^3 D^5} \left(\frac{\sum_{p=1}^{4} \left(-A_p^{iljmkn}\right) I_{B_p^{iljmkn}}\left(-\frac{1}{D}\right) \left(\tilde{Q}^{il}(\omega_0)\tilde{Q}^{jm}(\omega_0)\tilde{Q}^{kn}(\omega_0)\right)}{\left(\tilde{Q}^{il}(\omega_0)\tilde{Q}^{jm}(\omega_0)\tilde{Q}^{kn}(\omega_0)\right)^2} \right.$$
$$+ \frac{\sum_{p=1}^{4} \left(\frac{\omega_0^2}{D^2} + A_p^{iljmkn}\right) I_{B_p^{iljmkn}}\left(-\frac{1}{D}\right)}{\left(\tilde{Q}^{il}(\omega_0)\tilde{Q}^{jm}(\omega_0)\tilde{Q}^{kn}(\omega_0)\right)^2} \times$$
$$\left. \times \left(\frac{q_{il}^2}{\omega_0^2}\tilde{Q}^{jm}(\omega_0)\tilde{Q}^{kn}(\omega_0) + \frac{q_{jm}^2}{\omega_0^2}\tilde{Q}^{il}(\omega_0)\tilde{Q}^{kn}(\omega_0) + \frac{q_{kn}^2}{\omega_0^2}\tilde{Q}^{il}(\omega_0)\tilde{Q}^{jm}(\omega_0) \right) \right). \tag{A.49}$$

Considering, the first order approximation of the summands, eq. (A.46), in the full equation for the variance, eq. (A.36), yields eq. (3.40), with

$$C(D, \omega_0) = \sum_{\substack{i=0 \\ j=0 \\ k=0}}^{\infty} \frac{(-1)^k}{i!j!k!} \left(\frac{1}{2D}\right)^{i+j+k} \sum_{l=0}^{i} \binom{i}{l} \sum_{m=0}^{j} \binom{j}{m} \sum_{n=0}^{k} \binom{k}{n} G_{iljmkn}(w, D). \tag{A.50}$$

ISI variance at strong noise

In order to obtain the strong noise behavior of eq. (A.50), we consider the first summands $G_{iljmkn}(w, D)$. At first, for $i = j = k = 0$, all q are zero and therefore $G_{iljmkn}(w, D) = 0$. Next, if either i, j, or k is one and the others are zero, we find that all A_p^{iljmkn} are zero and the B_p^{iljmkn} are either one or minus one. Furthermore, only one q is nonzero. considering eq. (A.49) and that $I_{\pm 1}(-1/D) \propto 1/D$, yields that the highest order of $G_{iljmkn}(w, D)$ is $1/D^4$. Due to the term $\left(\frac{1}{2D}\right)^{i+j+k}$, other combinations of i, j, k yield lower orders. Thus, $C(D, \omega_0)$ is of order $1/D^5$ and the corresponding term in eq. (3.40) can be neglected for strong noise.

A.3 Supplement to chapter 4

A.3.1 PDF of Ornstein-Uhlenbeck process

The time-dependent transition probability distribution $p(x, t|x_0, 0)$ associated with a Ornstein-Uhlenbeck process

$$\tau\dot{x} = -x + \sqrt{2D}\xi(t), \quad x(0) = x_0, \tag{A.51}$$

which we obtained in eq. (4.12) and (5.12) follows from the Fokker-Planck equation, see section 1.8:

$$\partial_t p = \frac{1}{\tau}\partial_x(x\ p) + \frac{D}{\tau^2}\partial_x^2 p. \tag{A.52}$$

Note that we suppressed the arguments of $p(x,t|x_0,0)$. Additionally, the initial condition is given by

$$p(x,0|x_0,0) = \delta(x - x_0). \tag{A.53}$$

Equation (A.52) can be solved using the Fourier transformation

$$\tilde{f}(k) = \int_{-\infty}^{\infty} dx\ e^{-Ikx} f(x). \tag{A.54}$$

I is the imaginary unit. Transformation of eq. (A.52) yields

$$\partial_t \tilde{p} + \frac{k}{\tau}\partial_k \tilde{p} = -\frac{D}{\tau^2}k^2\tilde{p} \tag{A.55}$$

and the Fourier-transformation of the initial condition

$$\tilde{p}_0 = e^{-Ikx_0}. \tag{A.56}$$

The left-hand side of eq. (A.55) can be interpreted as the total derivative of $\tilde{p}$ along the curve $k(t) = k_0 e^{\frac{t}{\tau}}$, which yields the condition

$$\frac{d}{dt}\tilde{p} = \partial_t\tilde{p} + \frac{\partial k}{\partial t}\partial_k\tilde{p} = \partial_t\tilde{p} + \frac{k}{\tau}\partial_k\tilde{p}. \tag{A.57}$$

On this curve eq. (A.55) can be integrated and we find

$$\begin{aligned} \frac{d\tilde{p}}{dt} &= -\frac{D}{\tau^2}k_0^2 e^{\frac{2t}{\tau}}\tilde{p} \\ \Longrightarrow \tilde{p} &= \tilde{p}_0 e^{-\frac{Dk_0^2}{2\tau}\left(e^{\frac{2t}{\tau}}-1\right)}. \end{aligned}$$

Considering the initial condition, eq. (A.56), results in

$$\begin{aligned} \tilde{p} &= e^{-Ik_0x_0 - \frac{Dk_0^2}{2\tau}\left(e^{\frac{2t}{\tau}}-1\right)} \\ \Longrightarrow \tilde{p} &= e^{-Ix_0ke^{-\frac{t}{\tau}} - \frac{Dk^2}{2\tau}\left(1-e^{-\frac{2t}{\tau}}\right)} \\ &= e^{-IkM(t,x_0) - \frac{k^2}{2}\sigma^2(t,x_0)}, \end{aligned}$$

which is the Fourier transformation of a Gaussian with mean $M(t, x_0)$ and standard deviation $\sigma(t, x_0)$. Thus, the time-dependent transition probability distribution is given by

$$p(x, t|x_0, 0) = \frac{1}{\sqrt{2\pi}\sigma(t)} e^{-\frac{(x-M(t,x_0))^2}{2\sigma(t)^2}}, \tag{A.58}$$

with

$$\begin{aligned} M(t, x_0) &= x_0\ e^{-\frac{t}{\tau}} \\ \sigma^2(t) &= \frac{D}{\tau}\left(1 - e^{-\frac{2t}{\tau}}\right). \end{aligned} \tag{A.59}$$

A.3.2 Calculation of correlation function

Starting from the definition of $\eta(t)$ eq. (4.15), we aim at calculating the correlation function $\langle \eta(t)\eta(t')\rangle$. Considering eq. (4.15), the correlation function is given by

$$\begin{aligned} \langle \eta(t)\eta(t')\rangle = \Bigg\langle &\left(\sqrt{2D_\theta}\xi_\theta(t) - \kappa_\theta \int_{-\infty}^{t} dt_1\ e^{\kappa_+(t_1-t)}\sqrt{2D_-}\xi_-(t_1)\right) \\ &\left(\sqrt{2D_\theta}\xi_\theta(t') - \kappa_\theta \int_{-\infty}^{t'} dt_2\ e^{\kappa_+(t_2-t')}\sqrt{2D_-}\xi_-(t_2)\right)\Bigg\rangle. \end{aligned} \tag{A.60}$$

This results in the following terms

$$\begin{aligned} \langle \eta(t)\eta(t')\rangle =& 2D_\theta\langle \xi(t)\xi(t')\rangle \\ &- \sqrt{2D_\theta}\sqrt{2D_-}\kappa_\theta \int_{-\infty}^{t} dt_1\ e^{\kappa_+(t_1-t)}\langle \xi_\theta(t')\xi_-(t_1)\rangle \\ &- \sqrt{2D_\theta}\sqrt{2D_-}\kappa_\theta \int_{-\infty}^{t'} dt_2\ e^{\kappa_+(t_2-t')}\langle \xi_\theta(t)\xi_-(t_2)\rangle \\ &+ 2D_-\kappa_\theta^2 \int_{-\infty}^{t} dt_1 \int_{-\infty}^{t'} dt_2\ e^{\kappa_+(t_1-t)}e^{\kappa_+(t_2-t')}\langle \xi_-(t_1)\xi_-(t_2)\rangle. \end{aligned} \tag{A.61}$$

Next, considering eq. (4.9), one finds that $\langle\sqrt{2D_\theta}\xi_\theta(t)\sqrt{2D_-}\xi_-(t')\rangle = 2D_\theta\delta(t-t')$. Furthermore, using the delta-like correlations of the white Gaussian noises, we find

$$\begin{aligned} \langle \eta(t)\eta(t')\rangle &= 2D_\theta\delta(t-t') - 2D_\theta\kappa_\theta e^{-\kappa_+|t-t'|} \\ &+ 2D_-\kappa_\theta^2 \int_{-\infty}^{t} dt_1 \int_{-\infty}^{t'} dt_2\ e^{\kappa_+(t_1-t)}e^{\kappa_+(t_2-t')}\delta(t_1-t_2). \end{aligned} \tag{A.62}$$

The double integral can be evaluated by considering the cases $t > t'$ and $t < t'$, respectively. Finally, we obtain

$$\begin{aligned}\langle \eta(t)\eta(t')\rangle &= 2D_\theta \delta(t-t') - 2D_\theta \kappa_\theta e^{-\kappa_+|t-t'|} \\ &+ 2D_- \frac{\kappa_\theta^2}{2\kappa_+} e^{-\kappa_+|t-t'|}. \end{aligned} \tag{A.63}$$

Using $D_- = D_\theta + D_\phi$ yields the result presented in eq. (4.16).

A.4 Supplement to chapter 5

A.4.1 Bursting in electrically-coupled Morris-Lecar model

Besides the transition from Fold-Homoclinic to Circle-Circle burster, other transitions are possible. For instance, if we start in regime b in fig. 5.3A and increase g_{eff}, a *saddle-node homoclinic orbit bifurcation* occurs and transforms the regime b back into a regime with the same bifurcations sequence as in regime a.

A qualitative change in the dynamics occurs when the low I_{eff} saddle-node curve meets the Andronov Hopf curve in a Bogdanov-Takens bifurcation, see fig. 5.3A (inset). For higher values of g_{eff}, the system is in regime c and an increase of I_{eff} leads to the following dynamics: first only the resting state equilibrium exists, then an additional stable and an unstable equilibrium are born via saddle-node bifurcation, and third, the stable one of those becomes unstable in an Andronov Hopf bifurcation leading to the birth of the spiking state limit cycle. Then, the resting state equilibrium annihilates with one of the unstable equilibria in a saddle-node bifurcation. Thus, the transition to the spiking state is the same as in region a. However, once the system has reached the limit cycle it remains there, even for decreasing I_{eff}. Finally, the periodic orbit vanishes via Hopf bifurcation. Thus, the bursting is of Fold-Hopf type. Phase portraits and voltage time series for Fold-Homoclinic and Fold-Hopf bursting close to the transition between region a and c are illustrated in fig. A.1A and A.1B, respectively.

For large g_{eff} the behavior changes again. In regime d, the saddle-node bifurcation that leads to the vanishing of the resting state equilibrium occurs for lower values of I_{eff} than the Andronov-Hopf bifurcation, leading to the birth of the spiking-state periodic orbit. Consequently, after the low-voltage resting state has vanished via the saddle-node bifurcation, the system first relaxes to the stable high-voltage equilibrium. Then, for higher I_{eff} the high-voltage equilibrium becomes unstable via supercritical Andronov-Hopf bifurcation, leading to *resonator*-neuron-like behavior, see sec. 1.4. Since the spiking state vanishes via supercritical Andronov-Hopf bifurcation too, the corresponding bursting type for sufficiently high-amplitude oscillations of I_{eff} is Hopf-Hopf, see sec. 1.6. Phase portraits and voltage time series close to the transition from for Fold-Hopf (region c) to Hopf-Hopf bursting (region d in fig. 5.3) are illustrated in fig. A.2A and A.2B, respectively. Interestingly, when leaving the resting or spiking state, the system feels the vicinity to the saddle-node bifurcation. This results in very small real parts of the eigenvalues close to the resting state equilibrium and leads to the interesting effect that,

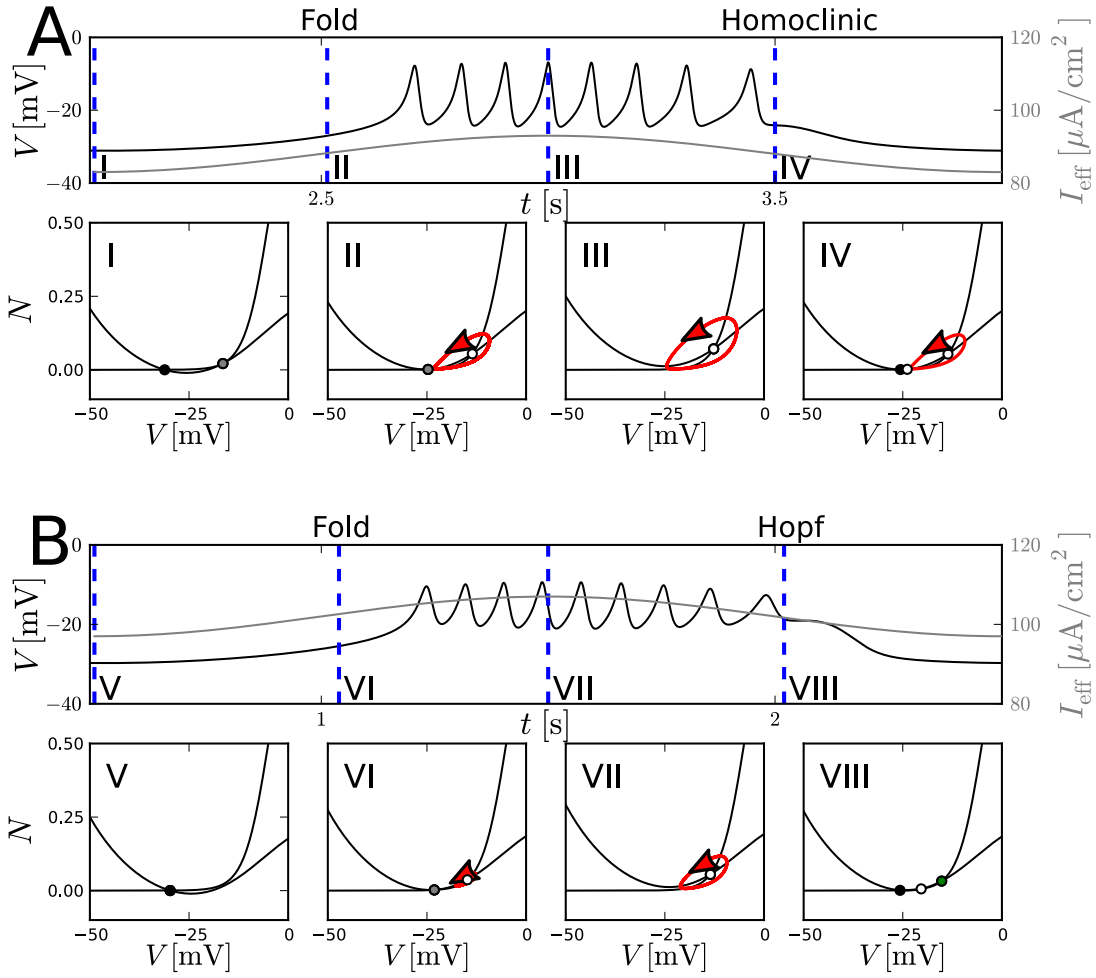

Figure A.1: Transition from region a to region c in fig. 5.3. Voltage time series for the Fold-Homoclinic burster (A) and the Fold-Hopf burster (B) and phase portraits for fixed I_{eff} (I-VIII) that are realized by the oscillating I_{eff} at corresponding times (blue dashed lines). The phase portraits show stable fixed points (black), unstable fixed points (white), saddle-nodes (gray), Hopf bifurcations (green), periodic orbits (red line), and nullclines (black lines). Directions of motion on the limit cycle are illustrated by red arrows. Values of I_{eff} for phase portraits (I-VIII) in μA/cm^2: 83, 88.2, 93, 88, 97, 102.6, 107, and 101.7. Parameters: $V_{\text{K},1} = -5$ mV, $\omega = 0.5$ Hz, $I_{\text{amp}} = 5$ μA/cm^2, (A): $g_{\text{eff}} = 3.6$ mS/cm^2, $I_0 = 88$ μA/cm^2 and (B): $g_{\text{eff}} = 4$ mS/cm^2, $I_0 = 102$ μA/cm^2

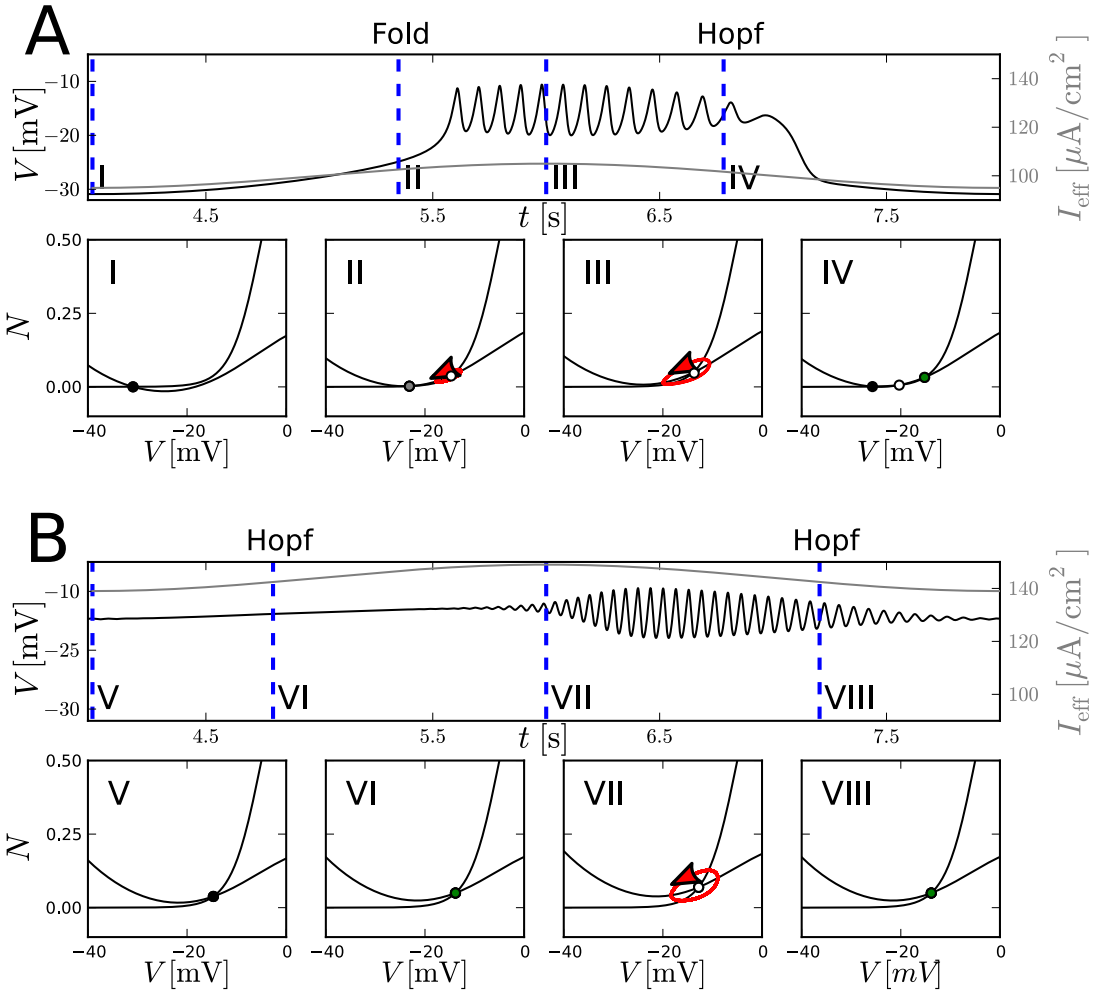

Figure A.2: Transition from region c to region d in fig. 5.3. Voltage time series for the Fold-Hopf burster (A), the Hopf-Hopf burster (B), and phase portraits for fixed I_{eff} (I-VIII) that are realized at times marked by blue dashed lines. The phase portraits show stable fixed points (black), unstable fixed points (white), saddle-nodes (gray), Hopf bifurcations (green), periodic orbits (red line), and nullclines (black lines). Directions on the limit cycle are illustrated by red arrows. Values of I_{eff} for phase portraits (I-VIII) in μA: 95, 102.5, 105, 101.68, 139, 142.42, 149, and 142.42. Parameters: $V_{\mathrm{K},1} = -5$ mV, $\omega = 0.25$ Hz, $I_{\mathrm{amp}} = 5\ \mu\mathrm{A/cm}^2$ (A): $g_{\mathrm{eff}} = 4.0\ \mathrm{mS/cm}^2$, $I_0 = 100\ \mu\mathrm{A/cm}^2$ and (B): $g_{\mathrm{eff}} = 4.8\ \mathrm{mS/cm}^2$, $I_0 = 144\ \mu\mathrm{A/cm}^2$

after the Hopf bifurcation has been past, the system escapes the equilibrium very slowly. For the parameters used in fig. A.2B it cannot even follow the increasing amplitude of the periodic orbit. This results in a relative phase shift between the spiking state and the maximum of the periodic driving I_{eff}. Finally, when I_{eff} decreases again, the same effect leads to a much slower decrease of the oscillation amplitude than is realized by the periodic orbit. Furthermore, it leads to a hysteresis effect, i.e. the system performs oscillations even after the second Hopf bifurcation. During these oscillations, the amplitude decays to zero until the system has reached the resting state equilibrium. Corresponding phase portraits and voltage time series are illustrated in fig. A.2B.

For even higher g_{eff}, a Cusp bifurcation occurs in which both saddle-node bifurcations meet. Afterwards, only one stable equilibrium exists, which represents the resting state and becomes unstable via supercritical Andronov-Hopf bifurcation. However, the Morris-Lecar model still behaves like a *resonator* neuron or, accordingly, performs Hopf-Hopf bursting for sufficient oscillations of I_{eff}.

A.4.2 Parameter estimation from experimental data

In order to fit the parameters of the canonical model eq. (5.7), i.e. I, d, and τ to experimental data for the isolated PD neuron, we minimized the quadratic distance

$$Q = (t_0 T_{\text{B}} - \langle \text{IBI} \rangle)^2 + \sum_{n=1}^{M} (t_0 T_n - \langle \text{ISI}_n \rangle)^2, \tag{A.64}$$

between the average nth ISIs in the bursts of the PD neuron $\langle \text{ISI}_n \rangle$ and corresponding ISIs in the model T_n. The T_n are obtained from simulations of eq. (5.7), complemented by the reset eq. (5.8), with initial conditions $v(t = 0) = -3$ and $u(t = 0) = I + 3$, $v_{\text{res}} = 1$, and Euler integration time step $h = 10^{-6}$. However, results do not depend on the particular choice of initial conditions since all trajectories that start close to the stable branch of the v-nullcline with $u > I$ approach before they reach the voltage cutoff, see dotted lines in fig. 5.5D. Furthermore, the average interburst interval of the PD neuron $\langle \text{IBI} \rangle$ is compared with T_B, which is the time the slow variable u needs to decay from $I + 1$ to its value at the beginning of the first ISI in a burst $u_0 = u_1 - d$, i.e.

$$T_B = \tau \ln \left(\frac{I + 1}{u_0} \right). \tag{A.65}$$

This is obtained from integration of the u dynamics in eq. (5.7). Furthermore, in order to fit the dimensionless time of the model to that of the experimental data, we have introduces the timescale t_0 [ms].

The first term in eq. (A.64) accounts for the distance of interburst intervals. The second term considers the distances to the first M interspike intervals. In order to fit the model parameters, we minimized Q for $M = 5, 6, ..., 11$. Parameters that minimize Q are obtained using the python function *scipy.optimize.minimize* of scipy 0.15.0 with method *Nelder-Mead*, which searches for local minima starting from an initial set of

the parameters. In particualar, 100 random initial sets (t_0, I, τ, d) of the parameters were drawn from a uniform distribution in the region $t_0 \in (0.02, 0.05)$, $I \in (2, 15)$, $\tau \in (60, 150)$, and $d \in (0.2, 0.5)$. Finally, we compared the values of Q for each local minimum and ended up with the parameters shown in tab. A.1. Parameters for different local minima mainly differ in the absolute values of I and τ, while the ratio of these parameters differs only slightly. This can be understood from the fact that the dynamics of the canonical model depends mainly on the ratio of I/τ [125]. Furthermore, we find that the optimization procedure leads to similar values of t_0, I/τ, and d for $M = 5, 6, 7, 8$. While the values of I/τ and d for $M = 8, 9, 10$ are smaller. This may be caused by noise in the biological neuron, which mainly affects ISIs in the end of the regular part of the burst and those in the irregular part. Finally, we used the parameter set for $M = 11$ in chapter 5. It properly accounts for ISIs in the beginning of a burst, and, since it also considers ISIs in the beginning of the irregular part, produces bursts with a proper number of ISIs in the regular part. Note that this set of parameters was also used for the noisy model eq. (5.11).

M	t_0 [s]	I	τ	I/τ	d	Q	u_0
5	0.0343	15.7893	252.6474	0.0650	0.2160	$6.5 * 10^{-7}$	15.4251
6	0.0340	12.5422	206.1706	0.0608	0.2211	$1.0 * 10^{-6}$	12.1852
7	0.0340	11.6263	191.1154	0.0608	0.2201	$1.0 * 10^{-6}$	11.2697
8	0.0340	11.0421	182.4973	0.0605	0.2203	$1.0 * 10^{-6}$	10.6870
9	0.0344	2.8556	52.5185	0.0545	0.2097	$1.5 * 10^{-5}$	2.5359
10	0.0356	2.9478	51.5683	0.0572	0.2084	$3.4 * 10^{-5}$	2.6174
11	0.0349	3.2159	44.0224	0.0731	0.2323	$1.9 * 10^{-}5$	2.5858

Table A.1: Optimal sets of parameters obtained from minimizing eq. (A.64). Results, except those for Q, are rounded to four decimal places. Gray marked parameters are used in chapter 5.

Bibliography

[1] L. F. Abbott, E. Marder, and S. L. Hooper. Oscillating networks: Control of burst duration by electrically coupled neurons. *Neural Computation*, 3(4):487–497, 1991.

[2] J. A. Acebrón, L. L. Bonilla, C. J. P. Vicente, F. Ritort, and R. Spigler. The Kuramoto model: A simple paradigm for synchronization phenomena. *Reviews of Modern Physics*, 77(1):137–185, 2005.

[3] R. Adler. A study of locking phenomena in oscillators. *Proceedings of the IEEE*, 34(6):351–357, 1946.

[4] R. M. Amro, B. Lindner, and A. B. Neiman. Phase diffusion in unequally noisy coupled oscillators. *Physical Review Letters*, 115(3):034101, 2015.

[5] V. S. Anishchenko, V. Astakhov, A. B. Neiman, T. Vadivasova, and L. Schimansky-Geier. *Nonlinear Dynamics of Chaotic and Stochastic Systems*. Springer Series in Synergetics. Springer, Berlin, 2nd edition, 2007.

[6] F. T. Arecchi and A. Politi. Transient fluctuations in the decay of an unstable state. *Physical Review Letters*, 45(15):1219–1222, 1980.

[7] L. Arnold. *Stochastic differential equations*. Wiley, New York, 1974. (english translation of original German language edition published by R. Oldenbourg Verlag, Munich. 1973).

[8] L. Arnold. *Random Dynamical Systems*. Springer Monographs in Mathematics. Springer, Berlin, 1998.

[9] M. Augustin, J. Ladenbauer, and K. Obermayer. How adaptation shapes spike rate oscillations in recurrent neuronal networks. *Frontiers in Computational Neuroscience*, 7(9):1–11, 2013.

[10] R. Aust, P. Hövel, J. Hizanidis, and E. Schöll. Delay control of coherence resonance in type-I excitable dynamics. *The European Physical Journal Special Topics*, 187 (1):77–85, 2010.

[11] O. Avila-Akerberg and M. J. Chacron. Nonrenewal spike train statistics: Causes and functional consequences on neural coding. *Experimental Brain Research*, 210 (3):353–371, 2011.

[12] R. Azouz and C. M. Gray. Cellular mechanisms contributing to response variability of cortical neurons in vivo. *The Journal of Neuroscience*, 19(6):2209–2223, 1999.

[13] T. Bal, F. Nagy, and M. Moulins. The pyloric central pattern generator in crustacea: A set of conditional neuronal oscillators. *Journal of Comparative Physiology A*, 163(6):715–727, 1988.

[14] R. W. Banks, M. Hulliger, K.A. Scheepstra, and E. Otten. Pacemaker activity in a sensory ending with multiple encoding sites: The cat muscle spindle primary ending. *The Journal of Physiology*, 498(1):177–199, 1997.

[15] M. Bazhenov, I. Timofeev, M. Steriade, and T. J. Sejnowski. Potassium model for slow (2-3 Hz) in vivo neocortical paroxysmal oscillations. *Journal of Neurophysiology*, 92(2):1116–1132, 2004.

[16] J. M. Bekkers. Synaptic transmission: Excitatory autapses find a function? *Current Biology*, 19(7):R296–R298, 2009.

[17] J. M. Bekkers and C. F. Stevens. Excitatory and inhibitory autaptic currents in isolated hippocampal neurons maintained in cell culture. *Proceedings of the National Academy of Sciences of the United States of America*, 88(17):7834–7838, 1991.

[18] J. Benda and A. V. M. Herz. A universal model for spike-frequency adaptation. *Neural Computation*, 15(11):2523–2564, 2003.

[19] J. Benda, L. Maler, and L. Longtin. Linear versus nonlinear signal transmission in neuron models with adaptation currents or dynamic thresholds. *Journal of Neurophysiology*, 104(5):2806–2820, 2010.

[20] R. Benzi, A. Sutera, and A. Vulpiani. The mechanism of stochastic resonance. *Journal of Physics A*, 14(11):L453–L457, 1981.

[21] R. Benzi, G. Parisi, A. Sutera, and A. Vulpiani. Stochastic resonance in climatic change. *Tellus*, 34(1):10–16, 1982.

[22] A. Bergner, M. Frasca, G. Sciuto, A. Buscarino, E. J. Ngamga, L. Fortuna, and J. Kurths. Remote synchronization in star networks. *Physical Review E*, 85(2): 026208, 2012.

[23] G. Bhanot, R. Salvador, S. Black, P. Carter, and R. Toral. Accurate estimate of ν for the three-dimensional ising model from a numerical measurement of its partition function. *Physical Review Letters*, 59(7):803–806, 1987.

[24] D. Bhatt and I. Bahar. An adaptive weighted ensemble procedure for efficient computation of free energies and first passage rates. *The Journal of Chemical Physics*, 137(10):104101, 2012.

[25] D. Bhatt, B.W. Zhang, and D.M. Zuckerman. Steady-state simulations using weighted ensemble path sampling. *The Journal of Chemical Physics*, 133(1): 014110, 2010.

[26] W. Bialek, F. Rieke, R. de R. van Steveninck, and D. Warland. Reading a neural code. *Science*, 252(5014):1854–1857, 1991.

[27] A. L. Bianchi, M. Denavit-Saubie, and J. Champagnat. Central control of breathing in mammals: Neuronal circuitry, membrane properties, and neurotransmitters. *Physiological Reviews*, 75(1):1–45, 1995.

[28] E. K. Blum. *Numerical Analysis and Computation*. Addison-Wesley, Reading MA, 1972.

[29] P. Bonifazi, M. Goldin, M. A. Picardo, I. Jorquera, A. Cattani, G. Bianconi, A. Represa, Y. Ben-Ari, and R. Cossart. GABAergic hub neurons orchestrate synchrony in developing hippocampal networks. *Science*, 326(5958):1419–1424, 2009.

[30] T. Branco and K. Staras. The probability of neurotransmitter release: Variability and feedback control at single synapses. *Nature Reviews Neuroscience*, 10(5):373–383, 2009.

[31] N. Brenner, O Agam, W. Bialek, and R. de R. van Steveninck. Statistical properties of spike trains: Universal and stimulus-dependent aspects. *Physical Review E*, 66 (3):031907, 2002.

[32] R. Brette and W. Gerstner. Adaptive exponential integrate-and-fire model as an effective description of neuronal activity. *Journal of Neurophysiology*, 94(5):3637–3642, 2005.

[33] L. Brochini, P. V. Carelli, and R. D. Pinto. Single synapse information coding in intraburst spike patterns of central pattern generator motor neurons. *The Journal of Neuroscience*, 31(34):12297–12306, 2011.

[34] D. Brown, J. Feng, and S. Feerick. Variability of firing of Hodgkin-Huxley and FitzHugh-Nagumo neurons with stochastic synaptic input. *Physical Review Letters*, 82(23):4731–4734, 1999.

[35] T. G. Brown. On the nature of the fundamental activity of the nervous centres; together with an analysis of the conditioning of rhythmic activity in progression, and a theory of the evolution of function in the nervous system. *The Journal of Physiology*, 48(1):18–46, 1914.

[36] N. Brunel and P. E. Latham. Firing rate of the noisy quadratic integrate-and-fire neuron. *Neural Computation*, 15(10):2281–2306, 2003.

[37] N. Brunel, F. S. Chance, N. Fourcaud, and L. F. Abbott. Effects of synaptic noise and filtering on the frequency response of spiking neurons. *Physical Review Letters*, 86(10):2186–2189, 2001.

[38] A. N. Burkitt. A review of the integrate-and-fire neuron model: I. Homogeneous synaptic input. *Biological Cybernetics*, 95(1):1–19, 2006.

[39] A. N. Burkitt. A review of the integrate-and-fire neuron model: II. Inhomogeneous synaptic input and network properties. *Biological Cybernetics*, 95(2):97–112, 2006.

[40] O. Burylko, Y. Kazanovich, and R. Borisyuk. Bifurcations in phase oscillator networks with a central element. *Physica D*, 241(12):1072–1089, 2012.

[41] J. C. Butcher. *The numerical analysis of ordinary differential equations*. Wiley-Interscience, New York, 1987.

[42] D. A. Butts, C. Weng, J. Jin, C. I. Yeh, N. A. Lesica, J. M. Alonso, and G. B. Stanley. Temporal precision in the neural code and the timescales of natural vision. *Nature*, 449(7158):92–95, 2007.

[43] R. L. Calabrese, J. D. Angstadt, and E. A. Arbas. A neural oscillator based on reciprocal inhibition. In T. J. Carew and D. B. Kelley, editors, *Perspectives in Neural Systems and Behavior*, volume 10, pages 33–50. Liss, New York, 1989.

[44] R. L. Calabrese, F. Nadim, and Ø. H. Olsen. Heartbeat control in the medicinal leech: A model system for understanding the origin, coordination, and modulation of rhythmic motor patterns. *Journal of Neurobiology*, 27(3):390–402, 1995.

[45] R. M. Capocelli and L. M. Ricciardi. Diffusion approximation and first passage time problem for a model neuron. *Kybernetik*, 8(6):214–223, 1971.

[46] P. V. Carelli, M. B. Reyes, J. C. Sartorelli, and R. D. Pinto. Whole cell stochastic model reproduces the irregularities found in the membrane potential of bursting neurons. *Journal of Neurophysiology*, 94(2):1169–1179, 2005.

[47] M. J. Chacron, A. Longtin, and L. Maler. Negative interspike interval correlations increase the neuronal capacity for encoding time-dependent stimuli. *The Journal of Neuroscience*, 21(14):5328–5343, 2001.

[48] M. J. Chacron, B. Lindner, and A. Longtin. Noise shaping by interval correlations increases information transfer. *Physical Review Letters*, 92(8):080601, 2004.

[49] P. Channell, G. Cymbalyuk, and A. Shilnikov. Applications of the poincaré mapping technique to analysis of neuronal dynamics. *Neurocomputing*, 70(10-12):2107–2111, 2007.

[50] C. C. Chow and N. Kopell. Dynamics of spiking neurons with electrical coupling. *Neural Computation*, 12(7):1643–1678, 2000.

[51] E. A. Coddington and N. Levinson. *Theory of ordinary differential equations*. International series in pure and applied mathematics. McGraw-Hill, New York, 1955.

[52] D. R. Cox and P. A. W. Lewis. *The Statistical Analysis of Series of Events*. Wiley, New York, 1966.

[53] P. Dayan and L. F. Abbott. *Theoretical Neuroscience*. MIT Press, Cambridge MA, 2001.

[54] M. Deger, T. Schwalger, R. Naud, and W. Gerstner. Fluctuations and information filtering in coupled populations of spiking neurons with adaptation. *Physical Review E*, 90(6):062704, 2014.

[55] R. Dermietzel and D. C. Spray. Gap junctions in the brain: Where, what type, how many and why? *Trends in Neurosciences*, 16(5):186–192, 1993.

[56] A. Destexhe. Is the purpose of reverse spike-frequency adaptation to enhance correlations? Focus on "A model of reverse spike frequency adaptation and repetitive firing of subthalamic nucleus neurons". *Journal of Neurophysiology*, 91(5): 1943–1944, 2004.

[57] A. Destexhe, Z. F. Mainen, and T.J. Sejnowski. Synthesis of models for excitable membranes, synaptic transmission and neuromodulation using a common kinetic formalism. *Journal of Computational Neuroscience*, 1(3):195–230, 1994.

[58] A. Destexhe, M. Rudolph, J.-M. Fellous, and T. J. Sejnowski. Fluctuating synaptic conductances recreate in vivo-like activity in neocortical neurons. *Neuroscience*, 107(1):13–24, 2001.

[59] A. Destexhe, M. Rudolph, and D. Paré. The high-conductance state of neocortical neurons in vivo. *Nature Reviews Neuroscience*, 4(9):739–751, 2003.

[60] A. Dickson and A. R. Dinner. Enhanced sampling of nonequilibrium steady states. *Annual Review of Physical Chemistry*, 61:441–459, 2010.

[61] E. J. Doedel and B. E. Oldeman. Auto-07p: Continuation and bifurcation software for ordinary differential equations (with HomCont), 2012.

[62] F. Dörfler and F. Bullo. Synchronization and transient stability in power networks and nonuniform kuramoto oscillators. *SIAM Journal on Control and Optimization*, 50(3):1616–1642, 2012.

[63] J. L. A. Dubbeldam, B. Krauskopf, and D. Lenstra. Excitability and coherence resonance in lasers with saturable absorber. *Physical Review E*, 60(6):6580–6588, 1999.

[64] J. Duysens and H. W. A. A. Van de Crommert. Neural control of locomotion; part 1: The central pattern generator from cats to humans. *Gait & Posture*, 7(2): 131–141, 1998.

[65] R. C. Elson, A. I. Selverston, R. Huerta, N. F. Rulkov, M. I. Rabinovich, and H. D. I. Abarbanel. Synchronous behavior of two coupled biological neurons. *Physical Review Letters*, 81(25):5692–5695, 1998.

[66] T. A. Engel, L. Schimansky-Geier, A. V. M. Herz, S. Schreiber, and I. Erchova. Subthreshold membrane-potential resonances shape spike-train patterns in the entorhinal cortex. *Journal of Neurophysiology*, 100(3):1576–1589, 2008.

[67] T. A. Engel, B. Helbig, D. F. Russell, L. Schimansky-Geier, and A. B. Neiman. Coherent stochastic oscillations enhance signal detection in spiking neurons. *Physical Review E*, 80(2):021919, 2009.

[68] G. B. Ermentrout. Type I membranes, phase resetting curves, and synchrony. *Neural Computation*, 8(5):979–1001, 1996.

[69] G. B. Ermentrout and N. Kopell. Parabolic bursting in an excitable system coupled with a slow oscillation. *SIAM Journal on Applied Mathematics*, 46(2):233–253, 1986.

[70] G. B. Ermentrout, M. Pascal, and B. Gutkin. The effects of spike frequency adaptation and negative feedback on the synchronization of neural oscillators. *Neural Computation*, 13(6):1285–1310, 2001.

[71] G. B. Ermentrout, R. F. Galán, and N. N. Urban. Reliability, synchrony and noise. *Trends in Neurosciences*, 31(8):428–434, 2008.

[72] L. Euler. *Institutionum Calculi integralis*, volume 1-3. Impensis Academia Imperialis Scientiarum, Petersburg, 1768-1770.

[73] A. A. Faisal, L. P. J. Selen, and D. M. Wolpert. Noise in the nervous system. *Nature Reviews Neuroscience*, 9(4):292–303, 2008.

[74] M. Falcke, R. Huerta, M. I. Rabinovich, H. D. I. Abarbanel, R. C. Elson, and A. I. Selverston. Modeling observed chaotic oscillations in bursting neurons: The role of calcium dynamics and IP3. *Biological Cybernetics*, 82(6):517–527, 2000.

[75] F. Farkhooi, E. Muller, and M. P. Nawrot. Adaptation reduces variability of the neuronal population code. *Physical Review E*, 83(5):050905, 2011.

[76] J. Feng. Is the integrate-and-fire model good enough? – a review. *Neural Networks*, 14(6-7):955–975, 2001.

[77] G. Filatrella, A. H. Nielsen, and N. F. Pedersen. Analysis of a power grid using a Kuramoto-like model. *The European Physical Journal B*, 61(4):485–491, 2008.

[78] R. S. Fisher, T. A. Pedley, and D. A. Prince. Kinetics of potassium movement in normal cortex. *Brain Research*, 101(2):223–237, 1976.

[79] R. FitzHugh. Mathematical models of threshold phenomena in the nerve membrane. *The bulletin of mathematical biophysics*, 17(4):257–278, 1955.

[80] R. FitzHugh. Impulses and physiological states in theoretical models of nerve membrane. *Biophysical Journal*, 1(6):445–466, 1961.

[81] N. Fourcaud-Trocmé, D. Hansel, C. van Vreeswijk, and N. Brunel. How spike generation mechanisms determine the neuronal response to fluctuating inputs. *The Journal of Neuroscience*, 23(37):11628–11640, 2003.

[82] R. F. Fox. Stochastic versions of the Hodgkin-Huxley equations. *Biophysical Journal*, 72(5):2068–2074, 1997.

[83] R. F. Fox and Y.-n. Lu. Emergent collective behavior in large numbers of globally coupled independently stochastic ion channels. *Physical Review E*, 49(4):3421, 1994.

[84] M. I. Freidlin and A. D. Wentzell. *Random Perturbations of Dynamical Systems*, volume 260 of *Grundlehren der mathematischen Wissenschaften*. Springer, Berlin, 3rd edition, 2012.

[85] F. Fröhlich, M. Bazhenov, I. Timofeev, M. Steriade, and T. J. Sejnowski. Slow state transitions of sustained neural oscillations by activity-dependent modulation of intrinsic excitability. *The Journal of Neuroscience*, 26(23):6153–6162, 2006.

[86] L. Gammaitoni, P. Hänggi, P. Jung, and F. Marchesoni. Stochastic resonance. *Reviews of Modern Physics*, 70(1):223–287, 1998.

[87] A. Gavrielides, T. Erneux, V. Kovanis, P. M. Alsing, and T. B. Simpson. Subharmonic transition in an optically injected semiconductor laser: Theory and experiments. *Quantum and Semiclassical Optics*, 9(4):575–585, 1997.

[88] G. L. Gerstein and B. Mandelbrot. Random walk models for the spike activity of a single neuron. *Biophysical Journal*, 4(1 Pt 1):41–68, 1964.

[89] W. Gerstner and W. M. Kistler. *Spiking Neuron Models*. Cambridge University Press, Cambridge, 2002.

[90] G. Giacomelli, M. Giudici, S. Balle, and J. R. Tredicce. Experimental evidence of coherence resonance in an optical system. *Physical Review Letters*, 84(15):3298–3301, 2000.

[91] C. Giardina, J. Kurchan, and L. Peliti. Direct evaluation of large-deviation functions. *Physical Review Letters*, 96(12):120603, 2006.

[92] M. Giudici, C. Green, G. Giacomelli, U. Nespolo, and J. R. Tredicce. Andronov bifurcation and excitability in semiconductor lasers with optical feedback. *Physical Review E*, 55(6):6414, 1997.

[93] J. H. Goldwyn and E. Shea-Brown. The what and where of adding channel noise to the Hodgkin-Huxley equations. *PLoS Computational Biology*, 7(11):e1002247, 2011.

[94] M. Gosak, D. Korošak, and M. Marhl. Optimal network configuration for maximal coherence resonance in excitable systems. *Physical Review E*, 81(5):056104, 2010.

[95] D. Goulding, S. P. Hegarty, O. Rasskazov, S. Melnik, M. Hartnett, G. Greene, J. G. McInerney, D. Rachinskii, and G. Huyet. Excitability in a quantum dot semiconductor laser with optical injection. *Physical Review Letters*, 98(15):153903, 2007.

[96] J. Grau-Moya, A. J. Pons, and J. Garcia-Ojalvo. Noise-induced up/down dynamics in scale-free neuronal networks. *International Journal of Bifurcation and Chaos*, 22(7):1250175, 2012.

[97] S. Grillner and P. Wallen. Central pattern generators for locomotion, with special reference to vertebrates. *Annual Review of Neuroscience*, 8:233–261, 1985.

[98] J. R. Groff, H. DeRemigio, and G. D. Smith. Markov chain models of ion channels and calcium release sites. In C. Laing and G. J. Lord, editors, *Stochastic Methods in Neuroscience*, pages 29–64. Oxford University Press, Oxford, 2009.

[99] J. Guckenheimer and P. Holmes. *Nonlinear oscillations, dynamical systems, and bifurcations of vector fields*, volume 42 of *Applied Mathematical Sciences*. Springer, New York, 1983.

[100] B. S. Gutkin and G. B. Ermentrout. Dynamics of membrane excitability determine interspike interval variability: A link between spike generation mechanisms and cortical spike train statistics. *Neural Computation*, 10(5):1047–1065, 1998.

[101] N. E. Hallworth, C. J. Wilson, and M. D. Bevan. Apamin-sensitive small conductance calcium-activated potassium channels, through their selective coupling to voltage-gated calcium channels, are critical determinants of the precision, pace, and pattern of action potential generation in rat subthalamic nucleus neurons in vitro. *The Journal of Neuroscience*, 23(20):7525–7542, 2003.

[102] S. K. Han, T. G. Yim, D. E. Postnov, and O. V. Sosnovtseva. Interacting coherence resonance oscillators. *Physical Review Letters*, 83(9):1771–1774, 1999.

[103] P. Hänggi and H. Thomas. Stochastic processes: Time evolution, symmetries and linear response. *Physics Reports*, 88:207–319, 1982.

[104] P. Hänggi, P. Talkner, and M. Borkovec. Reaction-rate theory: Fifty years after Kramers. *Reviews of Modern Physics*, 62(2):251–341, 1990.

[105] K. D. Harris and A. Thiele. Cortical state and attention. *Nature Reviews Neuroscience*, 12(9):509–523, 2011.

[106] R. M. Harris-Warrick and A. H. Cohen. Serotonin modulates the central pattern generator for locomotion in the isolated lamprey spinal cord. *Journal of Experimental Biology*, 116(1):27–46, 1985.

[107] C. S. Herrmann and A. Klaus. Autapse turns neuron into oscillator. *International Journal of Bifurcation and Chaos*, 14(2):623–633, 2004.

[108] S. Hestrin and M. Galarreta. Electrical synapses define networks of neocortical GABAergic neurons. *Trends in Neurosciences*, 28(6):304–309, 2005.

[109] K. Heun. Neue Methode zur approximativen Integration der Differentialgleichungen einer unabhängigen Veränderlichen. *Zeitschrift für Mathematik und Physik*, 45:23–38, 1900. (in German).

[110] J. Hidalgo, L. F. Seoane, J. M. Cortés, and M. A. Muñoz. Stochastic amplification of fluctuations in cortical up-states. *PloS ONE*, 7(8):e40710, 2012.

[111] A. L. Hodgkin. The local electric changes associated with repetitive action in a non-medullated axon. *The Journal of Physiology*, 107(2):165–181, 1948.

[112] A. L. Hodgkin and A. F. Huxley. A quantitative description of membrane current and its application to conduction and excitation in nerve. *The Journal of Physiology*, 117(4):500–544, 1952.

[113] D. Holcman and M. Tsodyks. The emergence of up and down states in cortical networks. *PLoS Computational Biology*, 2(3):e23, 2006.

[114] K. G. Horn, H. Memelli, and I. C. Solomon. Emergent central pattern generator behavior in gap-junction-coupled hodgkin-huxley style neuron model. *Computational Intelligence and Neuroscience*, 2012:173910, 2012. 173910.

[115] B. Hu and C. Zhou. Phase synchronization in coupled nonidentical excitable systems and array-enhanced coherence resonance. *Physical Review E*, 61(2):R1001–R1004, 2000.

[116] G.A. Huber and S. Kim. Weighted-ensemble brownian dynamics simulations for protein association reactions. *Biophysical Journal*, 70(1):97, 1996.

[117] A. J. Ijspeert. Central pattern generators for locomotion control in animals and robots: A review. *Neural Networks*, 21(4):642–653, 2008.

[118] K. Ikeda and J. M. Bekkers. Autapses. *Current Biology*, 16(9):R308, 2006.

[119] K. Itô. Stochastic integral. *Proceedings of the Imperial Academy*, 20(8):519–524, 1944.

[120] K. Itô. Stochastic differentials. *Applied Mathematics and Optimization*, 1(4):374–381, 1975.

[121] E. M. Izhikevich. Neural excitability, spiking and bursting. *International Journal of Bifurcation and Chaos*, 10(6):1171–1266, 2000.

[122] E. M. Izhikevich. Resonate-and-fire neurons. *Neural Networks*, 14(6-7):883–894, 2001.

[123] E. M. Izhikevich. Simple model of spiking neurons. *IEEE Transactions on Neural Networks*, 14(6):1569–1572, 2003.

[124] E. M. Izhikevich. Which model to use for cortical spiking neurons? *IEEE Transactions on Neural Networks*, 15(5):1063–1070, 2004.

[125] E. M. Izhikevich. *Dynamical Systems in Neuroscience*. MIT Press, Cambridge MA, 2007.

[126] E. M. Izhikevich, N. S. Desai, E. C. Walcott, and F. C. Hoppensteadt. Bursts as a unit of neural information: Selective communication via resonance. *Trends in Neurosciences*, 26(3):161–167, 2003.

[127] A. B. Karabelas and D. P. Purrura. Evidence for autapses in the substantia nigra. *Brain Research*, 200(2):467–473, 1980.

[128] Y. Kazanovich, O. Burylko, and R. Borisyuk. Competition for synchronization in a phase oscillator system. *Physica D*, 261:114–124, 2013.

[129] J. P. Keener and J. Sneyd. *Mathematical Physiology*, volume 8/1 of *Interdisciplinary Applied Mathematics*. Springer, New York, 2nd edition, 2009.

[130] T. B. Kepler, E. Marder, and L. F. Abbott. The effect of electrical coupling on the frequency of model neuronal oscillators. *Science*, 248(4951):83–85, 1990.

[131] I. Z. Kiss, Y. Zhai, and J. L. Hudson. Emerging coherence in a population of chemical oscillators. *Science*, 296(5573):1676–1678, 2002.

[132] I. Z. Kiss, J. L. Hudson, G. J. E. Santos, and P. Parmananda. Experiments on coherence resonance: Noisy precursors to Hopf bifurcations. *Physical Review E*, 67(3):035201(R), 2003.

[133] H. Kitajima and J. Kurths. Bifurcation in neuronal networks with hub structure. *Physica A*, 388(20):4499–4508, 2009.

[134] H. Kitajima and T. Yoshihara. Cluster synchronization in coupled systems with hub structure. *Physica D*, 241(21):1804–1810, 2012.

[135] Y. L. Klimontovich. Itô, Stratonovich and kinetic forms of stochastic equations. *Physica A*, 163(2):515–532, 1990.

[136] Y. L. Klimontovich. Nonlinear brownian motion. *Physics-Uspekhi*, 37(8):737–767, 1994.

[137] P. E. Kloeden and E. Platen. *Numerical solution of stochastic differential equations*. Stochastic Modelling and Applied Probability. Springer, Berlin, 3rd edition, 1999.

[138] C. Koch. *Biophysics of Computation*. Computational Neuroscience Series. Oxford University Press, New York, 1999.

[139] N. Komin and R. Toral. Order parameter expansion and finite-size scaling study of coherent dynamics induced by quenched noise in the active rotator model. *Physical Review E*, 82(5):051127, 2010.

[140] H. A. Kramers. Brownian motion in a field of force and the diffusion model of chemical reactions. *Physica*, 7(4):284–304, 1940.

[141] T. Kreuz, S. Luccioli, and A. Torcini. Coherence resonance due to correlated noise in neuronal models. *Neurocomputing*, 70(10-12):1970,1976, 2007.

[142] J. A. Kromer, L. Schimansky-Geier, and R. Toral. Weighted-ensemble brownian dynamics simulation: Sampling of rare events in nonequilibrium systems. *Physical Review E*, 87(6):063311, 2013.

[143] J. A. Kromer, B. Lindner, and L. Schimansky-Geier. Event-triggered feedback in noise-driven phase oscillators. *Physical Review E*, 89(3):032138, 2014.

[144] J. A. Kromer, R. D. Pinto, B. Lindner, and L. Schimansky-Geier. Noise-controlled bistability in an excitable system with positive feedback. *EPL (Europhysics Letters)*, 108(2):20007, 2014.

[145] J. A. Kromer, B. Marin, L. Schimansky-Geier, R. C. Elson, and R. D. Pinto. Geometrical modeling captures complex dynamics of a bursting neuron observed in synaptic isolation and under pacemaker drive. (in preparation), 2015.

[146] J. A. Kromer, L. Schimansky-Geier, and A. B. Neiman. Emergence and coherence of oscillations in star networks of stochastic excitable elements. (to be submitted), 2015.

[147] Y. Kuramoto. *Chemical Oscillations, Waves, and Turbulence*, volume 19 of *Springer Series in Synergetics*. Springer, New York Tokyo, 1984.

[148] Y. Kuramoto. Self-entrainment of a population of coupled non-linear oscillators. In H. Araki, editor, *International Symposium on Mathematical Problems in Theoretical Physics*, volume 39 of *Lecture Notes in Physics*, pages 420–422, Springer, Berlin, 1975.

[149] W. Kutta. Beitrag zur näherungsweisen integration totaler differentialgleichungen. *Zeitschrift für Mathematik und Physik*, 46:435–453, 1901. (in German).

[150] A. M. Lacasta, F. Sagués, and J. M. Sancho. Coherence and anticoherence resonance tuned by noise. *Physical Review E*, 66:045105(R), 2002.

[151] J. Ladenbauer, M. Augustin, L.J. Shiau, and K. Obermayer. Impact of adaptation currents on synchronization of coupled exponential integrate-and-fire neurons. *PLoS Computational Biology*, 8(4):e1002478, 2012.

[152] P. Lánský. On approximations of Stein's neuronal model. *Journal of Theoretical Biology*, 107:631–647, 1984.

[153] C. Y. Lee, W. Choi, J.-H. Han, and M. S. Strano. Coherence resonance in a single-walled carbon nanotube ion channel. *Science*, 329(5997):1320–1324, 2010.

[154] S. G. Lee, A. B. Neiman, and S. Kim. Coherence resonance in a Hodgkin-Huxley neuron. *Physical Review E*, 57(3):3292–3297, 1998.

[155] Y. Li, P. Schmid, G. Hänggi, and L. Schimansky-Geier. Spontaneous spiking in an autaptic Hodgkin-Huxley setup. *Physical Review E*, 82(6):061907, 2010.

[156] D. Linaro, M. Storace, and M. Giugliano. Accurate and fast simulation of channel noise in conductance-based model neurons by diffusion approximation. *PLoS Computational Biology*, 7(3):e1001102, 2011.

[157] B. Lindner. Interspike interval statistics of neurons driven by colored noise. *Physical Review E*, 69(2):022901, 2004.

[158] B. Lindner. Moments of the first passage time under external driving. *Journal of Statistical Physics*, 117(3):703–737, 2004.

[159] B. Lindner. Superposition of many independent spike trains is generally not a Poisson process. *Physical Review E*, 73(2):022901, 2006.

[160] B. Lindner and L. Schimansky-Geier. Analytical approach to the FitzHugh-Nagumo system and coherence resonance. *Physical Review E*, 60(6):7270–7276, 1999.

[161] B. Lindner and L. Schimansky-Geier. Coherence and stochastic resonance in a two-state system. *Physical Review E*, 61(6):6103–6110, 2000.

[162] B. Lindner, M. Kostur, and L. Schimansky-Geier. Optimal diffusive transport in a tilted periodic potential. *Fluctuation and Noise Letters*, 01(01):R25, 2001.

[163] B. Lindner, L. Schimansky-Geier, and A. Longtin. Maximizing spike train coherence or incoherence in the leaky integrate-and-fire model. *Physical Review E*, 66 (3):031916, 2002.

[164] B. Lindner, A. Longtin, and A. Bulsara. Analytic expressions for rate and CV of a type I neuron driven by white Gaussian noise. *Neural Computation*, 15(8): 1761–1788, 2003.

[165] B. Lindner, J. García-Ojalvo, A. B. Neiman, and L. Schimansky-Geier. Effects of noise in excitable systems. *Physics Reports*, 392(6):321–424, 2004.

[166] J. E. Lisman. Bursts as a unit of neural information: Making unreliable synapses reliable. *Trends in Neurosciences*, 20(1):38–43, 1997.

[167] Y.-H. Liu and X.-J. Wang. Spike-frequency adaptation of a generalized leaky integrate-and-fire model neuron. *Journal of Computational Neuroscience*, 10(1): 25–45, 2001.

[168] J. Lübke, H. Markram, M. Frotscher, and B. Sakmann. Frequency and dendritic distribution of autapses established by layer 5 pyramidal neurons in the developing rat neocortex: Comparison with synaptic innervation of adjacent neurons of the same class. *The Journal of Neuroscience*, 16(10):3209–3218, 1996.

[169] S. Luccioli, E. Ben-Jacob, A. Barzilai, P. Bonifazi, and A. Torcini. Clique of functional hubs orchestrates population bursts in developmentally regulated neural networks. *PLoS Computational Biology*, 10(9):e1003823, 2014.

[170] Z. F. Mainen and T. J. Sejnowski. Reliability of spike timing in neocortical neurons. *Science*, 268(5216):1503–1506, 1995.

[171] G. Major and D. Tank. Persistent neural activity: Prevalence and mechanisms. *Current Opinion in Neurobiology*, 14(6):675–684, 2004.

[172] E. Marder. Variability, compensation, and modulation in neurons and circuits. *Proceedings of the National Academy of Sciences of the United States of America*, 108(Supplement 3):15542–15548, 2011.

[173] E. Marder and D. Bucher. Central pattern generators and the control of rhythmic movements. *Current Biology*, 11(23):R986–R996, 2001.

[174] E. Marder and R. L. Calabrese. Principles of rhythmic motor pattern generation. *Physiological Reviews*, 76(3):687–717, 1996.

[175] E. Marder and A. L. Taylor. Multiple models to capture the variability in biological neurons and networks. *Nature Neuroscience*, 14(2):133–138, 2011.

[176] B. Marin, R. D. Pinto, R. C. Elson, and E. Colli. Noise, transient dynamics, and the generation of realistic interspike interval variation in square-wave burster neurons. *Physical Review E*, 90(4):042718, 2014.

[177] G. Maruyama. Continuous markov processes and stochastic equations. *Rendiconti del Circolo Matematico di Palermo*, 4(1):48–90, 1955.

[178] M. Matsumoto and T. Nishimura. Mersenne twister: A 623-dimensionally equidistributed uniform pseudo-random number generator. *ACM Transactions on Modeling and Computer Simulation*, 8(1):3–30, 1998. ISSN 1049-3301.

[179] E. J. McShane. *Stochastic calculus and stochastic models*. Academic Press, New York, 1974.

[180] G. S. Medvedev. Reduction of a model of an excitable cell to a one-dimensional map. *Physica D*, 202(1-2):37–59, 2005.

[181] G. S. Medvedev and S. Zhuravytska. The geometry of spontaneous spiking in neuronal networks. *Journal of Nonlinear Science*, 22(5):689–725, 2012.

[182] G. S. Medvedev and S. Zhuravytska. Shaping bursting by electrical coupling and noise. *Biological Cybernetics*, 106(2):67–88, 2012.

[183] J. W. Middleton, M. J. Chacron, B. Lindner, and A. Longtin. Firing statistics of a neuron model driven by long-range correlated noise. *Physical Review E*, 68(2): 021920, 2003.

[184] J. P. Miller and A. I. Selverston. Mechanisms underlying pattern generation in lobster stomatogastric ganglion as determined by selective inactivation of identified neurons. IV. Network properties of pyloric system. *Journal of Neurophysiology*, 48 (6):1416–1432, 1982.

[185] R. Moreno-Bote and N. Parga. Auto- and crosscorrelograms for the spike response of leaky integrate-and-fire neurons with slow synapses. *Physical Review Letters*, 96(2):028101, 2006.

[186] C. Morris and H. Lecar. Voltage oscillations in the barnacle giant muscle fiber. *Biophysical Journal*, 35(1):193–213, 1981.

[187] F. Moss and P. V. E. McClintock, editors. *Noise in nonlinear dynamical systems*, volume I-III, New York, 1989. Cambridge University Press.

[188] J. Mulet and C. R. Mirasso. Numerical statistics of power dropouts based on the Lang-Kobayashi model. *Physical Review E*, 59(5):5400–5405, 1999.

[189] J. S. Nagumo, S. Arimoto, and S. Yoshizawa. An active pulse transmission line simulating nerve axon. *Proceedings of the IRE*, 50(10):2061–2070, 1962.

[190] R. Naud, N. Marcille, C. Clopath, and W. Gerstner. Firing patterns in the adaptive exponential integrate-and-fire model. *Biological Cybernetics*, 99(4):335–347, 2008.

[191] A. B. Neiman, P. I. Saparin, and L. Stone. Coherence resonance at noisy precursors of bifurcations in nonlinear dynamical systems. *Physical Review E*, 56(1):270–273, 1997.

[192] A. B. Neiman, A. Silchenko, V. Anishchenko, and L. Schimansky-Geier. Stochastic resonance: Noise-enhanced phase coherence. *Physical Review E*, 58(5):7118–7125, 1998.

[193] W. Nernst. Zur Kinetik der in Lösung befindlichen Körper. *Zeitschrift für physikalische Chemie*, 2:613–637, 1888. (in German).

[194] A. Ochab-Marcinek, G. Schmid, I. Goychuk, and P. Hänggi. Noise-assisted spike propagation in myelinated neurons. *Physical Review E*, 79(1):011904, 2009.

[195] K. Pakdaman, S. Tanabe, and T. Shimokawa. Coherence resonance and discharge time reliability in neurons and neuronal models. *Neural Networks*, 14(6):895–905, 2001.

[196] M. R. Park, J. W. Lighthall, and S. T. Kitai. Recurrent inhibition in the rat neostriatum. *Brain Research*, 194(2):359–369, 1980.

[197] T. K. D. M. Peron and F. A. Rodrigues. Collective behavior in financial markets. *EPL (Europhysics Letters)*, 96(4):48004, 2011.

[198] A. Pikovsky. Comment on "Asymptotic phase for stochastic oscillators". *Physical Review Letters*, 115:069401, 2015.

[199] A. Pikovsky, M. Rosenblum, and J. Kurths. *Synchronization*, volume 12 of *Cambridge Nonlinear Science Series*. Cambridge University Press, Cambridge, 2001.

[200] A. Pikovsky, A. Zaikin, and M. A. de La Casa. System size resonance in coupled noisy systems and in the ising model. *Physical Review Letters*, 88(5):050601, 2002.

[201] A. S. Pikovsky. On the interaction of strange attractors. *Zeitschrift für Physik B Condensed Matter*, 55(2):149–154, 1984.

[202] A. S. Pikovsky and J. Kurths. Coherence resonance in a noise-driven excitable system. *Physical Review Letters*, 78(5):775–778, 1997.

[203] H. E. Plesser and W. Gerstner. Noise in integrate-and-fire neurons: From stochastic input to escape rates. *Neural Computation*, 12(2):367–384, 2000.

[204] L. Pontryagin, A. Andronov, and A. Witt. *Zhurnal Eksperimental'noi i Teoreticheskoi Fiziki*, 3:165–180, 1933. Reprinted in *Noise in nonlinear dynamical systems*, 1989, ed. by F. Moss and P. V. E. McClintock (Cambridge University Press, Cambridge), vol. 1, pp. 329-348.

[205] D. E. Postnov, S. K. Han, T. G. Yim, and O. V. Sosnovtseva. Experimental observation of coherence resonance in cascaded excitable systems. *Physical Review E*, 59(4):R3791–R3794, 1999.

[206] D. E. Postnov, F. Müller, R. B. Schuppner, and L. Schimansky-Geier. Dynamical structures in binary media of potassium-driven neurons. *Physical Review E*, 80(3): 031921, 2009.

[207] C. Pouzat and A. Marty. Autaptic inhibitory currents recorded from interneurones in rat cerebellar slices. *The Journal of Physiology*, 509(3):777–783, 1998.

[208] J. R. Pradines, G. V. Osipov, and J. J. Collins. Coherence resonance in excitable and oscillatory systems: The essential role of slow and fast dynamics. *Physical Review E*, 60(6):6407–6410, 1999.

[209] M. Qian, G.-X. Wang, and X.-J. Zhang. Stochastic resonance on a circle without excitation. *Physical Review E*, 62(5):6469, 2000.

[210] D. C. Quick, W. R. Kennedy, and R. E. Poppele. Anatomical evidence for multiple sources of action potentials in the afferent fibers of muscle spindles. *Neuroscience*, 5(1):109–115, 1980.

[211] M. I. Rabinovich, H. D. I. Abarbanel, R. Huerta, R. Elson, and A. I. Selverston. Self-regularization of chaos in neural systems: Experimental and theoretical results. *IEEE Transactions on Circuits and Systems I*, 44(10):997–1005, 1997.

[212] P. Reimann, C. Van den Broeck, H. Linke, P. Hänggi, J. M. Rubi, and A. Pérez-Madrid. Diffusion in tilted periodic potentials: Enhancement, universality, and scaling. *Physical Review E*, 65(3):031104, 2002.

[213] M. B. Reyes, P. V. Carelli, J. C. Sartorelli, and R. D. Pinto. A modeling approach on why simple central pattern generators are built of irregular neurons. *PloS ONE*, 10(3):e0120314, 2015.

[214] F. Rieke, D. Warland, R. de R. van Steveninck, and W. Bialek. *Spikes*. Computational Neuroscience. MIT Press, Cambridge MA, 1997.

[215] A. Rinberg, A. L. Taylor, and E. Marder. The effects of temperature on the stability of a neuronal oscillator. *PLoS Computational Biology*, 9(1):e1002857, 2013.

[216] J. Rinzel and B. Ermentrout. Analysis of neural excitability and oscillations. In C. Koch and I. Segev, editors, *Methods in Neuronal Modeling*, pages 135–169, Cambridge MA, 1989. MIT Press.

[217] H. Risken. *The Fokker-Planck Equation*, volume 18 of *Springer Series in Synergetics*. Springer, Berlin, 2nd edition, 1996.

[218] W. Rümelin. Numerical treatment of stochastic differential equations. *SIAM Journal on Numerical Analysis*, 19(3):604–613, 1982.

[219] C. Runge. Ueber die numerische Auflösung von Differentialgleichungen. *Mathematische Annalen*, 46(2):167–178, 1895. (in German).

[220] R. Saada, N. Miller, I. Hurwitz, and A. J. Susswein. Autaptic excitation elicits persistent activity and a plateau potential in a neuron of known behavioral function. *Current Biology*, 19(6):479–484, 2009.

[221] J. A. Sanders, F. Verhulst, and J. Murdock. *Averaging Methods in Nonlinear Dynamical Systems*, volume 59 of *Applied Mathematical Sciences*. Springer, New York, 2nd edition, 2007.

[222] G. J. E. Santos, M. Rivera, and P. Parmananda. Experimental evidence of coexisting periodic stochastic resonance and coherence resonance phenomena. *Physical Review Letters*, 92(23):230601, 2004.

[223] R. A. Satterlie. Reciprocal inhibition and postinhibitory rebound produce reverberation in a locomotor pattern generator. *Science*, 229(4711):402–404, 1985.

[224] E. Schneidman, B. Freedman, and I. Segev. Ion channel stochasticity may be critical in determining the reliability and precision of spike timing. *Neural Computation*, 10(7):1679–1703, 1998.

[225] J. T. C. Schwabedal and A. Pikovsky. Phase description of stochastic oscillations. *Physical Review Letters*, 110(20):204102, 2013.

[226] T. Schwalger and B. Lindner. Patterns of interval correlations in neural oscillators with adaptation. *Frontiers in Computational Neuroscience*, 7(164):1–8, 2013.

[227] T. Schwalger and L. Schimansky-Geier. Interspike interval statistics of a leaky integrate-and-fire neuron driven by Gaussian noise with large correlation times. *Physical Review E*, 77(3):031914, 2008.

[228] T. Schwalger, K. Fisch, J. Benda, and B. Lindner. How noisy adaptation of neurons shapes interspike interval histograms and correlations. *PLoS Computational Biology*, 6(12):e1001026, 2010.

[229] T. Schwalger, J. Tiana-Alsina, M. C. Torrent, J. Garcia-Ojalvo, and B. Lindner. Interspike-interval correlations induced by two-state switching in an excitable system. *EPL (Europhysics Letters)*, 99(1):10004, 2012.

[230] A. I. Selverston and M. Moulins. Oscillatory neural networks. *Annual Review of Physiology*, 47:29–48, 1985.

[231] A. I. Selverston, D. F. Russell, J. P. Miller, and D. G. King. The stomatogastric nervous system: Structure and function of a small neural network. *Progress in Neurobiology*, 7(3):215–290, 1976.

[232] A. I. Selverston, M. I. Rabinovich, H. D. I. Abarbanel, R. Elson, A. Szűcs, R. D. Pinto, R. Huerta, and P. Varona. Reliable circuits from irregular neurons: A dynamical approach to understanding central pattern generators. *Journal of Physiology-Paris*, 94(5-6):357–374, 2000.

[233] S. Sergeyev, K. O'Mahoney, S. Popov, and A. T. Friberg. Coherence and anticoherence resonance in high-concentration erbium-doped fiber laser. *Optics Letters*, 35(22):3736–3738, 2010.

[234] H. S. Seung, D. D. Lee, B. Y. Reis, and D. W. Tank. The autapse: A simple illustration of short-term analog memory storage by tuned synaptic feedback. *Journal of Computational Neuroscience*, 9(2):171–185, 2000.

[235] A. A. Sharp, F. K. Skinner, and E. Marder. Mechanisms of oscillation in dynamic clamp constructed two-cell half-center circuits. *Journal of Neurophysiology*, 76(2): 867–883, 1996.

[236] L. J. Shiau, T. Schwalger, and B. Lindner. Interspike interval correlation in a stochastic exponential integrate-and-fire model with subthreshold and spike-triggered adaptation. *Journal of Computational Neuroscience*, 38(3):589–600, 2015.

[237] S. Shinomoto and Y. Kuramoto. Phase transitions in active rotator systems. *Progress of Theoretical Physics*, 75(5):1105–1110, 1986.

[238] E. Shlizerman and P. Holmes. Neural dynamics, bifurcations, and firing rates in a quadratic integrate-and-fire model with a recovery variable. I: Deterministic behavior. *Neural Computation*, 24(8):2078–2118, 2012.

[239] A. J. F. Siegert. On the first passage time probability problem. *Physical Review*, 81(4):617–623, 1951.

[240] G. Söhl, S. Maxeiner, and K. Willecke. Expression and functions of neuronal gap junctions. *Nature Reviews Neuroscience*, 6(3):191–200, 2005.

[241] I. M. Sokolov. Itô, Stratonovich, Hänggi and all the rest: The thermodynamics of interpretation. *Chemical Physics*, 375(2-3):359–363, 2010.

[242] B. Sonnenschein, M. A. Zaks, A. B. Neiman, and L. Schimansky-Geier. Excitable elements controlled by noise and network structure. *The European Physical Journal Special Topics*, 222(10):2517–2529, 2013.

[243] B. Sonnenschein, T. K. D. M. Peron, F. A. Rodrigues, J. Kurths, and L. Schimansky-Geier. Cooperative behavior between oscillatory and excitable units: The peculiar role of positive coupling-frequency correlations. *The European Physical Journal B*, 87(182):1–11, 2014.

[244] W. C. Stewart. Current-voltage characteristics of josephson junctions. *Applied Physics Letters*, 12:277–280, 1968.

[245] R. L. Stratonovich. A new representation for stochastic integrals and equations. *SIAM Journal on Control,*, 4(2):362–371, 1966.

[246] R.L. Stratonovich. *Topics in the theory of random noise Vol. II*, volume 3 of *Mathematics and Its Applications*. Gordon and Breach, New York, 1967.

[247] S. H. Strogatz. *Nonlinear Dynamics and Chaos*. Studies in Nonlinearity. Westview Press, Reading MA, 1994.

[248] A. Szűcs, R. D. Pinto, M. I. Rabinovich, H. D. I. Abarbanel, and A. I. Selverston. Synaptic modulation of the interspike interval signatures of bursting pyloric neurons. *Journal of Neurophysiology*, 89(3):1363–1377, 2003.

[249] G. Tamás, E. H. Buhl, and P. Somogyi. Massive autaptic self-innervation of GABAergic neurons in cat visual cortex. *The Journal of Neuroscience*, 17(16): 6352–6364, 1997.

[250] C. J. Tessone, A. Scirè, R. Toral, and P. Colet. Theory of collective firing induced by noise or diversity in excitable media. *Physical Review E*, 75(1):016203, 2007.

[251] P. J. Thomas and B. Lindner. Asymptotic phase for stochastic oscillators. *Physical Review Letters*, 113(25):254101, 2014.

[252] R. Toral, C. R. Mirasso, and J. D. Gunton. System size coherence resonance in coupled FitzHugh-Nagumo models. *EPL (Europhysics Letters)*, 61(2):162–167, 2003.

[253] G. M. Torrie and J. P. Valleau. Nonphysical sampling distributions in Monte Carlo free-energy estimation: Umbrella sampling. *Journal of Computational Physics*, 23 (2):187–199, 1977.

[254] J. Touboul. Bifurcation analysis of a general class of nonlinear integrate-and-fire neurons. *SIAM Journal on Applied Mathematics*, 68(4):1045–1079, 2008.

[255] J. Touboul and R. Brette. Dynamics and bifurcations of the adaptive exponential integrate-and-fire model. *Biological Cybernetics*, 99(4):319–334, 2008.

[256] A. Treves. Mean-field analysis of neuronal spike dynamics. *Network*, 4(3):259–284, 1993.

[257] K. Tsumoto, H. Kitajima, T. Yoshinaga, K. Aihara, and H. Kawakami. Bifurcations in Morris–Lecar neuron model. *Neurocomputing*, 69(4-6):293–316, 2006.

[258] H. C. Tuckwell. *Introduction to theoretical neurobiology*, volume 8 of *Cambridge Studies in Mathematical Biology*. Cambridge University Press, Cambridge, 2006.

[259] E. Urdapilleta. Onset of negative interspike interval correlations in adapting neurons. *Physical Review E*, 84(4):041904, 2011.

[260] O. V. Ushakov, H.-J. Wünsche, F. Henneberger, I. A. Khovanov, L. Schimansky-Geier, and M. A. Zaks. Coherence resonance near a hopf bifurcation. *Physical Review Letters*, 95(12):123903, 2005.

[261] H. Van Der Loos and E. M. Glaser. Autapses in neocortex cerebri: Synapses between a pyramidal cell's axon and its own dendrites. *Brain Research*, 48:355–360, 1972.

[262] N. G. van Kampen. Itô versus Stratonovich. *Journal of Statistical Physics*, 24(1): 175–187, 1981.

[263] R. de R. van Steveninck, G. D. Lewen, S. P. Strong, R. Köberle, and W. Bialek. Reproducibility and variability in neural spike trains. *Science*, 275(5307):1805–1808, 1997.

[264] T. Verechtchaguina, I. M. Sokolov, and L. Schimansky-Geier. First passage time densities in resonate-and-fire models. *Physical Review E*, 73(3):031108, 2006.

[265] C. von Euler. On the central pattern generator for the basic breathing rhythmicity. *Journal of Applied Physiology*, 55(6):1647–1659, 1983.

[266] J. A. White, J. T. Rubinstein, and A. R. Kay. Channel noise in neurons. *Trends in Neurosciences*, 23(3):131–137, 2000.

[267] C. J. Wilson, A. Weyrick, D. Terman, N. E. Hallworth, and M. D. Bevan. A model of reverse spike frequency adaptation and repetitive firing of subthalamic nucleus neurons. *Journal of Neurophysiology*, 91(5):1963–1980, 2004.

[268] A. T. Winfree. Biological rhythms and the behavior of populations of coupled oscillators. *Journal of Theoretical Biology*, 16(1):15–42, 1967.

[269] A. T. Winfree. *The Geometry of Biological Time*, volume 12 of *Interdisciplinary Applied Mathematics*. Springer, New York, 2nd edition, 2001.

[270] J. Wojcik, R. Clewley, and A. Shilnikov. Order parameter for bursting polyrhythms in multifunctional central pattern generators. *Physical Review E*, 83(5):056209, 2011.

[271] E. Wong. *Stochastic Processes in Information and Dynamical Systems*. McGraw-Hill series in systems science. McGraw-Hill, New York, 1971.

[272] S. Wu, W. Ren, W. R. Kaifen He, and Z. Huang. Burst and coherence resonance in Rose-Hindmarsh model induced by additive noise. *Physics Letters A*, 279(5-6): 347–354, 2001.

[273] Y. Xu, R. Gu, H. Zhang, W. Xu, and J. Duan. Stochastic bifurcations in a bistable Duffing–Van der Pol oscillator with colored noise. *Physical Review E*, 83(5):056215, 2011.

[274] L. Yang, Z. Hou, and H. Xin. Stochastic resonance in the absence and presence of external signals for a chemical reaction. *The Journal of Chemical Physics*, 110(7): 3591–3595, 1999.

[275] A. Zakharova, T. Vadivasova, V. Anishchenko, A. Koseska, and J. Kurths. Stochastic bifurcations and coherencelike resonance in a self-sustained bistable noisy oscillator. *Physical Review E*, 81(1):011106, 2010.

[276] A. Zakharova, A. Feoktistov, T. Vadivasova, and E. Schöll. Coherence resonance and stochastic synchronization in a nonlinear circuit near a subcritical hopf bifurcation. *The European Physical Journal Special Topics*, 222(10):2481–2495, 2013.

[277] M. A. Zaks, A. B. Neiman, S. Feistel, and L. Schimansky-Geier. Noise-controlled oscillations and their bifurcations in coupled phase oscillators. *Physical Review E*, 68(6):066206, 2003.

[278] B. W. Zhang, D. Jasnow, and D. M. Zuckerman. The "weighted ensemble" path sampling method is statistically exact for a broad class of stochastic processes and binning procedures. *The Journal of Chemical Physics*, 132(5):054107, 2010.

[279] G. Zheng and A. Tonnelier. Chaotic solutions in the quadratic integrate-and-fire neuron with adaptation. *Cognitive Neurodynamics*, 3(3):197–204, 2009.

Acknowledgement

First of all, I would like to thank Lutz Schimansky-Geier, who gave me this interesting topic and took the time for various helpful discussions and critical remarks. I also like to thank him for all the scientific and human support during the last years. At second, I would like to acknowledge Benjamin Lindner, who supported my work with many interesting ideas, his great knowledge in the field of neurophysics, and offered me financial support subsequent to my PhD fellowship from the International Research Training Group 1740. Third, I would like to thank Reynaldo Daniel Pinto for several fruitful discussions on neurons in the pyloric central pattern generator, the great time in Brazil, and the deep insight, I could get, into the experiments and the gap between conceptional models and real neurons. Furthermore, I would like to thank him for providing the data for the pyloric dilator neuron.
I would also like to thank Alexander Neiman and Rául Toral for several fruitful discussions and Robert C. Elson for providing the data for the isolated pyloric dilator neuron.

The results presented in this thesis have been developed at the Humboldt-Universität zu Berlin in Germany and at the University of São Paulo in São Carlos, Brazil. In this context I would like to thank the members of the Brazil group for the great time in São Carlos. In particular, I would like to acknowledge Matias Paulo, Rafael Tuma Guariento, Lirio Almeida, and Thomas Peron for their extensive support during the time in Brazil. Furthermore, I would like to thank Bóris Marin for helpful discussions on the work on the pyloric neurons.
On the German side, I would like to acknowledge Steffen Martens, who helped me to improve my knowledge on stochastic processes and Martin Rückl who was never tired to suggest improvements for my simulation algorithms. Furthermore, I would like to thank Christian Schmeltzer, Bernard Sonnenschein, and Felix Thiel for many helpful discussions.

I would also like to thank David Hansmann, who supported me organizing the bureaucratic efforts during my PhD studies. Finally, I thank my family for their persistent support during the last years.

Selbständigkeitserklärung

Ich erkläre, dass ich die vorliegende Arbeit selbständig und nur unter Verwendung der angegebenen Literatur und Hilfsmittel angefertigt habe.

Berlin, den 27. Oktober 2015 Justus Alfred Kromer